Generation and application of dynamic gratings in optical fibers using stimulated Brillouin scattering

PAR

Nikolay PRIMEROV

ÉCOLE POLYTECHNIQUE
FÉDÉRALE DE LAUSANNE

Suisse
2013

To my parents and Denise Bayard

"The most beautiful thing we can experience is the mysterious. It is the source of all true art and all science. He to whom this emotion is a stranger, who can no longer pause to wonder and stand rapt in awe, is as good as dead: his eyes are closed."

Albert Einstein

Abstract

Since the invention of optical fiber cable data transmission using light has become ubiquitous in the past years. Nonlinear optical effects, which are hardly noticed in our daily life, have become crucial and highly influential for the design and performance of advance high-capacity systems. Future optical systems will definitely require signal processing operations to be performed on data signals "on the fly" solely in the optical domain. Brillouin scattering is currently one of the most prominent nonlinear effects in optical fibers, as it has found many applications in various fields of photonics, such as slow light, new high coherent sources, filters, optical fiber sensing, etc. In this thesis we investigate a novel phenomenon based on Stimulated Brillouin Scattering, which is called dynamic Brillouin grating (DBG). Investigating the process of DBG generation in optical fibers we propose several new approaches to realize new tools for signal processing of the optical signal by using phonon-photon interactions.

First an analytical model is proposed to describe localized DBG generation in optical fibers using three coupled equations for Stimulated Brillouin Scattering. Based on this model we can show how the grating is generated and which shape it has in time when two pump pulses are used with optical frequency difference equal to the Brillouin shift of the fiber. Moreover optical phase conjugation is also theoretically predicted for the optical wave reflected from DBG.

Several applications of Dynamic Brillouin grating are identified and investigated.

An optical signal delay line or buffer is proposed and experimentally demonstrated using DBG principle. Storage of an input optical pulse is achieved by changing the position of the localized DBG inside the fiber. Here DBG acts as a Bragg reflector for the optical pulse and change in DBG position defines the time-of-flight of the input and reflected pulse. Single pulse delays can be dynamically controlled with a buffer capacity ranging from several picoseconds to more than one microsecond. Such delays show that DBG based signal delay lines can easily outperform slow light based delay lines in terms of delay-bandwidth product. Optical delay of pulse trains is also achieved, but with maximum limited amount of delay governed by the acoustic wave decay constant, which in standard silica fibers is around 10-12 ns. Moreover microwave photonic signals can be also delayed using DBG demonstrating true time delay. In this configuration, the reflection bandwidth of the DBG defines the maximum operational radio frequency. Relation of the DBG bandwidth as a function of its length was measured and it was determined that DBG exhibits similar properties as weak uniform fiber Bragg grating (FBG).

Another application of the DBG gratings is demonstrated by exploiting this phenomenon to realize microwave photonic filters. For the first time, two-, three- and four-tap microwave photonic filter configurations are realized based on DBG. Free spectral range and

stop band central frequencies of the proposed microwave filters can be easily tuned by adjusting the properties and positions of DBGs.

Dynamic gratings generated by amplitude modulated pump waves are used to realize optical differentiation, integration and time reversal of input optical signals. Performed experiments demonstrate that a DBG based signal processor performs operations on the complex amplitude of the input optical wave. The DBG based integrator offers high flexibility in terms of operational wavelength and variable integration time, which can be controlled by changing the DBG length. For the first time, new operations of true time reversal of several bit sequences are performed using dynamic Brillouin grating.

To overcome the problem of the decay of the localized acoustic grating, a novel method based on phase modulation by pseudo-random bit sequence (PRBS) is proposed, which allows generation of localized and stationary DBG at random positions inside the fiber. Such a method opens up new possibilities for signal control, and for optical fiber sensing. Advantages and limitations of the PRBS technique in terms of signal-to-noise ratio are discussed. It is experimentally verified that PRBS generation of DBG is highly attractive for the operations on optical signals where time averaging is possible, such as in the fields of microwave photonics and distributed fiber sensing. On the other hand, it was experimentally verified that realization of the optical buffer for continuous digital data using the PRBS technique is difficult due to the substantial amount of instantaneous noise.

A separate chapter of this thesis is devoted to the application of DBG to the field of distributed fiber sensing. A DBG based distributed temperature and stress sensor in polarization maintaining fibers has been realized, showing 1 cm spatial resolution, which is - to the best of our knowledge - first time, demonstrated using a pulsed-based Brillouin sensor. The demonstration is performed in a 20 m fiber, but the sensing range of the proposed DBG based sensor can be expanded up to several hundred meters. In addition, it is shown that the demonstrated spatial resolution is not the ultimate limit, and a finer spatial resolution can be achieved by simply reducing the probe pulse duration.

Another Brillouin distributed temperature and stress sensor is proposed based on the DBG principle. Here DBG is generated by modulating the phases of a continuous Brillouin pump and probe waves by common PRBS with unipolar encoding and modulation speeds faster than phonon lifetime. By choosing the proper parameters of PRBS, only one localized and permanent dynamic Brillouin grating is placed inside the sensing fiber. Distributed measurements of temperature or strain are accomplished by scanning the position of the DBG inside the fiber and determining the Brillouin resonance condition at each position. Using this technique, a random access sensor with 1 cm spatial resolution is demonstrated over a 40 m standard single mode fiber. In the proposed scheme the spatial resolution can be easily changed by changing the bit duration of the PRBS, while the measurement range is controlled by the length of the PRBS sequence.

Keywords: fiber optics, nonlinear fiber optics, Brillouin scattering, dynamic Brillouin grating, delay line, optical signal processing, optical fiber sensors

Version abrégée

L'utilisation de la fibre optique pour transmettre l'information à l'aide de la lumière est omniprésente dans notre société depuis plusieurs années. Les phénomènes d'optique non linéaire, qui sont à peine remarqués dans notre vie quotidienne, sont devenus indispensables pour la conception et le développement de systèmes de transmission à hauts débits. Les futurs systèmes de transmission par fibres optiques requièrent des opérations de traitement du signal « à la volée » où le traitement serait effectué directement sur les signaux optiques. La diffusion Brillouin qui est un des effets non linéaire les plus important dans les fibres optiques a su trouver de nombreuses applications dans les domaines de la photonique comme la lumière lente, la génération de sources très fortement cohérentes, les filtres ou encore les capteurs à fibres optiques. Dans cette thèse, nous présentons un nouveau phénomène, basé sur la diffusion Brillouin stimulée, qui est appelé réseau dynamique Brillouin (DBG, Dynamic Brillouin Grating). En se basant sur le processus de réseau dynamique Brillouin dans les fibres optiques, nous proposons plusieurs approches pour réaliser de nouveaux outils de traitement du signal optique en utilisant les interactions phonon/photon.

Tout d'abord, un modèle analytique est proposé pour décrire la génération localisée des réseaux dynamiques Brillouin dans les fibres optiques en utilisant les trois équations couplées décrivant la diffusion Brillouin stimulée. Sur la base de ce modèle, on peut voir comment le réseau est généré et quel est son évolution au cours du temps lorsque deux impulsions optiques dont la différence de fréquence correspond au décalage Brillouin de la fibre sont utilisés. En outre, le phénomène de conjugaison de phase optique est également prédit pour une onde optique réfléchie par le réseau dynamique.

Ensuite, plusieurs applications des réseaux dynamiques Brillouin sont présentées et analysées.

Une ligne à retard optique ou 'mémoire optique' est proposée et démontrée expérimentalement en utilisant le principe du DBG. Le stockage d'une impulsion optique est obtenu en changeant la position du réseau dynamique Brillouin à l'intérieur de la fibre. Dans ce cas, le DBG agit comme un réflecteur de Bragg pour l'impulsion optique et le changement de position du DBG définit le temps de vol de l'impulsion d'entrée et de l'impulsion réfléchie. Le délais d'une impulsion unique peut être contrôlé de manière dynamique avec une capacité de stockage allant de quelques picosecondes à plusieurs microsecondes. Ces retards montrent que l'utilisation de DBG pour la création de ligne à retard peut facilement surpasser les lignes à retard basés sur les effets de lumière lente en regardant le produit délais par bande passante.

Le retard optique de trains d'impulsions est également atteint, mais le délais est limité par le temps d'amortissement de l'onde acoustique qui est de l'ordre de 10-12ns pour une fibre optique de télécommunication standard. Néanmoins, les signaux micro-ondes photoniques peuvent également être retardés à l'aide du DBG démontrant ainsi un réel délais. Dans cette

configuration, la largeur de bande de réflexion du réseau dynamique définie la fréquence radio maximale. La mesure expérimentale de la relation liant la bande passante du réseau dynamique à sa longueur a démontré qu'un DBG présente des propriétés similaires à celles d'un réseau uniforme de fibres à réseau de Bragg (FBG, Fiber Bragg Grating).

Une autre application des réseaux DBG est démontrée en créant des filtres micro-ondes photoniques. Pour la première fois, plusieurs configurations de filtres micro-ondes photoniques sont réalisées à l'aide d'un réseau dynamique Brillouin. La plage spectrale et les fréquences de la bande d'arrêt centrale des filtres hyperfréquences peuvent être facilement réglées en ajustant les propriétés et les positions des DBGs.

De plus, les réseaux dynamiques générés par la modulation d'amplitude des ondes optiques sont utilisés pour réaliser l'intégration et le renversement temporel de signaux optiques. Les expériences ont démontré que le DBG agis sur l'amplitude complexe de l'onde optique incidente. L'intégrateur à base DBG offre une grande souplesse en termes de longueur d'onde de fonctionnement et le temps d'intégration peut être commandé en changeant la longueur du réseau dynamique Brillouin. Pour la première fois, des expériences de retournement temporel de plusieurs séquences de bits sont effectuées à l'aide d'un réseau dynamique Brillouin.

Pour contourner la désintégration du réseau acoustique localisé une nouvelle méthode basée sur la modulation de phase par une séquence binaire pseudo-aléatoire (PRBS, pseudorandom binary sequence) est proposée. Elle permet la génération de DBG qui sont à la fois localisés et fixes à des positions aléatoires le long de la fibre optique. Cette méthode ouvre de nouvelles possibilités pour le contrôle des signaux optiques, et pour les capteurs à fibres optiques. Dans le manuscrit, les avantages et les limites de la technique PRBS en termes de rapport signal-sur-bruit sont discutés. Il est vérifié expérimentalement que la génération de réseau dynamique Brillouin par signaux PRBS est très attractif pour les opérations sur les signaux optiques où la moyenne temporelle est possible, comme les domaines de la photonique micro-ondes où des capteurs distribuées à fibres optiques. D'autre part, il a été expérimentalement vérifié que la réalisation de mémoire optique pour des données numériques en utilisant la technique PRBS est difficile en raison de la quantité importante de bruit instantané.

Par ailleurs, un chapitre distinct de cette thèse est consacré à l'application des DBG dans le domaine des capteurs distribués à fibres optiques. Un capteur à base de réseau dynamique Brillouin distribué pour la mesure de la température et des contraintes mécaniques dans les fibres à maintien de polarisation a été réalisé avec une résolution spatiale de 1 cm. C'est à notre connaissance la première fois qu'une telle résolution est atteinte à l'aide d'un capteur Brillouin pulsé. La démonstration est réalisée dans une fibre d'une longueur de 20 m, mais la plage de détection du capteur DBG peut être étendue jusqu'à plusieurs centaines de mètres. En outre, il est démontré que la résolution spatiale peut être améliorée en réduisant simplement la durée des impulsions.

Un autre capteur distribué Brillouin de température et de contrainte mécanique est proposé et repose également sur le principe du DBG. Ici le DBG est généré en modulant

d'une part la phase d'une onde optique continue et d'autre part les ondes de sonde par PRBS avec un codage unipolaire et des vitesses de modulation plus rapides que la durée de vie des phonons. En choisissant les paramètres appropriés des signaux PRBS, un seul réseau dynamique Brillouin localisé et permanent est présent à l'intérieur de la fibre optique. Les mesures distribuées de températures ou de contraintes sont réalisées par balayage de la position du DBG à l'intérieur de la fibre et la détermination de la condition de résonance Brillouin à chaque position. Grâce à cette technique, un capteur distribué avec une résolution spatiale de 1 cm à l'aide d'une fibre optique monomode de 40 m est démontré. Dans le schéma proposé la résolution spatiale peut être facilement ajustable en modifiant la durée des bits des signaux PRBS et la plage de mesure est contrôlée par la longueur de la séquence PRBS.

Mots-clés: fibres optiques, fibres optiques non linéaires, diffusion Brillouin, réseau Brillouin dynamique, ligne à retard optique, traitement du signal, capteurs à fibres optiques

Acknowledgement

I must avow that during my last 4-5 years while working on this thesis I had one of the best times of my life and I met so many wonderful people. I would like to thank many of them here, since this thesis would not have been possible without them. My life palette became richer with "colors" from all these people. First of all I would like to especially thank and express my sincere gratefulness to my thesis advisor Prof. Luc Thévenaz. He believed in me and gave me this amazing opportunity to work in his group. Luc is great person, great researcher and wonderful supervisor. He always found time for my questions and gave me valuable advice which deepened my understanding of the problem. He is also an excellent teacher. His explanations about complex problems are detailed and very intuitive, and he tries to look at the question from different angles. I very much enjoyed our discussions on various topics ranging from research to private life.

Special thanks go to my very good friend and my unofficial supervisor, Dr. Sanghoon Chin. Thanks to him I learned how to work in the lab. Basically, he taught me everything I know about working in the lab. He spent so much time explaining to me how all the equipment in the lab works. I learned something new from every single conversation we have had. He always welcomes my questions and he spent his time explaining to me every single detail of the question. He gave me so many new interesting ideas to try out. His enthusiasm and his passion to try new things were very inspiring to me and we did many experiments together. It was the greatest experience and pleasure to work with him.

I also would like to greatly thank all the jury members who agreed to read this manuscript Prof. Kwang Yong Song from the Chung-Ang University in South Korea, Prof. Marco Santagiustina from University of Padova in Italy, Prof. Camille Sophie Brès from EPFL, and Prof. Olivier Martin from EPFL.

Special thanks go to Prof. Moshe Tur from Tel Aviv University in Israel. I had the chance to work with him during his summer visit in our group in 2009. I also worked in his lab during my scientific mission in December 2009 and I had a great time and met very nice people there. Moreover I would like to express my truly gratefulness to Prof. Avinoam Zadok from Bar-Ilan University in Israel. He is a brilliant researcher and an amazing person. It was an honor for me to work with him during his stay in our group in the summer of 2012. I admire his ability to quickly understand the essence of the concept and propose an original solution. I enjoyed discussing different topics with him, both scientific and personal. I really value his opinion on many things in this world. I would like to greatly thank Prof. Kwang Yong Song for his very fruitful collaboration during his stay in our group. His priceless advice and clear directions helped me to conduct many successful experiments. I would like to spend more time with such people because I feel like I learn every second.

Extensive help during my Ph.D. was provided by my previous colleagues in the Group for Fiber Optics (GFO). Thanks go to: Dr. Jean-Charles Beugnot, Dr. Stella Foaleng Mafang, and Dr. Isabelle Dicaire for their support and interesting discussions during lunch and coffee breaks. I also would like to thank current members of GFO: Marcelo, Mehdi, Andrey and Xin – your help is greatly appreciated. I enjoyed our discussions about life and science. My warm gratitude goes to Paulou Pierrette, secretary of the photonics doctoral school, for her assistance with all my troubles concerning administrative issues and for her friendly and understanding attitude. I also highly appreciate the help and versatile assistance of the secretary of our group Alexandra Morrison.

I would like to separately thank three very talented young researchers with whom I had the pleasure to collaborate with during my Ph.D. Dr. Juan Sancho and Dr. Juan Lloret from Optical and Quantum Communication Group at Polytechnical University of Valencia spent their time and energy to explain many physical phenomena to me. I enjoyed spending time with them during our trips to conferences and meetings. Yair Antman, or simply "Matlab master", from Bar-Ilan University in Israel deserves my deep appreciation for his support and friendly working atmosphere. I hope our friendship will last for many years. I'm proud that I have friends like you guys.

I also would like to thank my climbing buddies with whom I spent most of my free time in the beautiful Swiss mountains. I'm thankful to my friends Samuel Arey, Olov Isaksson, Thomas Riss-Johannessen, Stephan Kontos, and Kristen Lorentz. Spending free time with these guys was always fun and relaxing. I'll never forget it. Other friends I met in EPFL also deserve my sincere appreciation. I thank Sean Costello for his support with my thesis and for his unchangeable positive and optimistic attitude. Thanks to Evgeny Bogdanov for his support and long discussions about sport, life and new ideas. Thanks also go to Ekaterina Gelman, Andrey Laktionov, Marc Calaf, and Marc Diebold. My previous scientific advisor Prof. Liya Zhukova, and my previous colleagues Dr. Alexandr Korsakov and Andrey Chazov deserve my gratitude for their support. In addition I would like thank my close friends from Russia, Evgeny Shirokov, Alexandr Kosterin, Ilya Bublik, Sergey Sinicin, Oleg Konovalov, Alexey Zotov, Evgeniya and Olesya Roslavtcevi, Nadya Netsvetaeva and others, for their friendship and continuous support despite the great distance. I want to express my sincere gratitude to Kseniia Sheyko who became a very good friend to me. She offered a lot of support, help and understanding during difficult times and also during the tough period of writing this thesis.

Last but not least, I express my warmth thankfulness to my parents for their endless support, encouragement and motivation. They were there for me in good and bad times. They raised me in the atmosphere of love, understanding and respect for nature. Special thanks go to my brothers Daniil and Pavel. Even though I missed them a lot during my Ph.D. they helped me and supported me in all my decisions.

Finally I would like to thank one person who played very crucial role in my life. Actually, thanks to her I have done the most valuable projects in my life so far including this Ph.D. dissertation. Her name is Denise Bayard. She is unique person and I am happy that I

met her during my life. I admire her ability to do various things at the highest level. She is an exceptional medical doctor and at the same time a passionate mountaineer. I owe her my deepest appreciations for all her support and love she gave me. I would like also to thank her family. They were helping me in every situation. Moments spend with them are unforgettable, and I will keep them in my heart preciously through all my life.

Content

List of Figures

List of Tables

Chapter 1

Introduction

The work presented in this thesis was only possible thanks to the series of discoveries and inventions which have happened over nearly one century. Two physicists played a crucial role in the development of physics of molecular light scattering, or generally, speaking by the fluctuations of physical quantities that give rise to optical inhomogeneities. The brilliant theoretician Leon Brillouin, used results of Einstein's work on heat capacity and Debye theory of heat capacity of solids to derive and theoretically describe that light can be scattered on fluctuations of the crystalline lattice of the material [1]. At the same time, the Russian physicist and very skillful experimenter L.I. Mandelstam worked on the propagation of electromagnetic waves in different media. These two scientists deserve equal attention when discussing the history of light scattering, while in many publications and books the name of Russian physicist is not mentioned. The reason for this lies mainly in the inherent to L.I. Mandelstam exceptional demand on himself and thoroughness, because of which he did not publish new discoveries before subjecting them to multiple verifications. Moreover, lack of communication between the Russian and the European scientific communities at that time was obvious. L.I. Mandelstam is widely known as the author of many works in physics. Just to mention few, while working with another Russian physicist G. S. Landsberg, L.I. Mandelstam made a great theoretical and experimental contribution to the fields of combinational light scattering (now known as Raman scattering), predicted and explored the fine structure of the Rayleigh line, investigated resonance scattering in vapors, and contributed to many other fields of physics. It should be pointed out that Mandelstam worked on the theory of spectrum of light scattered by a condensed medium as early as 1918, as mentioned by his colleague G.S. Landsberg [2, 3]. Already at this time he discussed with Landsberg about frequency shift of the scattered light, while publishing a full article on the subject much later in 1926 [4]. In this thesis we adhere to the conventional definition of scattered light from the density fluctuations in a medium as Brillouin scattering while we imply the so-called Brillouin-Mandelstam scattering.

As a chair of the Physics Department of Moscow State University and after his theoretical prediction of scattered light, Mandelstam formulated the task of the experimental detection of the fine-structure splitting of Rayleigh line in 1925. The experimental discovery was made several years later by the Russian experimentalist E.F. Gross, who worked at the State Optical Institute in Leningrad and was colleague of Mandelstam and Landsberg [5]. Due to the poor experimental equipment at this time, the observation of the fine structure of the scattered light was obstructed and required enormous experimental effort. With the invention of intense and narrow lasers in the 1960's Stokes and anti-Stokes components of the Brillouin scattering were observed and investigated in various media. Further experiments with

Brillouin scattering by I. L. Fabelinskii revealed that Brillouin scattering could be used to study acoustical and kinetic properties of gases, liquids and solids [6].

Several years later, developments of coherent optical sources and semiconductor materials revealed that optical glass fiber can be used to transmit information if the losses can be reduced. While working on this topic in 1969, Charles Kao convinced himself and later the whole communication society that purified fused silica can be used as highly efficient, low loss light communication media. Nowadays, thanks to Kao's invention, practically all information transport is realized using fiber-optic communication systems at extremely high data rates.

Brillouin scattering in optical fibers was first observed in 1964 by Chiao, slightly later than another inelastic scattering process, so-called Raman scattering [7]. With the fast development of the telecommunication industry, scattering processes were identified as unwanted effects for optical signal transmission since they were limiting the maximum transmitted power through the glass fiber. Stimulated Brillouin scattering (SBS) was discovered to have the lowest threshold power to occur. Since light propagates in optical fibers over many kilometers, spontaneous process may turn into stimulated process which can scatter most of the input light intensity. Geometry of the fiber basically defines two propagation directions of the scattered light – forward and backward. It turned out that forward Brillouin scattering is negligible in optical fibers, while backward scattering can generate a high-intensity Stokes wave in the direction opposite to the incident light. In communication systems various precautions are taken in order to avoid the effect of Brillouin scattering, such as building a communication link with concatenated short length fiber segments with different Brillouin frequency shifts, or phase modulating the incident light.

Even though SBS is considered a detrimental effect in optical communication systems, it can be also used for various useful applications. For example, SBS has been used to demonstrate Brillouin fiber lasers, where the laser output linewidth is narrower than the linewidth of the pump light used to feed the laser [8, 9]. Additionally, since Brillouin gain is very narrow, SBS can be used for efficient narrowband amplification. Such amplifiers find their application in microwave photonics, radio-over-fiber technology and optical fiber sensing [10-12]. The anti-stokes resonance in SBS can be also used as an adjustable narrow filter [13, 14]. Another interesting field of SBS application is slow light, which has been intensively investigated in recent years [15]. Since SBS process can induce a resonance in the optical fiber group index inside this resonance can be changed. Moreover, simply by controlling the pump power, the induced dispersion inside the Brillouin resonance can be controlled in a convenient way. This way depending on the induced dispersion, the group index can be increased (slow light) or decreased (fast light) consequently reducing or increasing the group velocity of the signal, respectively. Even though SBS based slow light was initially viewed as a potential mechanism to realize all-optical buffers, it was demonstrated that the storing capacity is rather limited due to the high signal distortion. On the other hand, SBS slow light was successfully implemented for other applications such as jitter compensation, synchronization of data packets, microwave photonics, etc. [16-19].

Another field of SBS application deserves special attention. Optical fiber sensors based on SBS were developed as early as 1989, and demonstrated their unique ability to perform distributed measurements of temperature and stress along the fiber [20]. More than two decades of research and development in this field substantially increased the performance of the SBS sensors. Nowadays SBS sensors are capable to measure at each meter temperature/strain changes for instance over 50 km distance, replacing 50'000 point sensors [21]. On the other extreme, Brillouin optical sensors can be used to measure distributed temperature/strain profiles with cm spatial resolution, but over a relatively short distance of several hundred meters [22].

Nowadays optical communication systems handle large amounts of data traffic over very long distances. In addition, the bit-rate distance product for optical fibers has grown exponentially over the last 30 years. Using dense wavelength division multiplexing technology speeds of data rates in the optical fiber rise up to 100 Gbits/s and higher, which is well beyond the current speeds of commercial electronics. Moreover, systems operating at the limit of electrical components need to be parallelized to process high data rate signals. Such sophisticated systems consume enormous amounts of power and require even more power to remove the generated heat. Obviously, alternative solutions are required. For this reason various nonlinear optical effects have been proposed to perform operations on high speed data channels. Cross gain modulation, self-phase modulation, and four-wave mixing together with interferometry techniques have been implemented to replace several functions previously performed in the electrical domain.

In this thesis we propose a novel phenomenon called Dynamic Brillouin Grating (DBG) [23]. The first objective of this thesis is to investigate and experimentally generate dynamic Brillouin grating in birefringent media such as polarization maintaining fiber (PMF) using the process of Stimulated Brillouin Scattering (SBS). DBG is essentially an acoustic wave which can be generated using two counter-propagating optical pump waves in one polarization of a PMF by using ordinary SBS process. The same DBG can be exploited as a Bragg reflector for the orthogonally polarized signal wave with the optical frequency different from that of the pump waves when the phase matching condition for Bragg reflection is met. The possibility of separating the two processes of DBG generation and interrogation opens up a broad range of interesting applications in the field of photonics, which were previously impossible to realize in optical fibers.

The second objective of this thesis is to investigate the properties of DBG to identify possible applications and to experimentally test the applicability of DBG. Several novel optical fiber systems based on dynamic Brillouin grating are realized, such as:

- an optical delay line with tunable storage time of more than one microsecond;
- a multi-tap microwave photonic filters with easily tunable filter response, free spectral range, and central stop frequency;
- an all-optical signal processor capable to produce integration, differentiation, and time reversal functionalities on optical signals;

- a distributed sensor with extremely fine spatial resolution and in addition with truly random access.

The content of this thesis is organized in the following order.

Chapter 2 describes several optical effects that occur when a light wave propagates along an optical fiber. The linear effect of dispersion for a signal in form of an optical pulse is described. In the second part of the chapter several nonlinear effects are described, such as four wave mixing, self-phase modulation and cross-phase modulation. Moreover light scattering mechanisms are described with particular emphasis on Brillouin scattering. Two types of Brillouin scattering, spontaneous and stimulated, are reviewed. In the last section several applications of nonlinear fiber effects for controlling optical signals are reviewed.

Chapter 3 is devoted to the phenomenon of dynamic Brillouin grating, which is the main object of exploration of this thesis. Firstly, the generation of DBG in polarization maintaining fibers is demonstrated where the dynamic grating can be generated using optical waves in one polarization, and interrogated using an optical wave in the orthogonal polarization with a distinct optical frequency. An analytical model of the dynamic Brillouin grating generation using pulsed pump waves is presented to better understand the shape and properties of the localized acoustic grating. The last part of the chapter is devoted to a short description of the unique property of the dynamic grating such as phase conjugation.

Chapter 4 describes the experimental part of this thesis. The application of dynamic Brillouin grating is demonstrated to realize an optical delay line for isolated pulses, for a train of pulses, and for optical waves carrying a microwave signal. Additionally, the bandwidth of the generated Brillouin grating is investigated as a function of grating length. A further alternative technique, to generate local and stationary DBG is presented. This method is based on the phase modulation of the optical waves involved in the DBG generation using a common pseudo-random bit sequence. The grating reflectivity as a function of the DBG length is measured using the PRBS method. Several implementations of microwave photonic filters are experimentally demonstrated using DBG, showing a tunability of both the free spectral range and the central frequency. In the last part of this chapter, DBG is explored to realize an all-optical signal processor. Basic functionalities, such as optical differentiation and integration, are successfully demonstrated. In addition, the possibility to perform true time reversal using DBG is experimentally verified.

Finally chapter 5 describes the conclusions and perspectives of the new phenomena.

Bibliography

1.   L. Brillouin, "Diffusion of Light and X-rays by a Transparent Homogeneous Body," Annals of Ph **17**, 88-122 (1922).
2.   G. I. Landsberg, in *Izbrannie Trudi*(Izd. Akad. Nauk SSSR, 1958).
3.   G. S. Landsberg, "Molecular scattering of light," Yubileinyi Sbornik (1947).
4.   L. I. Mandelstam, "Light scattering by inhomogeneous media," Zh. Russ. Fiz.-Khim. Obshch. **58**, 381 (1926).
5.   E. Z. Gross, "On variation of the wavelength upon scattering of light by crystals," Zeitschrift fur Physik **63**, 685 (1930).
6.   I. L. Fabelinskii, *Molecular Scattering of Light* (Plenum press, New York, 1968).
7.   R. Y. Chiao, C. H. Townes, and B. P. Stoicheff, "Stimulated Brillouin Scattering and Coherent Generation of Intense Hypersonic Waves," Physical Review Letters **12**, 592-595 (1964).
8.   J. C. Yong, L. Thevenaz, and B. Y. Kim, "Brillouin fiber laser pumped by a DFB laser diode," Journal of Lightwave Technology **21**, 546-554 (2003).
9.   G. Jihong, S. Staines, W. Zuolan, Z. Jie, M. Blake, and J. Shibin, "Highly stable low-noise Brillouin fiber laser with ultranarrow spectral linewidth," Photonics Technology Letters, IEEE **18**, 1813-1815 (2006).
10.   X. S. Yao, "Brillouin selective sideband amplification of microwave photonic signals," Photonics Technology Letters, IEEE **10**, 138-140 (1998).
11.   L. Thévenaz, "Brillouin distributed time-domain sensing in optical fibers: state of the art and perspectives," Frontiers of Optoelectronics in China **3**, 13-21 (2010).
12.   M. Junker, T. Schneider, M. J. Ammann, A. T. Schwarzbacher, and K.-U. Lauterbach, "Carrier Generation in the Millimetre Wave Range based on Stimulated Brillouin Scattering for Radio over Fibre Downlink Systems," in *Irish Signals and Systems Conference, 2006. IET*(2006), pp. 191-195.
13.   C. H. Yeh, C. W. Chow, Y. F. Wu, F. Y. Shih, Y. F. Liu, Y. H. Lin, J. Y. Sung, and C. L. Pan, "Employing SBS-assisted filter and FWM effect to achieve quadruple-wavelength output," in *Information Photonics and Optical Communications (IPOC), 2011 International Conference on*(2011), pp. 1-3.
14.   T. Tanemura, Y. Takushima, and K. Kikuchi, "Narrowband optical filter, with a variable transmission spectrum, using stimulated Brillouin scattering in optical fiber," Opt. Lett. **27**, 1552-1554 (2002).
15.   S. H. Chin, "Governing the speed of a light signal in optical fibers: Brillouin slow and fast light," (Ecole Polytechnique Fédérale de Lausane, Lausanne, 2009).
16.   A. E. Willner, Z. Bo, Z. Lin, Y. Lianshan, and I. Fazal, "Optical Signal Processing Using Tunable Delay Elements Based on Slow Light," Selected Topics in Quantum Electronics, IEEE Journal of **14**, 691-705 (2008).
17.   S. Chin, L. Thévenaz, J. Sancho, S. Sales, J. Capmany, P. Berger, J. Bourderionnet, and D. Dolfi, "Broadband true time delay for microwave signal processing, using slow light based on stimulated Brillouin scattering in optical fibers," Opt. Express **18**, 22599-22613 (2010).
18.   J. S. Dura, "Photonic-assisted RF Signal Processing based on Slow and Fast Light Technological Platforms," in *Department of Communications*(Polytechnical University of Valencia, Valencia, 2012).
19.   G. M. Gehring, R. W. Boyd, A. L. Gaeta, D. J. Gauthier, and A. E. Willner, "Fiber-Based Slow-Light Technologies," Lightwave Technology, Journal of **26**, 3752-3762 (2008).
20.   T. Horiguchi, and M. Tateda, "Optical-fiber-attenuation investigation using stimulated Brillouin scattering between a pulse and a continuous wave," Opt. Lett. **14**, 408-410 (1989).

21.   M. A. Soto, G. Bolognini, F. Di Pasquale, and L. Thévenaz, "Distributed strain and temperature sensing over 50 km of SMF with 1 m spatial resolution employing BOTDA and optical pulse coding," 750383-750383 (2009).

22.   K. Y. Song, S. Chin, N. Primerov, and L. Thévenaz, "Time-Domain Distributed Fiber Sensor With 1 cm Spatial Resolution Based on Brillouin Dynamic Grating," J. Lightwave Technol. **28**, 2062-2067.

23.   K. Y. Song, W. W. Zou, Z. Y. He, and K. Hotate, "All-optical dynamic grating generation based on Brillouin scattering in polarization-maintaining fiber," Optics Letters **33**, 926-928 (2008).

Chapter 2

Linear and nonlinear effects in silica fibers.

In this chapter we will look through basic mathematical expressions governing the propagation of light in silica optical fibers. We will see that the source of nonlinear effects in optical fibers is the nonlinear response of the media to the applied electrical field associated with the optical wave. Some of most prominent nonlinear effects in fibers are discussed, such as four wave mixing (FWM), self-phase modulation (SPM) and cross phase modulation (XPM). The second part of the chapter is devoted to stimulated scattering effects in optical fibers. The last part gives a short review of the applications of nonlinear effects in optical fibers for optical signal processing

2.1   Wave propagation in media.

Before discussing various effects happening with light wave propagating in optical fibers let us briefly remind what optical wave is and how it can be described. As it was brilliantly shown by Maxwell light is essentially a coupled electric and magnetic disturbance in the form of waves. Maxwell could summarize all the previous empirical knowledge in a single set of mathematical equations, which are probably the most referenced equations in the field of optics. Let us start with Maxwell's equations for a light wave propagating in a dielectric medium without free charges [1, 2]:

$$\nabla \times \boldsymbol{E}(\boldsymbol{r},t) = -\frac{\partial \boldsymbol{B}(\boldsymbol{r},t)}{\partial t} \tag{2.1}$$

$$\nabla \times \boldsymbol{H}(\boldsymbol{r},t) = \frac{\partial \boldsymbol{D}(\boldsymbol{r},t)}{\partial t} \tag{2.2}$$

$$\nabla \cdot \boldsymbol{D}(\boldsymbol{r},t) = 0 \tag{2.3}$$

$$\nabla \cdot \boldsymbol{B}(\boldsymbol{r},t) = 0, \tag{2.4}$$

where *E(r,t)* and *H(r,t)* are electric and magnetic field vectors, respectively, and *D(r,t)* and *B(r,t)* are electric and magnetic flux densities, respectively. For convenience we do not explicitly write the time and position dependence of the vector fields. Moreover the component fields of any time-harmonic electromagnetic wave (described in rectangular coordinates) must individually satisfy six partial differential equations. $\nabla \times$ and $\nabla \cdot$ represent the curl and the divergence vector operators. Relationships between electric flux *D* and electric field *E* as well as magnetic flux density *B* and magnetic field *H* depend on the electric and magnetic properties of the medium. Two equations are defined to describe these relations:

$$D = \varepsilon_0 E + P \tag{2.5}$$

$$B = \mu_0 \left(H + M \right), \tag{2.6}$$

where ε_0 and μ_0 are the electric permittivity and magnetic permeability of free space, respectively; P is the polarization density and M is the magnetization density. Since we are interested in the propagation of the light in optical fiber, we can write $M = 0$ since silica is a nonmagnetic medium. The relation between P and the electric field E describes the response of the media through which the light wave propagates.

$$P = \varepsilon_0 \chi^{(1)} E + \varepsilon_0 \chi^{(2)} E^2 + \varepsilon_0 \chi^{(3)} E^3 + ..., \tag{2.7}$$

where $\chi^{(i)}$ is medium's optical dielectric susceptibility of the i-th order. In general, coefficients in front of the electric field vector are tensor quantities. In a homogeneous, linear, nondispersive and isotropic medium the polarization density can be described using only the first term of the series, and χ is a scalar constant. This way the relation between P and E is linear and the medium can be called a linear medium. This is also true for a nonlinear medium where the intensity of the electromagnetic wave is small. In this section we consider linear regime, thus induced polarization will be described only by the first term and nonlinear terms are omitted. In the following sections we will describe nonlinear effects resulting from nonlinear terms in the induced polarization. Coming back to linear case, χ includes refractive index n and attenuation constant α. To find the wave equation for the linear regime, we take the time derivative of equation (2.2) and use the following vector identity $\nabla \times \nabla \times E = \nabla(\nabla \cdot E) - \nabla^2 E$ together with equation (2.3) to get:

$$\nabla^2 E - \frac{1}{c_0^2} \frac{\partial^2 E}{\partial t^2} = \mu_o \frac{\partial^2 P}{\partial t^2}, \tag{2.8}$$

where c_0 is the speed of light in vacuum. Now it is convenient to represent equation (2.8) in the frequency domain:

$$-\nabla^2 \widetilde{E} - \frac{\omega^2}{c_0^2} \widetilde{E} = \frac{\omega^2 \widetilde{\chi}(\omega)}{c_0^2} \widetilde{E}, \tag{2.9}$$

where $\widetilde{E}(r,\omega) = \int_{-\infty}^{\infty} E(r,t) \exp(i\omega t) dt$ is the Fourier transform of $E(r,t)$. Equation (2.9) can be rewritten in the following form:

$$-\nabla^2 \widetilde{E} - \varepsilon(\omega) \frac{\omega^2}{c_0^2} \widetilde{E} = 0 \tag{2.10}$$

where $\varepsilon(\omega) = 1 + \widetilde{\chi}(\omega)$ is the frequency-dependent relative dielectric constant. Its real and imaginary parts can be associated with refractive index n and absorption coefficient α:

$$\varepsilon = (n + i\alpha c_0 / 2\omega)^2 \tag{2.11}$$

The attenuation and refractive index of the fiber are related to the real and imaginary parts of the susceptibility by the following relations:

$$n(\omega) = 1 + \frac{1}{2}\text{Re}[\tilde{\chi}(\omega)] \tag{2.12}$$

$$\alpha(\omega) = \frac{\omega}{nc_0}\text{Im}[\tilde{\chi}(\omega)] \tag{2.13}$$

Due to the low optical losses in the fibers in the wavelength region of interest, the imaginary part of the dielectric constant is small compared to the real part. Neglecting losses we can substitute $\varepsilon(\omega)$ by $n^2(\omega)$ and write down the final expression for the wave equation:

$$\nabla^2 \widetilde{E} + n^2(\omega)\frac{\omega^2}{c_0^2}\widetilde{E} = 0 \tag{2.14}$$

Considering monochromatic light propagating in step-index fibers we aim at finding the electric field of a guided wave that is the solution of wave equation (2.14) taking into account boundary conditions imposed by the cylindrical core and cladding. By rewriting the wave equation (2.14) in cylindrical coordinates and choosing only two components of electric and magnetic fields ($\widetilde{E}_z$ and $\widetilde{H}_z$), which are independent, the solution for $\widetilde{E}_z$ will take form [3]:

$$E_z(\varphi, \rho, z, t) = E_0(\varphi, \rho)\exp\left(i\left(\omega t - \beta(\omega)z\right)\right) \tag{2.15}$$

where $E_z(\varphi, \rho, z, t)$ is electric field expressed in cylindrical coordinates, and $\beta(\omega)$ is the propagation constant. It can be shown that for a given optical frequency there is always a discrete number of solutions, called modes, which are guided in fiber. Each i-th mode is characterized by its own propagation constant β_i, and unique spatial distribution of $E_0(\varphi, \rho)$. The number of modes supported by a specific fiber at a given frequency depends on its design parameters, such as the core radius, a, and the index difference between core and cladding. The parameter V, which is called normalized frequency, determines how many modes can be guided in the given fiber.

$$V = \frac{2\pi a}{\lambda_0}\sqrt{n_{core}^2 - n_{clad}^2} \tag{2.16}$$

where n_{core}, n_{clad} are the refractive indices of the core and the cladding, respectively, and λ_0 is the wavelength of the light in vacuum. The condition for the fiber to be single mode is $V<2.405$, where only the fundamental mode HE_{11} is supported. Since in this thesis we only worked with single mode fibers we limit the discussion to such fibers. Using another classification and the weakly guiding approximation an alternative set of modes can be designated, known as LP modes, where LP means linearly polarized [4]. Using this

classification HE$_{11}$ becomes LP$_{01}$. It should be pointed out that even single mode fiber supports two modes of orthogonal polarizations: an LP$_{01}$ mode linearly polarized in the x direction and another LP$_{01}$ polarized orthogonally in the y direction. The field distribution $E(r,\omega)$ corresponding to the HE$_{11}$ mode in a single mode fiber polarized along the x direction should be expressed as a Bessel function [2], but it is often approximated by a Gaussian distribution of the form:

$$E_x(\boldsymbol{r},\omega) = E_0 \exp[-(x^2 + y^2)/w^2]\exp[i\beta(\omega)z], \tag{2.17}$$

where w represents the width parameter occupied by the fundamental mode. For values of V close to 2, it was demonstrated that width of the fundamental mode is very close to the radius of a fiber core, showing that for standard telecommunication fiber the core radius a provides a good estimate for w.

2.2   Dispersion in optical fibers.

In general information is transmitted along optical fibers through amplitude, phase or polarization modulation of an optical carrier. Now we are interested in transmitting one symbol of information from one point to another using optical fiber. Let us consider the propagation of an optical pulse through optical cable, where we would like to see how different components of the pulse propagate through a dispersive channel. For example we take a transform limited Gaussian pulse as an example of amplitude modulation over the optical carrier ω_0, with an effective frequency band $|\omega - \omega_0| \le \Delta\omega$, where $\Delta\omega \ll \omega_0$. The electrical field of such a pulse can be represented at the beginning of the fiber, z=0, as:

$$E(0,t) = F(0,t)\exp(i\omega_0 t) = E_0 \exp[-\frac{1}{2}(\frac{t}{T})^2]\exp(i\omega_0 t) \tag{2.18}$$

where $F(0,t)$ is a slowly varying envelope, E_0 is a constant amplitude, and T defines the pulse width. Equation (2.18) represents a sinusoidal carrier modulated by a slowly varying envelope $F(0,t)$, where a slow frequency spectrum, $\widetilde{F}(0,\omega)$, was translated to a frequency ω_0, $\widetilde{E}(0,\omega) = \widetilde{F}(0,\omega - \omega_0)$. Thus, we can write that slowly varying envelope $F(0,t)$ is:

$$F(0,t) = \frac{1}{2\pi}\int_{-\infty}^{+\infty} \exp(i(\omega - \omega_0)t)\widetilde{F}(0,\omega - \omega_0)d\omega \tag{2.19}$$

If such a pulse propagates through a dispersive medium with wavenumber $k(\omega) = 2\pi n(\omega)/\lambda_0$ to a distance z, it's electric field can be represented as:

$$E(z,t) = \frac{1}{2\pi}\int_{-\infty}^{+\infty} \exp(i(\omega t - \kappa z))\widetilde{E}(0,\omega)d\omega = \frac{1}{2\pi}\int_{-\infty}^{+\infty} \exp(i(\omega t - \kappa z))\widetilde{F}(0,\omega - \omega_0)d\omega \tag{2.20}$$

Defining $\kappa(\omega_0)=\kappa_0$ we can write the propagated wave in the form of a modulated plane wave:

$$E(z,t) = \exp(i(\omega_0 t - \kappa_0 z))F(z,t) \tag{2.21}$$

where $F(z,t)$:

$$F(z,t) = \frac{1}{2\pi}\int_{-\infty}^{+\infty}\exp\left(i\left[(\omega-\omega_0)t - (\kappa-\kappa_0)z\right]\right)\tilde{F}(0,\omega-\omega_0)d\omega \tag{2.22}$$

Now coming back to our Gaussian pulse we can write the Fourier transform of $F(0,t)$ as:

$$\tilde{F}(0,\omega) = \int_{-\infty}^{+\infty}F(0,t)\exp(-i\omega t)dt = \sqrt{2\pi}TE_0\exp\left(-\frac{T^2\omega^2}{2}\right) \tag{2.23}$$

and

$$\tilde{E}(0,\omega) = \tilde{F}(0,\omega-\omega_0) = \sqrt{2\pi}E_0 T\exp[-\frac{1}{2}T^2(\omega-\omega_0)^2] \tag{2.24}$$

where the effective width of the pulse spectrum is $\Delta\omega=1/T$. In general κ varies with frequency in a nonlinear way. Normally, κ is approximated by a Taylor series up to the third term if the condition that spectral width of the pulse $\Delta\omega$ is much smaller than carrier frequency ω_0 is satisfied. Thus we can expand κ around carrier frequency ω_0 :

$$\kappa(\omega) = \kappa_0 + (\omega-\omega_0)\kappa_1 + \frac{1}{2}(\omega-\omega_0)^2\kappa_2 + \frac{1}{6}(\omega-\omega_0)^3\kappa_3$$
$$\kappa_i = \frac{d^i\kappa}{d\omega^i}\bigg|_{\omega=\omega_0} \tag{2.25}$$

The cubic term is normally neglected if the pulse carrier is not in the vicinity of the zero-dispersion wavelength. By inserting equations (2.24) and (2.25) up to the quadratic term into (2.22) we can write:

$$F(z,t) = \frac{1}{2\pi}\int_{-\infty}^{+\infty}\exp\left(i(\omega-\omega_0)t - i(\kappa(\omega)-\kappa_0)\right)\sqrt{2\pi}E_0 T\exp\left[-\frac{1}{2}T^2(\omega-\omega_0)^2\right]d\omega \tag{2.26}$$

If $\kappa(\omega)$ is real, thus assuming that fiber is lossless, we can evaluate the integral (2.26):

$$F(z,t) = \frac{E_0 T}{\sqrt{2\pi}\sqrt{T^2+i\kappa_2 z}}\exp\left[-\frac{(t-\kappa_1 z)^2}{2(T^2+i\kappa_2 z)}\right] \tag{2.27}$$

By looking at this expression we can see that envelope propagates through the fiber with group velocity, v_g where $v_g = 1/\kappa_1 = z/t_g$. Moreover the width of the pulse is also modified. Assuming that κ_1 and κ_2 are real, we can find the magnitude of the propagated pulse:

$$\left|F(z,t)\right| = \frac{E_0 T}{\sqrt{2\pi}\sqrt[4]{T^4 + (\kappa_2 z)^2}} \exp\left(-\frac{(t^2 - \kappa_1 z)^2 T^2}{2(T^4 + (\kappa_2 z)^2)}\right) \tag{2.28}$$

Thus the effective width of the pulse can be found:

$$T_z^2 = \frac{T^4 + (\kappa_2 z)^2}{T^2} \rightarrow T_z = \sqrt{T^2 + \left(\frac{\kappa_2 z}{T}\right)^2} \tag{2.29}$$

We can see that while the pulse propagates through the fiber its width is constantly increasing. Such spreading of the pulse is due to the chromatic dispersion. Excess time spread of the pulse can be estimated in the form $\Delta T = \kappa_2 z \Delta\omega$, where $\Delta\omega = 1/T$ is the pulse width in the frequency domain. We can also explain pulse broadening as a consequence of the fact that each spectral component of the pulse experiences a different group delay:

$$\Delta T = \frac{dt_g}{d\omega}\Delta\omega = \frac{d\kappa_1}{d\omega}z\Delta\omega = \kappa_2 z\Delta\omega \tag{2.30}$$

This can also be expressed in terms of wavelength:

$$\Delta T = \frac{d\kappa_1}{d\lambda}z\Delta\lambda = Dz\Delta\lambda \tag{2.31}$$

where the parameter D is the dispersion coefficient, which is normally expressed in units of picosecond per km per nanometer:

$$D = \frac{d\kappa_1}{d\lambda} = -\frac{2\pi c}{\lambda^2}\kappa_2 = -\frac{\lambda}{c}\frac{d^2 n}{d\lambda^2}, \tag{2.32}$$

where we used the fact that group velocity can be represented as:

$$V_g = \frac{c}{N} = \frac{c}{n - \lambda\frac{dn}{d\lambda}} = \frac{1}{\kappa_1} = \frac{d\omega}{d\kappa} \tag{2.33}$$

2.3   Nonlinear effects.

In this section we will discuss optical effects occurring in optical fibers due to the nonlinear response of induced polarization in the medium to the electric field associated with an electromagnetic wave propagating through this media. Expressions presented in the first section assume a linear relationship between the electromagnetic light field and the responding atomic system constituting the medium. As any oscillator can be overdriven into nonlinear response through the application of large enough forces, we can anticipate that an extremely strong electric field associated with propagating light could generate appreciable

nonlinear optical effects. In order to describe such effects let us look at the expression for induced polarization, which can be rewritten here in the form [5]:

$$P = \varepsilon_0 (\chi^{(1)} E + \chi^{(2)} E^2 + \chi^{(3)} E^3 + ...) = P_L + P_{NL2} + P_{NL3} + ..., \qquad (2.34)$$

where $\chi^{(i)}$ is optical susceptibility of the ith order, and P_{NL2}, P_{NL3} are second and third-order nonlinear polarizations, respectively. This expression is written using scalar quantities, however generally **P** and **E** are vector quantities and $\chi^{(i)}$ is a tensor of rank *(i+1)*. Since silica is an isotropic medium $\chi^{(1)}$ can be represented by a single scalar element [3, 5], while $\chi^{(3)}$ has only four non-zero elements, which are reduced to one element by the symmetry rules $\chi^{(3)}_{xxxx}$ [5, 6]. Moreover, since silica is an isotropic medium and silica molecules show inversion symmetry, $\chi^{(2)}$ vanishes for such media, and consequently silica optical fibers cannot produce second-order nonlinear optical interactions. This is true only if we consider the dipole approximation. On the other hand non-centrosymmetric crystals can be used to obtain second-order nonlinear effects. Second-order nonlinear polarization is responsible for processes such as: second-harmonic generation, sum- and difference-frequency generation and optical parametric oscillation. However processes related to third-order nonlinear polarization can happen in media both with and without a center of symmetry. As a result many third-order nonlinear interactions were demonstrated in silica fiber, such as: third-harmonic generation, intensity-dependent refractive index, four-wave mixing, stimulated Brillouin scattering and stimulated Raman scattering. Third-order nonlinear polarization have three contributions: the instantaneous polarization due to the very fast response of bound electrons to the applied electric field (Kerr effect); delayed response due to molecular re-orientation (Raman effect); electrostriction contribution (Stimulated Brillouin scattering).

2.3.1 Four wave mixing.

Four wave-mixing (FWM) is an interaction among four waves as a result of third-order nonlinear polarization [5]. Generally, it involves a nonlinear interaction between four optical waves with different frequencies and propagation directions. Though degenerate four-wave mixing is possible when frequencies of the incident light wave are equal and the wave vectors are mutually antiparallel. If there are two or more waves present in the fiber their interaction through third order nonlinear polarization will lead to the generation of optical waves at other frequencies, which were not present at the input of the fiber. FWM can be very efficient in optical fibers and has been studied extensively from the early observations [7, 8]. Since FWM phenomena lead to the generation of new frequencies it has been used for tunable light source systems and efficient wavelength conversion stages [9-11]. However FWM can play a detrimental role as well. In modern optical networks using wavelength division multiplexing four wave mixing is a major source of system degradation [12, 13]. With equal channel spacing FWM induced cross talk generates new frequencies which coincide with the

existing channels resulting in coherent interference with the signal in these channels. This interference leads to fluctuations in the received power and overall deterioration of system performance. Even with unequal channel spacing most of the frequencies generated by FWM fall inside channels resulting in degradation of the noise figure for the channels. Induced cross talk between channels limits the maximum input power for each channel. In order to see the effect of FWM let us consider a simple case where two optical waves are launched at the input of the fiber with frequencies of ω_1, ω_2, respectively (Figure 1). If we insert the resulted electric field in the expression for third-order nonlinear polarization we will see that among other terms there will be new terms oscillating at frequencies $3\omega_1$, $3\omega_2$, $2\omega_1 \pm \omega_2$ and $2\omega_2 \pm \omega_1$. Terms, with frequencies triple that of the input waves, are responsible for phenomena such as third-harmonic generation. In general, it is difficult to satisfy the phase matching condition for such processes, resulting in low efficiencies. This also applies for those terms containing sums of frequencies: $2\omega_1 + \omega_2$ and $2\omega_2 + \omega_1$. Even though using specially prepared fibers it was demonstrated that third harmonic generation can be observed and can be quite efficient [14-16]. On the other hand terms with frequencies $2\omega_1 - \omega_2$ and $2\omega_2 - \omega_1$ will fall close to the input frequencies and the phase matching condition can easily be satisfied, thus generating new optical waves with high efficiency. The phase matching condition is a condition that requires matching of wave vectors. For the wave at new frequency $\omega_s = 2\omega_1 - \omega_2$ to be efficiently generated the associated phase matching condition should be fulfilled $\Delta k = 2k_1(\omega_1) - k_2(\omega_2) - k_s(\omega_s) = 0$. The condition can be easily met close to the fiber's zero dispersion wavelength [17]. FWM can also be interpreted in the following way. Interference between the two input optical waves generates a beating in the intensity with period $1/\Delta\omega$, where $\Delta\omega = \omega_2 - \omega_1$. Such an intensity pattern will induce periodic fluctuations in the refractive index due to the Kerr effect. Induced refractive index grating will give small phase fluctuations on both input electric fields. Such phase modulation on an optical wave with frequency ω_1 will give rise to two sidebands at frequencies $\omega_1 - \Delta\omega$ and $\omega_1 + \Delta\omega = \omega_2$. The same applies to the optical wave with frequency ω_2, which in turn gives rise to two sidebands at frequencies $\omega_2 - \Delta\omega = \omega_1$ and $\omega_2 + \Delta\omega$, as shown in Figure 1. Normally, the sideband that is higher in optical frequency is called the anti-Stokes component, and the sideband with lower optical frequency is called the Stokes component.
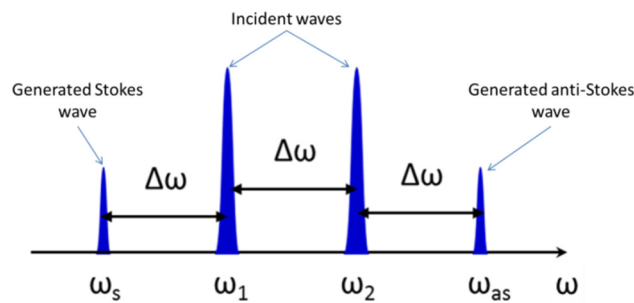
Figure 1. Optical spectrum illustrating non degenerate case of FWM phenomenon in optical fibers.

2.3.2   Self-phase modulation

Self-phase modulation may happen in third-order nonlinear media thanks to the intensity dependent refractive index or simply optical Kerr effect [2, 5]. As the name suggests the optical field can produce a change of its own phase, and this change is determined by the intensity profile of the electric field. The first observation of the SPM was made in 1967 using carbon disulfide liquid as a nonlinear media [18]. A few years later in 1978 R.H. Stolen and Ch. Lin demonstrated SPM spectral broadening of the pulse propagating in silica fibers [19]. Self-phase modulation can be intuitively described in the following way. When an intense pulse propagates along the optical fiber it creates a refractive index variation due to the Kerr effect. Moreover refractive index change is proportional to the intensity of the electric field across the pulse, resulting in maximum refractive index change at the center of the pulse. A different refractive index creates a phase modulation inside the pulse. This means that the peak of the pulse will experience a greater phase change compared to the leading or tailing parts, since there is a greater change in the refractive index. The resultant phase change with time causes the generation of different instantaneous frequencies across the pulse. Such a time dependent instantaneous frequency is referred as a frequency chirp, or equivalently instantaneous frequency is the time derivative of the phase. Since the pulse accumulates more and more phase change while propagating down the fiber, new frequency components are generated as a result of SPM. These new frequencies broaden the spectrum of the pulse. The extent of spectral broadening depends on the pulse shape. For a Gaussian pulse with incident field given by $\exp\left(-\dfrac{t^2}{2T^2}\right)$ the frequency chirp is given by:

$$\delta\omega = -\frac{\partial \phi_{NL}}{\partial t} = -L_{eff}\gamma P_0 \frac{d}{dt}\left|F(0,t)\right|^2 = \frac{2L_{eff}\gamma P_0 t}{T^2}\exp\left(-\left(\frac{t}{T}\right)^2\right),\tag{2.35}$$

where γ is the nonlinear parameter of the fiber, P_0 is the peak power of the pulse, and L_{eff} is the effective length of the fiber, which is smaller than the real length L because of fiber losses. Effective length is defined as $L_{eff} = \left(1 - \exp^{-\alpha L}\right)/\alpha$, where α is attenuation coefficient. By observing the evolution of the frequency chirp across the pulse we can remark several features. $\delta\omega$ is negative at the leading edge of the pulse, resulting in a shift of the components with lower frequency (red shift), while near the trailing edge, components with higher frequencies accumulate (blue shift). Over a large central region the chirp is linear and positive. It is clear that while the pulse propagates along the fiber its spectrum changes due to SPM. Such spectral broadening can be determined by knowing the initial spectral width of the pulse $\Delta\omega_0$ and the numerical value of the maximum phase shift ϕ_{max}. For the unchirped Gaussian pulse spectral broadening becomes:

$$\delta\omega_{max} = 0.86\Delta\omega_0\phi_{max} = 0.86\Delta\omega_0\gamma P_0 L_{eff}\tag{2.36}$$

If we look at the pulse spectrum after having undergone SPM we can remark that the spectrum has some oscillations. The number of peaks in these oscillations is given by the ϕ_{max} and increases linearly with it. Such an oscillatory structure can be explained by the interference among the new frequencies generated at the leading and trailing edges. The resulting spectrum depends on the initial pulse shape, as well as on the initial chirp imposed on the pulse. For the down-chirped input pulse, the initial chirp parameter has a negative value, so after propagation down the fiber the pulse can become narrower [20, 21]. The pulse spectrum can be reduced up to the point where the SPM-induced chirp compensates the initial chirp.

As we saw in the previous section the pulse shape is modified due to the group velocity dispersion. Actually, GVD results in pulse chirping where the positive or negative chirp depends on the sign of κ_2. Thus it is clear that combination of GVD and SPM can result in an interesting transformation of the initial pulse shape. Obviously both effects can amplify the pulse spectrum chirping resulting in even faster broadening of the pulse when compared to the broadening coming separately from GVD or SPM. The opposite is also possible. Then both effects cooperate in such a way that the pulse experiences little or none broadening while propagating in the fiber. This special form of pulse propagation without changing its shape is called soliton propagation. For example, if an initially unchirped pulse propagates in normal-dispersion regime ($\kappa_2 > 0$), its shape spreads out much faster than in the presence of either GVD or SPM alone. This is due to the fact, that SPM generates new frequency components that are red-shifted near the leading edge and blue-shifted near the trailing edge of the pulse. At the same time GVD favors faster propagation speeds for the red components of the pulse than for the blue components. As a result of the common work of SPM and GVD the shape of the initial pulse spreads much faster. The situation is completely different when pulse propagates in anomalous-dispersion regime ($\kappa_2 < 0$). In this case spreading of the pulse is much slower, because SPM generates positive chirp across the pulse, while GVD-induced chirp is negative resulting in a cancelation of the two chirp contributions. Moreover the pulse has a unique property that it adjusts itself during propagation in order to make such cancellation as complete as possible. The characteristic pulse shape associated with soliton propagation is a "sech" shape. If such a pulse is launched into the fiber it can propagate without changing its shape and spectrum.

2.3.3   Cross-phase modulation

When two or more optical waves propagate inside optical fibers, they can interact thanks to the nonlinear response of induced polarization. We saw in section 2.3.1 that FWM results in the generation of additional frequencies when the phase matching condition is satisfied. Moreover new waves can be generated through stimulated Raman or Brillouin scattering which will be described in the following chapters. Processes such as FWM, Raman or Brillouin scattering, or harmonic generation generate new waves at the expense of the

energy of the input waves. On the other hand cross phase modulation (XPM) can couple two waves without any energy transfer between them. Moreover XPM can occur not only between two optical waves with different wavelengths, but also between two polarization states of single frequency. The first experimental observation of XPM was made using two CW lasers and a 15 km silica fiber [22]. A few years later spectrum changes of ps pulses were observed due to the XPM [23]. In order to explain the effect of cross phase modulation let us consider two linearly polarized optical fields at different wavelength propagating along the fiber. Then we can express the total electric field as:

$$E(z,t) = E_1 \exp(i\omega_1 t) + E_2 \exp(i\omega_2 t) + c.c. \tag{2.37}$$

Now by inserting this expression into the equation for induced polarization (2.34) we can see that induced nonlinear polarizations oscillating at initial frequencies ω_1 and ω_2 will be as follows:

$$P_{NL3}(\omega_1) = \varepsilon_0 \chi^{(3)} (3|E_1|^2 + 6|E_2|^2) E_1 \left[\exp(i\omega_1 t) + c.c. \right] \tag{2.38}$$

$$P_{NL3}(\omega_2) = \varepsilon_0 \chi^{(3)} (6|E_1|^2 + 3|E_2|^2) E_2 \left[\exp(i\omega_2 t) + c.c. \right] \tag{2.39}$$

From these expressions we can see that nonlinear susceptibility is dependent on the intensities of both waves and effective susceptibility can be expressed as (j=1,2):

$$\chi_{eff} = \chi^{(1)} + \chi_{NL} = \chi^{(1)} + \chi^{(3)} \left(6|E_{3-j}|^2 + 3|E_j|^2 \right) \tag{2.40}$$

It's clear that refractive index of the wave gets modified both by the intensity of the wave itself, and also by the intensity of the co-propagating wave at another optical frequency [2, 5]:

$$\Delta n_j \approx \chi_{NL} / 2n_j \approx n_2' \left(|E_j|^2 + 2|E_{3-j}|^2 \right) \tag{2.41}$$

where n_2' is a nonlinear parameter of the fiber. Change in the refractive index of the wave at ω_1 due to its own intensity, $|E_1|^2$, is a result of SPM, and it is represented in the expression (2.41) by the first term. On the other hand, second term responsible for XPM changes refractive index twice more efficiently with the intensity of co-propagating wave, $|E_2|^2$. As a result phase of the wave is modulated by XPM twice more effective than due to the SPM. As in the case of SPM, where there is change in spectrum of the pulse due to its own intensity, XPM results also in a modification of the spectrum of the copropagating pulses. Moreover, cross phase interaction between two pulses happens only when two pulses physically overlap in time with each other. Similar to SPM effect, spectrum of the pulses develops multipeak structure and broadens. However, spectral shape is modified this time by both SPM and XPM. In order to clearly see the effect of XPM on the pulse spectrum it is convenient to consider two pulses with sufficiently large difference in peak powers. This situation can be considered as interaction between strong pump and weak probe pulses. In this case XPM contribution to

the pump spectrum can be neglected, as well as SPM contribution to the probe pulse spectrum. By looking at the probe spectrum we can see how XPM induced by the pump pulse modifies the probe spectrum. By solving numerically the equations describing pulse propagation in the presence of nonlinear effects as well as experimental demonstrations it was shown that probe pulse spectrum becomes chirped. The sign of the chirp as well as its magnitude strongly depends on which part of the pump pulse overlaps with the probe pulse during interaction and on the pump pulse peak power [2]. Thus, induced probe pulse chirp due to the XPM depends on initial delay of the two pulses and on the group velocity mismatch between two pulses. If the probe pulse mainly interacts with the trailing edge of the pump pulse it gets positive chirp due to the XPM. As a result probe pulse has only blue-shifted components in its spectrum. On the contrary, when the leading edge of the pump pulse interacts with the probe pulse its spectrum develops red shifted components and negative chirp. In the case when the pump pulse fully passes through the probe pulse, induced chirp is zero at the pulse center and its magnitude is small across the entire probe pulse. Pulse spectrum is broadened symmetrically, but only edges of the pulse contribute to the new frequencies generation. As tails carry relatively small amount of energy pulse spectrum preserves its shape at the carrier frequency.

Described pulse spectrum modifications are considered only by the XPM alone, but in many situations fiber nonlinearities and dispersion properties of the fiber act together on the shape and spectrum of the propagating pulse. More complex transformations in spectrum and temporal shape of the pulse are expected when effects from XPM, SPM and GVD are combined. Since only the phase of the pulse is modified as a result of XPM and SPM effects, the pulse shape remains unchanged, while the spectrum is modified. However, in the presence of GVD different spectral components of the pulse, generated through XPM and SPM, propagate at different velocities. As a result the shape is severely distorted in an asymmetric manner [24]. It was shown that actually GVD reduced the extent of asymmetry in pulse spectrum compared to the situation when XPM acts alone.

2.4   Light scattering in optical fibers

Light scattering occurs in any media where light propagates. Even in completely homogenous media light is scattered in the forward direction [5, 25]. In many systems light propagates in inhomogeneous medium. Optical inhomogenities present in the medium is the main source responsible for light scattering. Change in optical properties of the medium might arise from inclusion of foreign material or from thermal motion of the particles in the material. Optical inhomogeneties contribute to the fluctuations of the optical dielectric constant through fluctuations of the density of the substance and fluctuations in the orientation of the molecules. Different scattering mechanisms produce scattered light with specific characteristics such as spectrum, cross section, and polarization. Scattering of light can be divided into two specific forms: elastic and inelastic scattering. Elastic scattering imply that the energy of the scattered photon is conserved and only its direction is different to the initial

photon. Thus elastically scattered light has an identical spectrum as incident light. On the other hand during inelastic scattering, the scattered photon has a different energy compared to the incident photon. Such interaction between photon and molecule implies partial exchange of the energy between medium and incident photon. Inelastic scattering results in an optical frequency difference between incident and scattered light. When light scattering occurs without changes of the optical properties of the material it is called linear or spontaneous scattering.

Let us consider a general situation, when light propagates in an inhomogeneous media we can observe several spectral components related to the scattered light [5] as depicted in the Figure 2. By definition, those components of the scattered light that are shifted to lower frequencies are denoted as Stokes components, and those that are shifted to higher frequencies are denoted as anti-Stokes components. Generally four components can be observed. These are Raman, Brillouin, Rayleigh and Rayleigh-wing. Each scattering component represents a specific type of interaction between incident light and the matter.
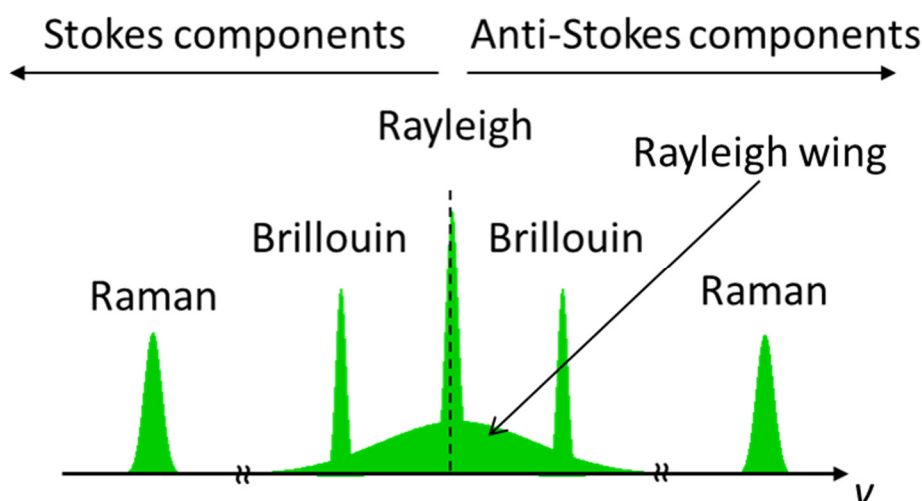
Figure 2. Spectral composition of the scattered light.

Rayleigh scattering is an elastic scattering representing light scattered from nonpropogating density fluctuations. It is scattering from the particles, which are much smaller than the wavelength of the light.

Rayleigh-wing scattering is scattering from fluctuations in the orientation of anisotropic molecules and it is as well considered an elastic process. Since the molecular reorientation is very rapid, this component occupies large spectrum.

Raman scattering is one of the inelastic scattering processes. The origin of the Raman scattering lies in interaction of light with vibrational modes of the molecules in the media. Formally it can be described as scattering from the fluctuations of the medium entropy. Due to the fast vibration and small momentum of these modes, scattered light has a substantial frequency shift in the order of 100 THz.

Brillouin scattering is generated from the variations in the pressure inside the medium. Due to the thermal motion of molecules inside the media density fluctuates creating sound type waves. Such waves represent acoustic phonons, and interaction of incident light with these phonons results in Brillouin scattering. The relatively low frequencies of the acoustic modes induce frequency shift in the order of 10 GHz for the scattered light.

Characteristic properties of the scattering processes are summarized in Table 1. We can see that gain provided by Brillouin and Raman scattering is the highest. This fact was a premise for widespread applications of these two processes for various optical signal processing techniques.

Table 1. Typical values of parameters describing light-scattering processes. The gain is specified for the stimulated version of the process in silica.

Process	Shift (nm)	Linewidth (pm)	Relaxation Time (s)	Gain coefficient (m/W)
Rayleigh	0	0.05	10^{-8}	10^{-12}
Rayleigh-wing	0	500	10^{-12}	10^{-12}
Raman	100	500	10^{-12}	$5*10^{-13}$
Brillouin	0.01	0.5	10^{-9}	10^{-11}

The origin of light scattering lies in the thermal motion of the molecules of the medium, which in turn leads to the fluctuations of the density and of the orientation of anisotropic molecules. Such fluctuations produce fluctuations in dielectric constant. It is useful to represent dielectric constant as [5, 25]:

$$\varepsilon_{ik} = \varepsilon_0 \delta_{ik} + \Delta\varepsilon_{ik},$$
(2.42)

where ε_0 represents dielectric constant of undisturbed medium and $\Delta\varepsilon_{ik}$ correction of the dielectric constant due to the fluctuations. First term in (2.42) determines the value of ε in the homogeneous medium, where light scattering is absent, while second term is responsible for the light scattering, and it can be decomposed as:

$$\Delta\varepsilon_{ik} = \Delta\varepsilon \delta_{ik} + \Delta\varepsilon_{ik}^{(s)} + \Delta\varepsilon_{ik}^{(a)},$$
(2.43)

where fluctuations $\Delta\varepsilon$ are isotropic, and are determined only by fluctuations of the pressure, entropy, density, or temperature. $\Delta\varepsilon$ fluctuations are responsible for the scalar light scattering such as Brillouin and Rayleigh scattering. Second and third terms in equation (2.43) are called tensor light scatterings. Fluctuations of dielectric constant due to these two terms determine the anisotropy of the medium that results from the thermal motion. Here $\Delta\varepsilon_{ik}^{(s)}$ is the symmetric part, which gives rise to Rayleigh-wing scattering, and $\Delta\varepsilon_{ik}^{(a)}$ is the antisymmetric

part, which gives rise to Raman scattering. The work in this thesis is mainly concerned on the Brillouin scattering. That is why only the detailed description of Brillouin scattering will be given in the following section.

2.4.1   Spontaneous Brillouin Scattering

Brillouin scattering appears in silica as a result of fluctuations of dielectric constant, $\Delta\varepsilon$, induced by variations of thermodynamic quantities. So we can assume that $\Delta\varepsilon$ is a function of two independent thermodynamic variables pressure, ρ, and temperature, T, and can be expressed as:

$$\Delta\varepsilon(\rho,T) = \left(\frac{\partial\varepsilon}{\partial\rho}\right)_T \Delta\rho + \left(\frac{\partial\varepsilon}{\partial T}\right)_\rho \Delta T \qquad (2.44)$$

It can be shown that density and temperature fluctuations arise independently of one another and are statistically independent [25]. Thus we can write that mean-square fluctuation in dielectric constant is represented by:

$$\left\langle \Delta\varepsilon^2 \right\rangle = \left(\frac{\partial\varepsilon}{\partial\rho}\right)_T^2 \overline{\Delta\rho^2} + \left(\frac{\partial\varepsilon}{\partial T}\right)_\rho^2 \overline{\Delta T^2} \qquad (2.45)$$

Intensity of the scattered light due to fluctuations of the dielectric constant can be expressed as [5, 25]:

$$I_S = I_0 \frac{\pi^2 V^2}{\lambda^4 L^2} \left\langle \Delta\varepsilon^2 \right\rangle \sin^2 \varphi \qquad (2.46)$$

where V is the scattering volume, φ is the scattering angle, L is the distance between the scattering volume and observation point, and I_0 is the incident intensity $I_0 = nc\varepsilon_0 \left\langle \left| E(t) \right|^2 \right\rangle$.

Second term in equation (2.44), which is responsible for dielectric constant fluctuations as a result of temperature fluctuations, is normally much smaller than isothermal fluctuations of density, first term. Thus, within 2 % accuracy we can consider that dielectric constant depends only on density:

$$\left\langle \Delta\varepsilon^2 \right\rangle = \left(\frac{\partial\varepsilon}{\partial\rho}\right)_T^2 \left\langle \Delta\rho^2 \right\rangle \qquad (2.47)$$

Then by assuming that change in density is a function of two independent thermodynamic variables pressure, p, and entropy, S, we can write:

$$\Delta\rho\left(p,S\right)=\left(\frac{\partial\rho}{\partial p}\right)_S\Delta p+\left(\frac{\partial\rho}{\partial S}\right)_p\Delta S \tag{2.48}$$

Due to the statistical independence of p and S, $\langle\Delta p\Delta S\rangle=0$, and, therefore:

$$\left\langle\Delta\rho^2\left(p,S\right)\right\rangle=\left(\frac{\partial\rho}{\partial p}\right)_S^2\left\langle\Delta p^2\right\rangle+\left(\frac{\partial\rho}{\partial S}\right)_p^2\left\langle\Delta S^2\right\rangle \tag{2.49}$$

Thus, we can see that scattered intensity will have two contributions: adiabatic and isobaric density fluctuations:

$$I\sim\left[\left(\frac{\partial\varepsilon}{\partial\rho}\right)_T^2\left(\frac{\partial\rho}{\partial p}\right)_S^2\left\langle\Delta p^2\right\rangle+\left(\frac{\partial\varepsilon}{\partial\rho}\right)_T^2\left(\frac{\partial\rho}{\partial S}\right)_p^2\left\langle\Delta S^2\right\rangle\right] \tag{2.50}$$

Using some statistical calculations it is possible to compute the intensity of the light scattered by isobaric and adiabatic densities fluctuations and write the total intensity as a sum of two:

$$I=I_{ad}+I_{is}=I_0\frac{\pi^2 V}{\lambda^4 L^2}kT\gamma_e^2 C_T\sin^2\varphi \tag{2.51}$$

where

$$\gamma_e=\left(\rho\frac{\partial\varepsilon}{\partial\rho}\right)_T \tag{2.52}$$

is electrostrictive constant and

$$C_T=-\frac{1}{V}\left(\frac{\partial V}{\partial p}\right)_T=C_S+\frac{T\sigma^2}{\rho c_p} \tag{2.53}$$

is isothermal compressibility. C_S, σ, c_p are adiabatic compressibility, coefficient of volume expansion, and specific heat at constant pressure, respectively.

In equation (2.50) the first term describes adiabatic density fluctuations and leads to Brillouin scattering. Second term is responsible for Rayleigh scattering. Both contributions are quite different in character and have different spectral distributions as a result of different behavior of $\left\langle\Delta p^2\right\rangle$ and $\left\langle\Delta S^2\right\rangle$.

Formula (2.46) for the scattered light was first demonstrated by Einstein. We can see that scattering intensity is proportional to $1/\lambda^4$, but this equation does not demonstrate time dependence of the scattered light. It means that adiabatic and isobaric fluctuations resulting in a light scattering are assumed to be fixed in time. Actually, such statistical fluctuations do not remain fixed, but change constantly in time. Moreover, different fluctuations change differently with time, and, consequently, they impose different modulation on the scattered

light. By studying the spectrum of the scattered light it is possible to extract knowledge about the kinetics of fluctuations. Since we are mainly interested in the Brillouin scattering we will consider changes in the spectrum of scattered light by temporal changes in the fluctuations of density. As equation (2.48) suggest density fluctuations are composed of pressure fluctuations and entropy fluctuations. Pressure fluctuations can be considered as a random local rarefactions and compressions of the medium. These thermal pressure waves can have different frequencies and travel in different directions as a result of elastic properties of the medium. This way we can write that change in Δp in time satisfies the wave equation and assume that $\Delta p \sim \Delta n \sim \Delta \tilde{p}$, where Δn is the change in the index of refraction and $\Delta \tilde{p}$ is the modulation function. Now we can write the scattered light due to the change in Δp as:

$$E^{sc}(t) = E^{in}(t)\Delta \tilde{p} = E_0^{in} \exp(i(\omega_0 t - kz))\Delta \tilde{p} \qquad (2.54)$$

where $E^{in}(t)$ is the incident monochromatic wave undergoing scattering due to the propagation of the elastic waves. Now let us consider the equation of motion for a pressure wave in viscous medium, which is known as Stokes equation. It can be written in the following form [5]:

$$\frac{\partial^2 \Delta \tilde{p}}{\partial t^2} - V^2 \nabla^2 \Delta \tilde{p} - \Gamma \nabla^2 \frac{\partial \Delta \tilde{p}}{\partial t} = 0 \qquad (2.55)$$

where V is the velocity of sound in the media and Γ is a damping parameter of the sound wave. These two parameters can be defined as:

$$V^2 = \frac{1}{C_s \rho} \qquad (2.56)$$

and

$$\Gamma = \frac{1}{\rho}\left(\frac{4}{3}\eta + \eta' + \frac{\iota}{c_p}(\frac{c_p}{c_V} - 1) \right) \qquad (2.57)$$

where C_s is adiabatic compressibility, η and η' are the shear and bulk viscosity coefficients, respectively, ι is the coefficient of thermal conductivity, and c_p and c_V are specific heat at constant pressure and specific heat at constant volume, respectively. Ratio $\frac{c_p}{c_V} = \gamma$ is known as the adiabatic index.

Now we shall look for the solutions in the form:

$$\Delta \tilde{p}(t) = \Delta p_0 \exp(i[mt - qz]) \qquad (2.58)$$

By substituting (2.58) in (2.55) we obtain

$$m = i\frac{\Gamma q^2}{2} \pm \left(q^2 V^2 - \frac{\Gamma^2 q^4}{4} \right)^{1/2} \tag{2.59}$$

where by using the relation $\Omega_0^2 = q^2 V^2$, we rewrite (2.59) as

$$m = i\frac{\Gamma q^2}{2} \pm \left(\Omega_0^2 - \frac{\Gamma^2 q^4}{4} \right)^{1/2} \tag{2.60}$$

Now we insert (2.60) in (2.58)

$$\Delta\tilde{p}(t) = \Delta p_0 \exp\left(i\left[i\frac{\Gamma q^2}{2} \pm \left(\Omega_0^2 - \frac{\Gamma^2 q^4}{4} \right)^{1/2} \right] t - iqz \right) \tag{2.61}$$

We take the real part to write the wave function of $\Delta\tilde{p}(t)$:

$$\Delta\tilde{p}(t) = \Delta p_0 \exp\left(-\frac{\Gamma q^2}{2} t \right) \cos\left(\left(\Omega_0^2 - \frac{\Gamma^2 q^4}{4} \right)^{1/2} - qz \right) \tag{2.62}$$

which we can rewrite:

$$\Delta\tilde{p} = \Delta p_0 \exp(-\delta t)\cos(\Omega t - qz) \tag{2.63}$$

Where we introduced

$$\delta = \frac{\Gamma q^2}{2}, \Omega = \left(\Omega_0^2 - \frac{\Gamma^2 q^4}{4} \right)^{1/2} \tag{2.64}$$

Now we can write that resulted scattered light according to (2.54) as:

$$E^{sc}(t) = E^{in}(t)\Delta\tilde{p} = \frac{E_0^{in}\Delta p_0}{2}\exp(-\delta t)\left[\exp\left(i[(\omega_0 - \Omega)t - (k-q)z] \right) + \exp\left(i[(\omega_0 + \Omega)t - (k+q)z] \right) \right] \tag{2.65}$$

It follows from (2.65) that the intensity of the scattered light can be expressed as:

$$I^{sc}(t) = nc_0\varepsilon_0 \left| E^{sc}(t) \right|^2 = nc_0\varepsilon_0 \left| E_0^{in} \right|^2 \left| \Delta p_0 \right|^2 \exp(-2\delta t)\left\{ 1 + \cos\left(2[\Omega t - qz] \right) \right\} \tag{2.66}$$

We can see that scattered light changes with time according to the expression (2.66), and modulation of the light depends on the ratio V/c, the frequency ω_0 of the incident light, and the angle of observation φ. This dependence will be evident later when we will consider two term of equation (2.65) which leads to the scattering of the incident light only from two elastic waves among many other waves. These two specific waves are selected due to the fact that only the wave vectors of these two waves, together with the wave vectors of incident and scattered light satisfy Bragg condition. Moreover we see that scattered light exponentially

decays with the time constant of 2δ. This happens because acoustic wave decays with time, which can be seen from expression (2.63):

$$\left|\Delta \widetilde{p}(t)\right|^2 = \left|\Delta p_0\right|^2 \exp(-2\delta t) \tag{2.67}$$

where decay rate can be defined as phonon lifetime:

$$2\delta = \Gamma q^2 = \frac{1}{\tau_{ph}} \tag{2.68}$$

Thus, we can see that acoustic wave intensity decays twice faster than acoustic wave amplitude, since decay constant for acoustic intensity is twice larger than that of the acoustic amplitude.

Now let us closely look at the equation (2.65). where we can see that scattered light has two components down- and up-shifted in frequency by the amount equal to frequency of the acoustic wave. First term leads to the Stokes scattering, while second term is responsible for the anti-Stokes scattering.

2.4.1.1 Stokes scattering

As it was already mentioned, elastic waves (acoustic waves) propagate in the medium in all possible directions due to the fluctuations of inhomogeneities. However, we consider the optical wave propagating in such medium with definite wave vector k and optical frequency ω_0 and scattered light with wave vector k_s and frequency ω_s, which is observed in a specific direction. Then there is only one specific elastic wave which can satisfy conditions for energy and momentum conservation. We can write these conditions in the form:

$$\vec{k_s} = \vec{k_0} - \vec{q} \tag{2.69}$$

and

$$\omega_s = \omega_0 - \Omega \tag{2.70}$$

Optical waves involved in this interaction satisfy dispersion relation:

$$\omega_i = \left|\vec{k_i}\right| c / n \tag{2.71}$$

where $i = 0,s$. At the same time dispersion relation for the acoustic wave is written as:

$$\Omega = \left|\vec{q}\right| V \tag{2.72}$$

Since the frequency of the acoustic wave is much smaller than that of the optical waves $(\Omega \ll \omega_i)$, one can approximate $\left|\vec{k_s}\right| \approx \left|\vec{k_0}\right| \approx \left|\vec{k}\right|$. This way we can write that $\left|\vec{q}\right| = 2\left|\vec{k}\right| \sin \dfrac{\varphi}{2}$, as depicted in Figure 3.
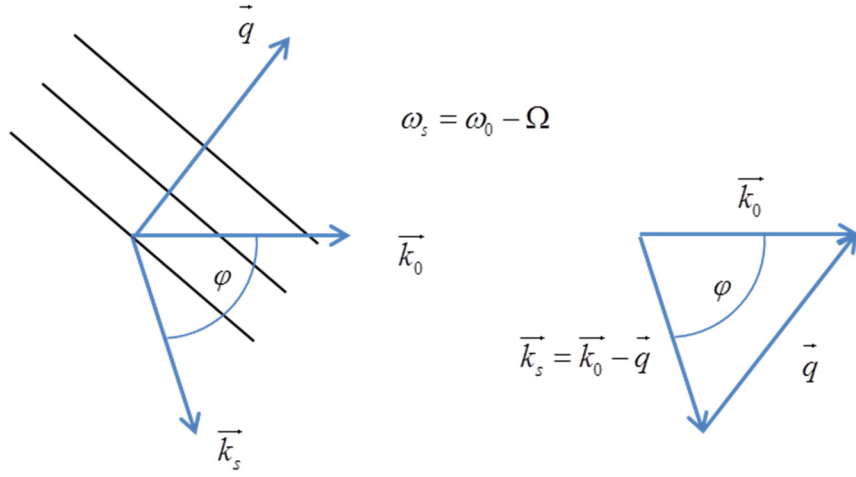
Figure 3. Illustration of the Stokes scattering using wavevector diagram

This way we can find the expression for the acoustic frequency as:

$$\Omega = V 2\left|\vec{k}\right| \sin \frac{\varphi}{2} = \frac{2V\omega_0 n}{c_0} \sin \frac{\varphi}{2} \qquad (2.73)$$

Change in optical frequency of the scattered light is called Stokes shift and it is equal to acoustic frequency, which in turn depends on the ratio V/c_0, frequency ω_0, and the angle of observation φ as it is clear from expression (2.73). It is clear that frequency shift is maximum for backscattering ($\varphi = 180^0$) and equal to zero for forward scattering. In optical fibers typical value for the Brillouin shift, $v_B = \dfrac{\Omega}{2\pi}$, at telecommunication wavelength of 1.55 um is 10.8 GHz, which is governed by the value of acoustic velocity in silica V=5900 m/s and refractive index n=1.46.

2.4.1.2   *Anti-Stokes scattering*

In similar approach we can describe second term in the equation (2.65) which is responsible for the anti-Stokes component of the scattered light. In this situation acoustic and optical waves satisfy momentum and frequency relations written in the following form:

$$\vec{k_s} = \vec{k_0} + \vec{q} \qquad (2.74)$$

and

$$\omega_s = \omega_0 + \Omega \qquad (2.75)$$

where as before $\omega = \left|\vec{k}\right| c / n$ and $\Omega = V\left|\vec{q}\right|$. These relations can be represented using Figure 4. It clear from the Figure 4 that anti-Stokes scattering results due to the scattering from incoming acoustic wave, while in the Stokes scattering acoustic wave is retreating from the incident light. We can make the same assumption as before that magnitude of the wavevector of the scattered light, $\left|\vec{k_s}\right|$, is approximately the same of the incident optical wave, $\left|\vec{k_0}\right|$. Using diagram in the Figure 4 and $\left|\vec{k_0}\right| \approx \left|\vec{k_s}\right| \approx \left|\vec{k}\right|$, we can write the expression for the acoustic wavevector as:

$$\left|\vec{q}\right| = 2\left|\vec{k}\right| \sin\left(\frac{\varphi}{2}\right) \qquad (2.76)$$

Hence, acoustic frequency in this case using (2.72) is given by

$$\Omega = V 2\left|\vec{k}\right| \sin\left(\frac{\varphi}{2}\right) = 2n\omega_0 \frac{V}{c_0} \sin\left(\frac{\varphi}{2}\right) \qquad (2.77)$$
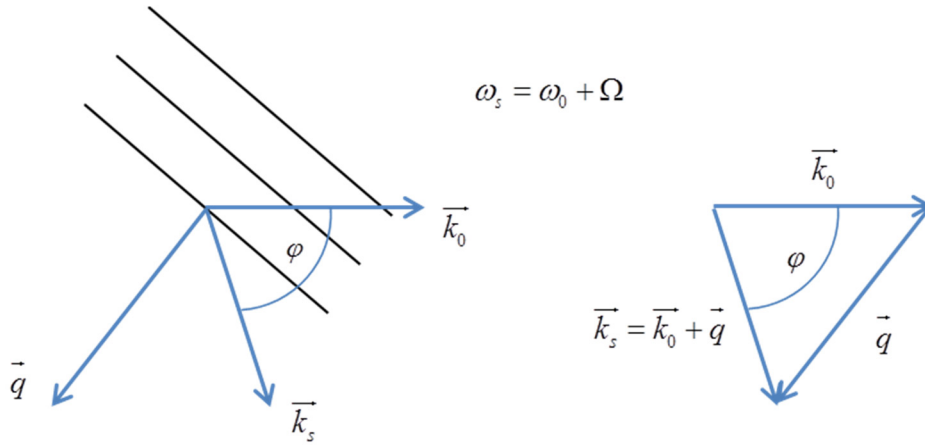
Figure 4. Illustration of the anti-Stokes scattering using wavevector diagram

Figure 5 represents experimentally observed spectrum in standard optical fiber, where lines corresponding to the Stokes, anti-Stokes and Rayleigh scatterings are clearly seen. In order to estimate the spectral width of the scattered light we should include effect of the attenuation of the acoustic wave. Using damping parameter of the acoustic wave we can write that full width at half maximum (FWHM) of the scattered light is given by

$$\Delta\Omega_B = 1/\tau_p = \Gamma q^2 = \Gamma 4n^2 \frac{\omega^2}{c_0^2} \sin^2\left(\frac{\varphi}{2}\right) \qquad (2.78)$$
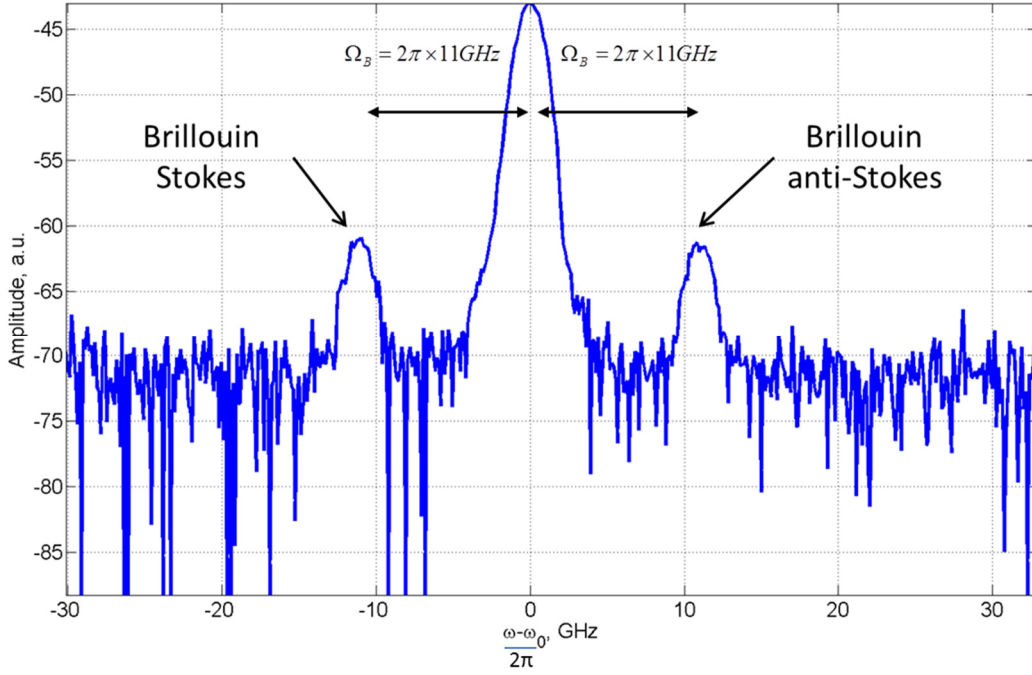
Figure 5. Spectrum of the backscattered light observed in standard single mode optical fiber, where incident wavelength λ=1551 nm. Stokes and anti-Stokes spontaneous Brillouin lines are observed with Brillouin frequency shift of 11 GHz.

2.4.2 Stimulated Brillouin Scattering

In the previous section we considered Brillouin scattering of light by optical inhomogeneity, which arises as the result of the thermal fluctuations of the density, and consequently fluctuations of the dielectric constant. This scattering is called "spontaneous" Brillouin scattering. In this situation intensity of the incident light is low and has no effect on the medium itself. The fluctuations of the density of the medium can be completely described by the Debye thermal waves. Moreover, intensity of the spontaneous scattering from the thermal fluctuations increases linearly with increase in the linear dimensions of the scattering volume in the direction of observation of the scattered light. On the other hand when the incident light intensity becomes high the process of scattering is said to be stimulated. This means that fluctuations in the optical properties of a material are induced by the presence of the optical wave. In other words, incident and scattered light affect the motion of the medium, and as a result of their interaction acoustic waves of high intensity can be generated. Such type of scattering is generally called stimulated Brillouin scattering (SBS). In stimulated Brillouin scattering the intensity of the scattering increases nonlinearly with increase in the linear dimensions of the scattering volume in the direction of observation of the scattered light. SBS was first observed in crystals of quartz and sapphire by Chiao, Townes, and Stoicheff [26]. Later on, it will become clear that it is the interference between the incident light of high intensity and generated Stokes wave that is responsible for the generation of powerful acoustic waves. There are two physical phenomena which can translate fluctuations in intensity into generation of phonons: electrostriction and optical absorption. The later one

is less commonly use, and moreover, it can occur only in lossy optical media. In the following section we show that effect of electrostriction is the one which is responsible for the generation of the elastic (acoustic) waves of high intensity in silica fibers.

2.4.2.1   *Electrostriction*

Electrostriction is the property of the dielectric to change its volume when external electric field is applied. When a dielectric medium is placed in the electric field an electrostricitve force arises as a consequence of the maximization of stored energy. Under this force molecules are pulled into the region where electric field is maximum, thus changing the density of the material by the amount of $\Delta\rho$. We can represent this change in density as a change in dielectric constant of the media using the following expression:

$$\Delta\varepsilon = \left(\frac{\partial\varepsilon}{\partial\rho}\right)\Delta\rho \tag{2.79}$$

Energy density of the medium also changes according to the expression [5]:

$$\Delta u = \frac{1}{2}\varepsilon_0\Delta\varepsilon E^2 = \frac{1}{2}\varepsilon_0\left(\frac{\partial\varepsilon}{\partial\rho}\right)\Delta\rho E^2 \tag{2.80}$$

According to the principles of thermodynamic change in energy density in this case will be equal to the work performed in compressing the material. Thus we can write:

$$\Delta w = p_{st}\frac{\Delta V}{V} = -p_{st}\frac{\Delta\rho}{\rho} = \Delta u \tag{2.81}$$

where p_{st} is the excess in pressure due to the presence of the electric field. Equating (2.80) and (2.81) we get:

$$p_{st} = -\frac{1}{2}\varepsilon_0\rho\left(\frac{\partial\varepsilon}{\partial\rho}\right)E^2 = -\frac{1}{2}\varepsilon_0\gamma_e E^2 \tag{2.82}$$

where γ_e is electrostrictive constant already defined in equation (2.52). Equation (2.82) shows that pressure is reduced in the region of the material where electric field is applied. Thus molecules of the material tend to move towards the region of reduced pressure increasing this way the density of the material. By representing the change in density of the material as $\Delta\rho = -\left(\frac{\partial\rho}{\partial p}\right)\Delta p$ and equating Δp with p_{st} we get:

$$\Delta\rho = -\rho\left(\frac{1}{\rho}\frac{\partial\rho}{\partial p}\right)p_{st} = -\rho C p_{st} = \frac{1}{2}\varepsilon_0\rho C\gamma_e E^2 \tag{2.83}$$

where C is the compressibility. Equation (2.83) describes change in density due to the applied static electric field. Now if we are considering optical waves as sources for electric fields, we must replace E with time averaged value $\left\langle E^2 \right\rangle$.

2.4.2.2 Mathematical description of Stimulated Brillouin Scattering

In this section we consider that stimulated Brillouin scattering is driven by the effect of electrostriction and we describe the situation where a strong pump wave and a weak signal waves are launched in the optical media (fiber) counterpropagating each other with frequency difference of $\omega_p - \omega_s \approx \Delta\Omega_B$. Under this condition the acoustic wave will be excited efficiently and we can represent the process using Figure 6. The beating between the two optical waves pump and probe results in a moving interference pattern, where the electrical field is spatially periodic. If the above condition is fulfilled, periodic intensity oscillation will be close or the same as the frequency of the acoustic vibration. Following the discussion in previous section electrostriction changes the density of the material accordingly resulting in the generation of a density wave. Generated periodicity in material density changes the refractive index of the material creating a moving grating. Such moving grating diffracts pump light towards the signal, resulting in a signal gain. As a result of full cycle, energy was transferred from pump wave to the signal wave. The process repeats again leading to the amplification of signal and acoustic wave.
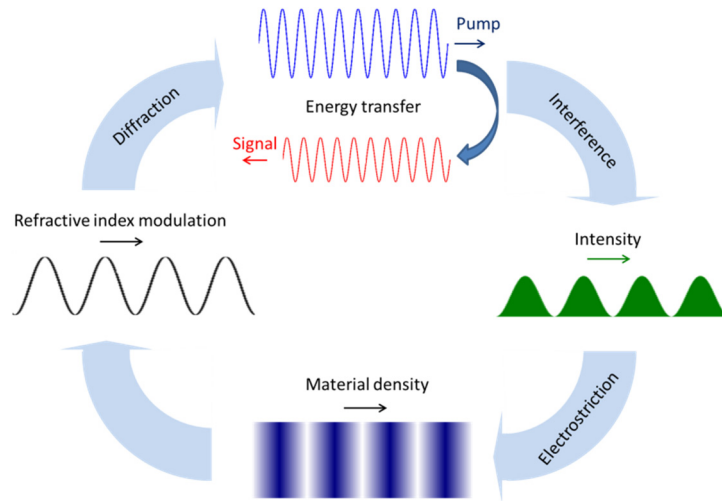
Figure 6. Stimulated Brillouin scattering process.

In order to describe interactions between optical waves and acoustic wave in stimulated Brillouin scattering we consider a situation when pump wave propagates in the optical fiber along the z axis from the beginning of the fiber at *z=0* to *z=L*. On the other hand signal wave is launched from the opposite end of the fiber, so it propagates from *z=L* to *z=0*. Thus we can write for pump and signal waves:

$$E_p(t,z) = \widehat{e}_p A_p(t,z) \exp\left(i\left(\omega_p t - k_p z\right)\right) + c.c. \tag{2.84}$$

$$E_s(t,z) = \widehat{e}_s A_s(t,z) \exp\left(i\left(\omega_s t + k_s z\right)\right) + c.c. \tag{2.85}$$

Total electric field in the medium then will be given by $E(t,z) = E_s(t,z) + E_p(t,z)$. For simplicity we assume that pump and signal wave have parallel polarization. This way we can drop the unit polarization vectors of the pump and the signal waves, $e_{p,s}$. We can represent acoustic field as a material density fluctuation, so we can describe it as:

$$\rho(t,z) = \rho_0 + \left(\rho(t,z)\exp\left(i(\Omega t - qz)\right) + c.c.\right) \tag{2.86}$$

where $\Omega = \omega_p - \omega_s, q = 2k_p$, and ρ_0 is the mean density of the medium. And assuming that density fluctuations propagate in a medium according to the acoustic wave equation we write:

$$\frac{\partial^2 \rho}{\partial t^2} - \Gamma\nabla^2\frac{\partial\rho}{\partial t} - V^2\nabla^2\rho = \nabla\bullet\nabla p_{st} \tag{2.87}$$

where Γ and V are damping coefficient defined in equation (2.57) and velocity of sound, respectively. Term on the right hand side of the equation (2.87) represents a source of the acoustic waves as a result of electrostriction. In the following derivations we use slowly varying envelop approximation (SVEA). By inserting the expression for electrostirictive pressure (2.82) in equation for propagation of acoustic wave (2.87) we get:

$$\frac{\partial^2 \rho}{\partial t^2} - \Gamma\nabla^2\frac{\partial\rho}{\partial t} - V^2\nabla^2\rho = -\frac{1}{2}\varepsilon_0\gamma_e\nabla\bullet\nabla\left\langle\left(A_p\exp\left(i\left(\omega_p t - k_p z\right)\right) + A_s\exp\left(i\left(\omega_s t + k_s z\right)\right) + c.c.\right)^2\right\rangle \tag{2.88}$$

Using equations for optical waves we can see that time average of the resulted electric field contains static and hypersonic components. Since we are interested in components oscillating at acoustic frequency we can write it as:

$$\left\langle\left(E_p + E_s\right)^2\right\rangle = 2A_p A_s^* \exp\left(i(\Omega t - qz)\right) + c.c \tag{2.89}$$

and

$$\nabla\bullet\nabla\left\langle\left(E_p + E_s\right)^2\right\rangle = -q^2 2\left(A_p^* A_s\exp\left(i(\Omega t - qz)\right) + c.c.\right) \tag{2.90}$$

By inserting equation (2.86) and (2.90) in the equation (2.88) and using SVEA approximation we arrive to the expression:

$$-2i\Omega\frac{\partial\rho(t,z)}{\partial t} - \rho(t,z)\Omega^2 + \Gamma q^2\frac{\partial\rho(t,z)}{\partial t} - 2\Gamma q\Omega\frac{\partial\rho(t,z)}{\partial z} - i\Gamma\Omega q^2\rho(t,z) - 2iqV^2\frac{\partial\rho(t,z)}{\partial z} + V^2 q^2\rho(t,z) = \varepsilon\gamma_e q^2 A_p A_s^* \tag{2.91}$$

If we insert $\Omega_B^2 = V^2 q^2$, $\Gamma q^2 = \dfrac{1}{\tau_p}$ and rearrange the terms we get following expression:

$$\left(-2i\Omega+\frac{1}{\tau_p}\right)\frac{\partial\rho(t,z)}{\partial t}+\left(\Omega_B^2-\Omega^2-\frac{i\Omega}{\tau_p}\right)\rho(t,z)-\left(2iqV^2+2\Omega\Gamma q\right)\frac{\partial\rho(t,z)}{\partial z}=\varepsilon_0\gamma_e q^2 A_p A_s^* \qquad (2.92)$$

Equation (2.92) can be simplified by omitting the last term on the left hand side, since propagation of phonons is considered negligible due to strong damping. Thus, $\frac{\partial\rho(t,z)}{\partial z}$ can be set to zerp. Moreover, if we consider steady state situation, time derivative also vanishes resulting in the following expression of the acoustic wave:

$$\rho(t,z)=\frac{\varepsilon_0\gamma_e q^2 A_p A_s^*}{\left(\Omega_B^2-\Omega^2-\dfrac{i\Omega}{\tau_p}\right)} \qquad (2.93)$$

To model the evolution of pump and probe waves along the propagation distance inside the fiber we write wave equations:

$$\frac{\partial^2 E_p}{\partial z^2}-\frac{n^2}{c^2}\frac{\partial^2 E_p}{\partial t^2}=\frac{1}{\varepsilon_o c^2}\frac{\partial^2 P_p}{\partial t^2} \qquad (2.94)$$

$$\frac{\partial^2 E_s}{\partial z^2}-\frac{n^2}{c^2}\frac{\partial^2 E_s}{\partial t^2}=\frac{1}{\varepsilon_o c^2}\frac{\partial^2 P_s}{\partial t^2} \qquad (2.95)$$

where nonlinear polarization terms can be represented as

$$P_p=\frac{\varepsilon_0\gamma_e}{\rho_0}\rho(t,z)A_s\exp\left(i\left(\omega_p t-k_p z\right)\right)+c.c. \qquad (2.96)$$

$$P_s=\frac{\varepsilon_0\gamma_e}{\rho_0}\rho^*(t,z)A_p\exp\left(i\left(\omega_s t+k_s z\right)\right)+c.c \qquad (2.97)$$

By introducing equations (2.96), (2.97) together with equations (2.84), (2.85) into equations (2.94), and (2.95) we obtain:

$$\frac{\partial A_p(t,z)}{\partial z}+\frac{n}{c_0}\frac{\partial A_p(t,z)}{\partial t}=\frac{i\omega_p\gamma_e}{2nc_0\rho_0}\rho(t,z)A_s(t,z) \qquad (2.98)$$

$$-\frac{\partial A_s(t,z)}{\partial z}+\frac{n}{c_0}\frac{\partial A_s(t,z)}{\partial t}=\frac{i\omega_s\gamma_e}{2nc_0\rho_0}\rho^*(t,z)A_p(t,z) \qquad (2.99)$$

Considering steady-state conditions the expressions for optical waves can be written as:

$$\frac{\partial A_p}{\partial z}=\frac{i\varepsilon_0\gamma_e^2 q^2\omega_p}{2nc_0\rho_0}\frac{A_p\left|A_s\right|^2}{\left(\Omega_B^2-\Omega^2-\dfrac{i\Omega}{\tau_p}\right)} \qquad (2.100)$$

$$-\frac{\partial A_s}{\partial z} = \frac{i\varepsilon_0 \gamma_e^2 q^2 \omega_s}{2nc_0\rho_0} \frac{A_s |A_p|^2}{\left(\Omega_B^2 - \Omega^2 + \frac{i\Omega}{\tau_p}\right)} \qquad (2.101)$$

By inserting the intensities as $I_i = 2n\varepsilon_0 c A_i A_i^*$ we can rewrite the equations (2.100) and (2.101) as:

$$\frac{\partial I_p}{\partial z} = -g I_p I_s \qquad (2.102)$$

$$\frac{\partial I_s}{\partial z} = -g I_p I_s \qquad (2.103)$$

where g is the SBS gain factor, which is represented to good approximation by:

$$g = \frac{\gamma_e^2 \tau_p \omega^2}{nVc_0^3\rho_0} \frac{\left(\frac{1}{2\tau_p}\right)^2}{(\Omega_B - \Omega)^2 + \left(\frac{1}{2\tau_p}\right)^2} \qquad (2.104)$$

Normally gain coefficient at the center of the Brillouin gain is represented by the equivalent expression [2]:

$$g_B = \frac{\gamma_e^2 \tau_p \omega^2}{nVc_0^3\rho_0} = \frac{2n^7\pi^2 p_{12}^2 \tau_p}{c_0\lambda_p^2\rho_0 V} \qquad (2.105)$$

where λ_p is the pump wavelength, p_{12} is longitudinal elasto-optic coefficient, and V is acoustic velocity. In bulk silica gain coefficient g is approximately 5×10^{-11} m/W. As it is seen from the equation (2.104) Brillouin gain has a Lorentzian shape with the FWHM given by the acoustic phonon lifetime. We repeat here the expression (2.78) for the linewidth of the gain spectrum:

$$\Delta\Omega_B = 1/\tau_p \qquad (2.106)$$

Thus:

$$\Delta v_B = \Delta\Omega_B / 2\pi = 1/2\pi\tau_p \qquad (2.107)$$

In standard optical fibers linewidth of the Brillouin gain is measured to be around 27 MHz. Value of the width of the Brillouin gain spectrum for fibers differs significantly from that of bulk silica ($\Delta v = 17$ MHz), because of the guided features of the optical and acoustic modes and the presence of dopants in fiber core. Increase of the spectral width can be also related to the inhomogeneties in the fiber-core cross section along the fiber length. Figure 7 shows the

Brillouin gain spectrum experimentally obtained in the Panda-type polarization maintaining fiber, where FWHM is measured to be 30 MHz.

By looking at the equation (2.103) we can see that intensity of the signal wave grows exponentially with propagation distance z:

$$I_s(z) = I_s^0(L)\exp\left(g\, I_p(L-z)\right) \tag{2.108}$$
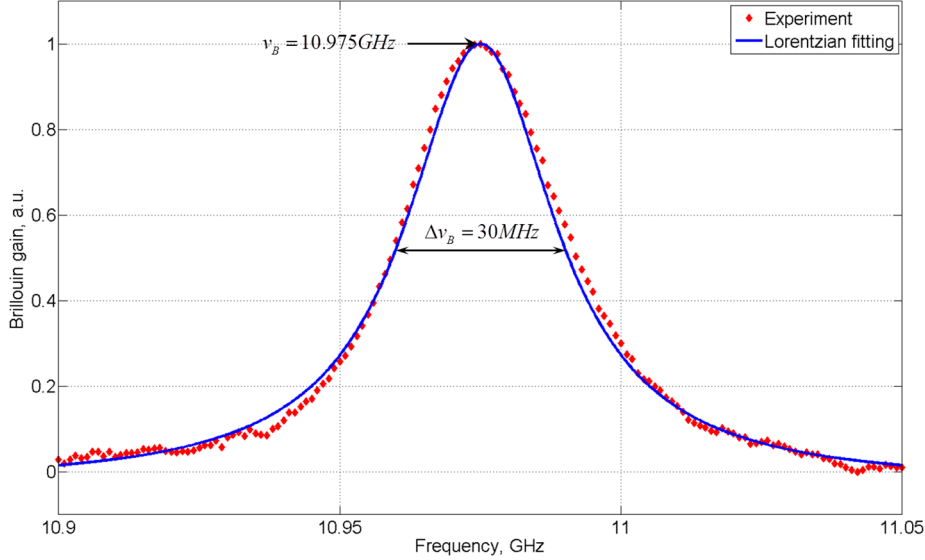
Figure 7. Measured Brillouin gain profile in Panda PM fiber at wavelength 1.55 µm (red diamonds). Lorentzian fitting (blue line).

where signal wave is launched from the fiber end at $z=L$. Here we approximated that pump power is constant along the fiber and fiber is lossless. Wave equations for pump and signal are modified if fiber attenuation, α, is included:

$$\frac{\partial I_p}{\partial z} = -gI_pI_s - \alpha I_p \tag{2.109}$$

$$\frac{\partial I_s}{\partial z} = -gI_pI_s + \alpha I_s \tag{2.110}$$

In such condition equation for signal wave (2.108) assuming constant pump power along the fiber should be rewritten as:

$$I_s(z) = I_s^0(L)\exp\left(gI_pL_{eff} - \alpha(z-L)\right) \tag{2.111}$$

where $L_{eff} = \dfrac{1-\exp(-\alpha L)}{\alpha}$ is effective length, which can be regarded as a length for which pump power is considered constant, or in other words in lossless medium.

By looking at the imaginary parts of the expressions (2.100) and (2.101) we can see the phase change of optical waves as a result of stimulated Brillouin scattering:

$$\frac{\partial \Phi_p}{\partial z} = \frac{\gamma_e^2 q^2 \omega_p I_s}{n^2 c_0^2 \rho_0} \frac{\left(\Omega_B^2 - \Omega^2\right)}{\left(\left(\Omega_B^2 - \Omega^2\right) + \frac{\Omega^2}{\tau_p^2}\right)} \cong 2 g_B I_s \frac{2\Delta v / \Delta v_B}{\left(1 + \left(2\Delta v / \Delta v_B\right)^2\right)} \qquad (2.112)$$

$$\frac{\partial \Phi_s}{\partial z} = \frac{\gamma_e^2 q^2 \omega_s I_p}{n^2 c_0^2 \rho_0} \frac{\left(\Omega_B^2 - \Omega^2\right)}{\left(\left(\Omega_B^2 - \Omega^2\right) + \frac{\Omega^2}{\tau_p^2}\right)} \cong 2 g_B I_s \frac{2\Delta v / \Delta v_B}{\left(1 + \left(2\Delta v / \Delta v_B\right)^2\right)} \qquad (2.113)$$

where we used approximation that $(\Omega_B^2 - \Omega^2) = 2\Omega(\Omega_B - \Omega)$, $2\pi\Delta v = \Omega_B - \Omega$ and $2\pi\Delta v_B = \Delta\Omega_B = 1/\tau_p$. Figure 8 represents Lorentzian distribution of the Brillouin gain and its associated nonlinear phase shift.
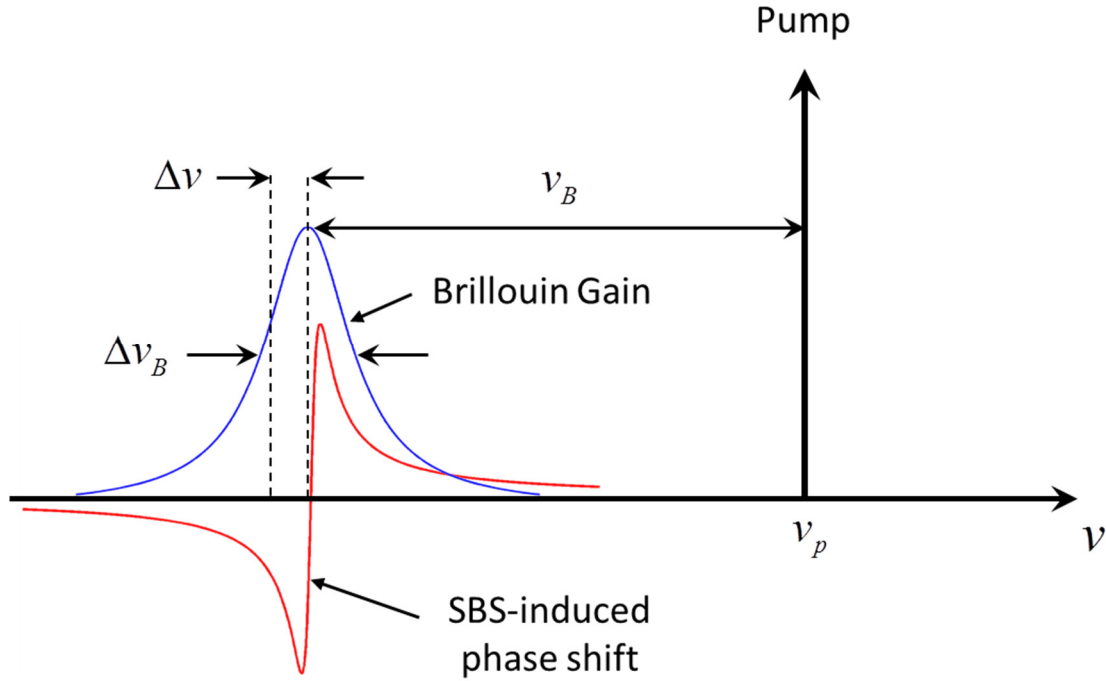
Figure 8. Lorentzian distribution of the Brillouin gain spectrum and its associated nonlinear phase shift.

2.5   Application of nonlinearities for signal processing

In the early 1970s, there was intensive development of the optical communication networks when one of the main limitations of optical fibers was resolved. At that time light absorption in optical fibers was reduced to less than 20 dB/km. Moreover chip semiconductor lasers were invented emitting highly coherent and stable light waves. When the advantages of optical fiber with respect to electrical cable became obvious, many communication companies started to install optical cables. Capacity achievable with fiber technology is more than 50 Tbps which is several orders higher than that of electrical systems. By installing fibers for long distances, information bit rate of the communication links raised from 45 Mbps to 100 Gbps. This impressive growth was made possible due to the resolution of the three main problems inherent to any transmitting media: attenuation, dispersion and nonlinear interaction. Attenuation of the fibers up to date has been reduced to 0.2 dB/km allowing transmission of the light signals for more than 50 km without any amplification. With the invention of the Er-doped fiber amplifier (EDFA), attenuation of the silica is no longer a problem for data transmission. The second impairment was the dispersion of the fibers, which caused optical pulses to spread while propagating. Dispersion engineering in fibers allowed to create fiber links where overall dispersion can be nearly fully compensated. Development of high power lasers and high gain amplifiers combined with increasing length of the links resulted in the fact that fiber nonlinearities started to play significant obstacle for using the full bandwidth of optical fiber. Even though in optical communication links fiber nonlinearities are considered as detrimental effects for the performance of the system, they can be useful for constructing optical devices capable of performing all-optical high speed processing functions on optical signals. After deep investigation of effects of group velocity dispersion, self-phase modulation, cross phase modulation, four-wave mixing, Brillouin and Raman scattering in optical fibers beneficial aspects can be extracted from these effects. Nonlinear effects can distort the transmitted pulses and as a consequence degrade the system performance. However the same nonlinear effects can be used to implement all-optical devices operating at extremely high rates.

FWM and XPM are two main effects used in ultrafast optical switching. Up to date time division multiplexing (TDM) is still one of the most common scheme to send the information through optical fibers. In this scheme bits from each individual channel at one wavelength are multiplexed onto a single line for fixed time slot. At the receiver end demultiplexing should be performed to select the bit (or packet of bits) of a given channel from an optical fiber and redirect it to another port of the switch. In such situations time-domain switches are needed which can be turned on for a specific duration using an external control. This operation can be done using nonlinear effect of XPM in optical fibers. The XPM-based switches make use of a Sagnac interferometer that converts phase modulation into amplitude modulation [12]. Sagnac interferometer acts as a perfect mirror when the 3-dB coupler is used. This is due to the fact that phase shifts acquired by the waves propagating in different directions are the same. To make the Sagnac loop transmits one of the waves acting as a switching device a control signal is injected into the loop such that it propagates only in

one direction and induces a XPM phase shift on the copropagating wave. Only the part of the wave which physically overlaps with the control pulse obtains an additional phase and can be transmitted through, while the rest of the input signal is reflected. As a result such a scheme provides the ability to select different temporal slices of the input signal and each slice can be quite short because of the femtosecond response time of the fiber nonlinearity.

Another nonlinear effect which can be used for ultra-fast optical signal switching is FWM. In this implementation the pump signal at the frequency ω_p is launched in the optical fiber copropagating with the signal (ω_s) to be demultiplexed. As a result of the four-wave mixing process the idler wave is generated at the frequency $\omega_i = 2\omega_p - \omega_s$. Now if the pump wave is switched on only for a short period of time, the idler wave is generated only during the duration of the pump pulse. Idler wave represents a "copy" of the slice of the signal that overlaps with the pump pulse, but at the different optical frequency. By inserting the optical filter resonant at the idler frequency we can receive only needed data packet from the rest of the OTDM channel. An individual bit can be selected if the pump pulse lasts only over the duration of a single bit. FWM-based packet switching as well as bit-level switching was successfully realized at a 40-Gb/s bit rate in a 2005 experiment. As we can see generated idler wave is at the other optical frequency than input signal. This way FWM can be used as a wavelength converter. Although four-wave mixing inside a semiconductor optical amplifier is often used for wavelength conversion, an optical fiber has the distinct advantage that it can operate with higher bit rates. Moreover signal and idler waves can get amplified in the FWM process, which is an extremely useful feature.

XPM can be also used as a wavelength converter for high bit rate optical signals [12]. The idea of such a converter can be realized using nonlinear optical loop mirror (NOLM) acting as a Sagnac interferometer. The data signal at wavelength λ_D needs to be converted to another wavelength. This data is launched inside a fiber of appropriate length together with continuous wave at wavelength λ_1 which is the desired wavelength of conversion. Data pulses act as pump and impose an XPM-induced phase shift on the CW wave only in the time intervals associated with the 1 bits. The phase shift is turned into amplitude modulation using and Sagnac interferometer implementation. The data channel is launched such that it affects the CW wave in only one direction, resulting in a differential phase shift that can be used to copy the bit pattern of the data channel onto the transmitted signal at λ_1. Wavelength converters based on NOLM are capable to operate at bit rates of up to 40 Gb/s [27]. XPM based wavelength converters can be also implemented without using optical interferometer. As an alternative, one can launch the signal bit stream together with a CW wave into a fiber and use a suitable bandpass filter at the output of the fiber. Signal pulses at the wavelength λ_s act as a pump and affect the phase and spectrum of the CW wave (at the desired wavelength λ_1) through XPM only in the time slots associated with the 1 bits. If the passband of the optical filter is shifted from λ_1 by a suitable amount, the output is a replica of the original bit stream at the new wavelength.

Another important optical processing tool for lightwave communication systems is data-format conversion, since different networks use various formats for coding a bit stream. Non-return-to-zero (NRZ) format is often employed in wavelength division multiplexing (WDM) networks as it is most efficient spectrally. On the other hand, return-to-zero (RZ) format is mainly used for OTDM systems. Another modern and widely used format is differential phase shift keying (DPSK). In certain cases it may become necessary to convert a data stream among different formats. It was shown that using XPM and NOLM it is possible to convert from NRZ to RZ and vice versa [28].

XPM and FWM phenomena in optical fiber were also shown to be used for all-optical sampling. Optical sampling is a method to measure high speed optical signals whose bandwidth can exceed 100 GHz. First FWM-based technique was demonstrated in 1991 and in 2006 this technique reached commercial stage [12]. XPM-based sampling techniques with highly nonlinear fiber showed temporal resolution of 0.7 ps for 320 Gb/s signal [12].

In previous sections we saw that a signal while propagating in the optical fiber link gets attenuated due to fiber losses. Moreover spectrum and temporal shape of each bit change through a combination of dispersive and nonlinear effects. Optical amplifiers can be used to recover the amplitude of the signal, but at the same time they degrade the bit stream by adding unnecessary amplified spontaneous emission (ASE). Additional ASE affects signal to noise ratio as well as increase timing jitter. To prevent further degradation of the signal it needs to be regenerated using optical regenerators. Such devices are capable of recovering original form of the degraded bit stream by performing three functions: amplification, reshaping, and retiming. 3R regenerators are the devices which can perform all three above mentioned functions. Devices, that perform only first two functions, are called 2R regenerators. Since for processing high bit rate signals optical devices should be able to operate in ps time scale, fiber nonlinearities (SPM, XPM, and FWM) are good candidates for realizing 2R and 3R regenerators. After 2003 SPM-based 2R regenerators were demonstrated using high nonlinear and bismuth-oxide glass fibers [12]. Degraded signal was first amplified by EDFA and launched inside the fiber, where spectrum is broadened considerably thanks to SPM. Afterwards signal is passed through a bandpass filter, whose central wavelength is set appropriately, resulting in a output bit stream with reduced noise and improved pulse characteristics. It should be pointed out that launched power into the fiber depends on the fiber length and filter offset, and it must be optimized for such regenerators to work well. The nonlinear phenomenon of XPM is also shown to be useful for optical regeneration in a set of experiments [12]. The basic scheme is similar to that used for SPM-based regenerators except that the OTDM signal is launched together with control pulses in the form of optical clock.

An FWM phenomenon was also used to implement 2R regenerators starting from 2000 [29]. Since FWM in optical fiber amplifies the signal and idler wave it is basically an optical amplifier, which is called fiber optic parametric amplifier (FOPA). Similar to any amplifier, FOPA gain can be saturated resulting in reduction of the fluctuations in peak power of a data stream.

3R regenerators were experimentally demonstrated employing XPM and SPM optical phenomena [12]. SPM-based 3R regenerator together with electro-optic modulator showed considerable reduction in time jitter for a fiber link. Moreover SPM was used to regenerate phase-encoded signals, such as DPSK signals. In the other setup XPM-based regenerator showed considerable improvement of the bit-error rate of 10 Gb/s signal because of reduced noise level and timing jitter.

Stimulated versions of various types of scatterings in fiber were also explored for application in optical signal processing. For instance, Raman scattering, which occurs in the fibers due to the vibrational motion of the silica molecules, is highly attractive for signal amplification. Raman scattering produces a large gain spectrum with bandwidth of around 3 THz and 13 THz lower than the pumping frequency. Such large bandwidth is very useful for amplification of optical signals in broadband transmission systems. Moreover Raman fiber amplifiers are capable to produce a low amplification per unit length with low noise and for very long distances. Such amplification is just enough to compensate the fiber loss, making optical fiber nearly lossless for a propagating signal [3]. Even though Raman scattering was used to demonstrate slow light experiments [30] efficiency is very low compared to the experiments with stimulated Brillouin scattering due to the low gain of the process.

Stimulated Brillouin scattering has even broader application range for optical signal processing, since this inelastic scattering requires less activation power than that for Raman scattering. Since the first observation in optical fibers by Ippen and Stolen [31], SBS attracted a lot of attention in the scientific community. Brillouin fiber lasers were demonstrated just few years later showing low threshold, high conversion efficiency and narrow output of the linewidth [32, 33]. Later SBS was used as a signal processing tool in order to control the group velocity of an optical pulse and a phase of optical wave for analog signals [34, 35].

Bibliography

1.   M. C. T. Bahaa E. A. Saleh, ed. *Fundamentals of phonotics* (John Wiley & Sons, Inc., 1991).
2.   G. P. Agrawal, *Nonlinear fiber optics* (2007).
3.   L. Thévenaz, ed. *Advanced fiber optics. Concepts and technology* (CRC Press, Lausanne, 2011).
4.   J. A. Buck, *Fundamentals of Optical Fibers* (John Wiley&Sons, Inc., New Jersez, 2004).
5.   R. W. Boyd, *Nonlinear optics* (Academic Press, Amsterdam ; Boston, Mass., 2003).
6.   D. A. Kleinman, "Nonlinear Dielectric Polarization in Optical Media," Physical Review **126**, 1977-1979 (1962).
7.   K. O. Hill, D. C. Johnson, B. S. Kawasaki, and R. I. MacDonald, "cw three-wave mixing in single-mode optical fibers," Journal of Applied Physics **49**, 5098-5106 (1978).
8.   R. H. Stolen, J. E. Bjorkholm, and A. Ashkin, "Phase-matched three-wave mixing in silica fiber optical waveguides," Applied Physics Letters **24**, 308-310 (1974).
9.   K. Washio, K. Inoue, and S. Kishida, "Efficient large-frequency-shifted three-wave mixing in low dispersion wavelength region in single-mode optical fibre," Electronics Letters **16**, 658-660 (1980).
10.   N. Shibata, R. Braun, and R. Waarts, "Phase-mismatch dependence of efficiency of wave generation through four-wave mixing in a single-mode optical fiber," Quantum Electronics, IEEE Journal of **23**, 1205-1210 (1987).
11.   K. Inoue, and H. Toba, "Wavelength conversion experiment using fiber four-wave mixing," Photonics Technology Letters, IEEE **4**, 69-72 (1992).
12.   G. P. Agrawal, *Applications of nonlinear fiber optics* (Elsevier Inc., 2008).
13.   E. Yamazaki, F. Inuzuka, K. Yonenaga, A. Takada, and M. Koga, "Compensation of Interchannel Crosstalk Induced by Optical Fiber Nonlinearity in Carrier Phase-Locked WDM System," Photonics Technology Letters, IEEE **19**, 9-11 (2007).
14.   L. Shenping, L. Ming-Jun, V. K. Dmitri, and A. N. Daniel, "Third Harmonic Generation in Optical Fibers," (Optical Society of America, 2009), p. TuI2.
15.   J. M. Gabriagues, "Third-harmonic and three-wave sum-frequency light generation in an elliptical-core optical fiber," Opt. Lett. **8**, 183-185 (1983).
16.   J. Thøgersen, and J. Mark, "Third harmonic generation in standard and erbium-doped fibers," Optics Communications **110**, 435-444 (1994).
17.   K. Inoue, "Four-wave mixing in an optical fiber in the zero-dispersion wavelength region," Lightwave Technology, Journal of **10**, 1553-1561 (1992).
18.   F. Shimizu, "Frequency Broadening in Liquids by a Short Light Pulse," Physical Review Letters **19**, 1097-1100 (1967).
19.   R. H. Stolen, and C. Lin, "Self-phase-modulation in silica optical fibers," Physical Review A **17**, 1448-1453 (1978).
20.   M. Oberthaler, and R. A. Hopfel, "Special narrowing of ultrashort laser pulses by self-phase modulation in optical fibers," Applied Physics Letters **63**, 1017-1019 (1993).
21.   B. R. Washburn, J. A. Buck, and S. E. Ralph, "Transform-limited spectral compression due to self-phase modulation in fibers," Opt. Lett. **25**, 445-447 (2000).
22.   A. R. Chraplyvy, and J. Stone, "Measurement of crossphase modulation in coherent wavelength-division multiplexing using injection lasers," Electronics Letters **20**, 996-997 (1984).

23.   M. N. Islam, L. F. Mollenauer, R. H. Stolen, J. R. Simpson, and H. T. Shang, "Cross-phase modulation in optical fibers," Opt. Lett. **12**, 625-627 (1987).
24.   G. P. Agrawal, P. L. Baldeck, and R. R. Alfano, "Optical wave breaking and pulse compression due to cross-phase modulation in optical fibers," Opt. Lett. **14**, 137-139 (1989).
25.   I. L. Fabelinskii, *Molecular Scattering of Light* (Plenum press, New York, 1968).
26.   R. Y. Chiao, C. H. Townes, and B. P. Stoicheff, "Stimulated Brillouin Scattering and Coherent Generation of Intense Hypersonic Waves," Physical Review Letters **12**, 592-595 (1964).
27.   J. Yu, X. Zheng, C. Peucheret, A. T. Clausen, H. N. Poulsen, and P. Jeppesen, "40-Gb/s All-Optical Wavelength Conversion Based on a Nonlinear Optical Loop Mirror," J. Lightwave Technol. **18**, 1001 (2000).
28.   S. Bigo, O. Leclerc, and E. Desurvire, "All-optical fiber signal processing and regeneration for soliton communications," Selected Topics in Quantum Electronics, IEEE Journal of **3**, 1208-1223 (1997).
29.   S. Yamashita, and M. Shahed, "Optical 2R regeneration using cascaded fiber four-wave mixing with suppressed spectral spread," Photonics Technology Letters, IEEE **18**, 1064-1066 (2006).
30.   J. Sharping, Y. Okawachi, and A. Gaeta, "Wide bandwidth slow light using a Raman fiber amplifier," Opt. Express **13**, 6092-6098 (2005).
31.   E. P. Ippen, and R. H. Stolen, "Stimulated Brillouin scattering in optical fibers," Applied Physics Letters **21**, 539-541 (1972).
32.   K. O. Hill, B. S. Kawasaki, and D. C. Johnson, "cw Brillouin laser," Applied Physics Letters **28**, 608-609 (1976).
33.   S. P. Smith, F. Zarinetchi, and S. Ezekiel, "Narrow-linewidth stimulated Brillouin fiber laser and applications," Opt. Lett. **16**, 393-395 (1991).
34.   K. Y. Song, M. G. Herraez, and L. Thevenaz, "Observation of pulse delaying and advancement in optical fibers using stimulated Brillouin scattering," Optics Express **13**, 82-88 (2005).
35.   A. Loayssa, and F. J. Lahoz, "Broad-band RF photonic phase shifter based on stimulated Brillouin scattering and single-sideband modulation," Photonics Technology Letters, IEEE **18**, 208-210 (2006).

Chapter 3

Brillouin dynamic grating.

In this chapter we introduce the phenomenon of dynamic Brillouin grating. A brief description of the structure of polarization maintaining fiber will be given in the first part of the chapter. The principle of DBG generation in PM fibers using stimulated Brillouin scattering is described. Afterwards an analytical model describing the generation of localized DBG using pulsed pump waves is presented. Some properties of DBG are discussed such as length, shape, bandwidth, reflectivity, resonant wavelength. Last part of the chapter is devoted to the calculation of the DBG phase response.

Fiber Bragg gratings are structures where optical property of the core such as index of refraction is modulated in a periodic fashion. Such devices were first demonstrated in 1978 by Hill et al. Since then fiber Bragg grating technology developed substantially, and nowadays various types of FBGs are used in many fields of research and commercial systems such as in the telecommunication industry (WDM, dispersion compensation, filtering) and for numerous sensing applications [1-3]. Periodic perturbation of the refractive index along the fiber is possible due to photosensitivity property of the Germania-doped fiber, where refractive index is changed under UV illumination. With the development of FBG technology it is possible nowadays to create a grating with desired spectral characteristics by modifying such parameters as induced index change, length, apodization, period chirp, and others. The only drawback of the FBG is that once it has been designed and fabricated it is difficult to change the spectral characteristics of the grating or erase the grating completely. In other word produced grating is fixed and the induced refractive index change can only be changed by high temperature annealing.

On the other hand, instead of inducing permanent change in optical properties of fiber core it is possible to achieve modulation of optical properties in real time using laser light and effect of four-wave mixing. It was an interesting topic of research from the early 1980s [4-9]. Interference pattern of two intersecting light beams can be used to produce dynamic grating in the material which is illuminated by the interference. The grating spacing and amplitude can be controlled by the intersection angle and intensity of the waves. Optical waves with different frequencies result in a propagating grating. In contrast to FBG dynamic gratings disappear after the inducing light waves have been switched off.

The modulation of optical properties in a dynamic grating can be described by an intensity dependent refractive index or absorption coefficient. Basically change of the optical properties has to be related to some material excitation, e.g., temperature, carrier density in a semiconductor, space charge in a photorefractive material, molecular vibrations, density and entropy variations, or molecular orientations. No special crystal symmetry is required to

observe such intensity-dependent effects so that gratings can be induced in any material. However, photosensitivity broadly varies for different materials.

Dynamic gratings have been induced in various solid, liquid, and gaseous materials. In general dynamic grating is induced by two optical waves and afterwards detected by diffraction of a third probing beam. Also, self-diffraction of the light waves inducing the grating is possible. Waves diffracted into the directions of the incident waves give rise to amplitude and phase changes. Moreover, diffraction from moving gratings is accompanied by frequency shifts.

In the presence of optical fields, different possible material excitations are stimulated, resonantly or nonresonantly, to different levels. The resonant excitation may or may not dominate. In any case, the overall material excitation is the sum of all the different individual excitations. In the case of SBS, as we saw in the previous chapter, material excitation in form of phonon grating can be generated by the electrostrictive force. This acoustic grating then scatters the pump wave to yield a frequency-shifted scattered light. In the case of four-wave mixing (FWM), instead of phonon excitation, the dynamic grating is forced out by optical mixing and following Kerr nonlinearity. With a special arrangement, FWM can generate a phase conjugated reflection to one of the input waves from generated dynamic grating. Because of wide range of applications of phase conjugation by degenerate FWM, this special case has been the focus of research for many years.

Later dynamic gratings were generated using resonant material excitations such as gain peak of erbium-doped fiber amplifiers [9]. Using a 12-m long erbium-doped fiber it was demonstrated that dynamic grating reflecting the 1535 nm light was generated with spectral width of 16-MHz. The center of reflection band could be tuned by changing the laser wavelength. Nevertheless tuning range is limited by the gain bandwidth of the EDFA. In this paper researchers mentioned that reflection wavelength can be offset from the wavelength generating the grating. They proposed to use different modes of the fiber or highly birefringent fibers. It can be mentioned that Er-doped fiber based dynamic grating suffered from few problems, such as the difficulty to separate write and read beams, as well as spontaneous emission noise arising from the optical pumping.

In this thesis we will investigate another type of dynamic grating, which is called dynamic Brillouin grating [10]. Such grating can be generated in optical fibers by two optical waves $E_1(v_1)$ and $E_2(v_2)$, which satisfy the Brillouin condition. Namely, optical frequencies of the light waves should be separated by the Brillouin frequency shift of the fiber, $\Delta v = v_1 - v_2 = \Delta v_B$, and they should propagate in opposite direction to each other. Produced dynamic Brillouin grating is not a static grating, but it moves with the velocity of sound in the fiber core. To observe the scattering from the generated grating we used polarization orthogonality of the writing and reading waves. Waves generating the grating are linearly polarized along one axis of the fiber. A third optical wave $E_3(v_3)$ polarized orthogonally to $E_1(v_1)$ and $E_2(v_2)$ is used to probe the dynamic grating. Frequency v_3 is distinct from the

frequencies v_1 and v_2, due to the different polarization of the waves. To preserve the polarizations of the interacting waves special type of fibers is employed, called polarization maintaining fibers.

3.1. Polarization maintaining fibers (PMF).

Standard single mode fibers in essence support two orthogonally linearly polarized modes, due to the cylindrical symmetry of the fiber core. Due to fiber imperfections as well as twists and bends, such modes propagate along the fiber with different velocities, giving rise to polarization mode dispersion. Moreover their phase velocities are not the same, resulting in a random evolution of the state of polarization of the electromagnetic field. For some applications it is important to control the state of polarization of the propagating wave. Specially fabricated high birefringence fibers are made especially anisotropic. This can be achieved by either using elliptical core, or by inducing anisotropic stress in the core region. Panda-type PMF is composed of two B_2O_3-doped silica stress applying rods that are inserted in a pure silica cladding and symmetrically placed beside a GeO_2-doped silica core, as shown in Figure 9. Holes for the boron-doped stress rods in the preform are drilled ultrasonically. Due to the difference in thermal contraction between boron-trioxide-silica and pure silica, core of the fiber experiences strong anisotropic stresses during the drawing process. The residual stress makes the refractive index along the line connecting the centers of the stress rods (n_x) slightly greater than that orthogonal to this line (n_y). Consequently light wave polarized linearly along the x-axis (slow axis or axis with n_x) propagates slower than that along y-axis (fast axis or axis with n_y). Furthermore, light launched into either of these two axes, remains parallel to that physical axis, even when the fiber is moderately twisted or bent.
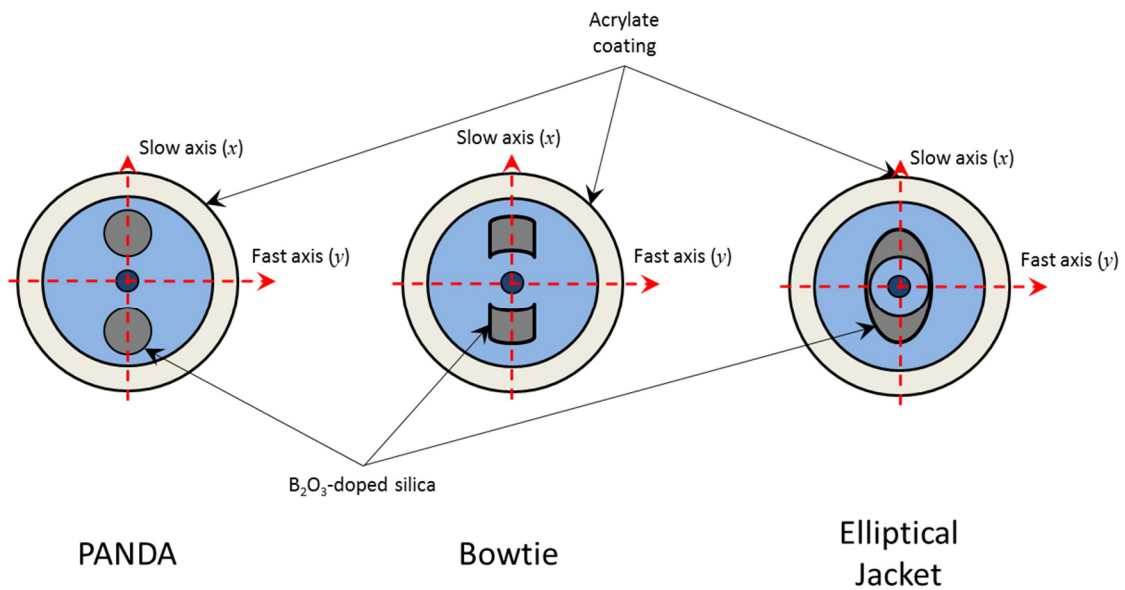
Figure 9. Cross section of Panda, bowtie, and elliptical jacket PM fibers

There exist two more widely used stress-birefringent types of PM fibers, Bowtie and elliptical jacket [11]. These fibers function in the same way as Panda type, namely birefringence is obtained by keeping the core of the fiber in tension. It should be pointed out that polarization maintenance is not a loss mechanism; under vast majority of practical circumstances, there is no measurable difference in attenuation between the fast and slow axes. The only difference among three mentioned types of PM fibers is the preform fabrication process. The fiber drawing process is practically identical for all fiber types.

Bowtie preforms are fabricated using inside vapor-phase oxidation with stress members created by the process of gas-phase etching. First of all, a ring of boron-doped silica is deposited within a high-purity, synthetic-silica substrate tube. When a sufficiently thick layer had been created, the rotation of the lathe is stopped to allow two diametrically opposed sections to be etched away. After the completion of the etching stage, rotation is recommenced and inner-cladding, followed by core layers, are deposited. Perform fabrication is completed with a controlled collapse process. When this preform is drawn, surface tension forces also ensure that geometry of the preform is faithfully reproduced in the fiber (Figure 9).

The fabrication method for elliptical jacket preforms combines processes from both bowtie and Panda manufacture: Boric oxide deposition by molecular chemical vapor deposition and ultrasonic machining. The initial fabrication steps are identical to those for a bowtie preform, except that the gas-phase etching is omitted, leaving an unbroken circular annulus of boron-doped material surrounding the core. After this circularly symmetric preform has been completed, its symmetry is broken by the ultrasonically machining of two flats, one on each side of the core. When drawn, the high surface tension forces within the molten glass force the preform to circularize, thereby creating the characteristic elliptical jacket shape, as shown in Figure 9.

Each of the three designs is capable of generating sufficient birefringence for even the most demanding of applications, so the precise choice of fiber is typically determined by other criteria, ranging from handling characteristics to history. In telecommunications applications, the fiber of choice is usually the Panda design, since, in essence, Panda is a telecommunications fiber, modified through the insertion of stress rods to provide PM properties. To this day, bowtie fibers are most typically encountered in sensor applications, and indeed, the majority of fiber optic gyroscopes worldwide use a fiber of this design.

3.2. Dynamic Brillouin grating (DBG)

Let us consider the generation of dynamic Brillouin grating in polarization maintaining fibers. Generation of the intense acoustic wave is possible using Stimulated Brillouin scattering phenomenon. As we saw in the previous chapter interference between two optical waves can stimulate an acoustic wave through electrostriction phenomenon if the phase matching condition for these waves is satisfied. Let us denote one optical wave

propagating in PM fiber along *x*-axis as pump 1, (v_x^{p1}), and counterpropagating wave as pump 2, v_x^{p2} , which is also polarized along slow axis, as depicted in the Figure 10. Under phase matching condition, $\Delta v = v_x^{p2} - v_x^{p1} = v_x^B$, energy transfer is established from pump 2 wave to counterpropagating pump 1 wave together with the generation of an acoustic wave. Brillouin shift v_x^B in this situation can be written as :

$$v_x^B = \frac{2n_x(v_x^{p2})V}{c} v_x^{p2} \tag{3.1}$$

where $n_x(v_x^{p2})$ is the refractive index at the pump 2 frequency, and *V* is the acoustic velocity in the fiber. If the interaction occurs in a birefringent medium, such as PMF, Brillouin shift, v^B , will be different for the two principle axis *x* and *y*, because of the different refractive indices, n_x and n_y . Thus, for the pump 2 wave polarized along the fast axis, *y*, Brillouin shift v_y^B will be written as :

$$v_y^B = \frac{2n_y(v_y^{p2})V}{c} v_y^{p2} \tag{3.2}$$

Here $n_x(v_x^{p2})$ is the refractive index at the pump 2 frequency polarized along the *y*-axis. Indeed, Figure 11 shows Brillouin gain spectra for two eigen polarizations of the 100-m PM fiber for pump 2 wave at 1551 nm.
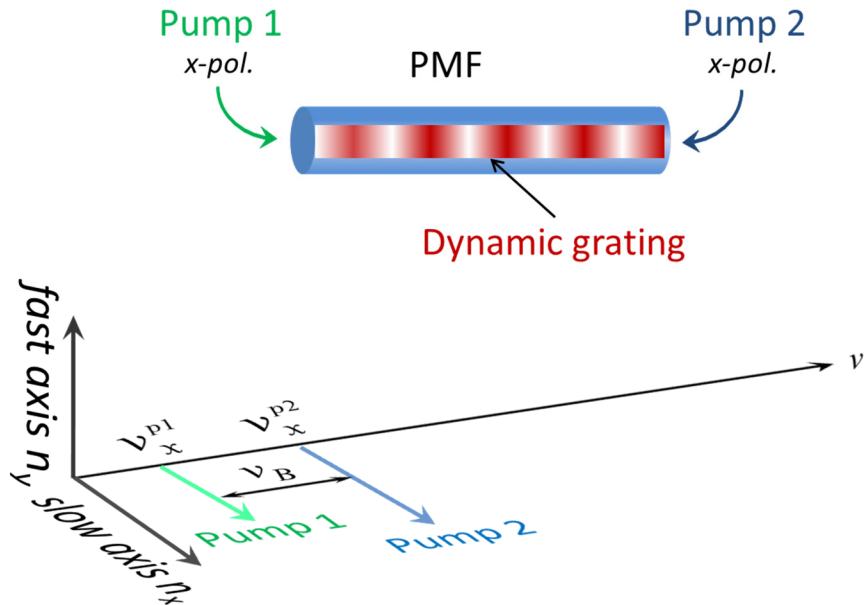
Figure 10. Generation of dynamic Brillouin grating using continuous waves pump1 and pump 2.
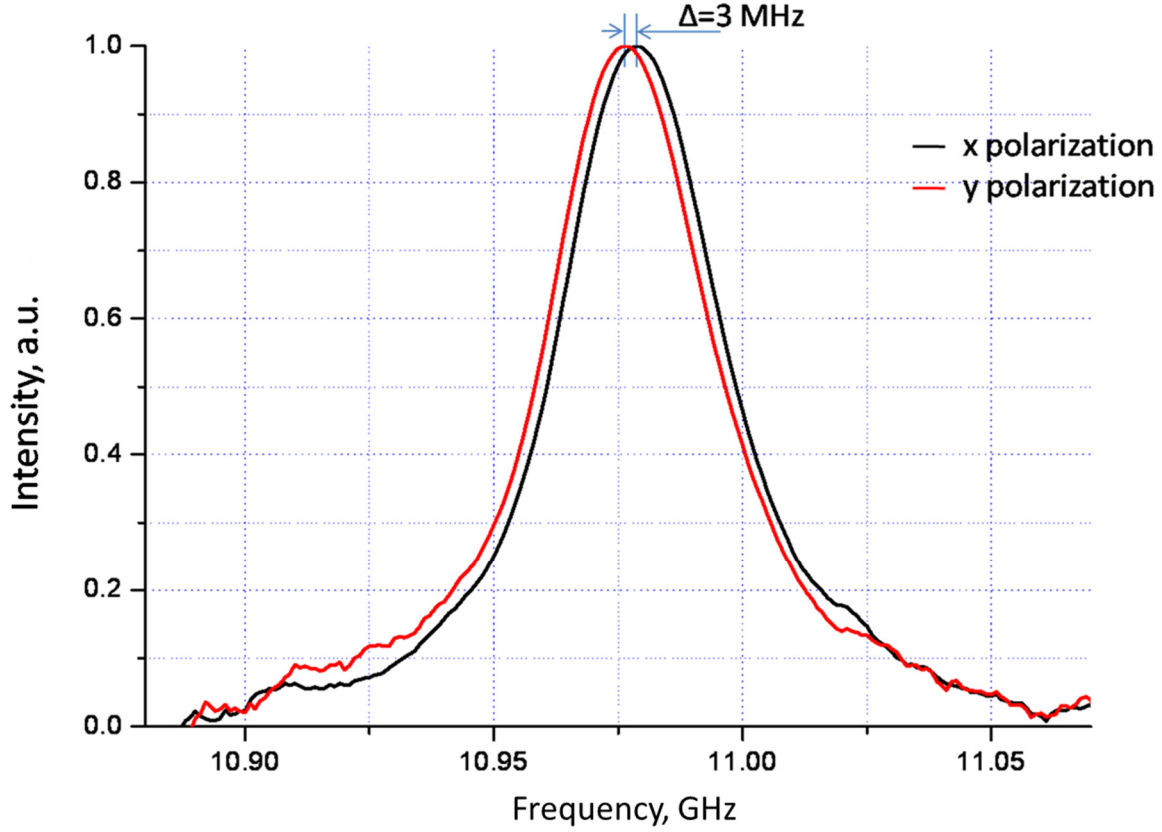
Figure 11. Brillouin gain spectra of the 100 m PM fiber along *x*-axis (black curve) and *y*-axis (red curve).

By measuring the difference in the peak of Brillouin gain spectra we can estimate the average birefringence of the polarization maintaining fiber. Figure 11 reveals a difference of 3 MHz, which corresponds to overall birefringence of the fiber $\Delta n \approx 3.9 \times 10^{-4}$.

On the other hand, there should be a situation where the same Brillouin shift is observed for *x* and *y* polarized optical waves with different frequencies. Actually the acoustic wave generated by the *x*-polarized optical waves is a longitudinal wave, which exhibits no transverse polarization. Thus, this acoustic wave can play the role of a dynamic grating to reflect an optical signal wave, v_y^s, polarized along the *y*-axis, providing that optical signal satisfy Bragg condition for the reflection. The condition when two optical waves polarized along *x* and *y* axis and with different optical frequencies share the same acoustic wave can be written as (Figure 12):

$$v_x^B = v_y^B = \frac{2 n_x (v_x^{p2}) V}{c} v_x^{p2} = \frac{2 n_y (v_x^{p2} + \Delta v) V}{c} \left(v_x^{p2} + \Delta v \right) = \frac{2 n_y (v_y^s) V v_y^s}{c}, \tag{3.3}$$

where we neglected the dispersion of the acoustic wave. We can rewrite this expression as :

$$n_x(v_x^{p2}) v_x^{p2} = n_y(v_y^s) v_y^s \tag{3.4}$$

Let us subtract from both parts following term $v_x^{p2} n_y \left(v_y^s \right)$:
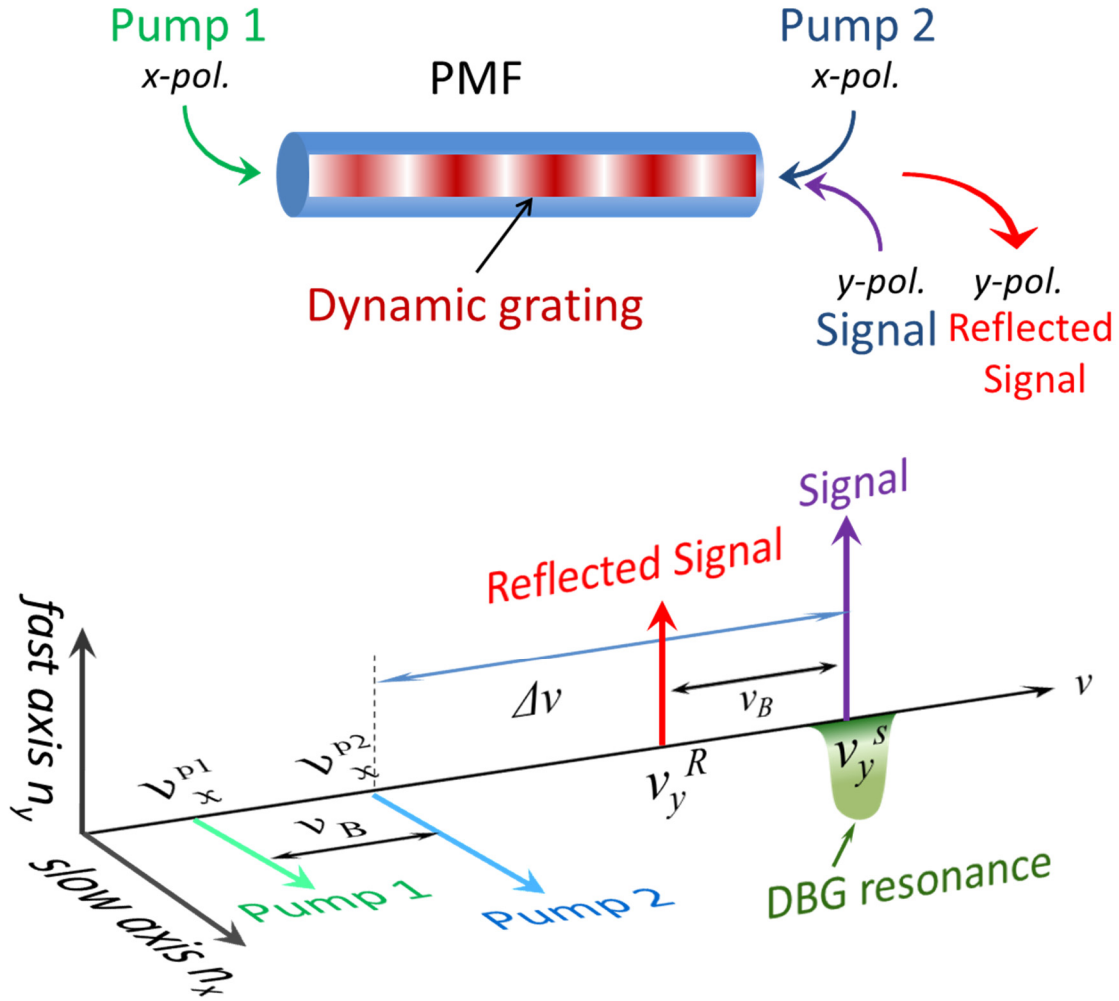
Figure 12. Polarizations, optical frequencies and directions of propagation of the optical waves used to generate and interrogate DBG.

$$n_y\left(v_y^s\right)v_y^s - v_x^{p2}n_y\left(v_y^s\right) = n_x(v_x^{p2})v_x^{p2} - v_x^{p2}n_y\left(v_y^s\right) \tag{3.5}$$

Rearranging we get :

$$n_y\left(v_y^s\right)(v_y^s - v_x^{p2}) = v_x^{p2}(n_x(v_x^{p2}) - n_y\left(v_y^s\right)) \tag{3.6}$$

This way we can write the difference in optical frequencies between pump 2 and signal, Δv , as:

$$\Delta v = (v_y^s - v_x^{p2}) = \frac{v_x^{p2}(n_x(v_x^{p2}) - n_y\left(v_y^s\right))}{n_y\left(v_y^s\right)} \tag{3.7}$$

Knowing that birefringence of the PM fiber at pump 2 frequency is $\Delta n(v_x^{p2}) = n_x(v_x^{p2}) - n_y(v_x^{p2})$, we can replace the $n_x\left(v_x^{p2}\right)$:

$$\Delta v = \frac{v_x^{p2}\left(\Delta n(v_x^{p2}) + n_y(v_x^{p2}) - n_y\left(v_y^s\right)\right)}{n_y\left(v_y^s\right)} \tag{3.8}$$

So:

$$\Delta v = \frac{v_x^{p2}\Delta n(v_x^{p2})}{n_y\left(v_y^s\right)} + v_x^{p2}\frac{n_y(v_x^{p2}) - n_y\left(v_y^s\right)}{n_y\left(v_y^s\right)} = \frac{v_x^{p2}\Delta n(v_x^{p2})}{n_y\left(v_y^s\right)} - \frac{v_x^{p2}}{n_y\left(v_y^s\right)}\frac{dn_y}{dv}\Delta v \tag{3.9}$$

Where we used $\Delta n_y = n_y(v_y^{p2}) - n_y(v_y^s) = -\dfrac{dn_y}{dv}\Delta v$

After rearranging we get the following expression:

$$\Delta v = \frac{v_x^{p2}\Delta n(v_x^{p2})}{n_y(v_y^s) + v_x^{p2}\dfrac{dn_y}{dv}} \approx \frac{\Delta n(v_x^{p2})}{n_y^g}v_x^{p2} \tag{3.10}$$

We can see that separation in frequency between the *x*-polarized pump 2 wave participating in the generation of the dynamic Brillouin grating and the *y*-polarized signal used to be reflected from grating is proportional to the birefringence of the polarization maintaining fiber. Thus, knowing the Δn we can estimate the optical frequency position of the signal, which can be used to interrogate the dynamic grating. Moreover, by measuring the local value of the frequency separation, Δv, we can extract the local value of birefringence of the PM fiber. We will come back to this issue in the sensing part of this thesis.

3.3. Analytical model for generation of localized dynamic Brillouin grating.

In this section we will present an analytical model for the generation of dynamic Brillouin grating inside the fiber using two pump pulses. We consider a segment of PM fiber from $z = 0$ to $z = z_0$ where interaction of two pump pulses with widths T results in the generation of dynamic Brillouin grating as depicted in Figure 13. In order to describe the interaction of pump pulses we use three coupled equations for slowly varying amplitudes derived in the previous chapter, namely equations (2.92), (2.98), and (2.99). We assume that the acoustic wave propagates a negligible distance over time when interaction between the optical pulses occurs. This way we can neglect the terms $\partial \rho / \partial z$ in the equation for an acoustic wave. Moreover we assume that pumps are undepleted, since in most of the experiments energy in the pump pulses is not high enough to substantiate depletion. In addition acoustic grating is considered as static. This means that when calculating the reflection of the signal pulse from acoustic grating we assume that DBG doesn't change its amplitude while signal pulse propagates through it. This assumption is valid when series of

pump pulses are used to regenerate the DBG, as well as when length of DBG is short, that signal pulse propagation time through the grating is much shorter than phonon lifetime. On the other hand when propagation time of the signal pulse through the DBG is longer or comparable with phonon lifetime, exponential decay of grating amplitude should be included to correctly obtain reflected waveform. We also assume that all pulses propagate with the same group velocity inside the fiber since their carrier frequency differs by only several tens of GHz (~80). We rewrite equations for pump 1, pump 2 and acoustic waves hereafter in the following form:

$$\frac{\partial A_{p1}}{\partial z} + \frac{1}{V_g}\frac{\partial A_{p1}}{\partial t} = i\frac{1}{2}g_2 A_{p2}\rho \tag{3.11}$$

$$\frac{\partial A_{p2}}{\partial z} - \frac{1}{V_g}\frac{\partial A_{p2}}{\partial t} = -i\frac{1}{2}g_2 A_{p1}\rho^* \tag{3.12}$$

$$\frac{\partial \rho}{\partial t} + \Gamma_A \rho = ig_1 A_{p1} A_{p2}^* , \tag{3.13}$$

where $g_2 = \frac{\omega\gamma_e}{nc_0\rho_0}$, $g_1 = \frac{\varepsilon_0\gamma_e q^2}{2\Omega}$, and $\Gamma_A = i\frac{\Omega_B^2 - \Omega^2 - i\Omega/\tau_p}{2\Omega}$ are electrostrictive coupling constant, elastooptic coupling constant and frequency detuning factor, respectively.

The amplitudes of pump pulses using step function can be represented as following:

$$A_1(t,z) = P_1^0 \alpha(u(z + TV_g - tV_g) - u(z - tV_g)) \tag{3.14}$$

$$A_2 = P_2^0 \beta\left(u\left(z - z_0 + tV_g\right) - u\left(z - z_0 - TV_g + tV_g\right)\right) \tag{3.15}$$

Figure 13 represents amplitudes of the pump waves in spatial domain (z-domain). The same pump waves can be described in time domain (t-domain). Pump pulses are represented in time domain as two following expressions:

$$A_1(t,z) = P_1^0 \alpha(u(t - z/V_g) - u(t - T - z/V_g)) \tag{3.16}$$

$$A_2(t,z) = P_2^0 \alpha(u(t - t_0 + z/V_g) - u(t - t_0 - T + z/V_g)) \tag{3.17}$$

where $t_0 = z_0/V_g$ is the time corresponding to the propagation time through fiber of length z_0. Equation describing the pump waves (3.16) and (3.17) can be plotted in time domain as shown in Figure 14.
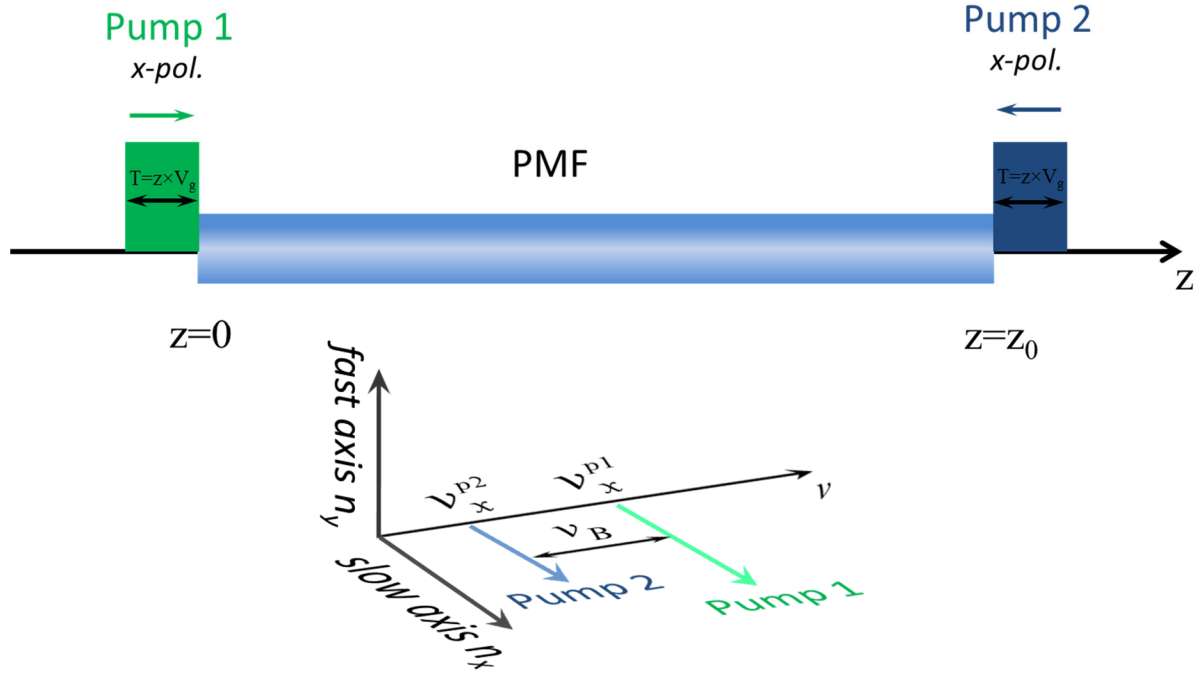
Figure 13. Amplitudes of the pump 1 and pump 2 pulses mapped in z domain at the time instant t=0.
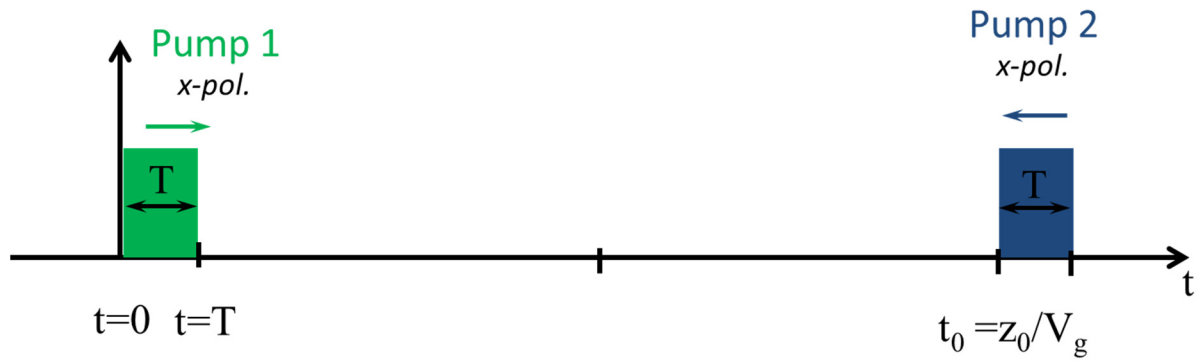
Figure 14. Time evolution of the amplitudes of the pump 1 and pump 2 pulses at position z=0.

First we find a solution of the acoustic wave amplitude. For this we take the Laplace transform of the equation (3.13):

$$s\widetilde{\rho} + \Gamma_A \widetilde{\rho} = ig_1 \widetilde{A_{p1} A_{p2}^*} \tag{3.18}$$

Solving for $\widetilde{\rho}$:

$$\widetilde{\rho} = \frac{ig_1 \widetilde{A_{p1} A_{p2}^*}}{(s + \Gamma_A)} \tag{3.19}$$

First step is to find the product of two pumps. Let us look at the four terms of the multiplication of equation (3.16) and (3.17):

$$A_{p1}A_{p2}^* = P_1^0 P_2^0 \alpha\beta^* \begin{cases} u(t-z/V_g) \times u(t-z_0/V_g+z/V_g) = \begin{cases} u(t-\dfrac{z_0-z}{V_g}) & z < \dfrac{z_0}{2} \\ \\ u(t-z/V_g) & z \geq \dfrac{z_0}{2} \end{cases} \\ \\ u(t-T-z/V_g) \times u(t-T-\dfrac{z_0-z}{V_g}) = \begin{cases} = u(t-T-\dfrac{z_0-z}{V_g}) & z \leq \dfrac{z_0}{2} \\ \\ = u(t-T-\dfrac{z}{V_g}) & z > \dfrac{z_0}{2} \end{cases} \\ \\ u(t-\dfrac{z}{V_g}) \times -u(t-T-\dfrac{z_0-z}{V_g}) = \begin{cases} -u(t-T-\dfrac{z_0-z}{V_g}) & z < \dfrac{z_0}{2}+\dfrac{TV_g}{2} \\ \\ -u(t-\dfrac{z}{V_g}) & z \geq \dfrac{z_0}{2}+\dfrac{TV_g}{2} \end{cases} \\ \\ -u(t-T-\dfrac{z}{V_g}) \times u(t-\dfrac{z_0-z}{V_g}) = \begin{cases} -u(t-T-\dfrac{z}{V_g}) & z > \dfrac{z_0}{2}-\dfrac{TV_g}{2} \\ \\ -u(t-\dfrac{z_0-z}{V_g}) & z \leq \dfrac{z_0}{2}-\dfrac{TV_g}{2} \end{cases} \end{cases} \quad (3.20)$$

Now we can see that there are four segments of the fiber where expression for multiplication of two pump pulses will result in different expressions:

$$A_{p1}A_{p2}^* = P_1^0 P_2^0 \alpha\beta^* \begin{cases} 0 & 0 < z < \dfrac{z_0-TV_g}{2} \\ \\ u(t-\dfrac{z_0-z}{V_g})-u(t-T-\dfrac{z}{V_g}) & \dfrac{z_0-TV_g}{2} < z < \dfrac{z_0}{2} \\ \\ u(t-\dfrac{z}{V_g})-u(t-T-\dfrac{z_0-z}{V_g}) & \dfrac{z_0}{2} < z < \dfrac{z_0+TV_g}{2} \\ \\ 0 & \dfrac{z_0+TV_g}{2} < z \end{cases} \quad (3.21)$$

Now we have expression for the multiplication of two pump pulses for four different segments of the fiber. To proceed further we take the Laplace transform of the expression (3.21):

$$
\widetilde{A_{p1}A_{p2}^*} = P_1^0 P_2^0 \alpha\beta^*
\begin{cases}
0 & 0 < z < \dfrac{z_0 - TV_g}{2} \\[3mm]
\dfrac{e^{-\left(\frac{z_0-z}{V_g}\right)s}}{s} - \dfrac{e^{-\left(T+\frac{z}{V_g}\right)s}}{s} & \dfrac{z_0 - TV_g}{2} < z < \dfrac{z_0}{2} \\[4mm]
\dfrac{e^{-\frac{z}{V_g}s}}{s} - \dfrac{e^{-\left(T+\frac{z_0-z}{V_g}\right)s}}{s} & \dfrac{z_0}{2} < z < \dfrac{z_0 + TV_g}{2} \\[4mm]
0 & \dfrac{z_0 + TV_g}{2} < z
\end{cases}
\tag{3.22}
$$

Now using the expression (3.19) we can write:

$$
\tilde{\rho}(z,s) = ig_1 P_1^0 P_2^0 \alpha\beta^*
\begin{cases}
0 & 0 < z < \dfrac{z_0 - TV_g}{2} \\[3mm]
\dfrac{e^{-\left(\frac{z_0-z}{V_g}\right)s}}{s(s+\Gamma_A)} - \dfrac{e^{-\left(T+\frac{z}{V_g}\right)s}}{s(s+\Gamma_A)} & \dfrac{z_0 - TV_g}{2} < z < \dfrac{z_0}{2} \\[4mm]
\dfrac{e^{-\frac{z}{V_g}s}}{s(s+\Gamma_A)} - \dfrac{e^{-\left(T+\frac{z_0-z}{V_g}\right)s}}{s(s+\Gamma_A)} & \dfrac{z_0}{2} < z < \dfrac{z_0 + TV_g}{2} \\[4mm]
0 & \dfrac{z_0 + TV_g}{2} < z
\end{cases}
\tag{3.23}
$$

Using cover-up method we can write each fraction in the expression (3.23) as a sum of fractions with simpler denominator:

$$
\tilde{\rho}(z,s) = ig_1 P_1^0 P_2^0 \alpha\beta^*
\begin{cases}
0 & 0 < z < \dfrac{z_0 - TV_g}{2} \\[3mm]
\dfrac{e^{-\left(\frac{z_0-z}{V_g}\right)s}}{s\Gamma_A} - \dfrac{e^{-\left(\frac{z_0-z}{V_g}\right)s}}{\Gamma_A(s+\Gamma_A)} - \dfrac{e^{-\left(T+\frac{z}{V_g}\right)s}}{\Gamma_A s} + \dfrac{e^{-\left(T+\frac{z}{V_g}\right)s}}{\Gamma_A(s+\Gamma_A)} & \dfrac{z_0 - TV_g}{2} < z < \dfrac{z_0}{2} \\[4mm]
\dfrac{e^{-\frac{z}{V_g}s}}{\Gamma_A s} - \dfrac{e^{-\frac{z}{V_g}s}}{\Gamma_A(s+\Gamma_A)} - \dfrac{e^{-\left(T+\frac{z_0-z}{V_g}\right)s}}{\Gamma_A s} + \dfrac{e^{-\left(T+\frac{z_0-z}{V_g}\right)s}}{\Gamma_A(s+\Gamma_A)} & \dfrac{z_0}{2} < z < \dfrac{z_0 + TV_g}{2} \\[4mm]
0 & \dfrac{z_0 + TV_g}{2} < z
\end{cases}
\tag{3.24}
$$

By taking the inverse Laplace transform of the equation (3.24) we can find the expression for the acoustic wave amplitude when two pump pulses have equal width of time T:

$$\rho(z,t) = \frac{ig_1 P_1^0 P_2^0 \alpha\beta^*}{\Gamma_A}
\begin{cases}
0 & 0 < z < \dfrac{z_0 - TV_g}{2} \\[2ex]
u\left(t - \dfrac{z_0 - z}{V_g}\right)\left(1 - e^{-\Gamma_A\left(t - \frac{z_0 - z}{V_g}\right)}\right) - u\left(t - T - \dfrac{z}{V_g}\right)\left(1 - e^{-\Gamma_A\left(t - T - \frac{z}{V_g}\right)}\right) & \dfrac{z_0 - TV_g}{2} < z < \dfrac{z_0}{2} \\[2ex]
u\left(t - \dfrac{z}{V_g}\right)\left(1 - e^{-\Gamma_A\left(t - \frac{z}{V_g}\right)}\right) - u\left(t - T - \dfrac{z_0 - z}{V_g}\right)\left(1 - e^{-\Gamma_A\left(t - T - \frac{z_0 - z}{V_g}\right)}\right) & \dfrac{z_0}{2} < z < \dfrac{z_0 + TV_g}{2} \\[2ex]
0 & \dfrac{z_0 + TV_g}{2} < z
\end{cases} \tag{3.25}$$

Expression (3.25) can be used to determine the shape of the acoustic wave generated by the two square pump pulses. For this purpose we consider two square-like pump pulses with width of 5 ns each counter propagating to each other in the segment of fiber of 2.7 m. At the time t=0 two pumps can represented in the z-domain as shown in Figure 15.
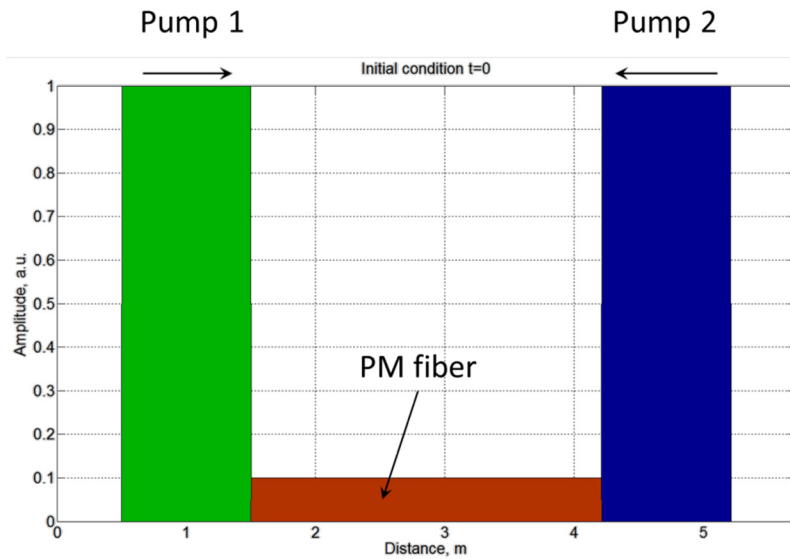
Figure 15. Configuration of the pump pulses at t=0. Fiber length is set to 2.7 m. Widths of both pump pulses are 5 ns.

Using the expression (3.25) we can track the evolution of the acoustic wave amplitude at any given point inside the fiber. Figure 16 represents the acoustic wave amplitude as a function of time and distance. Small pedestal under the acoustic wave represents the fiber where interaction occurs. In the simulation we used phonon lifetime of 4 ns.
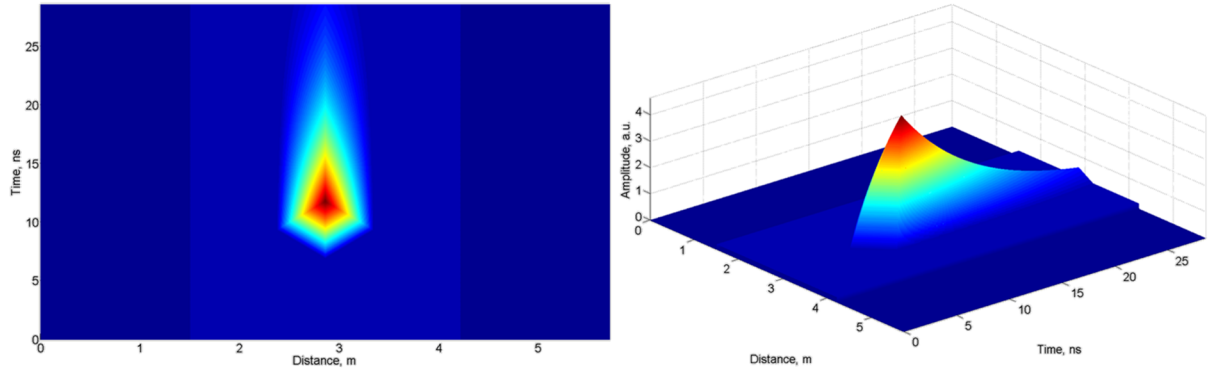
Figure 16. 3 D profile of the acoustic wave amplitude as a function of time and distance. Pump pulses used to generate acoustic grating have width of 5 ns.

At the position $z_0/2$ and time $t_0/2$ two pump pulses meet and acoustic wave starts to build up with characteristic exponential growth, where time constant is governed by the phonon lifetime. It is also visible that the longest interaction happens exactly in the middle of the fiber at the position $z_0/2$. Acoustic wave starts to decay in every position within a distance $\dfrac{z_0 - TV_g}{2} < z < \dfrac{z_0 + TV_g}{2}$ at the time when two pump pulses stop to overlap. In order to better understand the shape of the acoustic wave several shots are taken of the acoustic wave amplitude versus distance inside two characteristic periods of time: $\dfrac{t_0}{2} < t < \dfrac{t_0 + T}{2}$ and $\dfrac{t_0 + T}{2} < t < \dfrac{t_0}{2} + T$. The first period defines the time interval until two pump pulses completely overlap inside the fiber. The second interval is the interval when pump pulses leave each other. In our simulation fiber length was chosen arbitrary to be 2.71 m and the group velocity of the pump pulses is 0.2 m/ns, so the t_0 is 13.55 ns. Thus, at the time $t_0/2 = 6.77$ ns two pump pulses meet with each other in the middle of the fiber as shown in Figure 17. For the convenience pump pulses are plotted with different amplitude and the middle of the fiber is marked with the dashed line. In the first period of time, up to $\dfrac{t_0 + T}{2} = 9.27$ ns acoustic wave builds up everywhere in the fiber where two pump pulses overlap. At the time $t = \dfrac{t_0 + T}{2} = 9.27$ ns two pump pulses are exactly at the same position in the fiber, so they overlap completely. After this time pump pulses start to leave each other and the generation of the acoustic wave gradually halts starting from the two sides of the acoustic grating towards its middle. At the time $t = \dfrac{t_0}{2} + T = 11.77$ the two pump pulses completely leave each other and no overlapping is observed. At this time the grating shape is completely formed. With increasing time, the acoustic amplitude simply decays with decay rate of Γ_A. We can also see that full grating length is exactly equal to the length of the pump pulse (see Figure 17 (d)). In the case of 5 ns pump pulses full grating length will be 1 m, which corresponds to the length of the pump pulse in space. It is worth to mention that length of the grating at half of the amplitude maximum will be slightly less than full length of the grating. In our case it is

determined to be 0.486 m. This comes from the fact that the generated grating doesn't have strictly triangular shape, though it resembles such form after the interaction between the pump pulses is complete (see Figure 17 (f)).
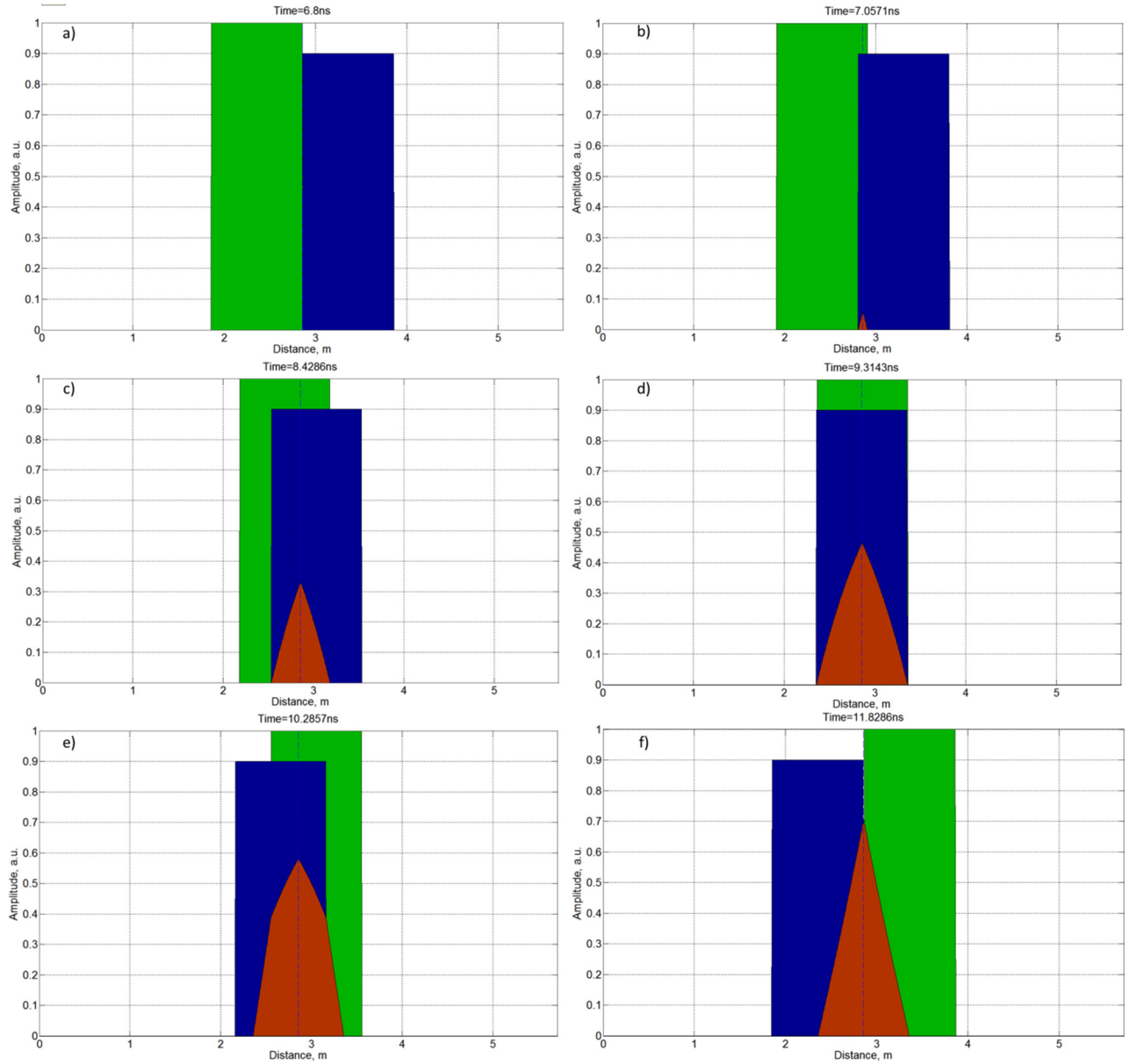
Figure 17. Amplitudes of pump 1 pulse (blue area), pump 2 pulse (green area), and acoustic wave (red area) for different times: a) two pump pulses meet at the position $z_0/2$; b) generation of acoustic wave starts from the middle of the fiber; c) acoustic grating grows in amplitude and in length; d) at the time $t_0/2+T/2$, when two pump pulses completely overlap acoustic wave reaches its full length; e) two pump pulses start to leave each other and sides of the acoustic grating starts to decay, while middle part is still continuing to build up; f) at the time $t_0/2+T$ two pump pulses completely leave each other and the shape of the acoustic grating is completely built. Further increase in time just reduces the amplitude of the grating with exponential decay, while the shape stays unchanged.

Next step is to determine the shape of the acoustic wave for the pump pulses with different widths. To find the solution for the acoustic wave we have to look at two different situations, namely width of pump 1 pulse is larger than width of pump 2 pulse, $T_1 > T_2$, or

width of the pump 2 pulse is larger than width of pump 1 pulse, $T_1 < T_2$. Let us consider first situation when $T_1 > T_2$. Following the same procedure as before we find the solution for the acoustic wave in the form:

$$\rho(z,t) = \frac{ig_1 P_1^0 P_2^0 \alpha \beta^*}{\Gamma_A} \begin{cases} 0 & 0 < z \leq \frac{z_0}{2} - \frac{T_1 V_g}{2} \\ u\left(t - \frac{z_0 - z}{V_g}\right)\left(1 - e^{-\Gamma_A\left(t - \frac{z_0 - z}{V_g}\right)}\right) - u\left(t - T_1 - \frac{z}{V_g}\right)\left(1 - e^{-\Gamma_A\left(t - T_1 - \frac{z}{V_g}\right)}\right) & \frac{z_0 - T_1 V_g}{2} < z \leq \frac{z_0}{2} + \frac{(T_2 - T_1)V_g}{2} \\ u\left(t - \frac{z_0 - z}{V_g}\right)\left(1 - e^{-\Gamma_A\left(t - \frac{z_0 - z}{V_g}\right)}\right) - u\left(t - T_2 - \frac{z_0 - z}{V_g}\right)\left(1 - e^{-\Gamma_A\left(t - T_2 - \frac{z_0 - z}{V_g}\right)}\right) & \frac{z_0}{2} + \frac{(T_2 - T_1)V_g}{2} < z \leq \frac{z_0}{2} \\ u\left(t - \frac{z}{V_g}\right)\left(1 - e^{-\Gamma_A\left(t - \frac{z}{V_g}\right)}\right) - u\left(t - T_2 - \frac{z_0 - z}{V_g}\right)\left(1 - e^{-\Gamma_A\left(t - T_2 - \frac{z_0 - z}{V_g}\right)}\right) & \frac{z_0}{2} < z \leq \frac{z_0 + T_2 V_g}{2} \\ 0 & \frac{z_0 + T V_g}{2} < z \end{cases} \quad (3.26)$$

Detailed calculation of the expression for the acoustic wave can be found in the appendix. Figure 18 (b, and c) show 3D map of acoustic amplitude in z- and t-domains. In this simulation pump 1 pulse width was increased up to 6 ns, and pump 2 pulse width was set to 3 ns (Figure 18 (a)). Length of the fiber was arbitrary set to 1.6 m. Time constant for the acoustic wave amplitude was set to 8 ns, while time constant for the acoustic wave intensity is twice smaller, 4 ns.
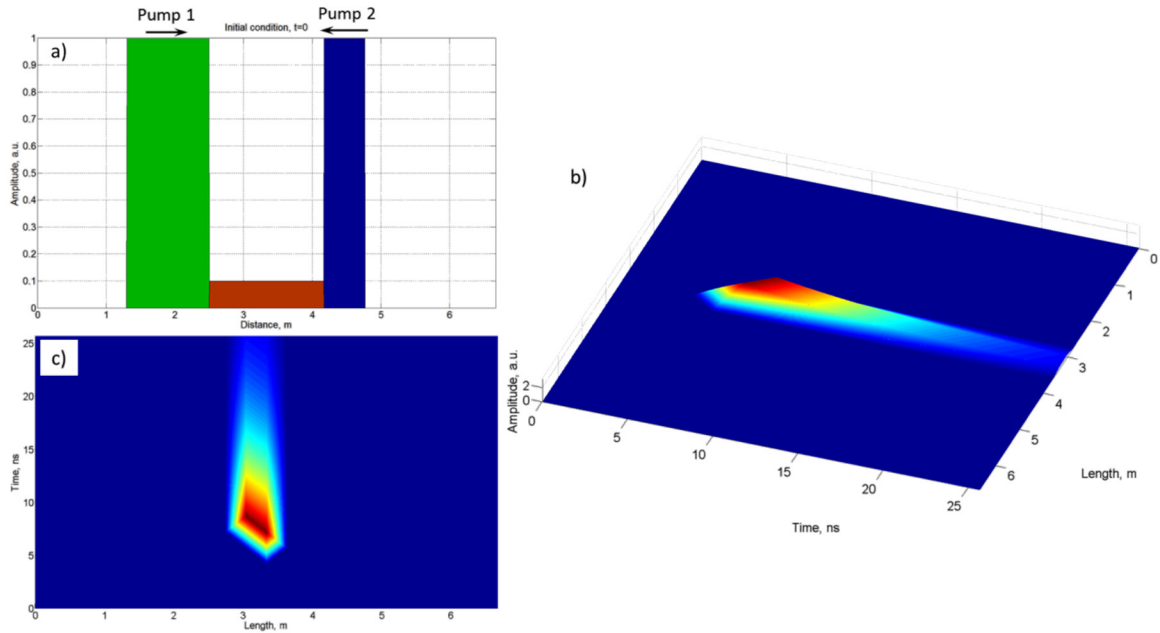
Figure 18. a) Initial condition: pump 1 pulse (green area) width is 6 ns, pump 2 pulse (blue area) width is 3 ns, b) 3 d plot of the acoustic wave amplitude in z- and t-domain. c) top view of the acoustic wave amplitude in z- and t-domain.

In order to better understand the shape evolution of the acoustic wave we plot it in z-domain at different times (Figure 19). The first time period is when the two pump pulses meet in the middle of the fiber and acoustic grating starts to build up. For the initial condition shown in

Figure 19 (a) this particular time corresponds to $t_0/2=4.17$ ns. Up to the time $t_0/2+T_2/2$ the acoustic grating is generated symmetrically around the position $z_0/2$ (Figure 19 (c)). After the time $t_0/2+T_2/2$, the grating is generated only at the positions where the two pump pulses overlaps and starts to decay at the position $z_0/2+T_2V_g/2$ towards the position $z_0/2$ with further increasing of the time.
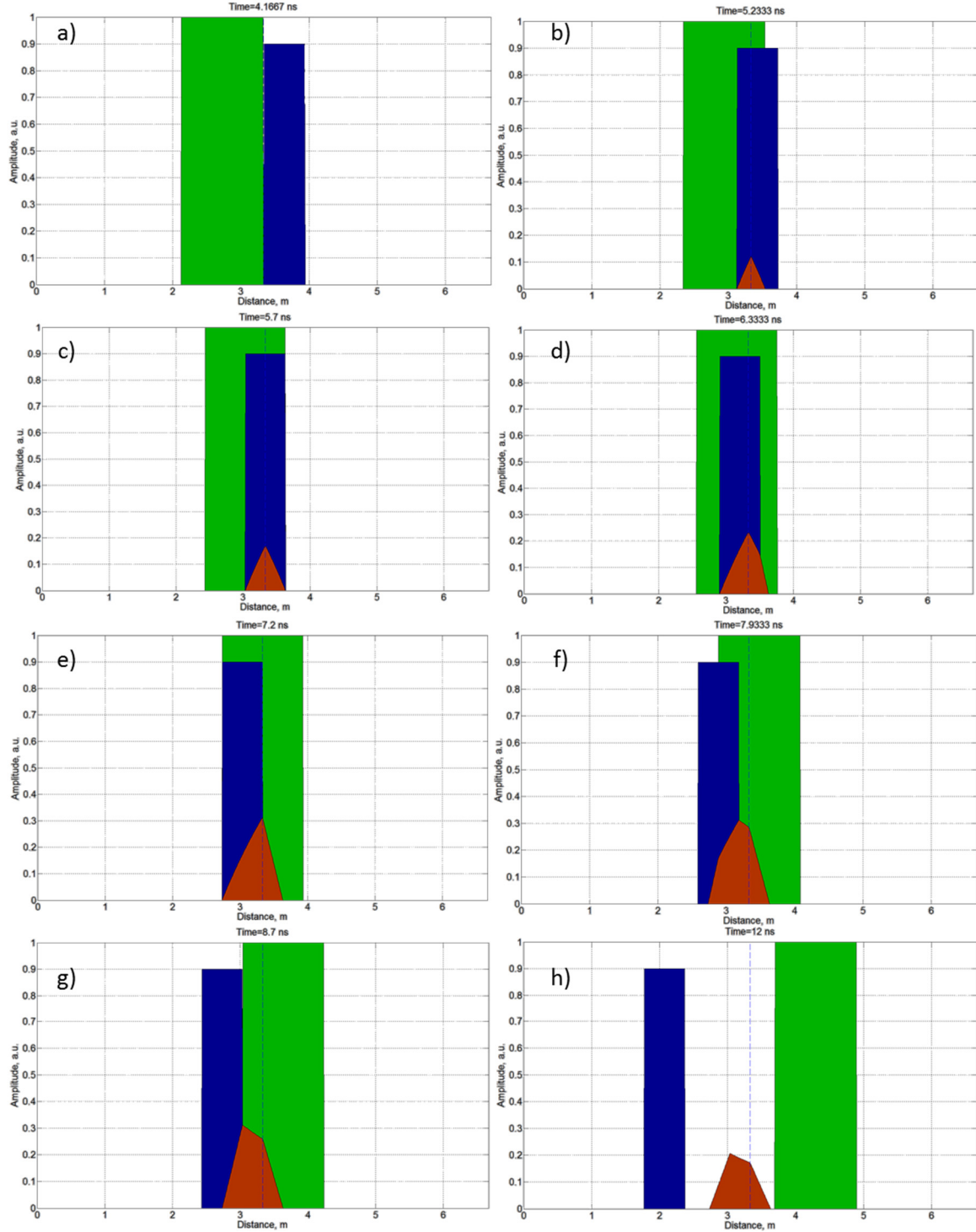
Figure 19. Amplitudes of the pump 1 pulse (green area), pump 2 pulse (blue area) and acoustic wave (red area) at different times.

After grating is growing at the positions where pump pulses overlap and since pump 1 pulse width is longer grating extends in space domain towards the end of the fiber where pump 1 pulse was launched (see Figure 19 (d, e)). At the time $t = t_0/2 + T_1/2$ leading edge of the pump 2 pulse reaches the end of the pump 1 pulse as shown in the Figure 19 (e). After this time pump pulses start to leave each other and the positions where pulses do not overlap acoustic grating starts to decay. Finally at the time $t_0/2+(T_1+T_2)/2$ pulses completely leave each other, and at this time the shape of the acoustic grating is completely formed (Figure 19 (g)). After with increasing time, the amplitude of the acoustic wave decays with the time constant of 8 ns, but the shape is preserved. In the case when pump 2 pulse width is longer than that of the pump 1 acoustic amplitude will have the following form:

$$\rho(z,t) = \frac{ig_1 P_1^0 P_2^0 \alpha \beta^*}{\Gamma_A} \begin{cases} 0 & 0 < z \le \frac{z_0}{2} - \frac{T_1 V_g}{2} \\[2ex] u(t - \frac{z_0 - z}{V_g})\left(1 - e^{-\Gamma_A(t - \frac{z_0 - z}{V_g})}\right) - u(t - T_1 - z/V_g)\left(1 - e^{-\Gamma_A(T_1 + z/V_g)}\right) & \frac{z_0}{2} - \frac{T_1 V_g}{2} < z \le \frac{z_0}{2} \\[2ex] u(t - \frac{z}{V_g})\left(1 - e^{-\Gamma_A(t - \frac{z}{V_g})}\right) - u(t - T_1 - \frac{z}{V_g})\left(1 - e^{-\Gamma_A\left(T_1 + \frac{z}{V_g}\right)}\right) & \frac{z_0}{2} < z \le \frac{z_0}{2} + \frac{(T_2 - T_1)V_g}{2} \\[2ex] u(t - \frac{z}{V_g})\left(1 - e^{-\Gamma_A(t - \frac{z}{V_g})}\right) - u(t - T_2 - \frac{z_0 - z}{V_g})\left(1 - e^{-\Gamma_A\left(T_2 + \frac{z_0 - z}{V_g}\right)}\right) & \frac{z_0}{2} + \frac{(T_2 - T_1)V_g}{2} < z \le \frac{z_0}{2} + \frac{T_2 V_g}{2} \\[2ex] 0 & \frac{z_0}{2} + \frac{T_2 V_g}{2} < z \end{cases} \qquad (3.27)$$

Basically, the behavior of the acoustic grating with time is similar. The only difference is that the grating extends from the middle, $z_0/2$, towards the end of the fiber where pump 2 pulse is launched, as depicted in Figure 20. The initial conditions are the same as in previous simulation only widths of the pumps are interchanged: T_1=3 ns, T_2=6 ns. Detailed calculations are presented in Appendix A. Solution for the acoustic wave is similar to the previous situation, only sections of the fiber are changed according to the length of the pulses. The acoustic grating amplitude is symmetric compared with the previous configuration, as like plane of symmetry is placed in the middle of the fiber.
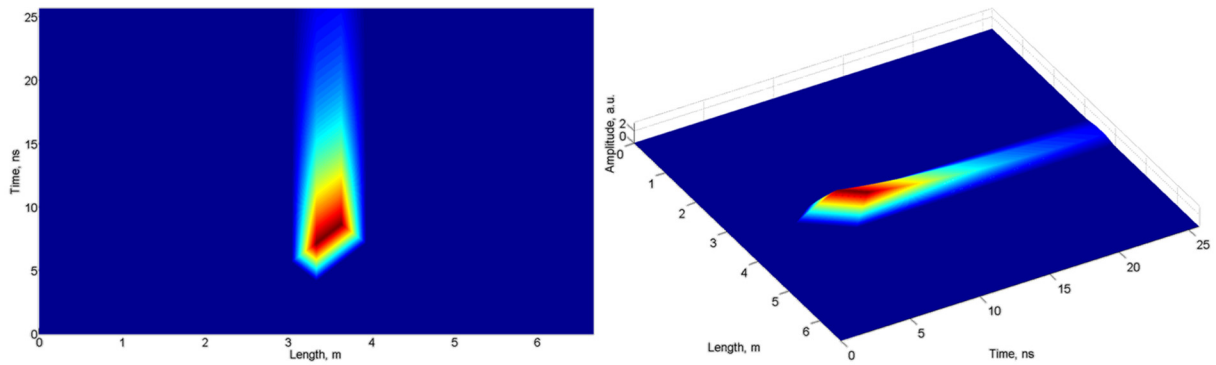
Figure 20. 3 D plot of the acoustic wave amplitude in z- and t-domain in the case when pump 2 pulse width is bigger than pump 1 pulse width.

Amplitudes of the optical waves were described using square pulses, because this way it is easier to operate with Laplace transform. Nevertheless, any kind of pulse shapes can be considered.

Once we know the form of the grating and know how it changes with time, it is interesting to calculate the reflection of the signal wave through the dynamic Brillouin grating. We consider the following situation. Pump pulses are represented by the step functions with equal width and with their carrier frequency detuning equal to that of the Brillouin shift of the fiber as depicted in Figure 21. Both pump waves are polarized along the slow axis of the polarization maintaining fiber. At first we are aiming to find an optical wave which will be reflected from the dynamic Brillouin grating if we use a reading signal at the optical frequency of v_y^s, which precisely coincidences with the maximum reflection frequency of the DBG. Moreover, we assume that the generation and interrogation of the dynamic grating are two distinct processes. So we split the problem into two parts: generation of the dynamic Brillouin grating using pump pulses and following interrogation of the generated DBG with signal wave. The first part was addressed previously and we know the shape of the grating along the fiber length at any time. Now we concentrate on the second task – reflection of the signal wave by the dynamic Brillouin grating. Actually, reflection of the signal from dynamic grating can be described with the help of the theory of fiber Bragg gratings (FBG), since for the signal wave the DBG is simply a FBG, which is moving inside the fiber with the speed of sound. Such feature of the DBG results in a spectrally shifted reflected wave, where the shift is proportional to the velocity of sound in the fiber.
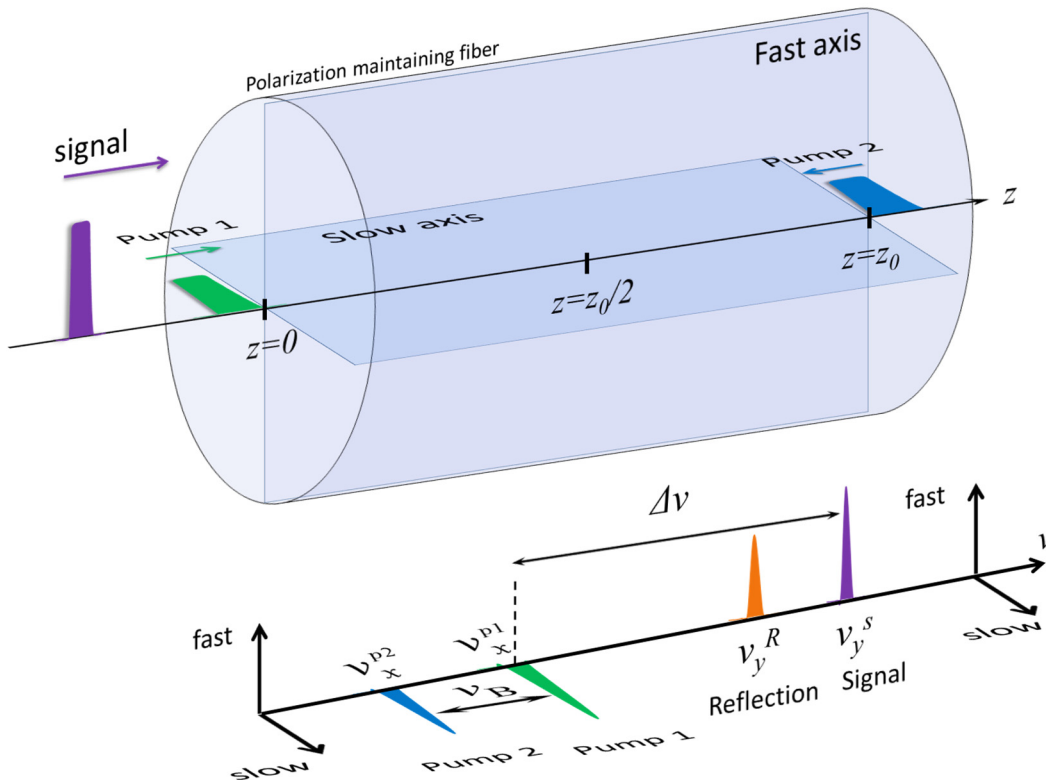
Figure 21. Polarization and optical frequency configuration of the interacting waves.

By using the coupled-mode theory we can write the two equations for forward propagating signal amplitude, S (z), and backward propagating reflected amplitude, R(z) [2, 12, 13]:

$$\frac{\partial S}{\partial z} + \frac{n}{c_0}\frac{\partial S}{\partial t} = -i\kappa_{ac}^{*}R - i\left[\kappa_{dc} + \frac{1}{2}\left(\Delta\beta - \frac{\partial\phi(z)}{\partial z}\right)\right]S \qquad (3.28)$$

$$\frac{\partial R}{\partial z} - \frac{n}{c_0}\frac{\partial R}{\partial t} = i\kappa_{ac}S + i\left[\kappa_{dc} + \frac{1}{2}\left(\Delta\beta - \frac{\partial\phi(z)}{\partial z}\right)\right]R \qquad (3.29)$$

where $\kappa_{ac} = \kappa$, κ_{dc}, $\Delta\beta$, $\partial\phi/\partial z$ are the "ac" coupling coefficient, "dc" coupling coefficient, detuning from the Bragg wavelength, and chirp of the grating. In the case of acoustic grating we can assume $\kappa_{dc} = 0$. Moreover, neglecting the chirp ($\partial\phi/\partial z = 0$) and assuming the signal frequency is tuned exactly to the maximum reflection wavelength of the grating ($\Delta\beta = 0$) we can write expressions (3.28) and (3.29) as:

$$\frac{\partial S}{\partial z} + \frac{n}{c_0}\frac{\partial S}{\partial t} = -i\kappa R \qquad (3.30)$$

$$\frac{\partial R}{\partial z} - \frac{n}{c_0}\frac{\partial R}{\partial t} = i\kappa S \qquad (3.31)$$

Moreover, we assume that dynamic Brillouin grating is a very weak grating, so the signal amplitude can be considered constant along the grating. Thus we can neglect equation (3.30). In the end we can write the equation for the reflected wave as:

$$\frac{\partial R}{\partial z} - \frac{n}{c_0}\frac{\partial R}{\partial t} = iS\kappa \qquad (3.32)$$

In the case of dynamic Brillouin grating "ac" coupling is related to the acoustic wave amplitude. We can represent the generated DBG as an apodized FBG with zero "dc" index change, without grating chirp. So the induced index change can be represented as:

$$\delta n_{eff}(z) = \overline{\delta n_{eff}}(z)\cos\left[\frac{2\pi}{\Lambda_0}z\right] \qquad (3.33)$$

In our case apodization function is given by $\rho(z)$. In the case of equal pump pulses induced index change along the fiber axis can be approximated by the acoustic wave as in Figure 17 (f). Thus we can write the apodization profile as:

$$\overline{\delta n_{eff}}(z) = \delta n_{eff}\rho(z), \qquad (3.34)$$

where δn_{eff} is the peak value of the index change.

For simplicity we assume that the "ac" coupling coefficient can be represented as in the case for an uniform grating:

$$\kappa_{ac} = \kappa_{ac}^{*} = \frac{\pi}{\lambda}\overline{\delta n_{eff}} \tag{3.35}$$

Thus we can write the (3.32) as:

$$\frac{\partial R}{\partial z} - \frac{n}{c_0}\frac{\partial R}{\partial t} = iS\frac{\pi}{\lambda}\delta n_{eff}\rho(z) \tag{3.36}$$

We can rewrite the equation (3.36) as:

$$\frac{\partial R}{\partial z} - \frac{n}{c_0}\frac{\partial R}{\partial t} = M\rho(z)S \tag{3.37}$$

where $M = i\frac{\pi}{\lambda}\delta n_{eff}$.

In order to obtain the solution for the reflected wave we need to assume that the acoustic grating is stationary while the reflected wave is propagating through the grating. This assumption is necessary since otherwise our system is a time variant system and it is very difficult to obtain response of such a system. The assumption that the grating doesn't change during propagation of the signal pulse is reasonable since the signal pulse is short, and the propagation time is smaller than decay time constant of the acoustic amplitude. For instance in typical experimental condition we use 1 ns pump pulses. Their interaction results in the generation of 20 cm DBG. If 600 ps signal pulse is used to interrogate the grating, time when signal pulse completely exits the grating will be 1.6 ns. This is much shorter than ~4-6 ns typical phonon lifetime for the silica fibers. If we assume that while the signal wave is propagating through the fiber our dynamic grating does not change, we can model this situation as a response of a time invariant system. Response of a time invariant system can be calculated using Laplace transform. For example, in the case when a DBG is generated by the pump pulses with equal widths, we can fix the shape of the DBG after the time $z_0/2+T$. This is the time when the dynamic grating is completely formed by the pump pulses.

At the time $z_0/2+T$, the acoustic wave amplitude will be given by the following expression (see expression (3.25)):

$$\rho(z,t) = \frac{ig_1 P_1^0 P_2^0 \alpha\beta^*}{\Gamma_A}\begin{cases} 0 & 0 < z < \frac{z_0 - TV_g}{2} \\ u\left(\frac{z_0}{2V_g} + T - \frac{z_0 - z}{V_g}\right)e^{-\Gamma_A\left(\frac{z_0}{2V_g} + T - \frac{z_0 - z}{V_g}\right)} - u\left(\frac{z_0}{2V_g} + T - T - \frac{z}{V_g}\right)e^{-\Gamma_A\left(\frac{z_0}{2V_g} + T - T - \frac{z}{V_g}\right)} & \frac{z_0 - TV_g}{2} < z < \frac{z_0}{2} \\ u\left(\frac{z_0}{2V_g} + T - \frac{z}{V_g}\right)e^{-\Gamma_A\left(\frac{z_0}{2V_g} + T - \frac{z}{V_g}\right)} - u\left(\frac{z_0}{2V_g} + T - T - \frac{z_0 - z}{V_g}\right)e^{-\Gamma_A\left(\frac{z_0}{2V_g} + T - T - \frac{z_0 - z}{V_g}\right)} & \frac{z_0}{2} < z < \frac{z_0 + TV_g}{2} \\ 0 & \frac{z_0 + TV_g}{2} < z \end{cases} \tag{3.38}$$

Signal pulse can be represented in time domain with the expression (Figure 22):

$$S(z,t) = u\left(t - \tau - \frac{z}{V_g}\right) - u\left(t - \tau - T_s - \frac{z}{V_g}\right)$$

(3.39)

where τ is the delay between the pump 1 pulse and signal pulse.
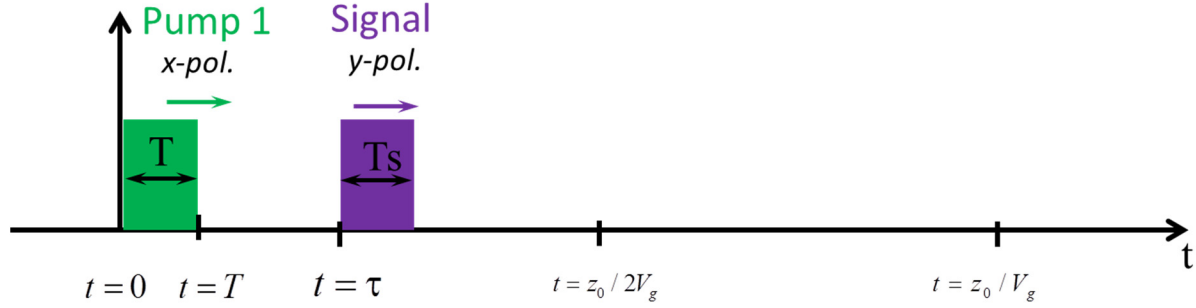
Figure 22. Time domain representation of the reading signal (violet area) pulse together with pump 1 pulse (green area).

Next we take the Laplace transform of equation (3.37):

$$\frac{\partial \tilde{R}(s,z)}{\partial z} - \frac{s}{V_g}\tilde{R}(s,z) = M\rho(z)\tilde{S}(s,z)$$

(3.40)

Laplace transform of signal pulse is easily found as:

$$\tilde{S}(s,z) = \frac{e^{-(\tau + \frac{z}{V_g})s}}{s} - \frac{e^{-\left(\tau + T_s + \frac{z}{V_g}\right)s}}{s} = \frac{e^{-\tau s}e^{-\frac{z}{V_g}s}}{s}\left(1 - e^{-T_s s}\right)$$

(3.41)

By multiplying both sides of equation (3.41) with $e^{-\frac{s}{V_g}z}$ we obtain:

$$e^{-\frac{s}{V_g}z}\frac{\partial \tilde{R}(s,z)}{\partial z} - \frac{s}{V_g}e^{-\frac{s}{V_g}z}\tilde{R}(s,z) = M\rho(z)\tilde{S}(s,z)e^{-\frac{s}{V_g}z}$$

(3.42)

We can rewrite the right hand side of equation (3.42) as:

$$\frac{d\left(e^{-\frac{s}{V_g}z}\tilde{R}(s,z)\right)}{dz} = M\rho(z)\tilde{S}(s,z)e^{-\frac{s}{V_g}z}$$

(3.43)

Or

$$d\left(e^{-\frac{s}{V_g}z}\tilde{R}(s,z)\right) = M\rho(z)\tilde{S}(s,z)e^{-\frac{s}{V_g}z}dz$$

(3.44)

Next we take the integral from z=0 to z=z₀:

$$\int_0^{z_0} d\left(e^{-\frac{s}{V_g}z}\tilde{R}(s,z)\right) = \int_0^{z_0} M\rho(z)\tilde{S}(s,z)e^{-\frac{s}{V_g}z}dz \tag{3.45}$$

Knowing that $\rho(z) \neq 0$ only in the interval from $\frac{z_0}{2} - \frac{TV_g}{2}$ to $\frac{z_0}{2} + \frac{TV_g}{2}$, when two pump pulses have equal width *T*, we rewrite equation (3.45):

$$e^{-\frac{s}{V_g}z_0}\tilde{R}(s,z=z_0) - \tilde{R}(s,z=0) = M\int_{\frac{z_0}{2}-\frac{TV_g}{2}}^{\frac{z_0}{2}+\frac{TV_g}{2}} \rho(z)\tilde{S}(s,z)e^{-\frac{s}{V_g}z}dz \tag{3.46}$$

At z=z₀, the amplitude of the reflected wave is 0, thus:

$$\tilde{R}(s,z=0) = -M\int_{\frac{z_0}{2}-\frac{TV_g}{2}}^{\frac{z_0}{2}+\frac{TV_g}{2}} \rho(z)\tilde{S}(s,z)e^{-\frac{s}{V_g}z}dz \tag{3.47}$$

Using the expression for the acoustic wave (3.38) we write:

$$\tilde{R}(s,z=0) = -M\frac{ig_1 P_1^0 P_2^0 \alpha\beta^*}{\Gamma_A}\left[\tilde{R}'(s,z=0) + \tilde{R}''(s,z=0)\right] \tag{3.48}$$

where

$$\tilde{R}'(s,z=0) = \int_{\frac{z_0}{2}-\frac{TV_g}{2}}^{\frac{z_0}{2}} e^{-\frac{s}{V_g}z}\left(-u\left(T-\frac{z_0}{2V_g}+\frac{z}{V_g}\right)e^{-\Gamma_A\left(T-\frac{z_0}{V_g}+\frac{z}{V_g}\right)} + u\left(\frac{z_0}{2V_g}-\frac{z}{V_g}\right)e^{-\Gamma_A\left(\frac{z_0}{2V_g}-\frac{z}{V_g}\right)}\right)\frac{e^{-\tau s}e^{-\frac{z}{V_g}s}}{s}\left(1-e^{-T_s s}\right)dz \tag{3.49}$$

and

$$\tilde{R}''(s,z=0) = \int_{\frac{z_0}{2}}^{\frac{z_0}{2}+\frac{TV_g}{2}} e^{-\frac{s}{V_g}z}\left(-u\left(T+\frac{z_0}{2V_g}-\frac{z}{V_g}\right)e^{-\Gamma_A\left(T+\frac{z_0}{2V_g}-\frac{z}{V_g}\right)} + u\left(-\frac{z_0}{2V_g}+\frac{z}{V_g}\right)e^{-\Gamma_A\left(-\frac{z_0}{2V_g}+\frac{z}{V_g}\right)}\right)\frac{e^{-\tau s}e^{-\frac{z}{V_g}s}}{s}\left(1-e^{-T_s s}\right)dz \tag{3.50}$$

By solving the integrals (3.49) and (3.50) we can get the expression of the reflected wave at position z=0. Detailed calculations to solve integrals (3.49) and (3.50) are presented in Appendix B. Using the inverse Laplace transform the reflected wave can be represented as:

$$R(z=0,t) = K\left(R'(t,z=0) + R''(t,z=0)\right) \tag{3.51}$$

Where $K = -M \dfrac{i g_1 P_1^0 P_2^0 \alpha \beta^*}{\Gamma_A}$

$$R'(t,z=0) = \frac{V_g}{\Gamma_A}\left(u\left(t-\frac{z_0}{V_g}+T-\tau\right)\cdot\left\{ e^{\frac{\Gamma_A}{2}\left(t-\frac{z_0}{V_g}-\tau\right)} - 2e^{\left(-\frac{\Gamma_A T}{2}\right)} + e^{-\frac{\Gamma_A}{2}\left(t-\frac{z_0}{V_g}+2T-\tau\right)}\right\} + u\left(t-\frac{z_0}{V_g}-\tau\right)\left\{ 1-e^{\frac{\Gamma_A}{2}\left(t-\frac{z_0}{V_g}-\tau\right)} + e^{-\Gamma_A T} - e^{-\frac{\Gamma_A}{2}\left(t-\frac{z_0}{V_g}+2T-\tau\right)}\right\}\right) -$$ (3.52)

$$\frac{V_g}{\Gamma_A}\left(u\left(t-\frac{z_0}{V_g}+T-\tau-T_s\right)\cdot\left\{ e^{\frac{\Gamma_A}{2}\left(t-\frac{z_0}{V_g}-\tau-T_s\right)} - 2e^{\left(-\frac{\Gamma_A T}{2}\right)} + e^{-\frac{\Gamma_A}{2}\left(t-\frac{z_0}{V_g}+2T-\tau-T_s\right)}\right\} + u\left(t-\frac{z_0}{V_g}-\tau-T_s\right)\left\{ 1-e^{\frac{\Gamma_A}{2}\left(t-\frac{z_0}{V_g}-\tau-T_s\right)} + e^{-\Gamma_A T} - e^{-\frac{\Gamma_A}{2}\left(t-\frac{z_0}{V_g}+2T-\tau-T_s\right)}\right\}\right)$$

and

$$R''(t,z=0) = \frac{V_g}{\Gamma_A}\left(u\left(t-\frac{z_0}{V_g}-\tau\right)\cdot\left\{ 1-e^{-\frac{\Gamma_A}{2}\left(t-\frac{z_0}{V_g}-\tau\right)} - e^{\frac{\Gamma_A}{2}\left(t-\frac{z_0}{V_g}-2T-\tau\right)} + e^{(-\Gamma_A T)}\right\} + u\left(t-\frac{z_0}{V_g}-T-\tau\right)\left\{ e^{-\frac{\Gamma_A}{2}\left(t-\frac{z_0}{V_g}-\tau\right)} - 2e^{\frac{\Gamma_A T}{2}} + e^{\frac{\Gamma_A}{2}\left(t-\frac{z_0}{V_g}-2T-\tau\right)}\right\}\right) -$$ (3.53)

$$\frac{V_g}{\Gamma_A}\left(u\left(t-\frac{z_0}{V_g}-\tau-T_s\right)\cdot\left\{ 1-e^{\frac{\Gamma_A}{2}\left(t-\frac{z_0}{V_g}-\tau-T_s\right)} - e^{\frac{\Gamma_A}{2}\left(t-\frac{z_0}{V_g}-2T-\tau-T_s\right)} + e^{(-\Gamma_A T)}\right\} + u\left(t-\frac{z_0}{V_g}-T-\tau-T_s\right)\left\{ e^{-\frac{\Gamma_A}{2}\left(t-\frac{z_0}{V_g}-\tau-T_s\right)} - 2e^{\frac{\Gamma_A T}{2}} + e^{\frac{\Gamma_A}{2}\left(t-\frac{z_0}{V_g}-2T-\tau-T_s\right)}\right\}\right)$$

In order to look at the reflection, we consider the following initial conditions: pump pulses have width of 5 ns and reading signal pulse has width of 1 ns. Fiber length is fixed to 2.7 m. Initial condition is represented in Figure 23. Delay between the beginning of the signal pulse and end of the pump 1 pulse was set to 5 ns. We fix the grating amplitude at the time $t = t_0/2 + T$ as shown in the Figure 24 (a). At this time two pump pulses completely pass each other and grating is fully generated. After this time we assume that the grating has fixed amplitude and increasing the time only results in the propagation of the signal pulse. The resulted reflection of the 1 ns signal pulse from the DBG of 1 m is depicted in the Figure 24 (b). We can see that the reflected wave start to appear at the position z=0 at the time $t = \tau + 2\left(\dfrac{t_0}{2} - \dfrac{T}{2}\right) = \tau + t_0 - T$. In our case this is the time 18.5 ns. It is clear that the length of the dynamic grating is equal to the length of the pump pulse width, namely 5 ns, which is approximately 1 m. On the other hand, the full width at half maximum of the grating amplitude is slightly less than 0.5 m, since the dynamic grating doesn't have a strictly triangular shape. In our case it is determined to be 0.488 m.
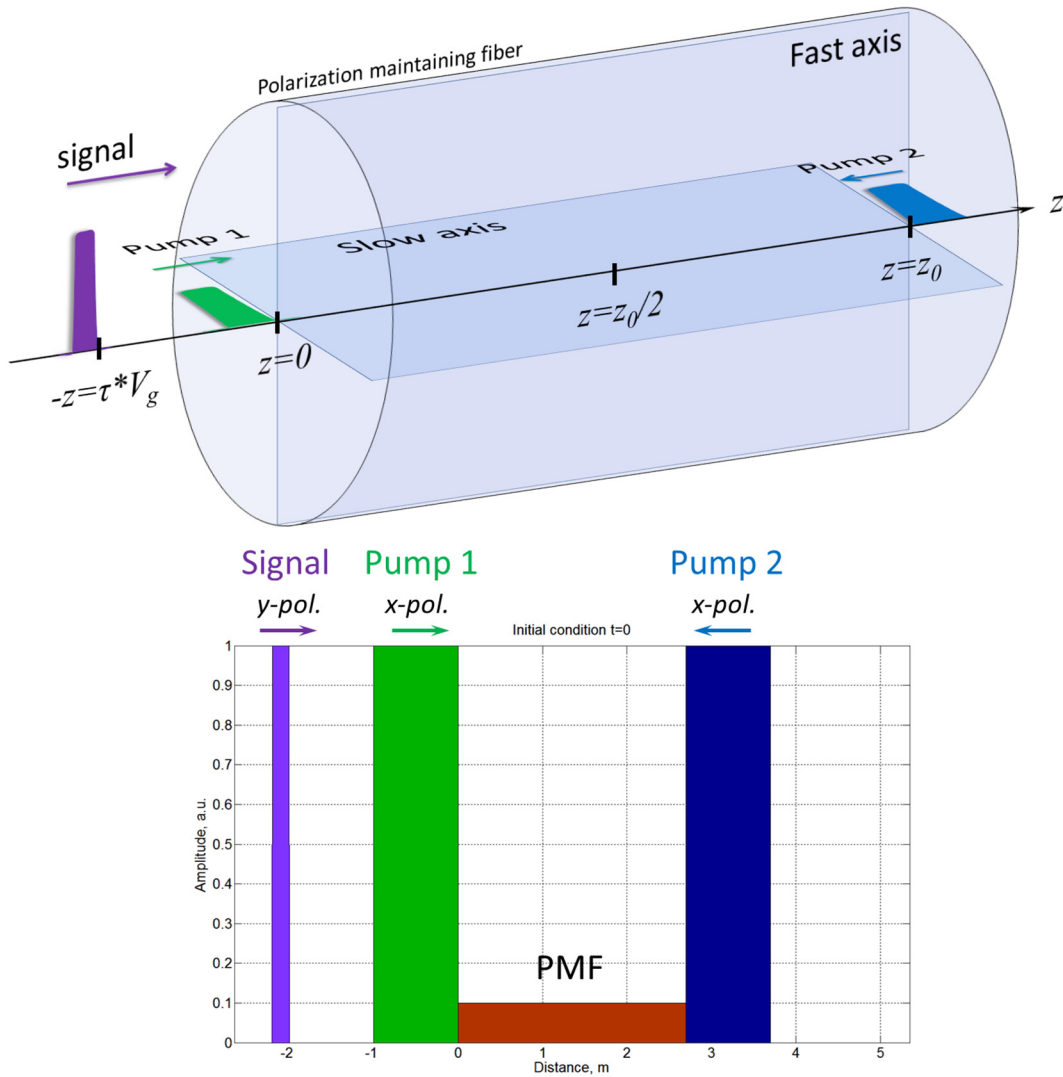
Figure 23. Initial conditions to obtain the reflected pulse form the grating generated using 5 ns pump pulses. Reading pulse is 1 ns. Length of the PMF is 2.7 m.

From Figure 24 it is seen that the reflected wave has length corresponding to the propagation time of 10.9 ns, which actually equals to the sum of the round trip propagation time through the dynamic grating and the signal pulse. As we can see, the reflected pulse resembles the shape of the dynamic Brillouin grating. Thus, by controlling the shape of the pump pulse(s) we can generate different shapes of the reflection. Moreover, the grating can be generated at any position inside the fiber, thus allowing to control the arrival time of the reflected pulse. Figure 24 (c, d) shows the reflected pulses when the width of the signal pulse was 3 and 5 ns, respectively. It is seen that reflected waveforms have shapes corresponding to the convolution of signal amplitude with DBG amplitude. The longer the signal pulse the larger the amplitude of the reflected waveform. The maximum amplitude for the reflected waveform will be achieved when signal pulse will be equal to the DBG length in space. In addition time span of

the reflected waveform is equal to the sum of the signal pulse width and time corresponding to the length of the DBG.
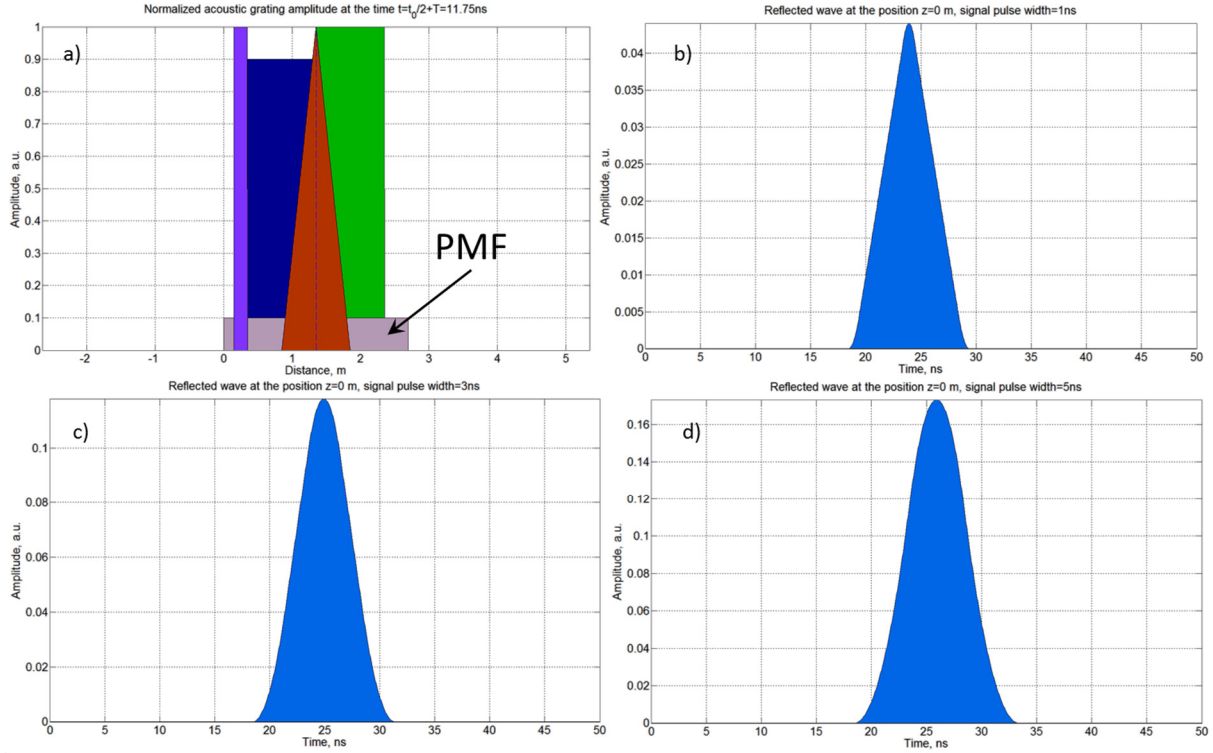
Figure 24. a) Acoustic grating at the time t=t₀/2+T. b), c), d)reflected wave at the position z=0 when square signal pulse with 1, 3, and 5 ns width is used, respectively.

Now we are interested in obtaining the reflected wave from the grating generated by pump pulses with different widths. We follow the same procedure as before. In order to consider our DBG as a time invariant system we represent the acoustic wave amplitude as a function only of distance, but not time. As before we take fixed acoustic wave amplitude at the time when the two pump pulses finish generating the acoustic grating. For this purpose we consider the situation when width of pump 1 pulse is bigger than the width of pump 2 pulse, $T_1 > T_2$. In this case the solution for the acoustic grating is given by expression (3.26). Moreover, we know that at the time $t = t_0 / 2 + T_1 / 2 + T_2 / 2$, the two pump pulses start to leave each other, so that the acoustic grating has its final shape. Further increase in time will simply change the acoustic grating amplitude, but the shape of the dynamic grating will stay the same. Thus, we fix the amplitude of the grating at the time $t = t_0 / 2 + T_1 / 2 + T_2 / 2$. After this time we assume that dynamic grating is static and we neglect the DBG amplitude decay while signal pulse propagates through the grating. Using expression (3.26) we can write the expression for the acoustic wave at time $t = t_0 / 2 + T_1 / 2 + T_2 / 2$:

$$\rho(z,t) = \frac{ig_1 P_1^0 P_2^0 \alpha\beta^*}{\Gamma_A} \begin{cases} 0 & 0 < z \le \dfrac{z_0}{2} - \dfrac{TV_g}{2} \\[2ex] u\left(\dfrac{z_0}{2V_g}+\dfrac{(T_1+T_2)}{2}-\dfrac{z_0-z}{V_g}\right)\left(1-e^{-\Gamma_A\left(\frac{z_0}{2V_g}+\frac{(T_1+T_2)}{2}-\frac{z_0-z}{V_g}\right)}\right) - u\left(\dfrac{z_0}{2V_g}+\dfrac{(T_1+T_2)}{2}-T_1-\dfrac{z}{V_g}\right)\left(1-e^{-\Gamma_A\left(\frac{z_0}{2V_g}+\frac{(T_1+T_2)}{2}-T_1-\frac{z}{V_g}\right)}\right) & \dfrac{z_0-T_1V_g}{2} < z \le \dfrac{z_0}{2}+\dfrac{(T_2-T_1)V_g}{2} \\[2ex] u\left(\dfrac{z_0}{2V_g}+\dfrac{(T_1+T_2)}{2}-\dfrac{z_0-z}{V_g}\right)\left(1-e^{-\Gamma_A\left(\frac{z_0}{2V_g}+\frac{(T_1+T_2)}{2}-\frac{z_0-z}{V_g}\right)}\right) - u\left(\dfrac{z_0}{2V_g}+\dfrac{(T_1+T_2)}{2}-T_2-\dfrac{z_0-z}{V_g}\right)\left(1-e^{-\Gamma_A\left(\frac{z_0}{2V_g}+\frac{(T_1+T_2)}{2}-T_2-\frac{z_0-z}{V_g}\right)}\right) & \dfrac{z_0}{2}+\dfrac{(T_2-T_1)V_g}{2} < z \le \dfrac{z_0}{2} \\[2ex] u\left(\dfrac{z_0}{2V_g}+\dfrac{(T_1+T_2)}{2}-\dfrac{z}{V_g}\right)\left(1-e^{-\Gamma_A\left(\frac{z_0}{2V_g}+\frac{(T_1+T_2)}{2}-\frac{z}{V_g}\right)}\right) - u\left(\dfrac{z_0}{2V_g}+\dfrac{(T_1+T_2)}{2}-T_2-\dfrac{z_0-z}{V_g}\right)\left(1-e^{-\Gamma_A\left(\frac{z_0}{2V_g}+\frac{(T_1+T_2)}{2}-T_2-\frac{z_0-z}{V_g}\right)}\right) & \dfrac{z_0}{2} < z \le \dfrac{z_0+T_2V_g}{2} \\[2ex] 0 & \dfrac{z_0+TV_g}{2} < z \end{cases}$$

$$(3.54)$$

In order to find the expression for the reflected wave we use the same expression (3.37) as before. We follow the same procedure to obtain the solution. Thus, we arrive to expression (3.47) where we use expression (3.54) to get the modulus of the acoustic wave. In this case we can write the solution for $\widetilde{R}(s, z=0)$ as following:

$$\widetilde{R}(s, z=0) = -M\frac{ig_1 P_1^0 P_2^0 \alpha\beta^*}{\Gamma_A}\left[\widetilde{R}'(s,z=0) + \widetilde{R}''(s,z=0) + \widetilde{R}'''(s,z=0)\right] \qquad (3.55)$$

where

$$\widetilde{R}'(s,z=0) = \int_{\frac{z_0}{2}-\frac{T_1V_g}{2}}^{\frac{z_0}{2}+\frac{(T_2-T_1)V_g}{2}} e^{-\frac{s}{V_g}z}\left(-u\left(\dfrac{z_0}{2V_g}+\dfrac{T_1}{2}+\dfrac{T_2}{2}-\dfrac{z_0}{2V_g}+\dfrac{z}{V_g}\right)e^{-\Gamma_A\left(\frac{z_0}{2V_g}+\frac{T_1}{2}+\frac{T_2}{2}-\frac{z_0}{2V_g}+\frac{z}{V_g}\right)} + u\left(\dfrac{z_0}{2V_g}+\dfrac{T_1}{2}+\dfrac{T_2}{2}-T_1-\dfrac{z}{V_g}\right)e^{-\Gamma_A\left(\frac{z_0}{2V_g}+\frac{T_1}{2}+\frac{T_2}{2}-T_1-\frac{z}{V_g}\right)}\right)\dfrac{e^{-\tau s}e^{-\frac{z}{V_g}s}}{s}\left(1-e^{-T_s s}\right)dz$$

$$(3.56)$$

$$\widetilde{R}''(s,z=0) = \int_{\frac{z_0}{2}+\frac{(T_2-T_1)V_g}{2}}^{\frac{z_0}{2}} e^{-\frac{s}{V_g}z}\left(-u\left(\dfrac{z_0}{2V_g}+\dfrac{T_1}{2}+\dfrac{T_2}{2}-\dfrac{z_0}{V_g}+\dfrac{z}{V_g}\right)e^{-\Gamma_A\left(\frac{z_0}{2V_g}+\frac{T_1}{2}+\frac{T_2}{2}-\frac{z_0}{V_g}+\frac{z}{V_g}\right)} + u\left(\dfrac{z_0}{2V_g}+\dfrac{T_1}{2}+\dfrac{T_2}{2}-T_2-\dfrac{z_0}{V_g}+\dfrac{z}{V_g}\right)e^{-\Gamma_A\left(\frac{z_0}{2V_g}+\frac{T_1}{2}+\frac{T_2}{2}-T_2-\frac{z_0}{V_g}+\frac{z}{V_g}\right)}\right)\dfrac{e^{-\tau s}e^{-\frac{z}{V_g}s}}{s}\left(1-e^{-T_s s}\right)dz$$

$$(3.57)$$

$$\widetilde{R}'''(s,z=0) = \int_{\frac{z_0}{2}}^{\frac{z_0}{2}+\frac{T_2V_g}{2}} e^{-\frac{s}{V_g}z}\left(-u\left(\dfrac{z_0}{2V_g}+\dfrac{T_1}{2}+\dfrac{T_2}{2}-\dfrac{z}{V_g}\right)e^{-\Gamma_A\left(\frac{z_0}{2V_g}+\frac{T_1}{2}+\frac{T_2}{2}-\frac{z}{V_g}\right)} + u\left(\dfrac{z_0}{2V_g}+\dfrac{T_1}{2}+\dfrac{T_2}{2}-T_2-\dfrac{z_0}{V_g}+\dfrac{z}{V_g}\right)e^{-\Gamma_A\left(\frac{z_0}{2V_g}+\frac{T_1}{2}+\frac{T_2}{2}-T_2-\frac{z_0}{V_g}+\frac{z}{V_g}\right)}\right)\dfrac{e^{-\tau s}e^{-\frac{z}{V_g}s}}{s}\left(1-e^{-T_s s}\right)dz$$

$$(3.58)$$

Solutions to the integrals (3.56),(3.57), and (3.58) as well as their Laplace transforms are presented in Appendix C. As before, to obtain the reflected wave at position z=0 in the time domain we take the inverse Laplace transform of equation (3.55):

$$R(t, z=0) = -M\frac{ig_1 P_1^0 P_2^0 \alpha\beta^*}{\Gamma_A}\left[R'(t,z=0) + R''(t,z=0) + R'''(t,z=0)\right] \qquad (3.59)$$

where

$$R'(t,z=0)=\frac{V_g}{\Gamma_A}\left(u\left(t-\frac{z_0}{V_g}+T_1-\tau\right)\cdot\left\{+e^{\frac{\Gamma_A}{2}\left(t-\frac{z_0}{V_g}+T_1-T_2-\tau\right)}-2e^{\left(-\frac{\Gamma_A T_2}{2}\right)}+e^{-\frac{\Gamma_A}{2}\left(t-\frac{z_0}{V_g}+T_1+T_2-\tau\right)}\right\}+u\left(t-\frac{z_0}{V_g}-T_2+T_1-\tau\right)\left\{1-e^{\frac{\Gamma_A}{2}\left(t-\frac{z_0}{V_g}-T_2+T_1-\tau\right)}+e^{-\Gamma_A T}-e^{-\frac{\Gamma_A}{2}\left(t-\frac{z_0}{V_g}+T_2+T_1-\tau\right)}\right\}\right)-$$

$$\frac{V_g}{\Gamma_A}\left(u\left(t-\frac{z_0}{V_g}+T_1-\tau-T_s\right)\cdot\left\{+e^{\frac{\Gamma_A}{2}\left(t-\frac{z_0}{V_g}+T_1-T_2-\tau-T_s\right)}-2e^{\left(-\frac{\Gamma_A T_2}{2}\right)}+e^{-\frac{\Gamma_A}{2}\left(t-\frac{z_0}{V_g}+T_1+T_2-\tau-T_s\right)}\right\}+u\left(t-\frac{z_0}{V_g}-T_2+T_1-\tau-T_s\right)\left\{1-e^{\frac{\Gamma_A}{2}\left(t-\frac{z_0}{V_g}-T_2+T_1-\tau-T_s\right)}+e^{-\Gamma_A T}-e^{-\frac{\Gamma_A}{2}\left(t-\frac{z_0}{V_g}+T_2+T_1-\tau-T_s\right)}\right\}\right)$$

$$(3.60)$$

$$R''(t,z=0)=\frac{V_g}{\Gamma_A}\left(e^{-\frac{\Gamma_A}{2}(T_1-T_2)}-e^{-\frac{\Gamma_A}{2}(T_1+T_2)}\right)\left[u\left(t-\frac{z_0}{V_g}-T_2+T_1-\tau\right)\cdot\left\{e^{-\frac{\Gamma_A(T_2-T_1)}{2}}-e^{-\frac{\Gamma_A}{2}\left(t-\frac{z_0}{V_g}-\tau\right)}\right\}+u\left(t-\frac{z_0}{V_g}-\tau\right)\left\{e^{-\frac{\Gamma_A}{2}\left(t-\frac{z_0}{V_g}-\tau\right)}-1\right\}-$$

$$\left(u\left(t-\frac{z_0}{V_g}-T_2+T_1-\tau-T_s\right)\cdot\left\{e^{-\frac{\Gamma_A(T_2-T_1)}{2}}-e^{-\frac{\Gamma_A}{2}\left(t-\frac{z_0}{V_g}-\tau-T_s\right)}\right\}+u\left(t-\frac{z_0}{V_g}-\tau-T_s\right)\left\{e^{-\frac{\Gamma_A}{2}\left(t-\frac{z_0}{V_g}-\tau-T_s\right)}-1\right\}\right)\right]$$

$$(3.61)$$

$$R'''(t,z=0)=\frac{V_g}{\Gamma_A}\left[u\left(t-\frac{z_0}{V_g}-\tau\right)\cdot\left\{e^{-\Gamma_A\left(\frac{T_1}{2}-\frac{T_2}{2}\right)}-e^{-\frac{\Gamma_A}{2}\left(t-\frac{z_0}{V_g}+T_1-T_2-\tau\right)}-e^{+\frac{\Gamma_A}{2}\left(t-\frac{z_0}{V_g}-T_1-T_2-\tau\right)}+e^{-\Gamma_A\left(\frac{T_1}{2}+\frac{T_2}{2}\right)}\right\}+u\left(t-\frac{z_0}{V_g}-T_2-\tau\right)\left\{e^{-\frac{\Gamma_A}{2}\left(t-\frac{z_0}{V_g}-T_2+T_1-\tau\right)}-2e^{-\frac{\Gamma_A T}{2}}+e^{\frac{\Gamma_A}{2}\left(t-\frac{z_0}{V_g}-T_2-T_1-\tau\right)}\right\}\right]-$$

$$\left[u\left(t-\frac{z_0}{V_g}-\tau-T_s\right)\cdot\left\{e^{-\Gamma_A\left(\frac{T_1}{2}-\frac{T_2}{2}\right)}-e^{-\frac{\Gamma_A}{2}\left(t-\frac{z_0}{V_g}+T_1-T_2-\tau-T_s\right)}-e^{+\frac{\Gamma_A}{2}\left(t-\frac{z_0}{V_g}-T_1-T_2-\tau-T_s\right)}+e^{-\Gamma_A\left(\frac{T_1}{2}+\frac{T_2}{2}\right)}\right\}+u\left(t-\frac{z_0}{V_g}-T_2-\tau-T_s\right)\left\{e^{-\frac{\Gamma_A}{2}\left(t-\frac{z_0}{V_g}-T_2+T_1-\tau-T_s\right)}-2e^{-\frac{\Gamma_A T}{2}}+e^{\frac{\Gamma_A}{2}\left(t-\frac{z_0}{V_g}-T_2-T_1-\tau-T_s\right)}\right\}\right]$$

$$(3.62)$$

To simulate the reflection from the dynamic Brillouin grating generated using two pumps with different widths, we use the following initial condition: pump 1 pulse width was set to 6 ns, pump 2 pulse width was set to 3 ns, and fiber segment was 2.7 m. The reading signal was launched 5 ns after the pump 1 pulse. The initial configuration of the pulses is depicted in Figure 25. As before, we fix the grating at the time when it is completely generated by the pump pulses. In this case it will be the time $t=t_0/2+(T_1+T_2)/2$. After this time we consider the grating as fixed. Figure 26 (b) represents the evolution of the acoustic grating amplitude in z- and t-domains, where the red line shows the time at which we consider the acoustic grating as stationary in time. As before this assumption is necessary to obtain analytical solution for the reflected wave. This assumption can be used if the propagation time of the signal pulse through the DBG is less than phonon lifetime. According to our initial condition, the dynamic Brillouin grating will be completely generated at time 11.25 ns. At this instant, the pump pulses start to leave each other as shown in Figure 26 (a). We also can determine the length of the grating at this time, which is given by the simple expression $L_{grat}=(T_1+T_2)V_g/2$. In our case, the DBG length will be 0.9 m with a trapezium-like shape (Figure 26 (a)). The reflection of the 1 ns signal pulse from dynamic grating is calculated using expression 5.60 and depicted in Figure 26 (c). It is clear that reflection at z=0 appears at time $t=\tau+\left(\frac{t_0}{2}-\frac{T_1}{2}\right)2=\tau+t_0-T_1$.

Since in our case τ is equal to $\tau = T_1 + 5$ ns, we get that reflected waveform arrives at the position $z = 0$ at time $t = t_0 + 5 \ ns = 18.5 \ ns$.
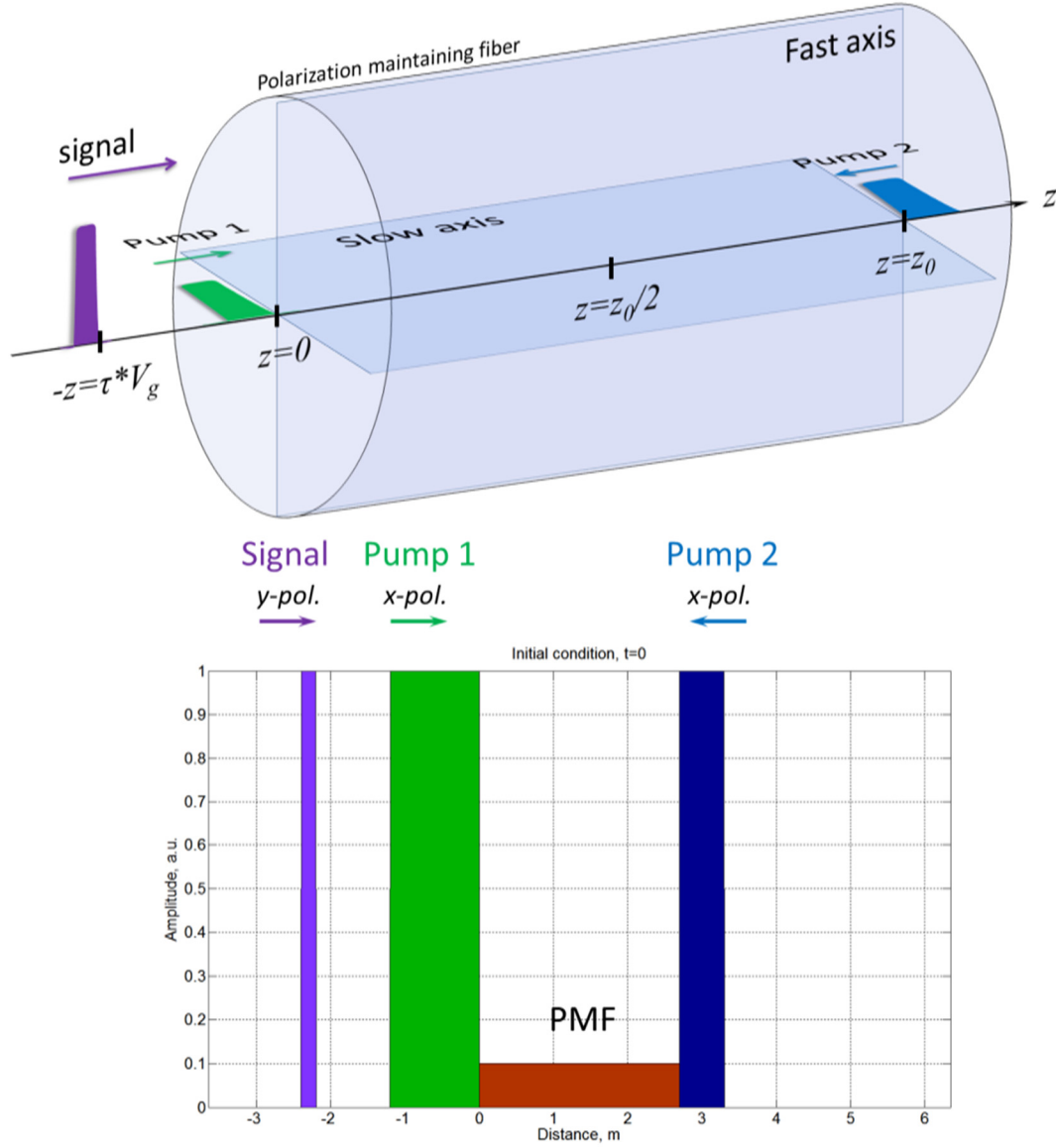
Figure 25. Initial conditions to obtain the reflection from the grating generated using 6 ns pump 1 pulse and 3 ns pump 1 pulse. Reading pulse is 1 ns. Length of the PMF 2.7 m.

It is clear from the Figure 26 (c) that when the signal pulse is short compared to the length of the acoustic grating, the reflection resembles the shape of acoustic grating itself. Basically, the reflection represents the convolution of the signal pulse with the dynamic grating amplitude. By increasing the signal pulse width up to 5 ns we can see that the reflection gets smoother as depicted in the Figure 26 (d).
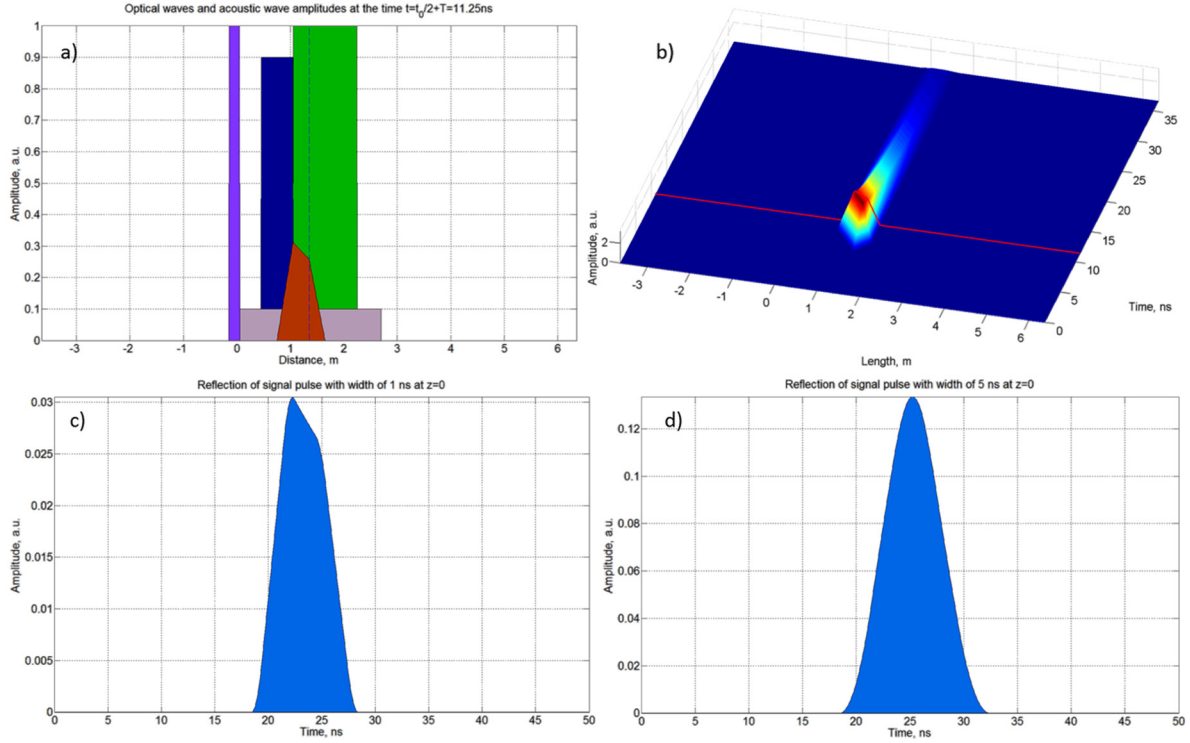
Figure 26. a) Optical pulses amplitudes together with acoustic wave amplitude at the time t=t_0/2+(T_1+T_2)/2. b) 3 d plot of the acoustic wave amplitude in z- and t-domain. Red line shows time when we fix the grating amplitude. c), d) Reflection of the 1 ns (20 cm) and 5 ns (1 m) signal pulse from the dynamic grating, respectively.

In conclusion, dynamic Brillouin grating can be generated locally at any arbitrary position inside the fiber. This can be done by simply delaying one of the pump pulses. Moreover, the shape of the grating depends on the shape of the pump pulses. Consequently shape and length of the reflection of the signal pulse from the generated grating can be controlled. In addition by changing the repetition rate of pump pulses, the number of the dynamic Brillouin gratings inside the polarization maintaining fiber can be varied. Such flexibility opens many opportunities to perform different operations on the optical signals, which will be demonstrated in the next chapter of this thesis.

3.4. Phase conjugation properties of the DBG

In the early Stimulated Brillouin scattering experiments it was observed that the generated backward Stockes light was highly directional [14, 15]. Such property of the scattered light was initially explained as the consequence of the geometrical conditions of the experimental setup. In 1972 Zel'dovich *et. al.* first pointed out that scattered light had a particular dependence on the incident wave. In their experiment pump wave was purposely distorted by a phase plate and then launched into the cell containing methane gas. Strong Stokes signal generated within this cell was monitored after the scattered light passed through the aberrator in the opposite direction. Surprisingly, scattered light at the detection was not diverged by the phase plate, but, on the contrary, it was converged to the spot size of the

initial laser beam. When the cell was replaced by a conventional mirror, the divergence of the reflected radiation was additionally increased after passing through the aberrator. This experiment demonstrated that SBS-reflected wave is indeed a phase conjugated wave with respect to the pump wave. Phase conjugation implies the following phenomena. For example, if we have an incident wave written as $E_1(r,t) = \frac{1}{2}|E(r)| \left[e^{i[\omega t - kr + \varphi(r)]} + e^{-i[\omega t - kr + \varphi(r)]} \right]$ than the phase-conjugated wave can be written as $E_{conj}(r,t) = \frac{1}{2}|E(r)| \left[e^{i[\omega t + kr - \varphi(r)]} + e^{-i[\omega t + kr - \varphi(r)]} \right]$. This means that phase conjugated wave travels in opposite direction, $k_{conj} = -k_1$, and its wavefront accurately coincides with the direct wave at any position in space. It can be written also as, $\varphi_{conj}(r) = -\varphi_1(r)$. The reason for SBS to generate phase conjugated scattering is not clear from inspection of the coupled-amplitude equations that describe SBS process [16] and requires complex mathematical analysis [17]. However physical explanation for the case of badly aberrated optical wave is the following. When the pump wave is highly aberrated, intensity distribution inside the media is nonuniform. This results in nonuniform distribution of the gain experienced by the Stokes wave, since it is proportional to the local pump intensity. Thus, components of the scattering wave, which match the best this uniform gain distribution, favor the maximum amplification. This means that scattered light must have wavefronts that match those of the incident laser beam, resulting in generation of phase conjugated wave. To make this explaination more clear we consider the equation satisfied by the Stokes field,

$$\frac{\partial I_s}{\partial z} = -g I_p I_s \qquad (3.63)$$

Now we consider the total power in each wave at a position z as,

$$P_p = \int I_p dA, \quad P_s = \int I_s dA \qquad (3.64)$$

where A is the area large enough to include all the power of the wave. Then we write equation (3.63) as

$$\int \frac{\partial I_s}{\partial z} dA = -g \int I_p I_s \partial A = \frac{\partial P}{\partial z} = -g \int I_p I_s dA \frac{P_p P_s}{P_p P_s} = -g \int I_p I_s dA \frac{P_p P_s}{\int I_p dA \int I_s dA} = -g P_p P_s \frac{\int I_p I_s dA}{\int I_p dA \int I_s dA} \quad (3.65)$$

We can rewrite equation (3.65) as:

$$\frac{\partial P_s}{\partial z} = -g \frac{P_p P_s}{A} C \qquad (3.66)$$

where

$$C = \frac{\int I_p I_s dA}{\int I_p dA \int I_s dA} \tag{3.67}$$

represents the normalized spatial cross-correlation function of the pump and Stokes fields intensity distributions.

We see that power gain experienced by the Stokes wave depends not only on the total power of the pump wave, but also on the degree of correlation between the pump and Stokes wave intensity distributions. When I_s and I_p are completely uncorrelated or when intensity distributions are uniform, the correlation function C takes on the value of unity. However, if I_p and I_s are correlated, for example, because the pump and Stokes fields are phase conjugates of one another, the correlation function can be greater than unity. This fact demonstrates that exponential gain experienced by the phase-conjugate portion of the Stokes backscattered wave will be larger than that experienced by any other mode of the Stokes field.

In the remaining part of the section we demonstrate that reading optical wave reflected from a DBG arrives at the beginning of the fiber, $z = 0$, with a constant phase independently of the DBG position inside the fiber. This fact demonstrates that DBG acts as a phase conjugate mirror.

In this subchapter we present some numerical calculations of the dynamic Brillouin grating phase response related to signal processing in the field of microwave photonics. For this purpose we consider a DBG reflection of the optical waves which can be modulated to carry a microwave signal. Let us consider a PM fiber where two counter-propagating pump pulses generate a localized dynamic Brillouin grating, as shown in the Figure 27. For simplicity, the origin of the optical phase is taken at the two ends of the fiber. Optical fields of two pumps can be expressed at the position d as:

$$E_{P1}\big|_{z=d} = A_{p1} e^{i\left(\omega_{P1}t - \frac{\omega_{P1}}{c} n_x d\right)} \quad and \quad E_{P2}\big|_{z=d} = A_{p2} e^{i\left(\omega_{P2}t + \frac{\omega_{P2}}{c} n_x (d-L)\right)}, \tag{3.68}$$

SBS interaction results in the generation of the acoustic wave, which can be written as:

$$Q\big|_{z=d} = CE_{p1}E_{p2}^* = CA_{p1}A_{p2}^* e^{i\left(\Omega_B t - \frac{\omega_{P1}}{c} n_x d - \frac{\omega_{P2}}{c} n_x (d-L)\right)} \tag{3.69}$$
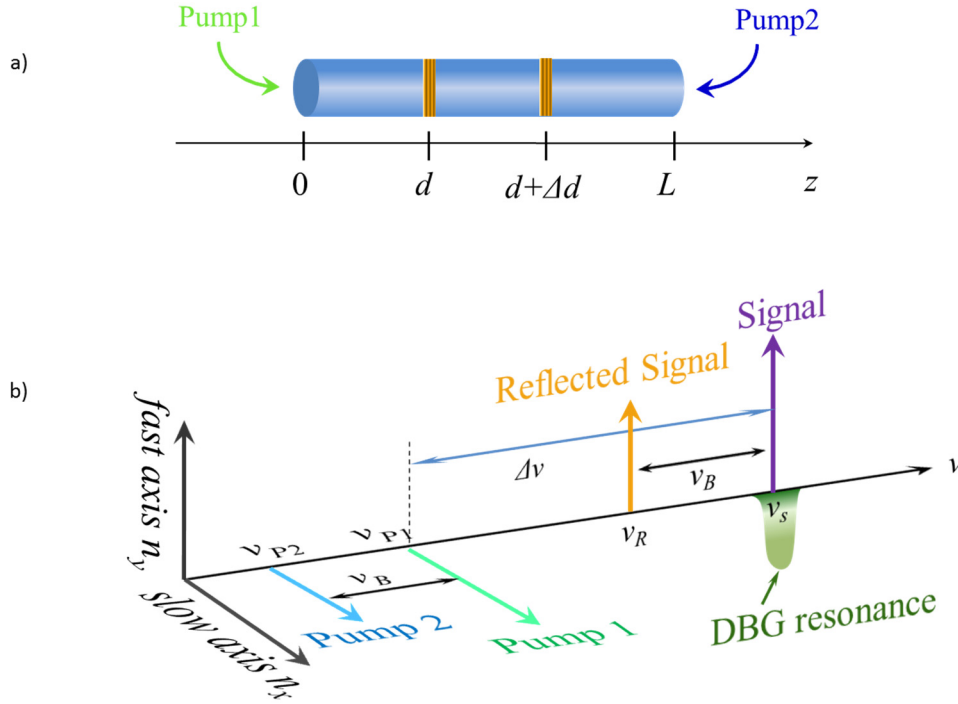
Figure 27. a) Generation of the DBG using counter-propagating pump pulses represented in z-domain. b) Polarizations and optical frequencies of interacting waves.

where C is the coupling constant. Considering now a CW signal, propagating through the fiber in the direction of the Pump 1 wave. After propagating the distance d, signal can be represented as:

$$E_S\big|_{z=d} = A_S e^{i\left(\omega_S t - \frac{\omega_S}{c} n_y d\right)}.$$
(3.70)

At the position d signal is reflected from the DBG and reflected wave can be expressed as:

$$E_R\big|_{z=d} = C_1 E_S Q^* = C_1 C A_S A_{p1}^* A_{p2} e^{i\left((\omega_S - \Omega_B)t + \frac{\omega_{p2}}{c} n_x (d-L)\right)}$$
(3.71)

where C_1 is the reflectivity of the DBG, and we used the expression (3.4), $\omega_S n_y = \omega_{p1} n_x$. At the position $z=0$ reflected signal propagated the distance d and can be written as:

$$E_R\big|_{z=0} = C_1 C A_S A_{p1}^* A_{p2} e^{i\left((\omega_S - \Omega_B)t + \frac{\omega_{p2}}{c} n_x (d-L) - \frac{\omega_R}{c} n_y d\right)}.$$
(3.72)

Using the expression (3.4) in the form:

$$(\omega_R + \Omega_B)n_y = (\omega_{p2} + \Omega_B)n_x \quad or \quad \omega_R n_y = \omega_{p2} n_x + \Omega_B \Delta n$$
(3.73)

we can rewrite (3.72) as:

$$E_R\big|_{z=0} = C_1 C A_S A_{p1}^* A_{p2} e^{i\left((\omega_S - \Omega_B)t - \frac{\omega_{p2}}{c}n_x L - \frac{\Omega_B}{c}\Delta n d\right)}$$ (3.74)

It is clear that the phase of the reflected wave does depend on the position of the dynamic grating inside the fiber, but the contribution to the phase of the wave from the last term is negligible. Thus, if we write that $\omega_R n_y = \omega_{p2} n_x$, the phase of the reflected wave is independent of the DBG position inside the fiber. This way the reflected wave arrives to the beginning of the fiber with the same phase independently where it was reflected, showing that it behaves like a phase conjugated wave.

Now we consider a RF signal which is reflected from the dynamic grating generated at the position d inside the fiber, as shown in Figure 28. Carrier of RF signal is tuned to the center of the resonance $\omega_{car} = \omega_S$. Upper sideband is slightly detuned from the center resonance frequency $\omega_S + \Omega_{RF} = \omega_{SB}$. After propagating a distance d the RF signal can be written as:

$$E_S\big|_d = A_{car} e^{i\left(\omega_S t - \frac{\omega_S}{c}n_y d\right)} + A_{SB} e^{i\left((\omega_S + \omega_{RF})t - \frac{(\omega_S + \omega_{RF})}{c}n_y d\right)}$$ (3.75)
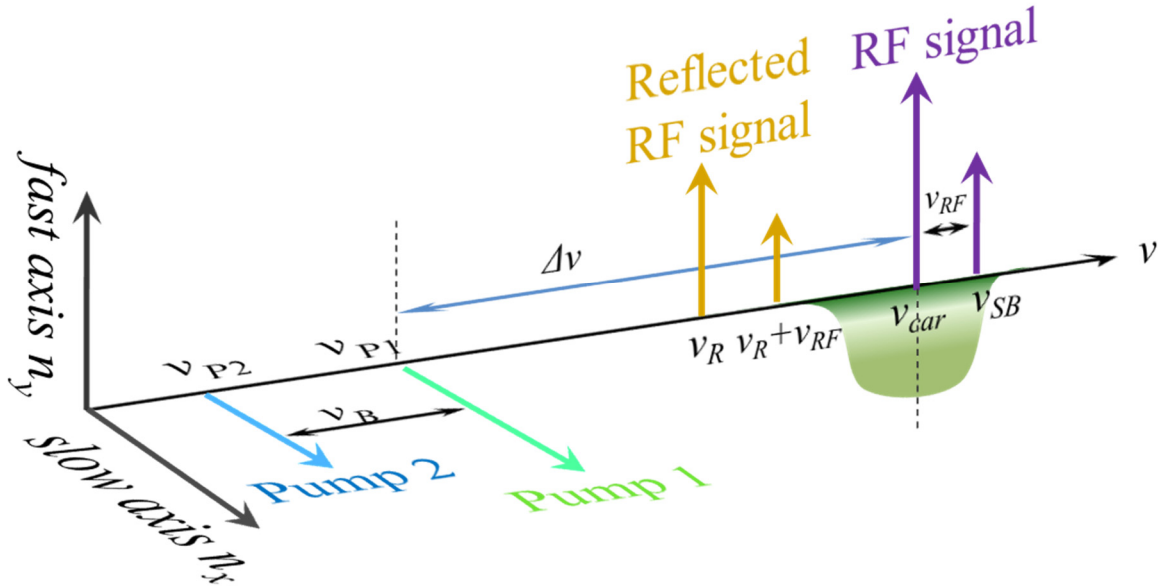
Figure 28. Configuration of the optical waves to realize a reflection of the RF signal from a single dynamic Brillouin grating.

Following the expression (3.71) reflected wave is given by:

$$E_R\big|_d = C_1 E_S Q^* = C_1 C A_{p1} A_{p2}^* \left[A_{car} e^{i((\omega_S - \Omega_B)t + \frac{\omega_{p2}}{c}n_x(d-L))} + A_{SB} e^{i\left((\omega_S + \omega_{RF} - \Omega_B)t - \frac{\omega_{RF}}{c}n_y d + \frac{\omega_{p2}}{c}n_x(d-L)\right)} \right]$$ (3.76)

Returning to the point $z=0$ reflected wave passes distance d:

$$E_R\big|_0 == C_1 C A_{p1} A_{p2}^* \left[A_{car} e^{i\left((\omega_S - \Omega_B)t - \frac{\omega_{p2}}{c}n_x L - \frac{\Omega_B}{c}\Delta n d\right)} + A_{SB} e^{i\left((\omega_S + \omega_{RF} - \Omega_B)t - \frac{\omega_{p2}}{c}n_x L - \frac{\Omega_B}{c}\Delta n d - \frac{\omega_{RF}}{c}n_y d\right)} \right] \quad (3.77)$$

Beating between the carrier and sideband will give an intensity oscillating at radio frequency as:

$$I\big|_{z=0} = I_{car}\big|_{z=0} + I_{SB}\big|_{z=0} + 2\sqrt{\left(I_{car}\big|_{z=0} I_{SB}\big|_{z=0}\right)} \cos\left(\omega_{RF}t - \frac{\omega_{RF}}{c}n_y d\right) \quad (3.78)$$

Thus, it is clear from (3.78) that the intensity varies sinusoidally at frequency ω_{RF}, and by changing the position d of the DBG the phase of the RF signal will be changed according to the delay of $n_y d / c$.

Now we consider the following situation. Two dynamic Brillouin gratings are generated at the position d inside the fiber with two pairs of pumps, as shown in Figure 29. Pump 1 pulse consists of two optical frequencies separated by frequency v_g, which is in the vicinity of the RF signal, v_{RF}. Pump 2 pulse as well consists of two frequencies separated by the same difference v_g and also down-shifted by the Brillouin shift from those of Pump 1.
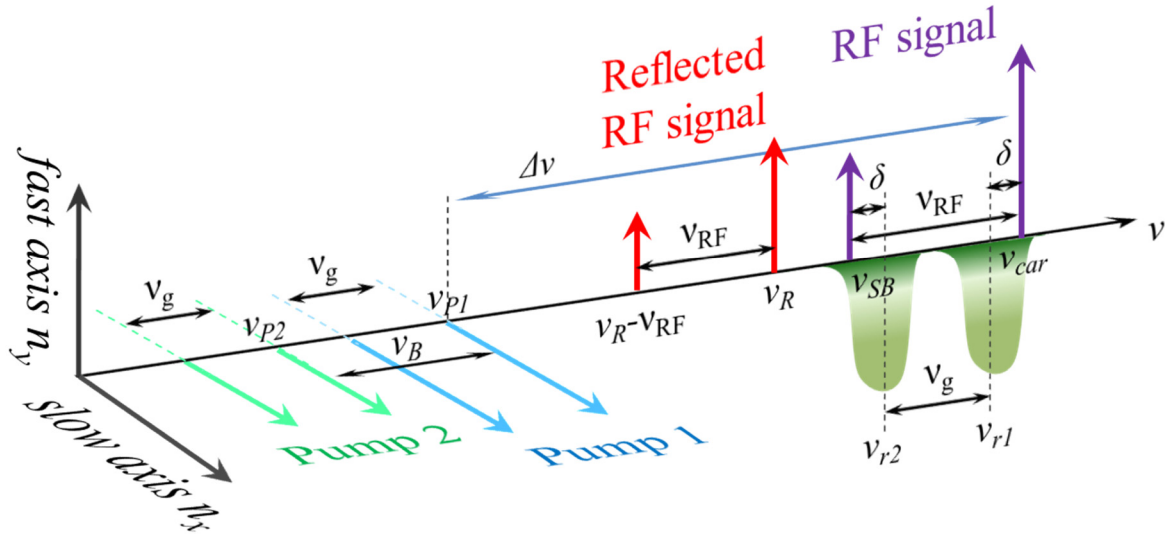
Figure 29. Relative frequencies of the optical waves to generate two DBGs used to reflect RF signal. Each DBG resonance is allocated to reflect each component of RF signal.

In given configuration carrier is slightly downshifted from the center of one resonance, and sideband is slightly upshifted from center of another resonance. By using the expression (3.77) we can write directly write expression for the reflected wave at the detection point, $z=0$:

$$E_R\big|_0 = C_1 C A_{p1} A_{p2}^* \left[A_{car} e^{i\left((\omega_{r1} + \delta - \Omega_B)t - \frac{\omega_{p2}}{c}n_x L - \frac{\Omega_B}{c}\Delta n d - \frac{\delta}{c}n_y d\right)} + A_{SB} e^{i\left((\omega_{r2} - \delta - \Omega_B)t - \frac{\omega_{p2}}{c}n_x L - \frac{\Omega_B}{c}\Delta n d + \frac{\delta}{c}n_y d\right)} \right], \quad (3.79)$$

where $\omega_{r1} = 2\pi v_{r1}, \omega_{r2} = 2\pi v_{r2}$ are the angular frequencies corresponding to the center frequencies of the dynamic gratings for carrier and sideband, respectively. Finally, beating of the two waves results in intensity fluctuation as:

$$I\big|_{z=0} = I_{car}\big|_{z=0} + I_{SB}\big|_{z=0} + 2\sqrt{(I_{car}\big|_{z=0} I_{SB}\big|_{z=0})} \cos\left((\omega_{r1} - \omega_{r2} + 2\delta)t - 2\frac{\delta}{c}n_y d) \right) \qquad (3.80)$$

We can see that phase shift of the radio frequency signal depends on the position of the dynamic gratings. However, when δ is equal to zero, or, when $v_g = v_{RF}$, phase is independent of the position of the DBG inside the fiber. Moreover, phase conjugation can be also achieved if carrier and sideband are shifted to the same side from the center of the gratings resonances.

This chapter demonstrated that dynamic Brillouin grating can be generated locally at any desired position inside the fiber. Properties of the generated grating can be adjusted dynamically. By changing the position and shape of the reflector various signal processing operations are available. The following chapter will demonstrate various ways to generate Brillouin gratings as well as their applications for processing signals in optical domain. Moreover, properties of the dynamic Brillouin grating are related to the intrinsic properties of the fiber, such as birefringence and Brillouin shift. Environmental changes in temperature and pressure affects properties of the fiber and consequently properties of the Brillouin grating. Thus, by measuring the local spectral characteristic of the dynamic Brillouin grating it is possible to extract information about change of the surrounding temperature or induced stress on the fiber. Distributed temperature and stress sensors can be realized using such dependence.

Bibliography

1. K. O. Hill, and G. Meltz, "Fiber Bragg grating technology fundamentals and overview," Lightwave Technology, Journal of **15**, 1263-1276 (1997).
2. T. Erdogan, "Fiber grating spectra," Lightwave Technology, Journal of **15**, 1277-1294 (1997).
3. W. W. Morey, G. A. Ball, and G. Meltz, "Photoinduced Bragg Gratings in Optical Fibers," Opt. Photon. News **5**, 8-14 (1994).
4. Y. Shen, "Basic considerations of four-wave mixing and dynamic gratings," Quantum Electronics, IEEE Journal of **22**, 1196-1203 (1986).
5. H. Eichler, "Introduction to the special issue on dynamic gratings and four-wave mixing," Quantum Electronics, IEEE Journal of **22**, 1194-1195 (1986).
6. A. Scott, and M. Hazell, "High-efficiency scattering in transient Brillouin-enhanced four-wave mixing," Quantum Electronics, IEEE Journal of **22**, 1248-1257 (1986).
7. B. Fischer, J. L. Zyskind, J. W. Sulhoff, and D. J. DiGiovanni, "Nonlinear wave mixing and induced gratings in erbium-doped fiber amplifiers," Opt. Lett. **18**, 2108-2110 (1993).
8. J. Vaitkus, K. Jarasiunas, E. Gaubas, L. Jonikas, R. Pranaitis, and L. Subacius, "The diffraction of light by transient gratings in crystalline, ion-implanted, and amorphous silicon," Quantum Electronics, IEEE Journal of **22**, 1298-1305 (1986).
9. S. J. Frisken, "Transient Bragg reflection gratings in erbium-doped fiber amplifiers," Opt. Lett. **17**, 1776-1778 (1992).
10. K. Y. Song, W. W. Zou, Z. Y. He, and K. Hotate, "All-optical dynamic grating generation based on Brillouin scattering in polarization-maintaining fiber," Optics Letters **33**, 926-928 (2008).
11. T. F. M. Alexis Mendez, *Specialty Optical Fibers Handbook* (Academic Press, 2006).
12. A. Yariv, *Optical Electronics* (CBS College Publishing, New York, 1985).
13. R. Kashyap, *Fiber Bragg gratings* (Academic Press, Burlington, 2010).
14. V. I. P. B. Ya. Zeldovich, V. V. Ragulsky, and F. S.Faizullov, "Relationship between Wavefronts of Reflected and Exciting Light in Stimulated Brillouin Scattering," Journal of Experimental and Theoretical Physics **109** (1972).
15. A. L. Schawlow, ed. *Principles of Phase Conjugation* (Springer-Verlag, 1985).
16. R. W. Boyd, *Nonlinear optics* (Academic Press, Amsterdam ; Boston, 2008).
17. P. Suni, and J. Falk, "Theory of phase conjugation by stimulated Brillouin scattering," J. Opt. Soc. Am. B **3**, 1681-1691 (1986).

Chapter 4

Optical signal processing using dynamic Brillouin gratings.

In order to follow the increasing demand for higher processing speeds implementation of all-optical circuits and optical processing elements is needed. To overcome the speed limitations imposed by electronic-based systems, optical based systems should be able to perform all necessary operation solely in optical domain. Many nonlinear effects in silica fibers are used for ultra-high speed optical processing in telecommunication networks. Even though these effects found their application in communication networks they are possibly even more attractive for applications in microwave photonics and optical computing as it will be demonstrated in this chapter.

In chapter 4 we demonstrate that dynamic Brillouin gratings can be used to perform operations on optical signal all-optically. A buffer or a delay line for isolated pulses will be demonstrated showing impressive values of delay bandwidth product. Delay of data streams and radio frequency signals is also realized. Applications of the DBG to the field of microwave photonic filters (MPF) will be highlighted. Several implementations of the MPF are realized offering tunability of free spectral range (FSR) and operational bandwidth. Generation of localized dynamic Brillouin grating can be realized by a stimulated Brillouin process, where amplitude modulated pump waves or phase modulated pump waves can be used. Each technique will be discussed in details highlighting the advantages and disadvantages. In addition, optical calculus will be shown using DBG.

4.1. Optical delay lines

Future optical networks, signal processing circuits and telecommunication systems will require components capable of buffing or delaying optical information. Efficiency and aggregate throughput can be greatly enhanced by exploiting tunable, wideband optical delay lines. Precise control of arrival time of optical signal is a critical element for future optically switched networks. Optical synchronization and multiplexing, optical equalization, optical correlation, optical logic gates and many other signal processing areas can have direct application for tunable delay lines [1-4]. In addition, optical delay lines find their applications in the field of microwave photonics, where processing and transport of the radio frequency waves are greatly enhanced by using optical carriers [5-11]. For example, phase array antennas are employed in RF radars in order to direct the beam of RF electromagnetic wave in a specific direction. In order for phase array antennas to operate in wide frequency range and without beam squint, tunable true time delays are needed. Novel techniques to implement true time delays using photonic solutions offers large tunability of operating frequency of phased array antenna without inducing beam squint effect. Moreover, by implementing optical delay lines capable to delay RF signal for more than a period, microwave photonic filters can offer

unprecedented performance in terms of tunability. Another field of application of tunable delay lines lies in optical coherence tomography [12].

Any optical delay line should offer the possibility to control the group velocity of the optical pulse in the case when data is encoded in digital format. In the case of microwave photonic signal, optical buffer should provide phase control of the optical carrier and/or optical sideband. Over the last several years, continuously tunable delays have been proposed based on different mechanisms, such as electromagnetically induced transparency [13-15], coherent population oscillation in semiconductor optical amplifiers[11, 16], dispersion engineering in semiconductor waveguides [17, 18], or nonlinear induced resonances in optical fibers [19-22]. All of these phenomena are referred to as "slow light" and are based on changing the group velocity by exploring a resonance in different materials. Even though slow light based delay lines offer the possibility to control precisely the group velocity of broadband optical signals, the maximum delay is restricted to a few pulse widths, as a result of the dispersion induced signal distortion as well as unequal signal amplification. Thus optical buffers, which require storage time of several hundred bits, are practically impossible to realize using slow light techniques.

On the other hand delays of one bit of the data stream are needed for optical synchronization, where independent timing control for each channel can improve the data fidelity of multiplexed data streams. Moreover, in the field of microwave photonics tunable delays up to one period of the radio frequency are needed. This can be done using slow light approach by inducing a 2π phase shift on the optical carrier. Another approach to delay optical data is based on the combination of wavelength conversion and group velocity dispersion. This technique can achieve remarkable delays of more than 1000 bits for 10 Gbit/s data signals. For optical buffering and telecommunication applications this method seems very attractive. However, like any other techniques pulse distortion due to the group velocity dispersion is one of the limiting factors here. To reduce the broadening of the pulse complex dispersion compensating tools are employed. Moreover, to achieve large delays the signal wavelength should be changed over a large range, which requires efficient and power hungry wavelength conversion stages. In addition delays are achieved by propagation the signal over long distances of fiber, which dramatically increased reconfiguration time of the delay line.

In the following sections of this chapter, alternative approaches to realize optical delay line based on dynamic Brillouin grating will be presented and experimental verification of optical signal delay will be demonstrated. The first approach to delay optical signal is based on the generation of localized dynamic grating using intensity modulated pump waves in polarization maintaining fiber. A single data pulse is continuously delayed to demonstrate extensive fractional delay, which by far outperforms slow light delays. In addition, the delay line is tested using microwave photonic signals, demonstrating more than 2π phase shifts for a RF signals. In the following part limitations of the proposed delay line will be discussed. Broadband digital and microwave optical signals is shown to be delayed continuously using the proposed technique. It should be pointed out that to realize DBG all-optical delay line localized DBG at different positions inside the fiber can be generated using position dependent Brillouin frequency [23]. But this technique requires special preparation of the fiber.

4.1.1   Principle of operation.

The proposed delay line is based on two main stages. Firstly, a dynamic Brillouin grating is generated at a predefined position of the PM fiber, secondly, the generated dynamic Brillouin grating is exploited as a Bragg reflector to reflect the signal of interest. As it was demonstrated in the previous chapter, in order to generate the dynamic Brillouin grating two pump pulses are launched in a polarization maintaining fiber counter-propagating each other and polarized along the slow axis (x-axis) as it is shown in Figure 30 (a). Moreover, optical frequency of pump 2 pulse v_{p2} is down-shifted from that of pump 1 v_{p1} by the Brillouin shift of the fiber, v_B (Figure 30 (d)). Stimulated Brillouin scattering interaction between the two pulses leads to the generation of an acoustic grating at the position in the fiber where the two pump pulses cross each other. Shortly after the dynamic grating has been generated, the signal pulse polarized along the fast axis (y-axis) enters the grating position. The optical frequency of the signal pulse, v_s, is tuned to the reflection resonance of the dynamic grating. Due to the high birefringence of the PM fiber, the signal frequency is shifted from that of the pump 1 frequency (Figure 30 (c)).

The reflected signal is detected at the beginning of the fiber. By modifying the delay of one of the pump pulses, position of the grating inside the fiber can be changed, as shown in Figure 30 (b). When the position of the grating is further from the beginning of the fiber, the signal pulse takes longer time to reach the reflector. As a result the reflected pulse arrives at the detector at a later time, resulting in a relative delay. In this scheme the optical delay line is very similar to a mechanical delay line, where time-of-flight simply determines the arrival of the reflection at the detector. While in mechanical systems delay is changed by power-driven stage, in DBG based delay line the position of the reflector is changed optically. Here the relative delay is equal to change of the round-trip time.
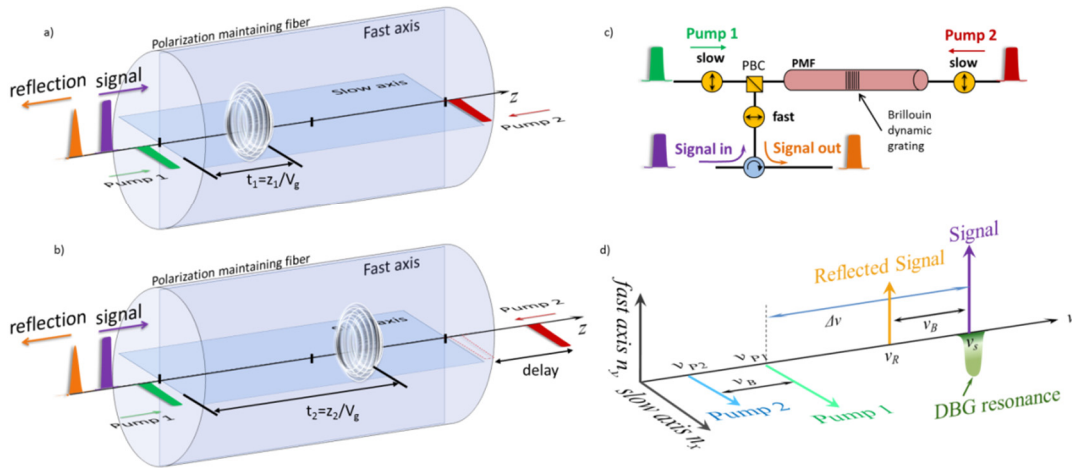
Figure 30. a), b) Principle to obtain the delay of the reflected signal. c) Schematic diagram of the experimental setup to realize DBG based optical delay line. d) Optical frequencies and polarization states of the interacting waves.

4.1.2   **Single pulse delays**.

Figure 31 shows the experimental setup, which was built to realize the DBG based optical delay line. Light from a distributed feedback laser diode 1 (DFB-LD1) operating at 1551 nm was split using a 3 dB coupler as shown in Figure 31. The upper branch was pulse modulated using an electro-optic modulator (EOM 1) driven by the first channel of pulse generator 1. Produced pump 1 pulses were amplified using high gain Er-doped fiber amplifier (EDFA) and launched into the polarization maintaining fiber along the x-axis. The lower branch from the DFB-LD 1 was RF modulated using another EOM 2 at frequency corresponding to Brillouin frequency of the fiber under test. DC bias applied to the EOM 2 was adjusted to suppress the optical carrier. The modulated wave was sent through a fiber Bragg grating (FBG) where the upper sideband was carefully filtered and used as a Pump 2 carrier wave. Using another electro-optic modulator (EOM 3) and second channel of pulse generator 1 Pump 2 pulses were prepared. After amplification with high gain EDFA, pump 2 pulses were launched into the polarization maintaining fiber through a polarization beam combiner (PBC) in direction opposite to Pump 1 pulses. It should be pointed out that the delay between two channels of the pulse generator 1 can be precisely controlled. In our case minimum step to delay the emission time of one of the pulses was 10 ps. By delaying the pump 1 pulses any position of the DBG inside the fiber under test can be achieved.

A distinct laser diode (DFB-LD2) operating at 1551 nm was exploited as a light source to prepare a signal. A pulse generator and an electro-optic modulator (EOM 4) were used to prepare the signal pulses. Afterwards, the signal pulses were amplified using EDFA 3, polarized along y-axis and launched into the PM fiber copropogating with pump 2 pulses. The reflected pulses from the DBG were redirected into the detection part using a circulator. Before detection they were pre-amplified using additional EDFA and spectrally separated from residual Pump 1 using a FBG. Leakage of the pump 1 pulses in the detection part is due to the finite extinction ratio of the polarization component used in our setup. Using PM components with high extinction ratio the FBG can be removed at the detection part thus simplifying the setup.
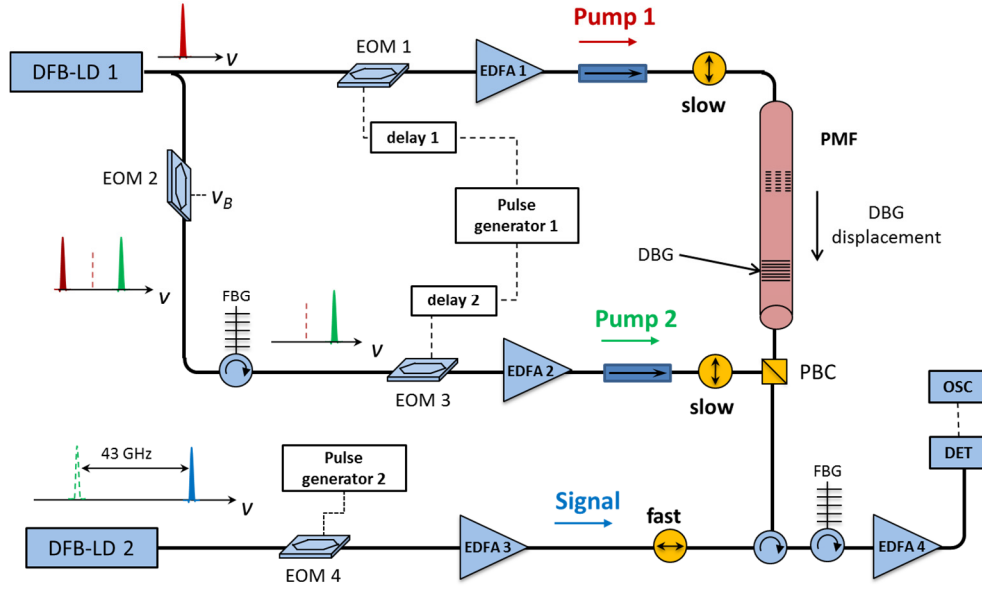
Figure 31. Experimental setup for DBG based optical delay line

120 m of Panda-type polarization maintaining fiber was used as a medium where the dynamic Brillouin grating was generated. Firstly, Brillouin shifts along the two primary axes of the PMF where measured at the pump 2 wavelength. The difference in Brillouin shifts of the fiber for slow and fast axes was measured to be ~3 MHz, which determines the birefringence of the fiber of $\sim 3.9 \times 10^{-4}$. Spectral position of the dynamic grating resonance above *x*-polarized pump wave was calculated to be ≈43 GHz according to the expression (3.10). Tuning the temperature on the laser controller module, the optical frequency of the DFB-LD 2 was set 43 GHz above the frequency of the pump 2 pulses for maximum DBG reflectivity. In order to generate only one grating in 120 m-long PM fiber the repetition rates of the pump pulses were adjusted to 2 µsec.

Peak power of the pump 1 pulses with full width at half maximum (FWHM) of 1 ns was around 30 W, while 1 ns FWHM pump 2 pulses had peak power of 300 mW. As a signal we used 650 ps pulses with repetition rate of 2 µs. Moreover pump 2 pulses were synchronized with the signal pulse in such way that a pump 2 pulse entered the PM fiber 1 ns before the signal pulse. This way we ensure that the dynamic Brillouin grating was generated just before reflecting the signal pulse, resulting in a maximum reflectance. Reflected pulses were recorded using a 12 GHz detector and oscilloscope while changing the time delay for pump 1 pulses from 0 to 1.2 µsec. By adjusting the delay of pump 1 pulse for 10 ns actually changes the position of the DBG for 5 ns or equivalently for 1 m due to the counter-propagation of pump pulses. 120 m of PM fiber gives us maximum delay of 1.2 µsec for the reflected pulse which is given by the round trip propagation through the fiber. Figure 32 (a) shows selected waveform of the reflected signal pulse where the first 7 waveforms are acquired while the grating position is shifted in 100 ps step, showing the precision of our delay line. Maximum delay achieved was 1.15 µsec showing fractional delay of 1769 bits, which by far exceeds delays offered by slow light based delay lines.

Figure 32 (b) shows initial signal pulse (FWHM 650 ps) together with one of the reflected pulses (FWHM 1 ns). Temporal broadening was measured to be 60%, which is

simply governed by the length of the dynamic grating. Temporal shape of the reflection is given by the convolution between the intensity profile of the signal pulse and the impulse response of the dynamic Brillouin grating. In the frequency domain this will result in a multiplication of the signal spectrum with the grating spectrum. Thus, to preserve signal fidelity and avoid distortion due to the filtering effect, bandwidth of the grating should be adjusted accordingly to encompass as much as possible of the signal bandwidth. Brillouin grating is a weak grating, since SBS induced refractive index perturbation is very weak [24]. In this case the bandwidth of the DBG is inversely proportional to its length. Grating shape and length in our experiment is given by the shape and width of the pump pulses. Shorter pump pulses would generate shorter grating with broader bandwidth. On the other hand grating reflectivity depends on the length of the grating. Thus shorter grating will result in lower reflection. Moreover it should be pointed out that it is difficult to decrease width of pump pulses to several tens of ps due to the fact that nonlinear effects such as self-phase modulation seriously modify pump pulse spectrum since relatively high powers are used. Moreover signal distortion may also depend on DBG position inside the fiber due to the birefringence non-uniformity. Thus PM fibers with low birefringence fluctuations are preferable.

Figure 32 (c) shows the delay of the signal as a function of the position of the DBG inside the PM fiber, where we see that by changing the grating by 20 m results in a signal delay equal to a round trip time, or equivalently to 200 ns.
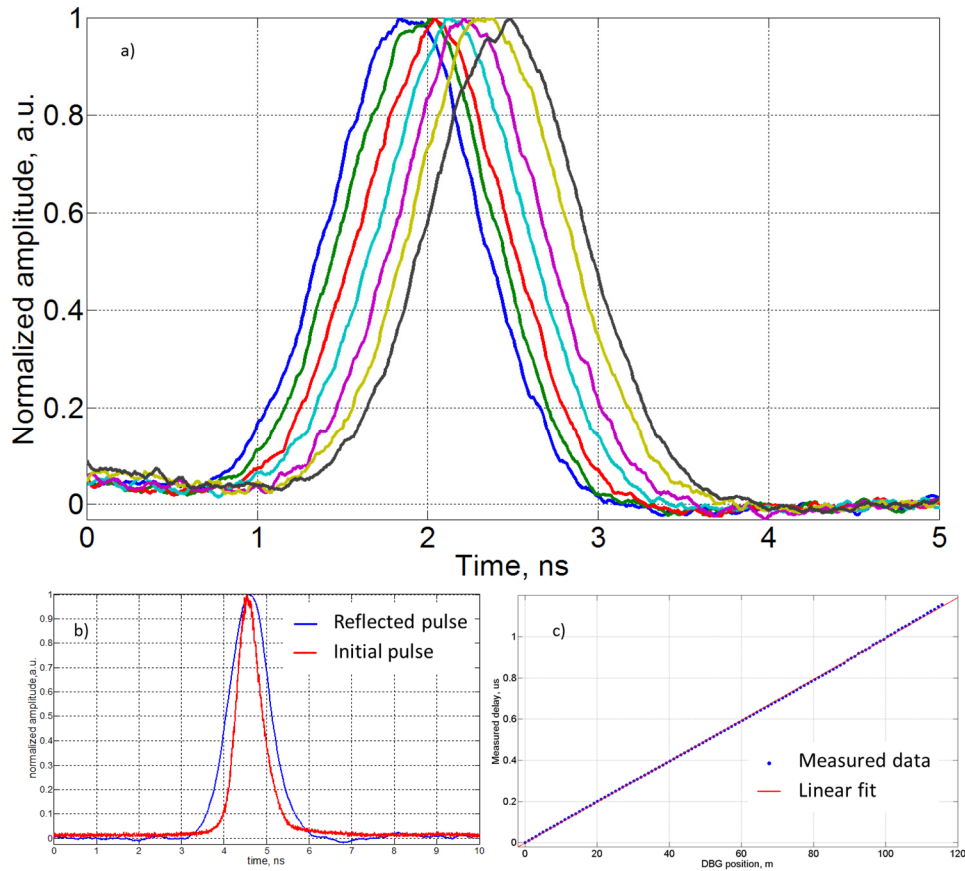

Figure 32. a) Time traces of the reflected pulse for different position of the DBG. b) Experimentally obtained traces of initial pulse and reflected pulse. c) measured signal delay as a function of DBG position inside the PM fiber.

It should be pointed out that broadening is independent of delay, which is an important feature of the proposed delay line. However due to the limited phonon lifetime, dynamic grating starts to decay when two pump pulses pass each other. In standard fibers phonon lifetime is around 4-6 ns, which is mainly determined by physical properties of the fiber, such as doping concentration, density and viscosity. For instance, Figure 33 (a) shows attenuation of the dynamic Brillouin grating amplitude, which was generated by the 500 ps pump pulses and probed with a CW signal. This graph shows that signal can be reflected only within several ns while the acoustic wave is present in the fiber. Thus such delay line is suitable for delaying isolated pulse or packets of limited length (up to 20-25 ns). Alternative media with longer phonon lifetime can be used to delay signal packets with longer length. Other types of fibers show slightly longer phonon lifetime than standard silica fibers, but the increment is minor and will not improve drastically the performance of the delay line. In order to keep acoustic wave oscillating at a given position inside the fiber it should be periodically regenerated by optical pump pulses with repetition rate faster than the complete grating vanishing, as shown in Figure 33 (b). It is obvious that amplitude of the acoustic grating will be fluctuating with repetition rate of the pump pulses. This results in amplitude fluctuation of the reflected signal.
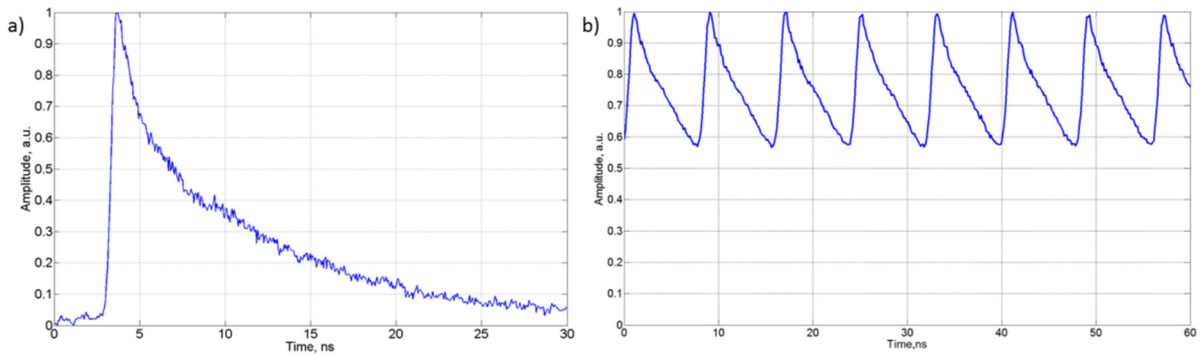
Figure 33. a) Acoustic wave decay generated using 500 ps pump pulses. b) Regeneration of DBG using pump pulses with 8 ns repetition rate

4.1.3 Continuous data stream delays.

The setup presented in the previous section 4.1.2. can offer high fractional delay for the single data pulse or for short packets. Length of the packet is limited by the acoustic decay lifetime. Here we present a modified scheme to obtain delays for continuous data streams. Obviously in order to maintain DBG grating at a given position inside the fiber it should be regenerated with periodicity faster than acoustic decay time. As it is seen in Figure 33 (b) acoustic grating can be regenerated by a train of pump pulses with repetition rate faster than DBG complete decay. As can be seen in the Figure 33 (a) the acoustic wave completely decays after ~25-27 ns. Thus by sending pump pulses with repetition rate of around 10 ns, grating can be regenerated before it completely vanishes. Obviously the faster the repetition rate of the pump pulses the less fluctuations would be in DBG amplitude. On the other hand with higher repetition rate of pump pulses the distance between two adjacent gratings

becomes shorter, limiting the maximum delay. Thus, if the grating is regenerated every 10 ns, two adjacent grating are separated by 5 ns or equivalently 1 m, limiting the maximum delay to 10 ns.

In order to realize the delay line for the continuous data stream, the length of the PM fiber was changed to 62 cm. Pump pulses had Gaussian like shape with FWHM of 250 ps and repetition rate of 8 ns. Two adjacent points where pump pulses meet are separated by 4 ns or equivalently by 0.8 m. This way we secure that only one grating is all the time present inside the 62 cm fiber under test, and it is periodically regenerated each 8 ns. Signal pulse train consisted of 400 ps pulses with 9 ns repetition rate. It should be pointed out that for the delay of data stream it is not needed to synchronize signal pulse and pump pulses, since dynamic grating is constantly present in the fiber. Figure 34 (a) shows selected reflected waveforms at different DBG positions in the PM fiber. Maximum delay was 6 ns showing delay-bandwidth product of 15. Moreover signal distortion is negligible and independent of the delay as one can see on the Figure 34 (a). Figure 34 (b) shows initial and reflected pulses where it is clear that reflected pulses have negligible broadening. Due to the low reflectivity of short DBG reflected pulse needs to be amplified with EDFA.
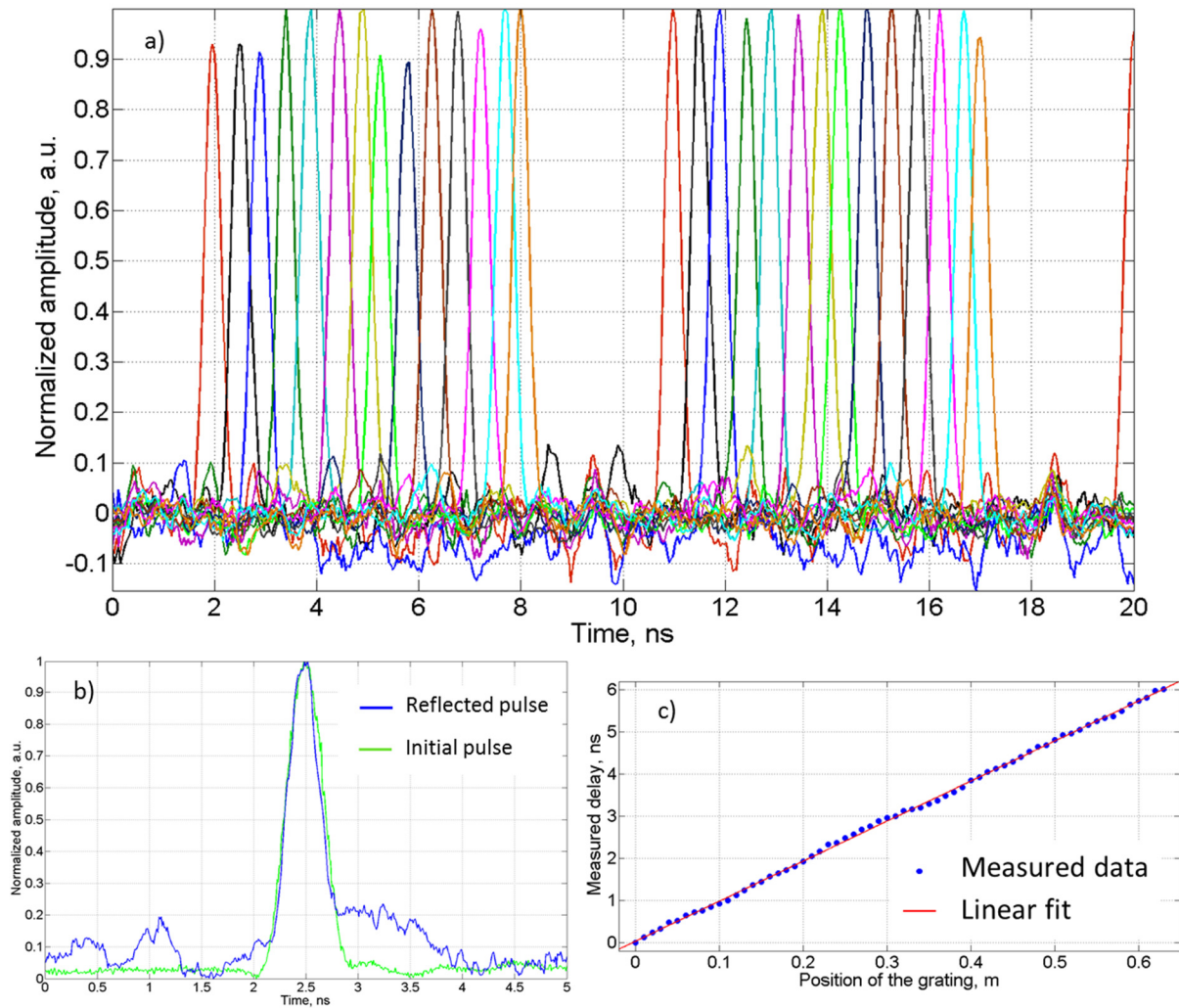

Figure 34. a) Time traces of the reflected pulse train (9 ns repetition rate) for different positions of the single DBG . b) Experimentally obtained traces of initial pulse and reflected pulse. c) Measured delay of the optical data stream versus dynamic grating position inside the fiber.

This degrades the signal to noise ratio of the reflected signal as can be seen in Figure 34 (b). Figure 34 (c) shows calculated reflected pulse together with signal pulse of FWHM 400 ps used for simulations. As we mentioned earlier, the operational bandwidth of the delay line can be easily controlled by the length of the dynamic grating. Nevertheless, there is a practical limitation on the operational bandwidth, since DBG reflectivity drops dramatically with reducing grating length. It will be shown later in the chapter that reflectivity of the DBG scales quadratically with the grating length in a similar way as for fiber Bragg gratings.

4.2. Microwave signal true time delay

In the field of microwave photonics true time delays are very important for the implementation of photonic filters or elements to feed phase array antennas. True time delay can be represented as linear phase change of the microwave signal with RF frequency, where the slope of the phase change as a function of RF frequency determines implemented time delay. True time delays can be implemented using slow light effects in various media, where the carrier and a sideband of the RF signal should be placed in the single gain (or loss) resonance [25, 26]. By controlling the induced resonance characteristics, such as bandwidth and amplitude, modification of the refractive index can be accomplished, which in turn translates into phase changes of the detected RF signal. Using the dynamic Brillouin grating resonance it is possible to reflect the RF signal if it fits inside the DBG resonance. By changing the position of the DBG inside the fiber we can obtain the true time delay for RF signal. Here true time delay is achieved not by changing the DBG resonance characteristics but simply by changing the time of flight of the optical wave carrying the RF signal. Experimental setup used to delay RF signal is very similar to the setup used to delay continuous data. Pump pulses of 600 ps width were used to generate the DBG inside the 40-cm long PM fiber. Emission from the DFB-LD 2 was modulated using EOM 4, which was driven by the 400 MHz RF sine wave coming from the electric signal generator. Bias of the EOM 4 was adjusted in order to suppress the carrier, resulting in a 800 MHz microwave photonic signal. This signal was launched in the PM fiber along the fast axis, and reflected signal was recorded using a 1 GHz detector and oscilloscope. Experimental setup is represented in Figure 35. Experimental setup to obtain true time delay for microwave signal using single dynamic Brillouin grating.Figure 36 (a) shows several acquired waveforms of the 800 MHz signal where delay of 100 ps was applied to the pump 1 pulse. 100 ps change in emission time of the pump pulse 1 results in a shift the dynamic Brillouin grating of only 1 cm.

Figure 36 (b) shows the phase shift of the RF signal versus position of the dynamic grating. It is clear that 2π phase shift can be easily achieved by changing the grating position for the distance corresponding to the half of the period of RF signal, namely 13 cm. Measured data deviates from the expected linear phase shift dependence as a function of grating position, due to the instrumental limitation. Setting 100 ps change in the emission of the pump1 pulse did not exactly results in 100 ps pump 1 delay, but this can be calibrated by

using external electronic delay line. Moreover fiber birefringence nonuniformity results in a signal distortion which affects the measured RF delay.
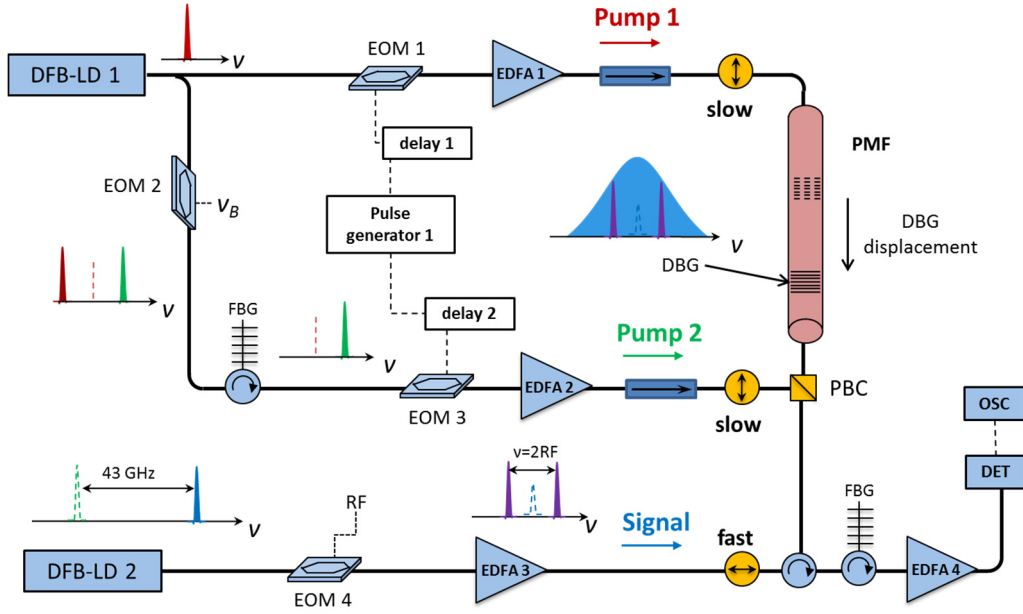
Figure 35. Experimental setup to obtain true time delay for microwave signal using single dynamic Brillouin grating.
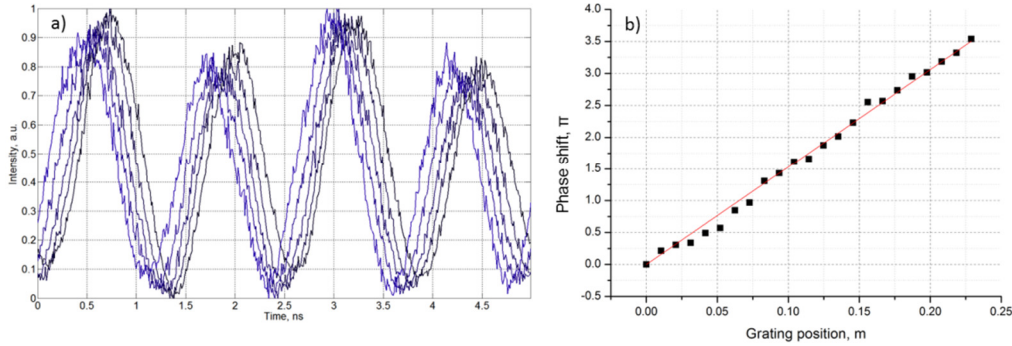
Figure 36. a) Experimental setup to obtain true time delay for microwave signal using single dynamic Brillouin grating. b) Obtained waveforms of 800 MHz signal. c) Obtained phase shift as a function of DBG position inside the fiber.

This way true time delay for the microwave photonic signals can be realized. However, such delay line has a limitation on the operational bandwidth of RF signal, which is given by the width of the DBG resonance.

In order to investigate the width of the DBG induced resonance several experiments were performed. Continuous wave pumps were launched in the fiber under test generating dynamic Brillouin grating all along the PM fiber. As a signal we used a continuous wave operation of the DFB-LD 2. Ramp current modulation was applied to the laser diode controller of the signal laser in order to sweep the emission frequency. By measuring the reflected power of the CW signal it was possible to measure the reflection bandwidth of the DBG resonance. 0.25, 0.42, 0.8, and 1 m long fibers were investigated. Figure 37 shows the

obtained spectra for different fiber lengths. It is clear that with reducing the length of the DBG its bandwidth is increased, in a similar way as bandwidth dependence of weak uniform fiber Bragg grating as a function of length. This way it is clear that bandwidth of the DBG is simply governed by its length. Figure 38 represents fitting of the experimental data using power function $FWHM\,(GHz) = \dfrac{a}{DBG\ length}$ with extrapolation up to the DBG length of 10 m. The fitting parameter a is found to be 0.0935. In order to compare the bandwidth of DBG with bandwidth of the weak uniform FBG it is necessary to estimate the refractive index change induced by the electrostriction effect. Refractive index change associated with induced acoustic wave amplitude can be represented as [24, 27]:

$$\Delta n = \frac{\gamma_e \Delta \rho}{2 n_0 \rho_0} \qquad (3.81)$$

where induced refractive index change is proportional to the amplitude of the acoustic wave. Using (2.93) equation (3.81) can be represented as:

$$\Delta n = \frac{\gamma_e^2 \, 2\pi \tau_p n_{eff} \sqrt{P_1 P_2}}{n_0 \rho_0 v_B \lambda_p^2 c_0 A_{eff}}, \qquad (3.82)$$

where $\gamma_e, \tau_p,\ P_1, P_2,\ n_0, \rho_0, v_B,\ \lambda_p, A_{eff}$ are electrostictive constant, phonon lifetime, pump 1 power, pump 2 power, refractive index of the silica, density of the silica, Brillouin frequency of the fiber, wavelength of the pump 1, and the effective area, respectively. To estimate refractive index change, the following parameters were used: pump 1 power 100 mW, pump 2 power 50 mW, phonon lifetime 10 ns, effective area 80 μm^2, pump wavelength 1551 nm, electrostictive constant 0.902 [28], density of the silica fiber 2210 kg/m^3, Brillouin frequency 10.8 GHz. Equation (3.82) gives change in the refractive index of $\sim 2 \times 10^{-9}$, which shows that DBG can be regarded as a weak FBG, since $\Delta n \ll \dfrac{\lambda_p}{DBG\ length}$. Normally bandwidth of the FBG is measured between the two first zeros around the main reflection peak. Bandwidth for weak FBG can be estimated using expression $\Delta\lambda \approx \dfrac{\lambda_D^2}{n_{eff} L}$, where λ_D is design wavelength, n_{eff} is effective refractive index and L is the grating length. For weak gratings such bandwidth can be noticeably broader than that at half maximum. For this reason we simulated the reflection spectra of the uniform weak FBG as a function of grating length, where we used induced refractive index change of 2×10^{-9}. Afterwards we measured the spectral width of the simulated FBG spectrum at half maximum of the main reflection peak. For comparison full width at half maximum of the weak uniform FBG as a function of FBG length is plotted in Figure 38 as well. By fitting the calculated FBG FWHM with the same power function we find that parameter a is equal to 0.08986, which is very close to the parameter a used for DBG fitting.
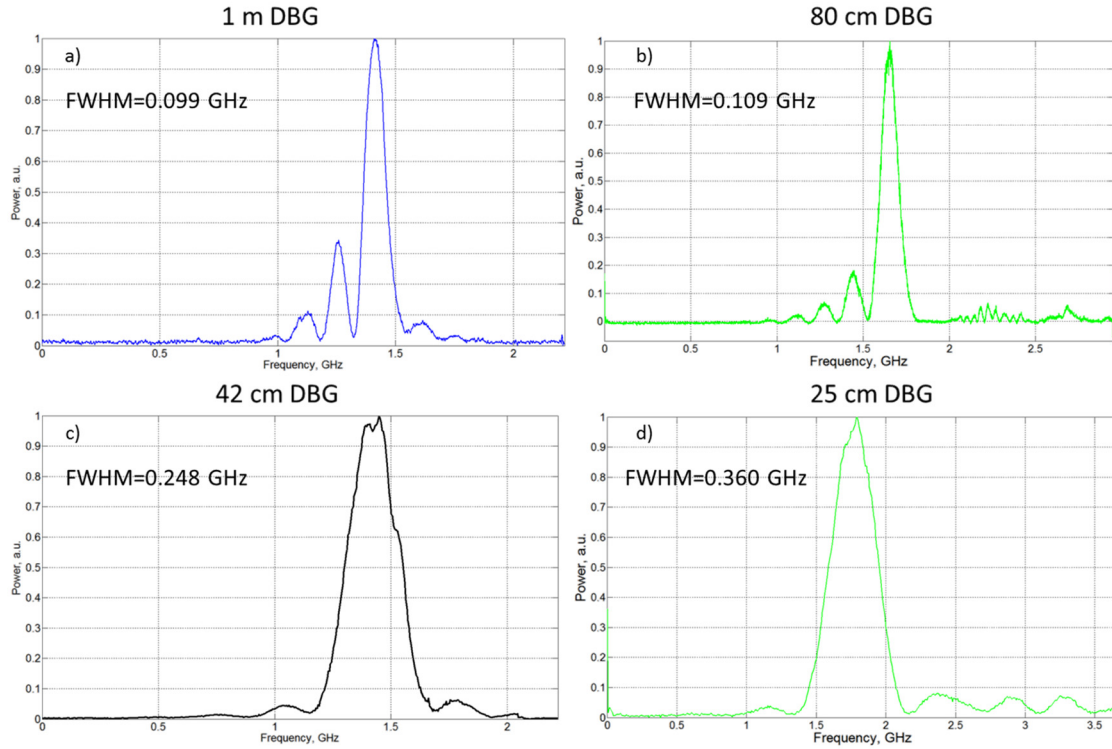
Figure 37. Measured spectrum of DBG with different length: a) 1 m, b) 80 cm, c) 42 cm, d) 25 cm.

It is seen that fitted curve for bandwidth of the DBG agrees well with the curve for the bandwidth of weak uniform FBG, proving that induced dynamic Brillouin grating can be considered as weak FBG. It should be noted that when the grating length is increased, the spectrum of the grating becomes more asymmetric, showing different amplitudes of side lobes. This can be caused by the birefringence nonuniformity along the fiber. Such irregularity of the birefringence can actually result in an apodization of the induced refractive index change, which in turn affects the spectrum of the dynamic Brillouin grating.
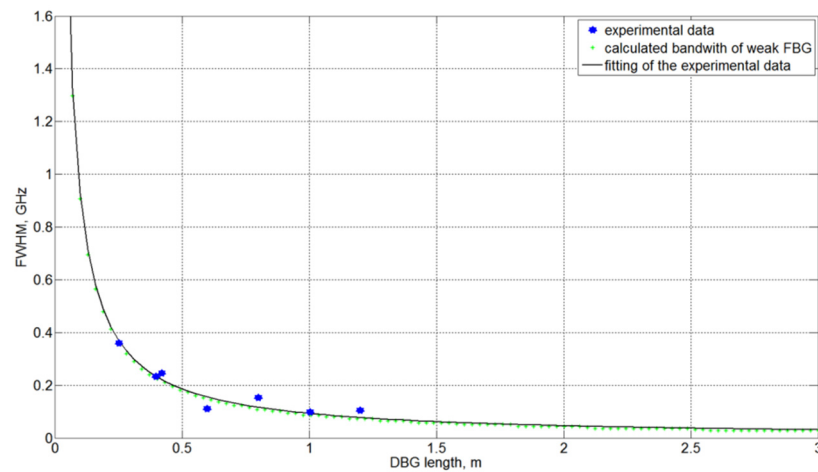
Figure 38. Full width at half maximum of DBG and FBG as a function of length.

4.3. Generation of localized DBG using pseudo random bit sequence phase modulation of pump waves.

In section 4.1.1 we demonstrated that dynamic Brillouin grating can be locally generated using pump pulses. However, once the interaction between pump pulses is over the DBG starts to decay. To keep DBG oscillating at a given position it is possible to refresh the grating using sequences of pump pulses with repetition rate faster than the acoustic wave decay time. Although this technique was shown to be efficient in sustaining DBG at a given position, it limits the maximum signal delay due to generation of adjacent gratings at each position where pump pulses intersect each other. Moreover we saw that fluctuations in acoustic grating amplitude results in fluctuations of the reflected signal amplitude, which adds additional signal distortion.

In order to localize the DBG inside the fiber and make it stationary, phase modulation of CW pump waves using pseudo random bit sequence (PRBS) was proposed [8, 29-31]. Actually localization of SBS interaction was an interesting topic for the past several years in different areas of SBS application. For instance, in the field of distributed optical sensing Brillouin optical correlation domain technique was proposed [32]. In this technique frequencies of two optical waves detuned by the Brillouin frequency shift of the fiber are synchronously modulated by a common sine wave. Due to the sine modulation, the frequency difference between the two counter-propagating waves remains stationary at a particular fiber locations only, known as correlation peaks, whereas the frequency difference elsewhere is oscillating. Consequently, effective SBS amplification is restricted to the correlation peaks. The distance between adjacent correlation peaks as well as the width of individual peak are interrelated. Thus when simple sine wave frequency modulation is used the longer correlation peak separation results in broader correlation peak and vice versa. This interrelation limits the application of BOCD technique in distributed sensing in particular. Another approach was proposed recently [33], where localization of the DBG can be achieved by phase modulating the pump waves with EOM driven by the chaotic signal, such as emission of chaotic laser. Up to now this technique was only demonstrated to work with numerical simulation and no experimental demonstration is reported.

In the following section a novel technique is proposed for the generation of dynamic Brillouin gratings that are both localized and stationary. The method relies on the phase modulation of the two pump waves by a common pseudorandom bit sequence (PRBS), with a symbol duration T that is much shorter than phonon lifetime of the fiber. The method allows for an effective SBS interaction in discrete, cm-scale correlation peaks only. The separation between neighboring correlation peaks is governed by the length of the PRBS, and it is uncorrelated with the length of the localized gratings. We experimentally demonstrate the generation of cm-scale, stationary and localized dynamic gratings over PM fibers of up to 100 m in length. The gratings are applied to the variable delay of periodic, 1 ns-long pulses by up to 770 ns. In addition, the combined reflections from a pair of dynamic gratings are used to implement a two-tap, radio-frequency (RF) photonic filter with a variable free spectral range (FSR). These results illustrate the potential impact of the proposed technique on various

applications of dynamic gratings. The method is equally applicable to the generation of a localized SBS interaction over standard fibers.

4.3.1   Principle of operation

In order to describe the principle of DBG localization using PRBS phase pump modulation let us denote the optical fields of the two pump waves of an SBS dynamic grating as $E_1(t,z)$ and $E_2(t,z)$, respectively, where t stands for time and z represents position along a PM fiber of length L. Pump 1 enters the fiber at $z = 0$ and propagates along the positive z direction, whereas pump 2 propagates from $z = L$ in the negative z direction. The optical frequencies of the two pump waves are separated by the Brillouin frequency of the fiber $\Omega_B = 2\pi v_B$. The complex envelopes of the two waves are denoted by $A_1(t,z)$ and $A_2(t,z)$, so that:

$$E_1(z,t) = A_1(z,t)\exp(i\omega_1 t) + c.c. \tag{3.83}$$

$$E_2(z,t) = A_2(z,t)\exp(i(\omega_1 - \Omega_B)t) + c.c. \tag{3.84}$$

In our proposed scheme for generating stationary and localized gratings, the phases of both pump waves are modulated by a common PRBS with symbol duration T:

$$A_1(t, z=0) = A_2(t, z=L) = A(t) = A_0 \left[\sum_n rect\left[(t - nT)/T\right]\exp(j\varphi_n) \right] \tag{3.85}$$

In Eq.(3.85), φ_n is a random phase variable which equals either 0 or π, rect (ξ) equals 1 for ξ < 0.5 and zero elsewhere, and A_0 denotes the constant magnitude of both pump waves. In the following, we consider both pumps to be of the same power, for simplicity. The analysis is equally valid for pumps having different power levels. The modulation is synchronized so that the phases of the two pumps, at their respective entry points into the fiber, are equal for all t. Both pumps are polarized along the same principal axis of the PM fiber.

Consider next the magnitude of the acoustic density wave $\rho(t,z)$ of frequency Ω that is generated by the two pumps. Acoustic wave is considered as nonpropogating disturbance of the density of the medium. Then temporal evolution of the density wave amplitude can be written as before in equation (2.92):

$$\frac{\partial \rho(t,z)}{\partial t} + j\frac{\Omega_B^2(z) - \Omega^2 - j\Omega/\tau_p}{2\Omega}\rho(t,z) = jg_1 A_1(t,z) A_2^*(t,z) \tag{3.86}$$

where g_1 is elastooptic constant and Ω is the frequency detuning between the pump waves. If exact Brillouin condition is met between the two pump waves and pump depletion is neglected solution of the equation (3.86) can be represented as:

$$\rho(t,z) = jg_1 \int_0^t \exp\left(-\frac{(t-t')}{2\tau_p}\right) A\left(t'-\frac{z}{V_g}\right) A^*\left(t'-\frac{L-z}{V_g}\right) dt'$$

(3.87)

When $t \gg \tau_p$, the acoustic wave amplitude becomes proportional to the product $A\left(t-z/V_g\right) A^*\left(t-(L-z)/V_g\right)$ weighed and summed by a moving exponential window of duration $1/2\tau_p$. When the pump waves are phase modulated using a form of modulation described by equation (3.85), we can distinguish two different sections of the fiber where $\rho(t,z)$ evolves differently with time. Within the short segment at the middle of the fiber $z = L/2$, $\rho(t,z) \sim A\left(t-z/V_g\right) A^*\left(t-(L-z)/V_g\right) = |A_0|^2$. The two pump waves are constantly correlated at this position, and thus driving force for the acoustic wave generation is stationary and of constant phase. Consequently, the acoustic wave in the vicinity of $z = L/2$ builds up to its steady state magnitude. The width of the correlation peak is on the order of $\Delta z = \frac{1}{2}V_g T$, which is determined by the bit length of the PRBS. In all other locations inside the fiber driving force randomly changes in sign due to the random change between 0 and π with each PRBS symbol $T \ll \tau_p$. Therefore with time $t \gg \tau_p$ the driving force averages to zero expectation value and the acoustic wave cannot build up. Thus by using PRBS phase modulation of the pump waves a dynamic Brillouin grating can be generated, which is localized and stationary. It should be taken into account that separation Z between the adjacent correlation peaks equals to $MV_g T/2$, where M is the length of the PRBS sequence. The correlation peaks, except the zero order, and thus position of the DBG can be moved along the fiber through changing code length M or the symbol duration T. In order to employ higher order correlation peak inside the fiber under test, a fixed delay line is inserted in one of the pump arm. Separation between the DBGs can be controlled by changing the M, while length of the DBG by changing T. These variables are completely decoupled as compared to the BOCD technique. Thus, it is possible to create localized and stationary DBG with arbitrary length within a long fiber under test.

Figure 39 shows the principle of DBG generation using PRBS modulated pumps and simulation results of the acoustic gratings magnitude, as a function of time and position, within a 1 m long fiber are shown in Figure 40. The gratings magnitude was calculated through direct integration of Eq. (3.87), subject to the PRBS modulation of the pumps phases as in Eq. (3.85) with T = 200 ps. The frequency shift Ω between the two modulated pumps was chosen to match Ω_B of the fiber. The simulation predicts the build-up of a localized and stationary grating in a narrow region at the center of the fiber, as suggested by the above considerations and depicted in Figure 40.
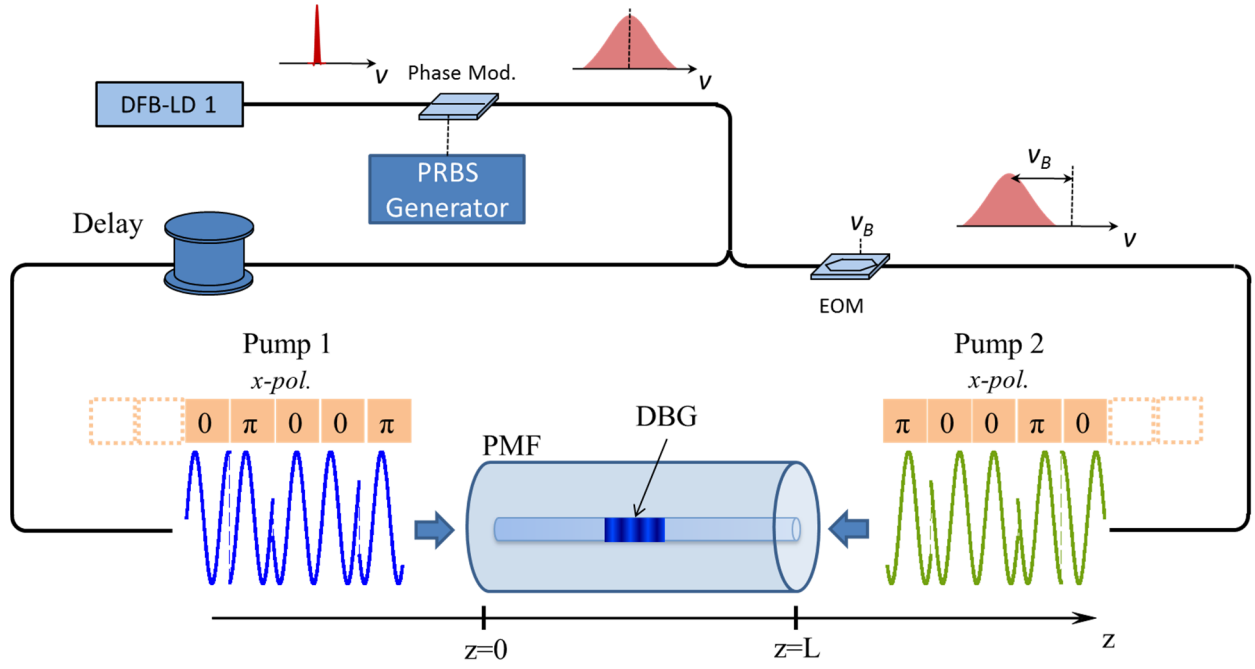
Figure 39. Schematic representation of localized and stationary grating generation using PRBS modulated pump waves.
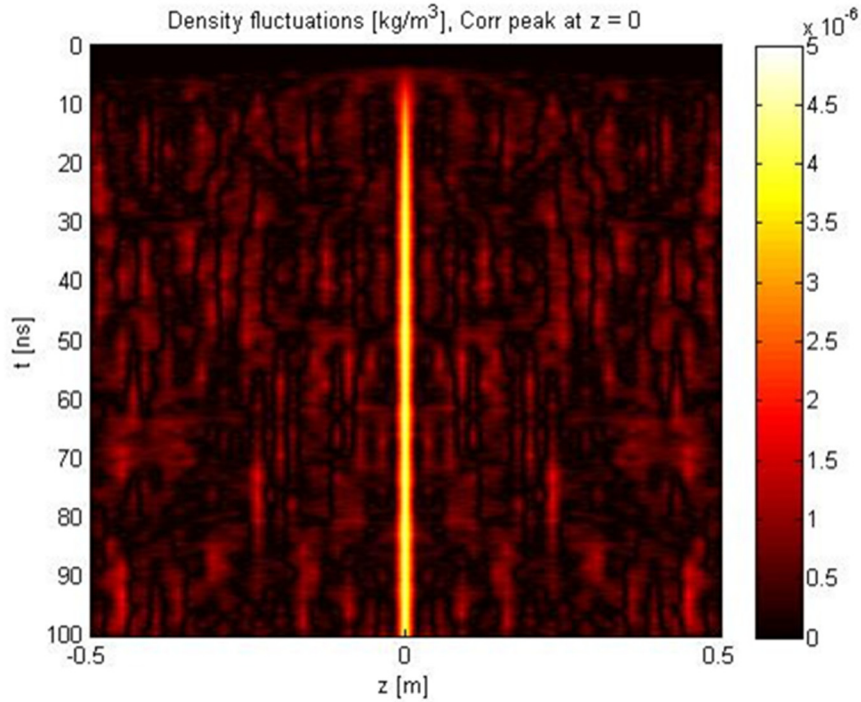
Figure 40. Simulated magnitude of the acoustic wave density fluctuations, as a function of position z and time t within a 1-m long fiber. The modulation symbol length T is 200 ps.

To demonstrate the localization of the dynamic Brillouin grating inside the 1 m long PM fiber isolated readout pulses of 260 ps were used. Figure 41 shows the reflected signal as a function of time. When CW pumps are used (PRBS generator is switched off), a distributed reflection along the DBG of readout pulses was observed (black curve). Duration of the

reflected signal is ~10 ns which correspond to the round trip propagation time along the 1 m DBG. The distributed reflection suggests that nearly uniform dynamic grating has been generated along the entire length of the fiber. On the other hand when the PRBS is turned on, localization of the DBG is clearly visible. PRBS bit lengths of 1 ns and 167 ps were used corresponding to the reflected waves in red and green in the Figure 41, respectively. The reflection from the shorter grating is weaker, as expected.
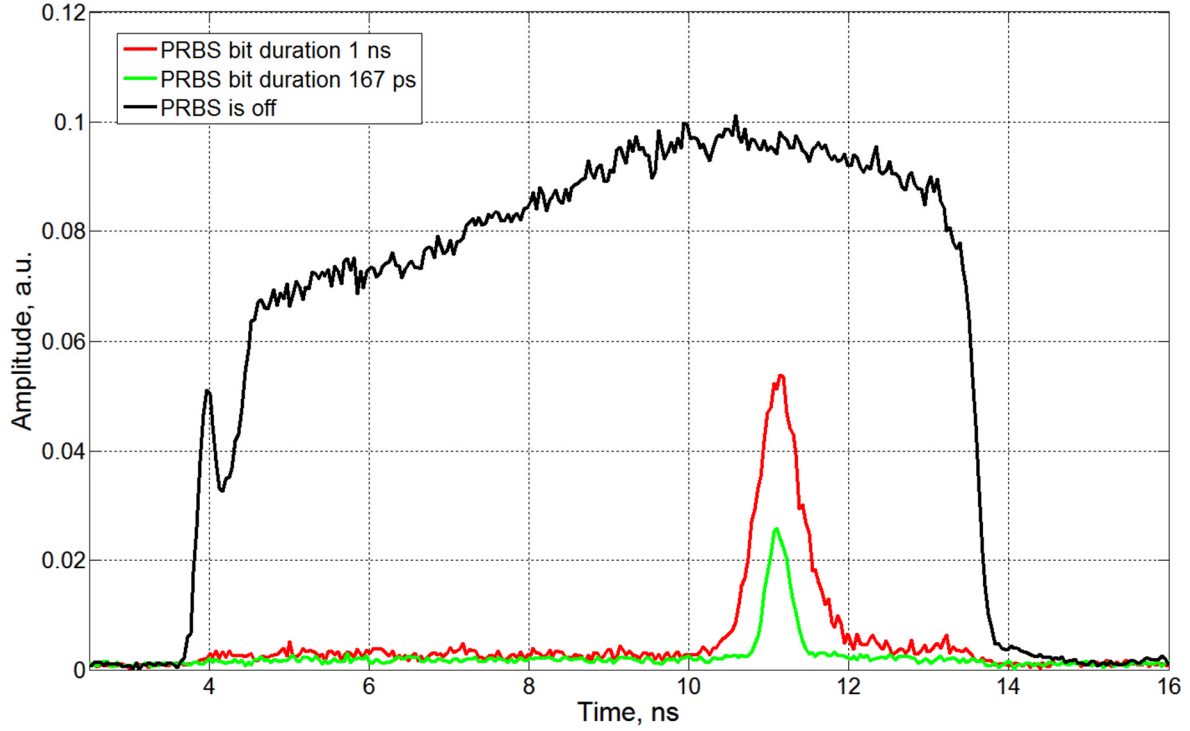
Figure 41. Reflection of the 260 ps isolated pulse from DBG when PRBS pump modulation is off (black); PRBS modulation is on with bit duration *T*=1ns (red), and *T*=167 ps (green), respectively.

4.3.2   Delay line

Localized and stationary dynamic Brillouin gratings using PRBS modulated pumps are applied to delay periodic, 0.5 ns-long pulses by up to 1 µs. To realize all optical delay line for pulses the setup shown in the Figure 42 was built. A single distributed feed-back (DFB) laser diode emitting at frequency ω_l was used to generate both pump waves. The output of the DFB was modulated by an electro-optic phase modulator (EOM), which was driven by a PRBS generator. The output peak-to-peak voltage of the PRBS generator was adjusted to match V_π of the EOM (~3.7 V). The bit rate of the PRBS generator was controlled by an external microwave generator. The modulated DFB light was split in two arms. Light in the upper arm was amplified by Er-doped fiber amplifier (EDFA) up to 200 mW, polarized by polarization beam combiner and launched in the PM fiber along the slow axis. Light in the other arm was intensity modulated by another EOM 2 with frequency Ω_B, where the bias of

the modulator was adjusted to suppress the carrier. By using a narrow FBG the upper sideband at frequency $\omega_2 = \omega_1 + \Omega_B$ was carefully filtered, amplified by another EDFA 2 to 200 mW and launched inside the PM fiber along the slow axis from the opposite direction as a pump 2. Light from a distinct DFB 2 was used to generate the signal wave. The optical frequency of the signal DFB was adjusted to match the DBG resonance along the fast axis using equation:

$$\omega_{sig} = \omega_2 + \Delta\omega = \omega_2 + \frac{\Delta n(\omega_x^{p2})}{n_y^g} \omega_x^{p2} \tag{3.88}$$

Light used as readout signal was pulse modulated using EOM 3 amplified by an EDFA 3 and redirected in the PM fiber along the fast axis. Reflection from the dynamic grating at frequency $\omega_{ref} = \omega_2 + \Delta\omega - \Omega_B$ was filtered by another FBG, boosted and detected using 6 GHz photodetector.
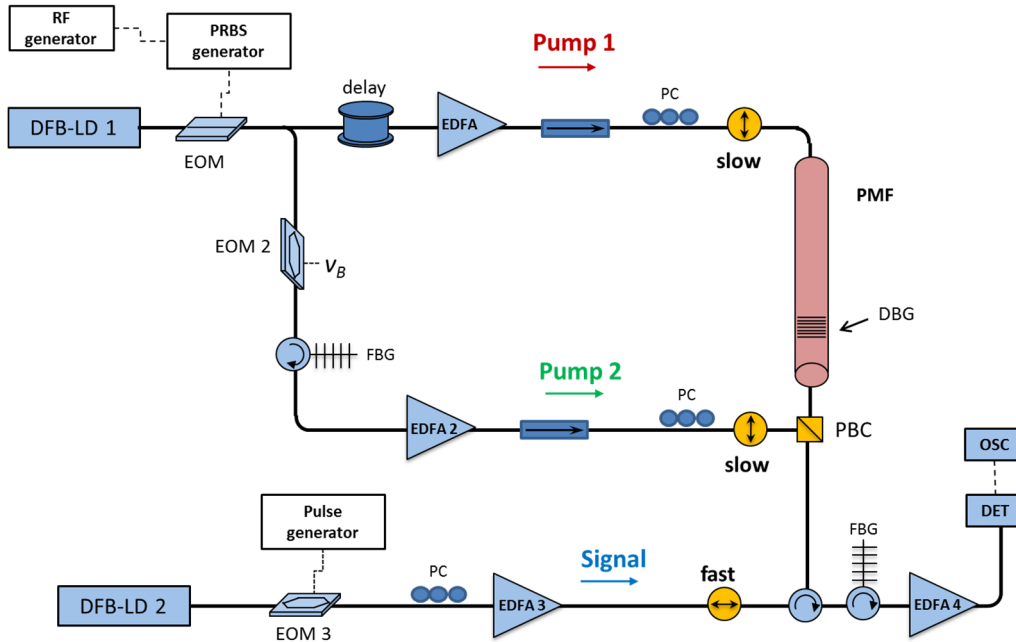
Figure 42. Experimental setup to realize all optical delay line using PRBS phase modulation of the pump waves.

To observe the delay for signal pulse, the position of the DBG was continuously changed from one end to the other end of the 100-m PM fiber through changing the bit duration of the PRBS generator. The Brillouin frequency of the fiber was measured to be 10.87 GHz, while fiber birefringence gives difference in frequencies between pump 2 and signal wave of $\Delta\omega = 2 \times \pi \times 57\,GHz$. A PRBS code word length was set to $M = 2^{10} - 1$ and a fixed delay imbalance was added to the path of pump 1 so that the 10th correlation peak was scanned along the fiber under test. Figure 43 shows seven selected time traces of the reflected pulses from the DBG at different grating positions, where the difference in arrival time between the black pulse and the blue pulse is 770 ns. A variable delay of 1 µs can be easily obtained which corresponds to the round trip time of 100 m fiber. The most right peak in Figure 43 corresponds to the parasitic reflection from connector, which was not filtered out.
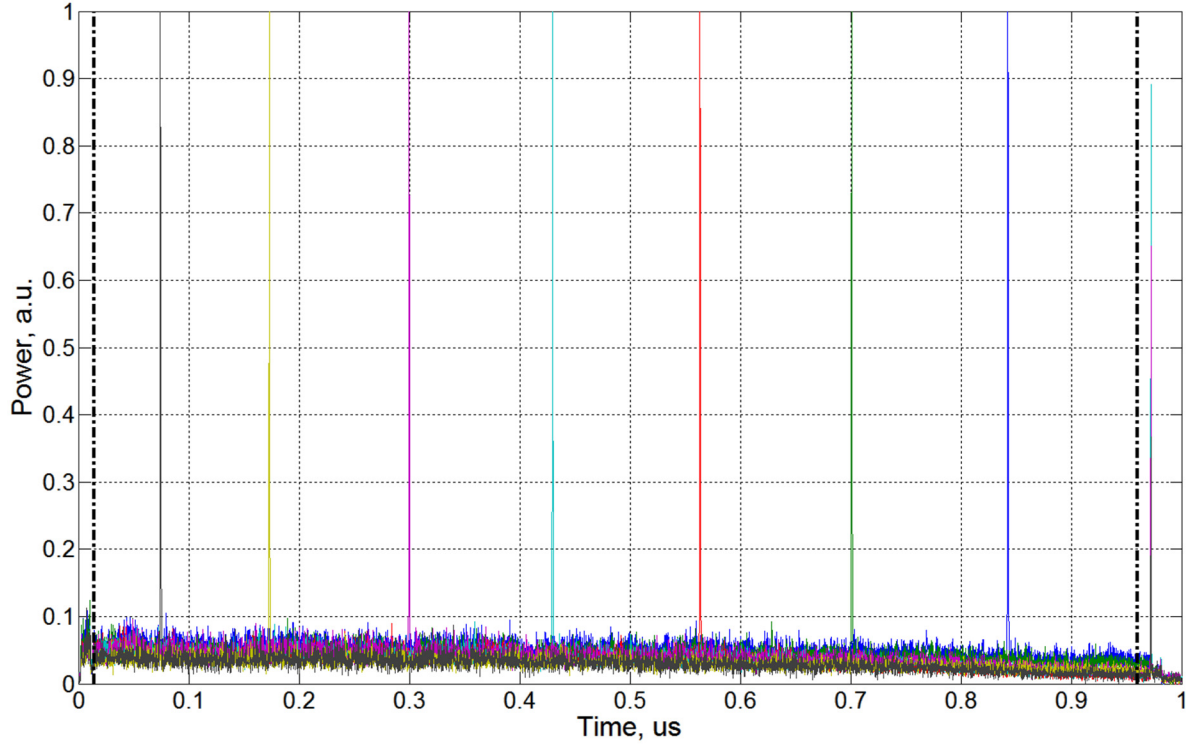
Figure 43. Detected pulse reflection from the DBG, localized at seven different positions along the fiber. Black dashed lines correspond to the beginning and the end of the fiber. The PRBS modulation clock rates *1/T* were (left to right): 1.12 GHz, 1.108 GHz, 1.093 GHz, 1.078 GHz, 1.063 GHz, 1.048 GHz, 1.033 GHz.

Initial and reflected pulses are represented in Figure 44 (a). It is clear that broadening is negligible in this case and as before it is governed by the length of the DBG. Slight distortion on the leading and trailing edges of the reflected pulse can be attributed to filtering effect of DBG. Figure 44 (b) demonstrates the fine tuning of the delay by sub-ns step. Delays (from left to right) in the Figure 44 (b) were obtained by changing the clock rate of the PRBS modulator with the increment of 100 kHz. It should be pointed out that position of the correlation peak can be controlled with extremely high accuracy. Accuracy depends on a precision of the microwave generator driving the PRBS as well as on a correlation peak number.
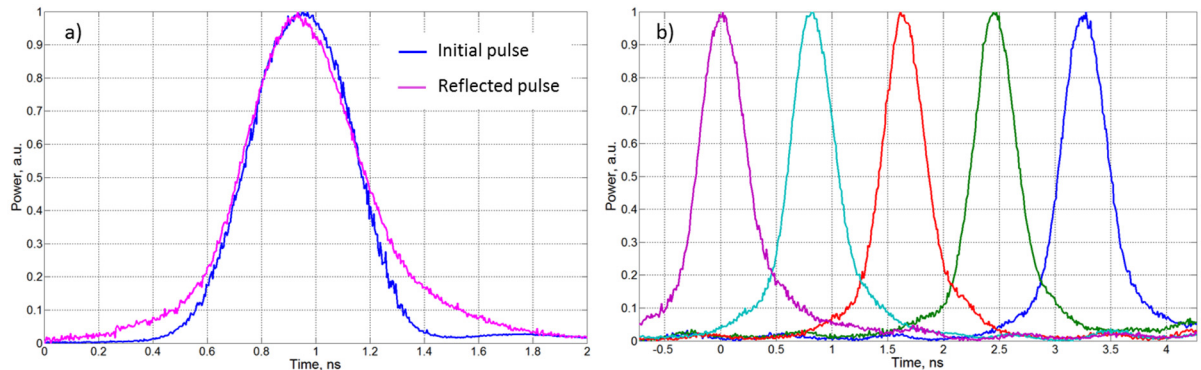
Figure 44. a) reflected (magenta curve) and initial pulse (blue curve). b) Selected waveforms of the reflected pulse demonstrating delays with sub-ns steps.

Bandwidth of the DBG gratings generated by the PRBS phase modulated pump waves was investigated using a Vector Network Analyzer (VNA). An EOM in the signal arm (see Figure 42) was driven by the output port of the VNA, and the detected reflection was analyzed using the input port of instrument. Figure 45 shows half of the bandwidth of the DBG generated by the phase modulated pumps, using PRBS with different clock rates. In Figure 45 the *x*-axis represents the offset frequency from ω_{sig}, which is at the center of the DBG resonance. It is clear that dynamic grating bandwidth becomes larger with increasing the PRBS clock rate (reducing the bit length), since the grating becomes shorter. Moreover the DBGs bandwidth is in the order of PRBS clock rate. This can be used to estimate the maximum bandwidth of the signal, which can be delayed without severe distortion. High reflection at the low frequency offset (<200 MHz) is due to the residual long grating, spanning over the entire PM fiber. Such residual grating can be removed if the driving voltage on the phase modulator match precisely V_{π}.
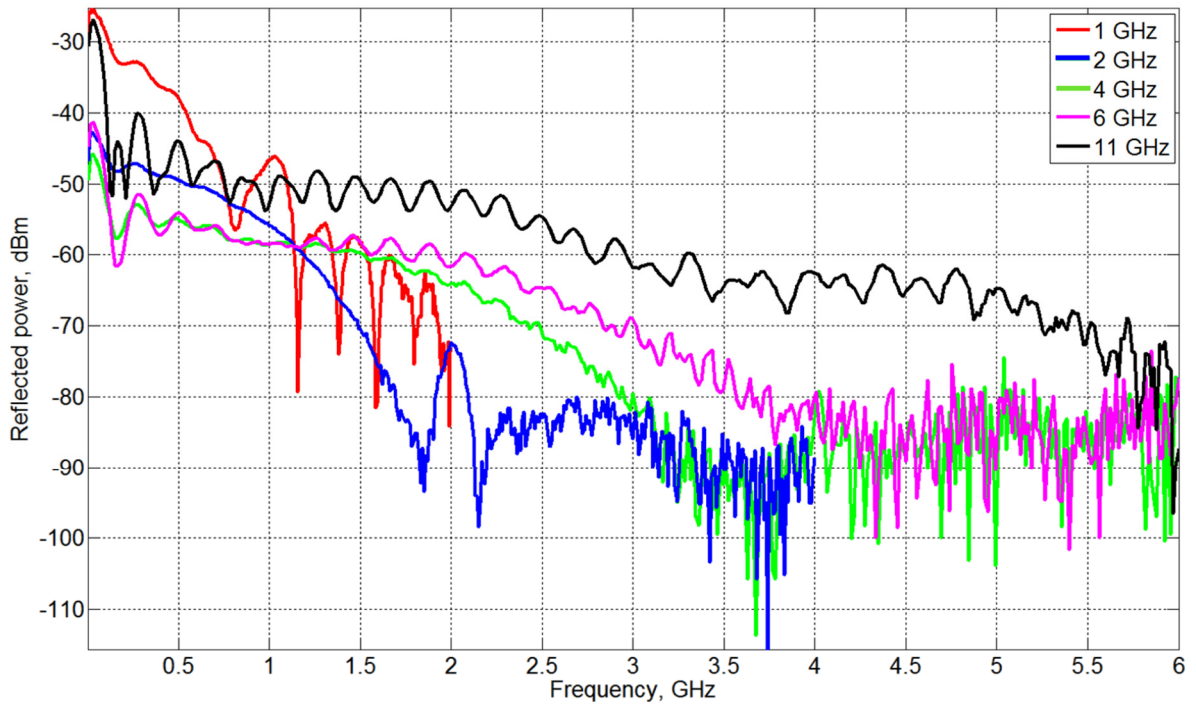
Figure 45. Measurements of the DBG reflection bandwidth using vector network analyzer. PRBS clock rates were: 1 GHz, 2 GHz, 4 GHz, 6 GHz, 11 GHz.

4.3.3   Data stream delay line using PRBS technique and noise issue.

It was experimentally demonstrated that stationary dynamic Brillouin grating can be generated by the PRBS phase modulated pumps waves at a given position inside the fiber. As it was shown, the dynamic grating is generated at the positions inside the fiber where the two pump waves are correlated. The driving force for the acoustic grating generation outside the correlation peaks is much weaker and fluctuates in sign every bit length. Moreover it is

instantaneously nonzero, as can be seen in both Eq. (3.87) and the simulation results of Figure 40. Reflections from residual gratings generate additional noise, which degrades the signal-to-noise ratio of the reflected signal. To see if the amount of noise is acceptable to realize optical delay line for data stream, PRBS intensity modulated signal was launched as a readout wave. In order to generate the data stream, EOM in the signal arm was driven by second PRBS generator (PRBS generator 2) as shown in Figure 46 (a). Clock rate of the PRBS generator 2 was set to 500 MHz resulting in readout signal represented in Figure 46 (b). Pump waves were phase modulated using PRBS generator 1, which was driven by the clock signal of 4 GHz from RF generator. In this case localized dynamic Brillouin grating has width of ~2.5 cm. Length of the fiber under test was 1 m. Figure 47 (a) represents eye diagram of the reflected signal. As it can be seen the noise coming from residual gratings degrades the SNR severely down to the level when eye diagram is completely closed. To observe if the degradation of the reflected signal mainly comes from the parasitic gratings outside the correlation peak local heating of the fiber was implemented. A 7 cm resistor was placed on the fiber where the correlation peak is present. When a short section of the fiber is heated, local birefringence is changed at this position, resulting in shifting the DBG resonance accordingly.
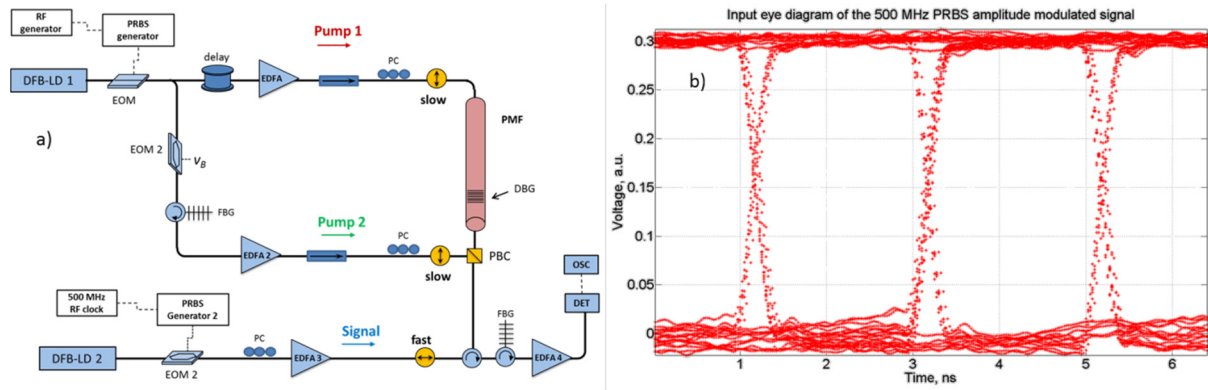
Figure 46. a) Experimental setup; b) eye diagram of the input readout signal

When the frequency of the signal laser is adjusted to match the resonance of the DBG of the heated section reflections from the rest of the fiber can be eliminated. Figure 47 (b) shows eye diagram of the reflected signal when the fiber with correlation peak is heated using a resistor. Eye diagram opens in this case, showing that the main degradation of the signal comes from residual grating outside the correlation peak. It should be pointed out that reflectivity of the DBG grating is very low due to the CW operation of pump waves and phase modulation. Measurements of the DBG reflectivity were performed when grating was generated using PRBS phase modulation of the pump waves. Relatively low pump powers were used to generate dynamic Brillouin grating: namely pump 1 power was set to 28 mW, while pump 2 was 0.245 mW. CW signal was had power of 56 mW. PRBS clock rate was changed from 408 MHz to 4260 MHz to change the length of the dynamic Brillouin grating. Figure 48 shows DBG reflectivity as a function of the length of the DBG, where length of the grating was estimated as $V_g / 2 f_{clock}$. It is clear that the reflectivity drops with the length of the grating. Of course grating reflectivity strongly depends on the pump powers and can reach -30 dB with pump powers in the order of 200 mW. In Figure 48, a fitting curve is plotted using

equation for the reflectivity of FBG. On the other hand when intensity pump pulses are used to generate the dynamic grating much higher peak powers can be obtained, resulting in the higher DBG reflectivity. In addition pulsed pumps do not create a residual grating between the points where they physically overlap. The only limitation for peak power of pulsed pumps can be fiber nonlinearities, such as self-phase modulation and modulation instability.
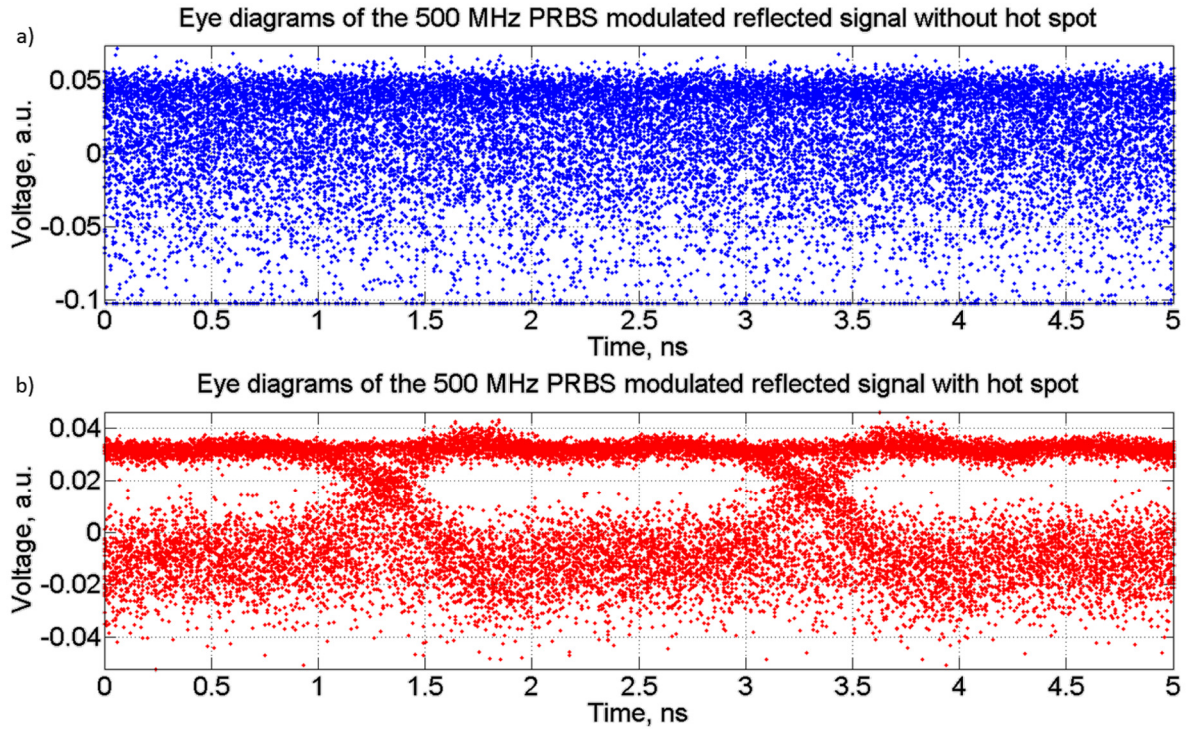

Figure 47. a) Eye diagram of the reflected signal from DBG generated by the PRBS phase modulated pump waves. b) The same as a) but heating the section of the fiber at the correlation point with resistor.
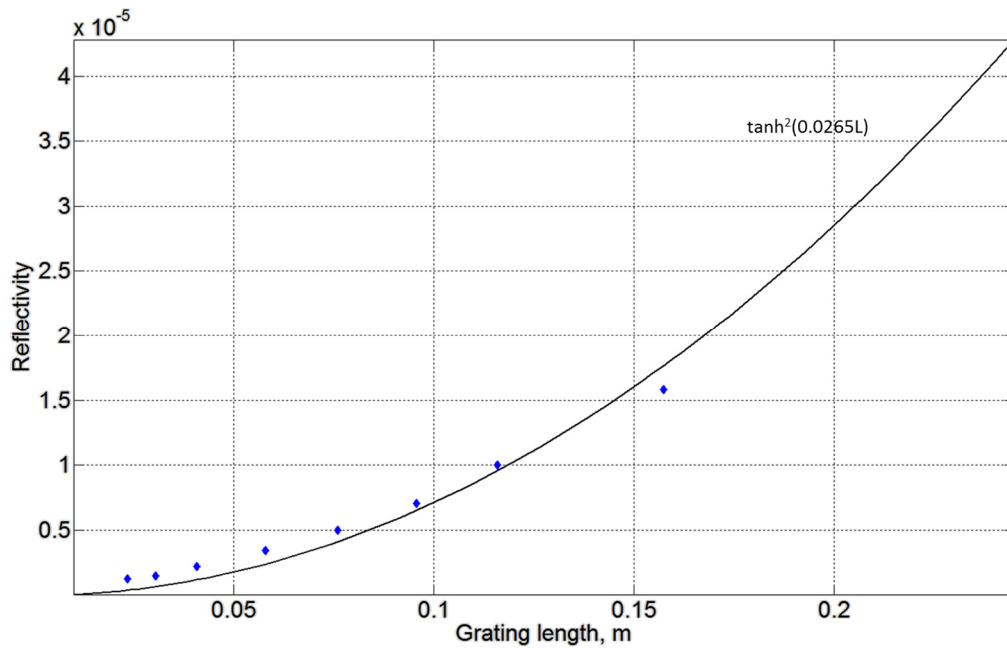

Figure 48. DBG grating reflectivity as a function of the grating length.

In order to estimate the amount of noise generated by the residual gratings an analytic model was proposed [29]. The model shows that in each fiber section $\Delta z = TV_g/2$ the acoustic wave magnitude can be described by the one-dimensional random walk process, with zero expected value and standard deviation of $\sigma = \sqrt{2\tau_p T} g_1 |A_0|^2$. Following equation (3.87) the magnitude of the grating at the correlation peak is given by $S = |\rho(t \gg \tau_p, z = L/2)| = 2\tau_p g_1 |A_0|^2$. Then the optical power of the reflected signal from the correlation peak will be proportional to $|S|^2 (\Delta z)^2$. The number of sections from which noise is accumulated can be calculated as: $N = L/\Delta z = T_D/T$, where T_D represents the maximum variable delay. It is assumed that contributions to overall noise from different sections are uncorrelated to one another. Then when signal to be delayed is on-off keying (OOK) data sequence, the noise field will consist of sum of $\frac{1}{2}N$ uncorrelated contributions of equal statistics. Average power for OOK data is divided by two. Thus optical signal-to-noise ratio (OSNR) is given by:

$$OSNR = \frac{|S|^2 (\Delta z)^2}{\frac{1}{2} N \sigma^2 (\Delta z)^2} = \frac{\frac{1}{2} 4\tau_p^2 g_1^2 |A_0|^4}{\frac{1}{2} \frac{T_D}{T} 2\tau_p T g_1^2 |A_0|^4} = \frac{2\tau_p}{T_D} \tag{3.89}$$

The remarkable result is that OSNR is independent of the symbol duration *T*. It is therefore concluded, that DBG generated by the PRBS pump phase modulation can not be used to delay optical communication data with OSNR in the order of 20-30 dB, unless the extend of delay is restricted to less than 1 ns. It should be pointed out that less demanding OSNR is required for the applications where periodic or repetitive patterns are used, such as distributed sensing or microwave photonics. Improvements to the OSNR might be possible if another coding sequence is employed, rather then pseudo-random bits.

4.4.   Microwave photonic filters.

In the fields of ground radars, broadband wireless access networks, universal mobile telecommunications, etc., radio frequency, millimeter-wave and microwave signal are used to transmit information. Efficient signal processing techniques are required to operate with these signals. In the past several decades extended research was done to improve and develop high performance subsystems which can carry equivalent tasks to those of an ordinary microwave circuit, bringing supplementary advantages of high bandwidth operation, reconfigurability and tunability. One of such improved elements is a microwave photonic (MWP) filter [5, 34], which was proposed to replace standard microwave filter used in RF systems. MWP filter is a hybrid photonic structure which can perform filtering of RF signals bringing at the same time

a series of advantages, such as tunability, reconfigurability, electromagnetic immunity, low loss, etc.

A scheme of the generic photonic microwave delay-line single source filter with a finite impulse response is sketched in Figure 49 (a) [25, 26, 34]. In this configuration light from an optical source is modulated by the RF input signal $s_i(t)$ using an electro-optic modulator. Signal is sampled using $1 \times N$ coupler, weighted by the attenuators a_i and optically delayed with delay $(N-1)T$, where N is the tap order and T is the filter basic delay. All the samples of the filter are evenly combined using $N \times 1$ coupler, and output RF signal $s_{out}(t)$ is produced by the photodetector. The electrical transfer function of such filter can be written as:

$$H(v) = \frac{s_{out}(v)}{s_{in}(v)} = \sum_{n=0}^{N-1} a_n \exp\left(-j2\pi vnT\right) = \sum_{n=0}^{N-1} |a_n| \exp\left(i\theta\right) \exp\left(-j2\pi vnT\right) \qquad (3.90)$$

where a_n denotes filter complex coefficient. Transfer function of the microwave photonic filter is spectrally periodic with the period of $1/T$. This period is called free spectral range ($FSR = 1/T$) and it depends on the basic delay between the adjacent filter taps. Thus, continuous control of T provides possibility to dynamically tune the FSR of the filter (Figure 49 (b)). On the other hand if the phase shift θ is changed, the shape of the frequency response of the filter is unaltered keeping the FSR, while center frequency of the stopband is modified (Figure 49 (c)). In addition, MWP filters are normally implemented to operate in the incoherent regime in order avoid any dependence on an optical phase, thus making the filter very stable against environmental conditions.
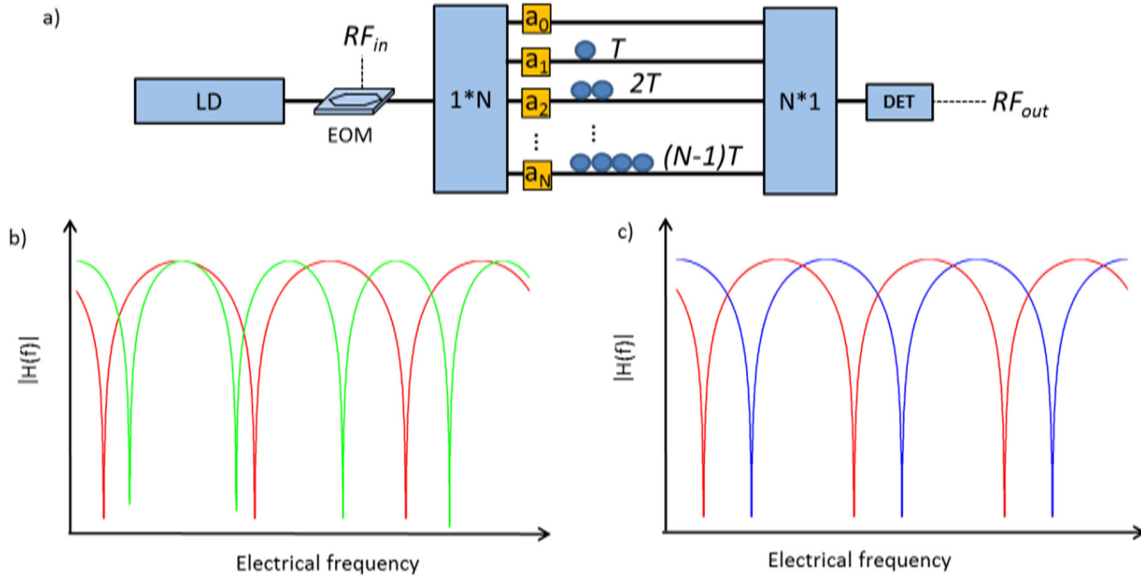

Figure 49. a) Realization of the single source microwave photonic filter with finite number of taps. b) Filter response when basic delay T is changed. c) Filter response when phase shift θ is changed.

4.4.1 Microwave photonic filter based on DBG generated by the intensity modulated pump waves.

The DBG principle was exploited to realize a novel type of MWP filters. As it was shown dynamic grating can be localized inside the fiber. Moreover, the number of gratings and their positions can be chosen on will. Thus it is possible to realize a finite impulse response MWP filter if the reflection from each grating is used as an individual tap of the filter [8].

First, the simplest microwave photonic filter with two taps can be realized using reflection from a single dynamic Brillouin grating and a fixed delay line. Principle of the proposed MWP filter is sketched in Figure 50 (a). As it is seen, an RF modulated optical wave is split using a fiber coupler. Upper branch is used as a first tap of the filter where RF signal is reflected from a dynamic Brillouin grating. Second tap is realized using a fixed fiber. Optical waves carrying RF signal and coming from both taps are combined using another coupler. Their interference is registered using photodetector. The dynamic Brillouin grating is localized inside the PM fiber using intensity modulated pump waves. As it was demonstrated earlier, DBG is generated as a result of SBS process at the crossing point where two pump pulses meet. By choosing repetition rate of the pump pulses faster than acoustic lifetime (~ 10 ns) localized grating can be sustained at the given position before it completely decays. In order to realize proposed setup 40 cm pm fiber was used to generate a dynamic Brillouin grating, serving as a tap with variable basic delay. Light from the signal laser was modulated using EOM driven by the RF signal coming from Vector Network Analyser (VNA), which was also used to obtain the filter response. Repetition rate of the pump pulses was chosen to be 5 ns, which determines the refreshment rate of the grating as well as distance between two adjacent gratings. In this case grating separation is ~ 50 cm, which secures that only one DBG is constantly present inside the fiber under test. Pump pulses had Gaussian-like shape with FWHM of 400 ps, resulting in generation of DBG with reflectivity bandwidth of more than 1 GHz. Fixed arm of the filter was implemented using ~80 m fiber, which include a fixed delay, polarization controller and attenuator. The fixed delay of such length was used to compensate the length of several optical components in the upper arm, such as EDFA, circulator, couplers, together with providing a length imbalance of ~1 m between the two taps. Transfer function of such a MWP can be represented as:

$$H(v) = a_0 + a_1 \exp\left(-i\left(2\pi v T_0 + 2\pi v 2\tau_{DBG}\right)\right) \tag{3.91}$$

where T_0 is a delay between the two taps when the DBG position is in the beginning of the PM fiber ($d = 0$), and $\tau_{DBG} = n_y d / c$ is the delay obtained when the position of the DBG is changed along the fiber. Figure 50 (b) represents the experimentally obtained frequency response of the realized two-tap MWP filter (markers) together with the calculated response (solid curves). It is clearly seen that by changing the basic delay of the filter ($T = T_0 + \tau_{DBG}$) from 4.2 ns up to 6.8 ns, filter center frequency can be continuously tuned with maximum change of FSR equal to 62%. It should be pointed out that the operational RF frequency is

limited in this case by the bandwidth of the DBG. Since two sidebands were reflected by the DBG, the filter bandwidth in this case was limited to 500 MHz.
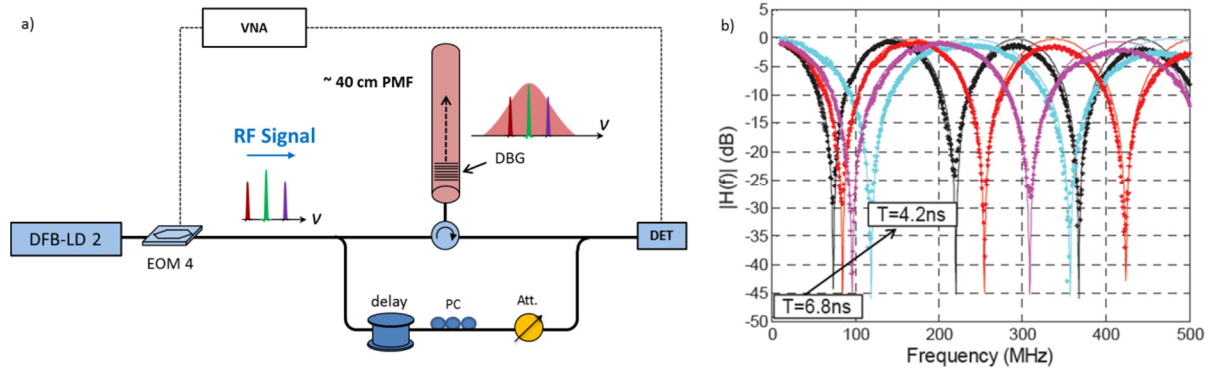

Figure 50. a) Schematic diagram showing principle to realize two-tap MWP filter using single dynamic Brillouin grating. Setup to generate localized DBG is not shown. b) Experimentally obtained filter response (diamonds); numerically calculated filter response (solid lines).

4.4.2 MWP filter based on multiple DBGs.

Another type of the MWP filter can be realized based on reflections from multiple DBGs, where each grating inside the PM fiber represents a filter tap. By changing the distance between the adjacent DBGs different basic time delays can be obtained, demonstrating the tunable MWP filter. Moreover filters with variable number of identical and positive taps can be realized by simply adjusting the number of the DBGs in the fiber under test. Figure 51 a) shows the experimental realization of the two tap filter, where both filter taps are realized using two dynamic gratings positioned at different locations inside the fiber. In this configuration repetition rate of the pulses determines the basic delay of the filter. Thus by changing the repetition rate of the pump pulses, the distance between two DBGs can be changed resulting in the tunability of the filter FSR. Two dynamic gratings were generated along the 60 cm-long fiber using pump pulses with high repetition rate. By controlling the repetition rate of the pump pulses, DBGs separation in position was changed from 33 cm (3.3 ns) up to 52 cm (5.2 ns), demonstrating 58% filter FSR tunability as shown in Figure 51 (b).
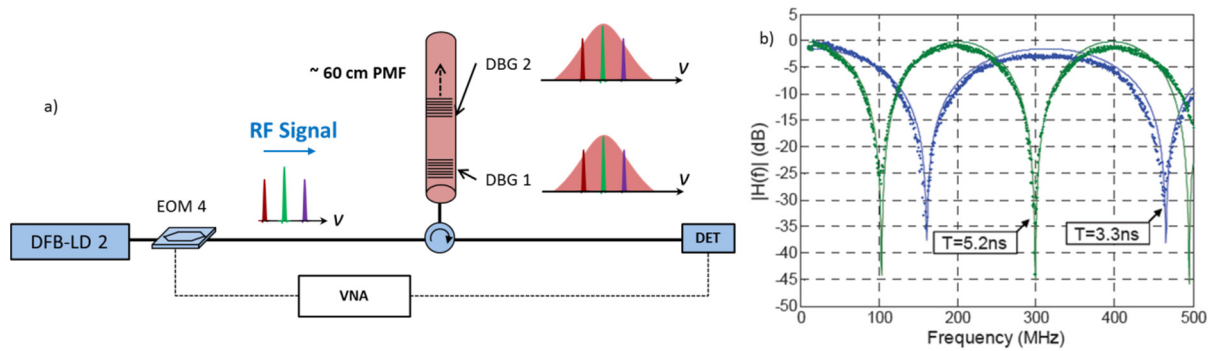

Figure 51. a) Principle to realize two tap filter based on reflections from two DBGs. b) Frequency response of the filter.

As in the previous configuration, two sidebands and carrier are reflected by each DBG. The operation frequency of the filter is thus limited by the DBG resonance, which is around 500 MHz. Moreover, independent control of weights of different taps cannot be realized in this configuration, since assuming no pump depletion, reflectivity of all DBGs generated in the fiber is the same. In the section 3.4 we showed that dynamic Brillouin gratings provide phase conjugated reflection. This property plays an important role in the implementation of microwave photonic filters, since reflections from different dynamic gratings appear to be in phase thus avoiding coherence problem.

4.4.3 MWP filter based on multiple spectrally detuned DBGs.

In microwave photonic filter systems, a radio frequency signal at frequency v_{RF} is modulated onto a laser beam oscillating at optical frequency v_0. In the case of amplitude sine modulation, the optical signal is represented by the three optical waves with different amplitudes and frequencies. One of the waves is the unaltered optical carrier v_0. The second wave is the upper sideband oscillating at optical frequency $v_0 + v_{RF}$, and the third wave called lower sideband has frequency $v_0 - v_{RF}$. The output radio frequency signal can be retrieved by beating optical carrier and one of the sidebands at the photodetector. It should be pointed out that in this case the information about the RF signal is determined by the amplitudes and phases of optical waves: carrier and one of the sidebands.

In order to overcome the operation frequency limitation of the two previously realized filters a new MWP configuration based on multiple spectrally detuned DBGs is proposed. Here several pairs of gratings are created at different locations inside the fiber, where two DBGs at the same fiber position have slightly different resonant frequency. Principle to realize the proposed filter is depicted in Figure 52 (a). In order to generate one pair of dynamic gratings at the same position inside the PM fiber, but with different resonant frequencies, emission of the pump laser diode was intensity modulated at the frequency v_g, which is in the vicinity of radio frequency, v_{RF}. This way at a position where pump pulses cross each other two dynamic Brillouin gratings are generated, where one of the gratings is intended to reflect the carrier wave of the RF, while the other one reflects one of the sidebands. Therefore, the bandwidth of the filter is still governed by the DBG's spectral width, while its central frequency can be adjusted with v_g. Configuration of optical frequencies of the interacting waves is the same as shown in the Figure 29, which is repeated here as Figure 52 (b).
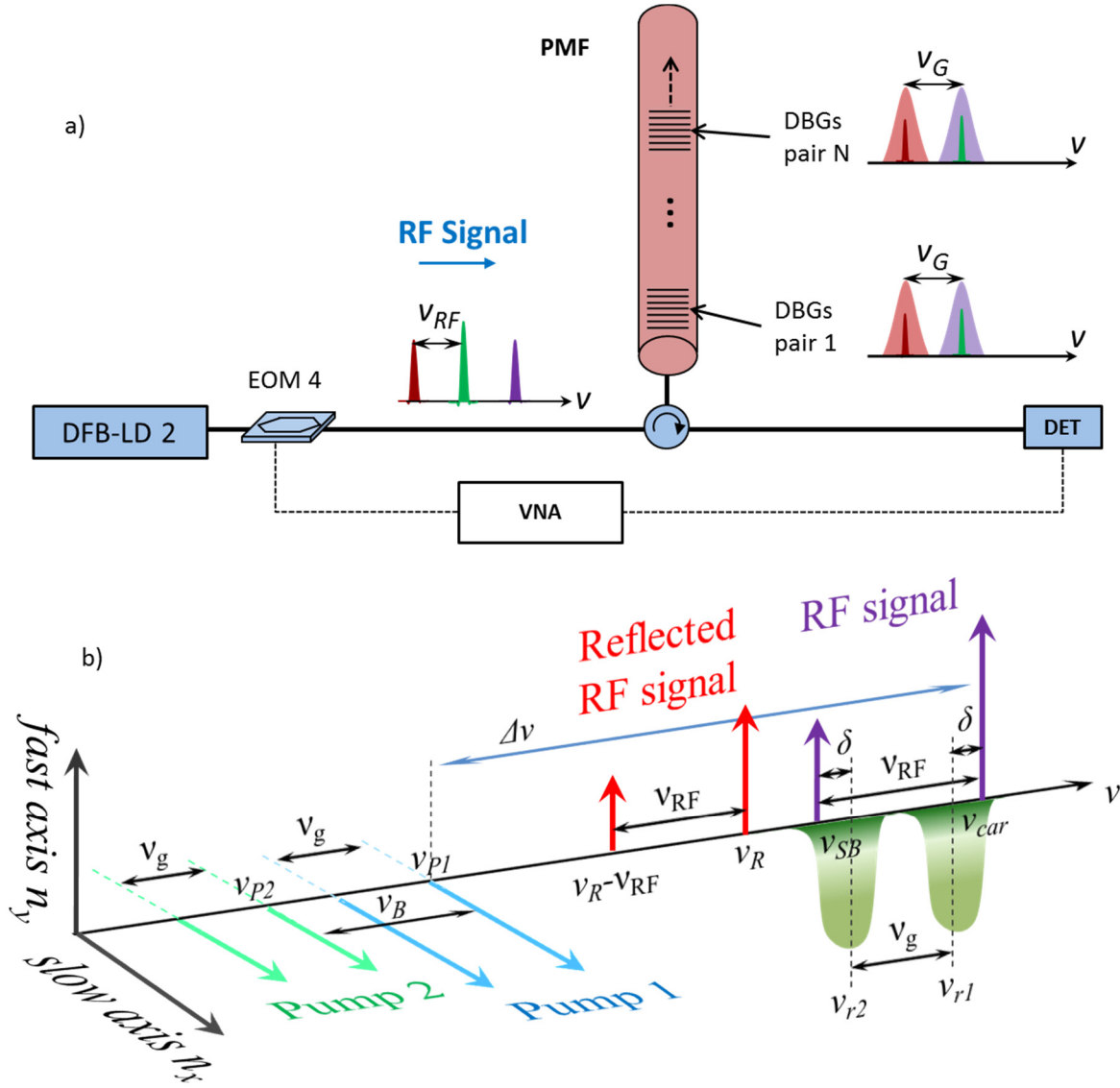
Figure 52. a) Experimental layout to realize multi-tap filter based on spectrally detuned DBGs. b) Configuration of optical frequencies of interacting waves.

To implement the proposed multi-tap MWP filter 110 cm PM fiber was used as a medium for DBGs generation. Two, three and four pairs of gratings were generated resulting in two-, three- and four-tap filter, respectively. The number of grating pairs was controlled by adjusting the repetition rate of the pump pulses. Frequency responses of two-, three- and four-tap filters are presented in Figure 53 a, b, and c, respectively. Solid lines on the graph represent numerically calculated responses. For two-tap filter, basic delay was changed from 4 to 6.6 ns resulting in FSR tunability of 65%, while bandwidth was kept constant at 1 GHz. 17 % FSR tunability is demonstrated for the tree-tap filter. For four-tap filter FSR tunability was not experimentally demonstrated, since fiber length limited the number of grating to four. Dashed curve in the Figure 53 (c) demonstrates numerically calculated four-tap filter response when modulation frequency of the pumps ν_g is changed by 200 MHz, resulting in a 187 $^{\circ}$ phase shift between the RF carrier and sideband.
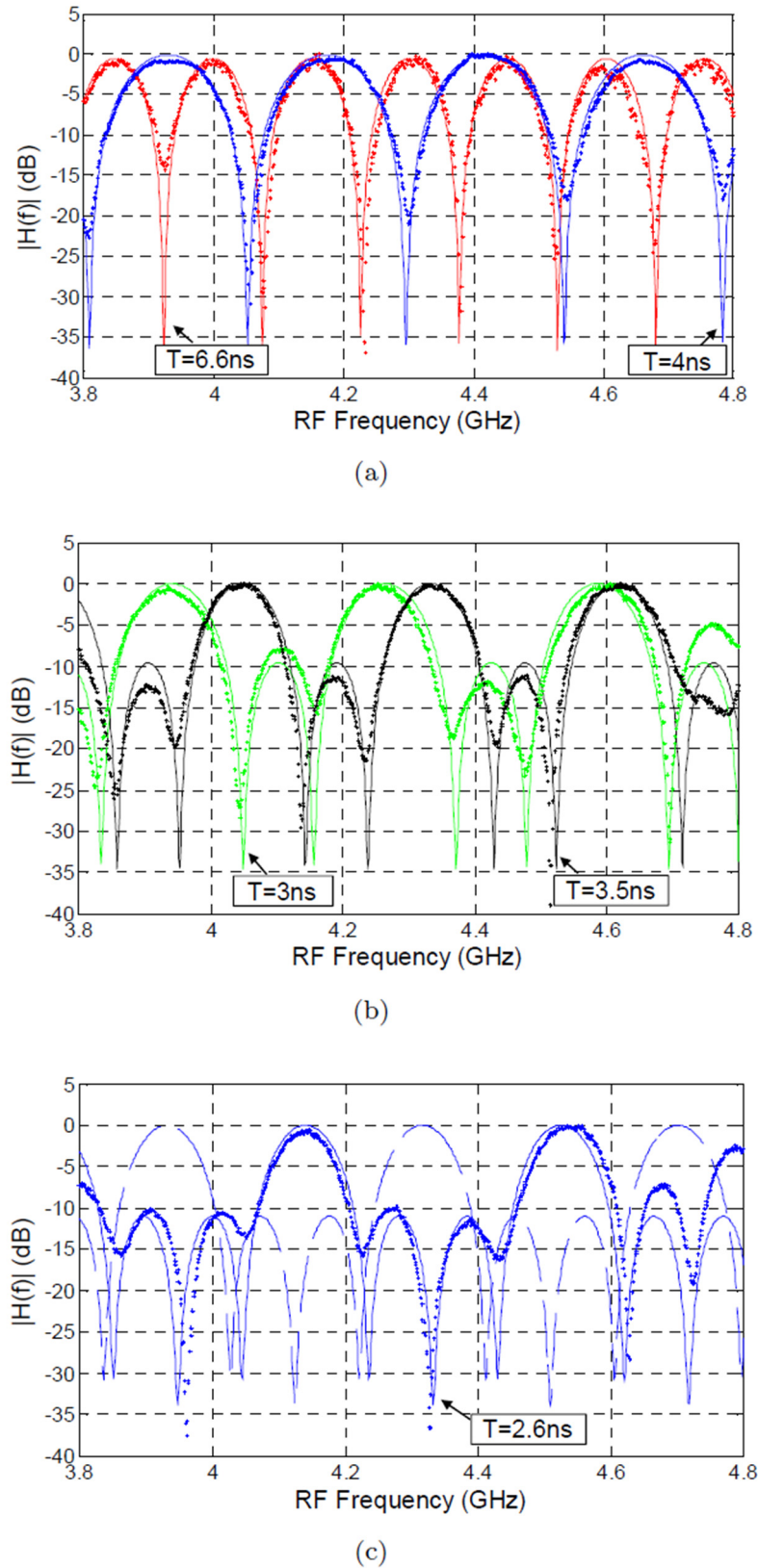
Figure 53. Experimentally obtained (markers) and numerically calculated (solid lines) frequency responses of DBG based MWP filters with two- (a), tree- (b), and four-taps (c).

It should be pointed out that discrepancies between measured filter responses with those numerically calculated are due to the nonuniform birefringence of the fiber. Such fiber

inhomogeneity leads to the dependence of the DBG resonance with grating position and as a result to unequal taps reflectivities. Figure 54(a) shows calculated phase shifts as a function of the dynamic gratings position inside the fiber d. Simulations were performed for 1.2 m long fiber and separation between the DBG resonances, v_g, of 5 GHz. Figure 54 (b) shows simulations when DBGs separation is fixed to 20 cm and the DBG resonance difference is changed. It is clear that origin of the RF phase is at 5 GHz, demonstrating that when $v_{RF} = v_g$ or equivalently when carrier and sideband are placed exactly in the middle of the gratings resonance no phase change is observed with increasing the separation between the pairs of gratings.
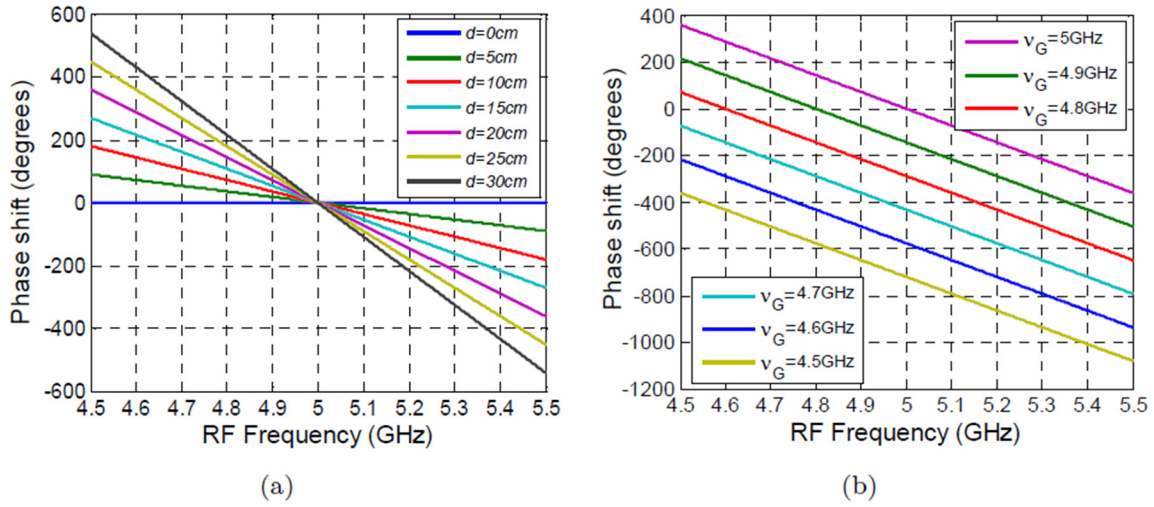

Figure 54. Phase shift as a function of radio frequency when signal is reflected from the pair of DBGs at different positions inside the fiber under test (a), and for fixed position but different separations of DBGs resonances, v_g (b).

4.4.4 Microwave photonic filters using PRBS technique.

As demonstrated in previous sections PRBS phase modulated pump waves can generate localized and stationary DBG inside the fiber. Moreover the number of gratings can be simply controlled with the code length of the PRBS generator. Thus multiple gratings generated by the PRBS technique can be exploited to realize microwave photonic filter. Two tap microwave photonic filter was demonstrated experimentally. A PRBS sequence was set to the minimum value of 127 bits, which results in the generation of two DBG inside the fiber under test. Figure 55 (a) shows reflection of an isolated pulse from dynamic gratings for two different grating separations. By changing the bit length T difference in position between the two correlation peaks can be changed from ~1.25 m to 2.1 m. This corresponds to the change in filter basic delay from 12.4 to 21 ns, resulting in 66% FSR tunability of the filter. Figure 55 (b) shows the spectral response of the two-tap filter using PRBS modulated pump waves.
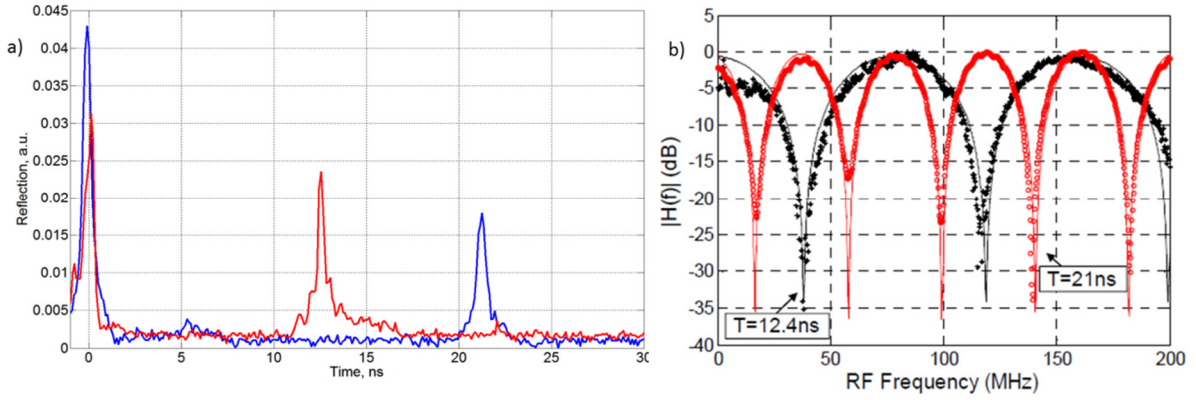
Figure 55. a) Reflection of the isolated pulse from two dynamic Brillouin gratings separated by 12.4 ns (red) and 21 ns (blue). b) Frequency response of the two-tap filter based on PRBS generated dynamic Brillouin gratings.

Multi-tap finite impulse response filter can be generated using the proposed technique if arbitrary length PRBS sequence is generated. Transfer function of this filter can be written as:

$$H(v) = \sum_{n=0}^{N} a_r \exp\left(-i2\pi v MT\right) \tag{3.92}$$

where M is the number of bits in PRBS sequence and T is a bit duration. In this case filter bandwidth is also given by the bandwidth of the dynamic Brillouin grating. Thus for higher bandwidth shorter bit duration is preferable.

4.5. Optical calculus using dynamic Brillouin gratings

For several decades optical computing has been considered an ultimate goal for researchers in order to satisfy the ever demanding growth in the amount of information to be processed. Electronic-based systems are reaching their limitations when information data rates approach several tens of GHz, whereas optical based systems could be used to overcome speed limitations and can be used to process information with speeds above hundreds of GHz. For high speed communication networks many functionalities such as demultiplexing, regeneration, routing, switching, etc. can be accomplished by using optical nonlinearities [35]. On the other hand implementation of an all-optical computer and control system requires the development of various all-optical circuits capable of providing wide variety of signal processing operations. Such devices can be considered as basic building blocks, which can perform various operations on optical signals, similar to the electronic components. For instance in electronics with operational amplifiers, resistors and capacitors many basic functionalities can be performed on the electrical signal, such as differentiation, integration, logic operations, filtering etc. Thus the development of photonic counterparts is a primary step toward a practical realization of all-optical information processing. Two of the main functionalities are photonic temporal integrator and differentiator.

An N-th order ($N = 1, 2, 3...$) photonic temporal differentiator is a device that produces at its output the N-th time derivative of the complex envelope of an input optical waveform [36-41]. Different approaches have been recently proposed for implementing all-optical differentiator [37-42]. Arbitrary order photonic differentiator was first realized using an asymmetric two-arm interferometer or basically two-tap FIR filter [42]. Spectral response of such device resembles that of optical differentiator over limited bandwidth centered at any of the destructive resonance frequencies. Another first-order time differentiator based on uniform long-period fiber grating operating in full-coupling condition was proposed by Kulishov and Azana [37]. Such differentiator has a large operation bandwidth in the range of terahertz, which allows processing of ultrafast optical signals. Specially designed FBGs operating in reflection can also be used as all-optical passive devices providing first- and higher order derivatives of complex envelopes of optical waveforms [43, 44].

A complementary function to the optical differention is the Nth-order temporal integration. Photonic temporal integrators have been proposed using active or passive resonant cavities [45], phase-shifted FBGs operated in transmission [46] and an active resonant cavity based on superimposed linearly chirped FBGs photo-inscribed in an Erbium-Ytterbium-codoped optical fiber [47]. Moreover single passive FBG filter operating in reflection can emulate the time response of an ideal integrator over a finite time window [48]. First and higher order integration can be realized using FBG filters with processing bandwidth up to the terahertz range. With proper apodization profile uniform-period FBG integrators offer operational time windows in the nanosecond range.

In the following section we propose an optical processor based on dynamic Brillouin grating, capable of performing both integration and differentiation of complex envelopes of an input arbitrary optical waveforms. Proposed DBG based signal processor might bring several advantages over other types of processors, such as tunable operation frequency, adjustable operational time window, and possibility to provide higher order operations.

4.5.1   All optical temporal integration using DBG.

A device operating as a first-order temporal integrator should provide at the output a first time cumulative integral of the comlex envelope of an incoming arbitrary optical waveform. For an optical carrier wave modulated by a signal $x(t)$ we can express an input optical signal to integrator in the form:

$$E_{in}(t) = \exp(i\omega_0 t) x(t) \tag{3.93}$$

The photonic integrator should yield the output optical waveform in the form:

$$E_{out}(t) = \exp(i\omega_0 t) y(t) \tag{3.94}$$

where $y(t)$ is proportional to the time integral of the input complex envelope [48]:

$$y(t) = \int_{-\infty}^{t} x(t')dt' = \int_{\tau=0}^{+\infty} x(t-\tau)d\tau = \int_{\tau=-\infty}^{+\infty} u(\tau)x(t-\tau)d\tau = u(t) * x(t) \tag{3.95}$$

where variable change, $t' = t - \tau$ was used and $u(\tau)$ is the unit step function. It is clear that last integral in the equation (3.95) represents a convolution of the input time envelope $x(t)$ and the unit step function $u(t)$. This means that desired integration can be obtained when the input signal is launched into the time invariant system with temporal impulse response proportional to the unit step function and spectrally centered at ω_0. Moreover since the unit step function extends to infinity, the desired system should include gain, which makes it more complex. On the other hand passive systems can emulate the temporal integration for a finite time duration T. Thus we can replace unit step function with the following function:

$$h(t) \propto \begin{cases} 1, & 0 \le t \le T \\ 0 & otherwise \end{cases} \tag{3.96}$$

Or we can rewrite it as:

$$h(t) = u(t) - u(t-T) \tag{3.97}$$

This way the complex envelope at the output of this system when subject to the input signal $x(t)$:

$$y(t) = \int_{\tau=-\infty}^{+\infty} u(\tau)x(t-\tau)d\tau - \int_{\tau=-\infty}^{+\infty} u(\tau-T)x(t-\tau)d\tau \tag{3.98}$$

Hence, the system defined by equation (3.98) produces a temporal waveform at its output that follows the profile of the integral of the input waveform over a finite time window of duration T. Moreover, after time T the system will produce the time inverted integral of the input waveform. The spectral transfer function of the finite time integrator is given by the Fourier transform of its impulse response. Thus we can write:

$$h(\omega - \omega_0) \propto \frac{\sin\big((\omega-\omega_0)T/2\big)}{(\omega-\omega_0)} \exp\big(-i(\omega-\omega_0)T/2\big) \tag{3.99}$$

It was demonstrated that the square-like temporal impulse response of a finite time integrator can be obtained by a weak uniform FBG operated in reflection [49]. FBG is considered weak if condition $kL \le \pi$ is satisfied, where k is the coupling coefficient and L is the FBG length. In practice this condition is satisfied when grating reflectivity is lower than $\sim 10\%$. Since reflection temporal impulse response of the FBG is approximately a square-like over a finite time duration equal to the round-trip propagation time, $T = 2nL/c$, it can be exploited as a temporal integrator. In previous chapters it was demonstrated that DBG shows temporal and spectral responses similar to a weak uniform FBG. Thus, DBG can be a very good candidate to realize photonic integrator. In addition, the center frequency of the DBG based integrator can be easily tuned by changing pump wavelength. Processing bandwidth can

also be controlled by changing the pump powers. Moreover, it is possible to generate arbitrary long gratings with operational integration of many nanoseconds.

All-optical DBG integrator is based on two subsequent processes. First, a uniform dynamic Brillouin grating is generated inside the polarization maintaining fiber under test using continuous pump waves polarized along the slow axis as shown in Figure 56. Generated DBG is used as a weak reflecting uniform grating to process input optical waveforms producing output signals proportional to the integration of the input complex envelope. The central frequency of the DBG is tuned to the central optical frequency of the input waveform. The proposed integrator was tested with several input optical waveforms. Figure 57 (a-d) shows different input waveforms such as a) Gaussian pulse with FWHM of ~ 370 ps, b) square-like pulse with FWHM of ~ 1.7 ns, c) two symmetric in-phase pulses with FWHM of ~370 ps and time separation of 2 ns, and d) two symmetric out-of-phase pulses with FWHM of ~370 ps and time separation of 2 ns. Theoretical expected outputs from ideal integrator are depicted in Figure 57 (a-d) with blue lines, while red line represents outputs from integrator with limited integration window of 4 ns. Similar experimental optical waveforms were launched into DBG integrator. To realize proposed temporal integrator 42-cm long PM fiber was used. The DBG physical length corresponds to an integration time window of ~4.2 ns.
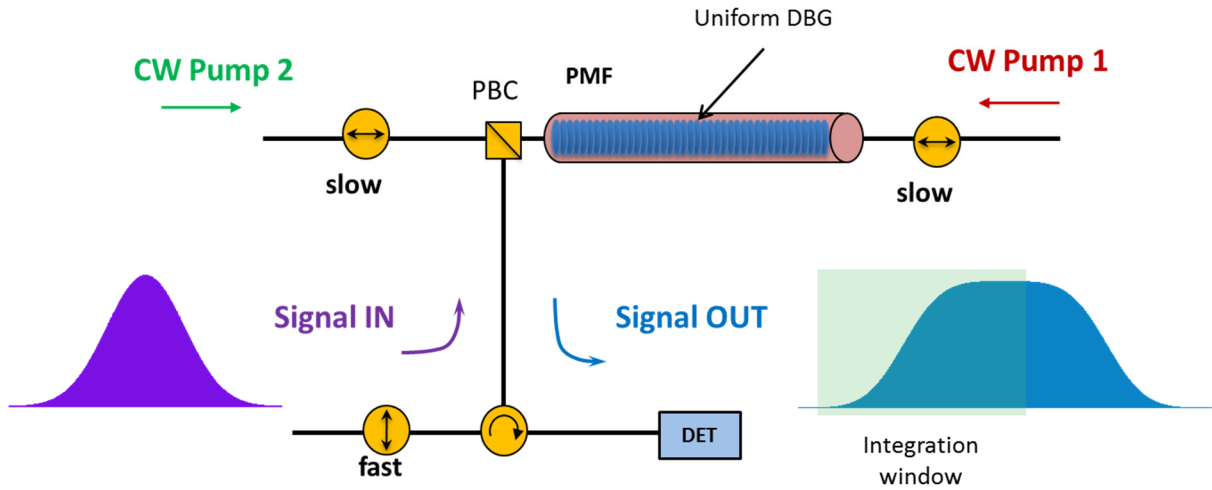

Figure 56. Principle to realize photonic temporal integrator based on DBG with limited integration window.
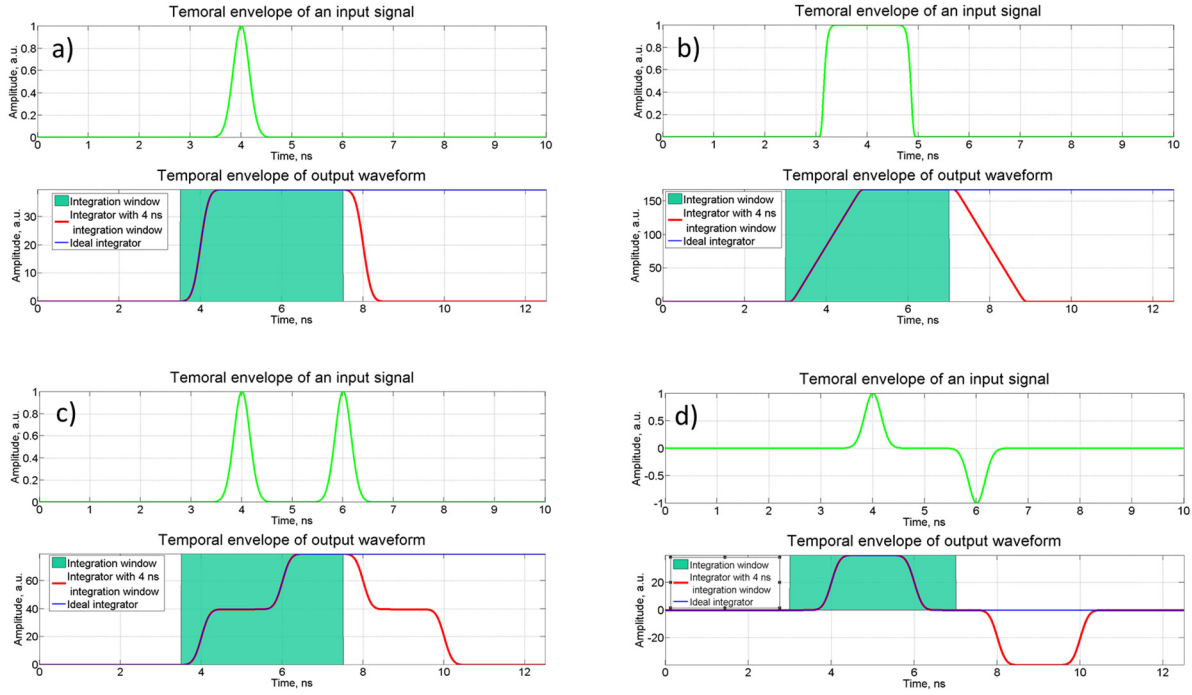
Figure 57. a)-d) Theoretical input (green) waveforms, output waveforms (blue) from ideal integrator, and output waveforms from integrator with 4 ns integration window. Green area represents 4 ns integration window.

Several input optical waveforms were launched into the proposed integrator. Figure 58 represents measured complex envelopes of the input and output optical signals. Input pulses with different widths were prepared using EOM and electrical pulse generator. Optical integration of the 0.8 ps data pulse is shown in Figure 58 (a). It is clear that reflected waveform from the DBG represents time integration over limited time window (shown as a green box). On the same graph numerically calculated integration of the input pulse is presented in blue line. Experimentally obtained integration is in good agreement with the numerical calculations. Figure 58 (b, c) show output waveforms from DBG based integrator, when square-like pulses with widths of 1 and 1.5 ns where launched as input signals. Finally, integration of double in phase pulses was performed. The two pulses were Gaussian-shaped with 300 ps width spaced by 900 ps as shown in Figure 58 (d). Again measured temporal profile shows good agreement with numerically calculated integration. Small deviations of the experimentally obtained temporal integrals with numerically calculated are due to the nouniformity of the fiber birefringence causing fluctuations of the acoustic grating amplitude. Presented results clearly demonstrate that uniform dynamic Brillouin grating can act as a photonic integrator with limited integration window. Moreover integration window of DBG based integrator is simply given by the fiber length. Notice that integration is performed on the complex amplitude of the optical wave. This means that when two in-phase pulses are integrated field integral is twice the field integral of a single pulse (Figure 58 d). In terms of measured intensity second step is three times higher than the first one.
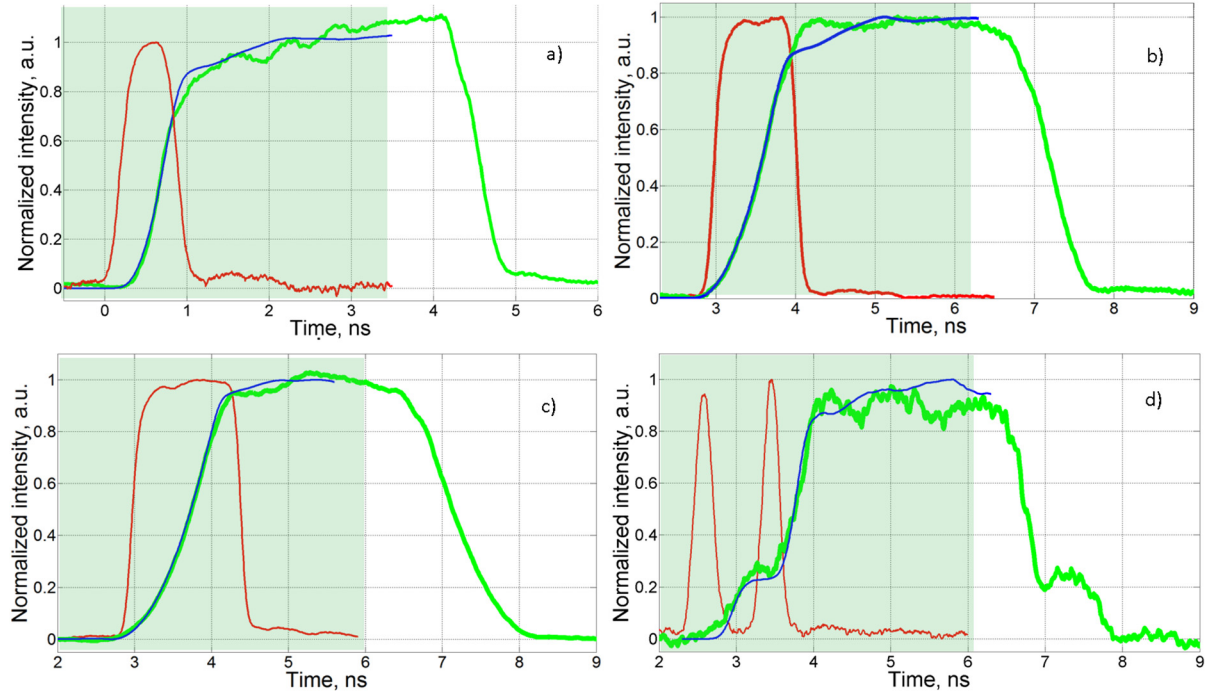
Figure 58. Experimentally obtained input (red) and output (green) waveforms for different integration experiments using DBG based integrator. a) Integration of a Bell-like pulse with FWHM of 0.8 ns. b), c) integration of square-like pulses with FWHM of 1 ns, and 1.5 ns, respectively. d) Integration of symmetric double pulses with FWHM of 300 ps each and separation of 900 ps. Green light area represents integration window. Numerical integration of input waveforms over a DBG integration time window is represented with blue line in each graph.

4.5.2   Optical DBG based differentiator

A first order optical differentiator is a device which performs the first time derivative of the complex envelope of incoming arbitrary optical waveform. Considering the incoming optical signal as:

$$E_{in}(t) = \exp(i\omega_0 t)x(t) \tag{3.100}$$

output optical signal from the ideal photonic differentiator can be written:

$$E_{out}(t) = \exp(i\omega_0 t)y(t) \tag{3.101}$$

where $y(t) \propto \partial x(t)/\partial t$. Transfer function of the optical differentiator can also be written in frequency domain using Fourier transform:

$$\widetilde{E}_{out}(\omega) = j\omega\widetilde{E}_{in}(\omega) \tag{3.102}$$

where $\widetilde{E}_{in}(\omega)$ and $\widetilde{E}_{out}(\omega)$ are the Fourier transforms of the input and output complex temporal envelopes of the, $x(t)$ and $y(t)$, respectively. For differentiators operating at the optical frequencies relation (3.102) should be written as $\widetilde{E}_{out}(\omega_{opt})/\widetilde{E}_{in}(\omega_{opt}) \propto j(\omega_{opt} - \omega_0)$,

where ω_{opt} is the variable angular optical frequency and ω_0 is the center frequency of the differentiator. Most of the experimentally realized photonic integrators emulate the spectral response of the ideal differentiator over a limited bandwidth [41].

On the other hand optical differentiator as well as other signal processing operations can be realized using dynamic volume holography in Raman media [50]. It was predicted that dynamic volume holography can be realized in arbitrary Raman media (gases, fibers, plasmas), where beating of high-frequency waves can resonantly excite low-frequency slowly propagating waves, such as, for example, sound or Langmuir waves, as long as these waves persist on a time scale suitable for storing the optical information. Stimulated Brillouin scattering is a good example where optical waves can resonantly induce low-frequency sound wave. Thus SBS can be used in the similar way to store and process the optical information by first recording it in the form of acoustic excitation and then retrieving it using a distinct optical wave in the suitable Brillouin media, such as optical fibers. Moreover acoustic phonon lifetime in optical fibers is in the order of several ns, which allow processing of optical signals with relatively long buffering time. Indeed in 2007 Z. Zhu et etc. showed storing of sequences of optical pulses using long-lived acoustic waves up to 12 ns [51]. Consider a case when the optical data pulse at optical frequency v_D is launched inside the PM fiber along the slow axis of the fiber, as shown in the Figure 59. At the same time a short write pules is launched along the slow axis at the opposite end of the fiber counter propagated to the data wave with optical frequency downshifted from the data frequency by the Brillouin shift of the fiber, $v_R = v_D - v_B$. As a result of the SBS interaction, an acoustic wave is excited along the fiber which has information about phase of the original data waveform and the amplitude proportional to the original data waveform, though its length is two times shorter due to the counter propagation of optical waves. The generated dynamic grating is then interrogated with the reading pulse whose shape is proportional to the first derivative of the delta-function. The reflected optical wave from the dynamic Brillouin grating as a result of interference actually has a shape that is the time derivative of the complex envelope of the data waveform (see Figure 59).
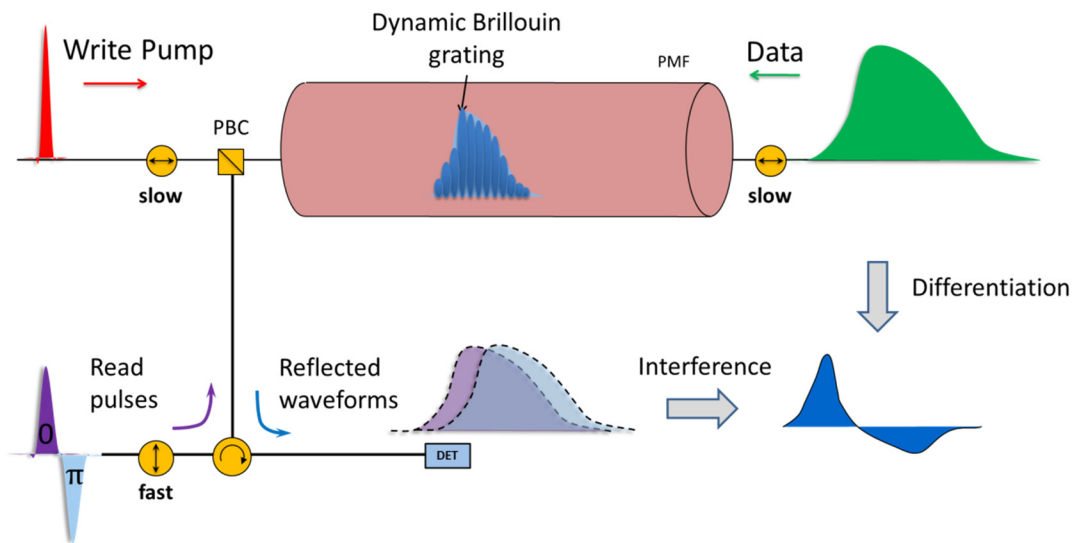

Figure 59. Principle to realize all-optical differentiator using dynamic Brillouin grating.

Analogously, higher derivatives can be realized by further varying the shape of the reading pulse. Time differentiation was realized in a 20 m-long PMF. A 7 ns optical data pulse was launched into PM fiber along slow axis (Figure 60 (b)). Its waveform was recorded along the fiber using a 300 ps writing pulse (Figure 60 (a)) in the form of an acoustic wave as a result of the SBS interaction. Double 800 ps pulses with phase difference of π and with a time interval of 800 ps are used as a reading waveform, which are shown in Figure 60 (c). Each pulse is then reflected by the DBG, resulting in two identical signal waveforms with a time delay of 800 ps, but with opposite phase. Resulted interference between two reflected waveforms eventually represents the first-order derivative of the initial envelope of the data pulse. Experimental results together with numerically calculated differentiation are presented in Figure 60. Clearly obtained time derivative is good agreement with numerically calculated. However discrepancy between measured and calculated intensities are due to the step phase smaller than π in the reading waveform as well as birefringence nonuniformity along 20 m pm fiber. Moreover, DBG based differentiator has several other limitations which restrict the performance. Read pulse is of finite duration and thus the operational bandwidth of differentiator is limited.
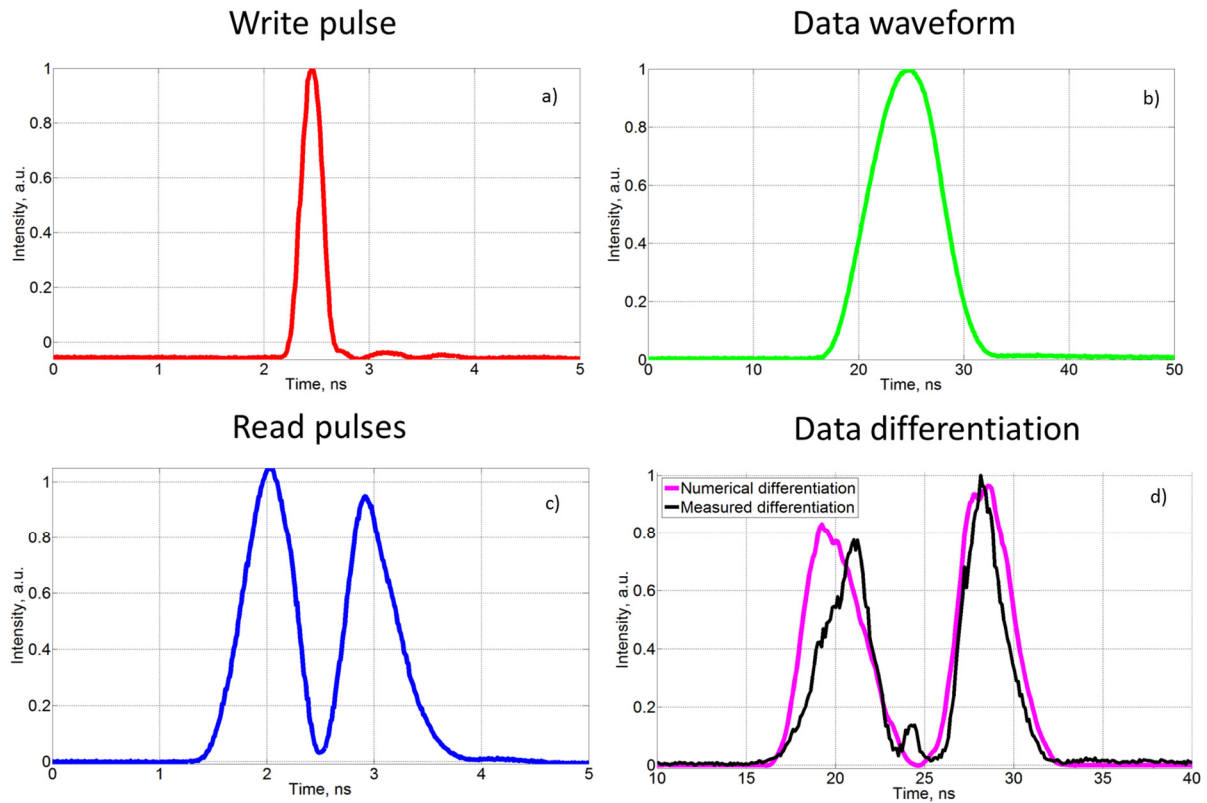

Figure 60. a) Write pulse of ~300 ps; b) Data waveform; c) Read waveform consisting of two 800 ps pulses out-of-phase; d) Experimental (black) and numerical (magenta) intensity temporal profiles showing differentiation of data waveform.

4.5.3 Optical true time reversal.

True time reversal is another unconventional operation on optical signals that can be performed using dynamic Brillouin gratings. Time reversal techniques already found their applications in medicine and acoustics [52]. It was also mentioned that true time reversal of electromagnetic waves can find wide range of applications in microwave wireless communications [53]. Experimental demonstration of ultrafast optical waveform time reversal was demonstrated using various phenomena such as four-wave mixing [54, 55], photon echo [56], spectral inversion [57]and spectral hole-buring holography [58]. Using DBG principle it is possible to show true time reversal of optical waveforms using all-fiber configuration and room temperature operation. Let us consider the situation when data pulse or sequence of pulses having central optical frequency v_{Data_IN} is launched in the polarization maintaining fiber along the slow axis, as depicted in Figure 61 (a). Counter-propagating write pulse is launched along the slow axis simultaneously from the other end of the fiber with the frequency $v_w = v_{Data\_IN} - v_B$, where v_B is the Brillouin frequency of the fiber. As the results of SBS interaction localized acoustic dynamic gratings are generated at each location where write pulse meets data pulses. Thus, the data sequence is spatially stored inside the fiber under test. Shortly after, a reading pulse linearly polarized along the fast axis is launched in the same direction as the data sequence, but at the optical frequency $v_r = v_{Data\_IN} + v_{Data\_IN} \Delta n / n_y$, where Δn is the fiber birefringence and n_y is the refractive index of the fast axis (Figure 61 (b)).
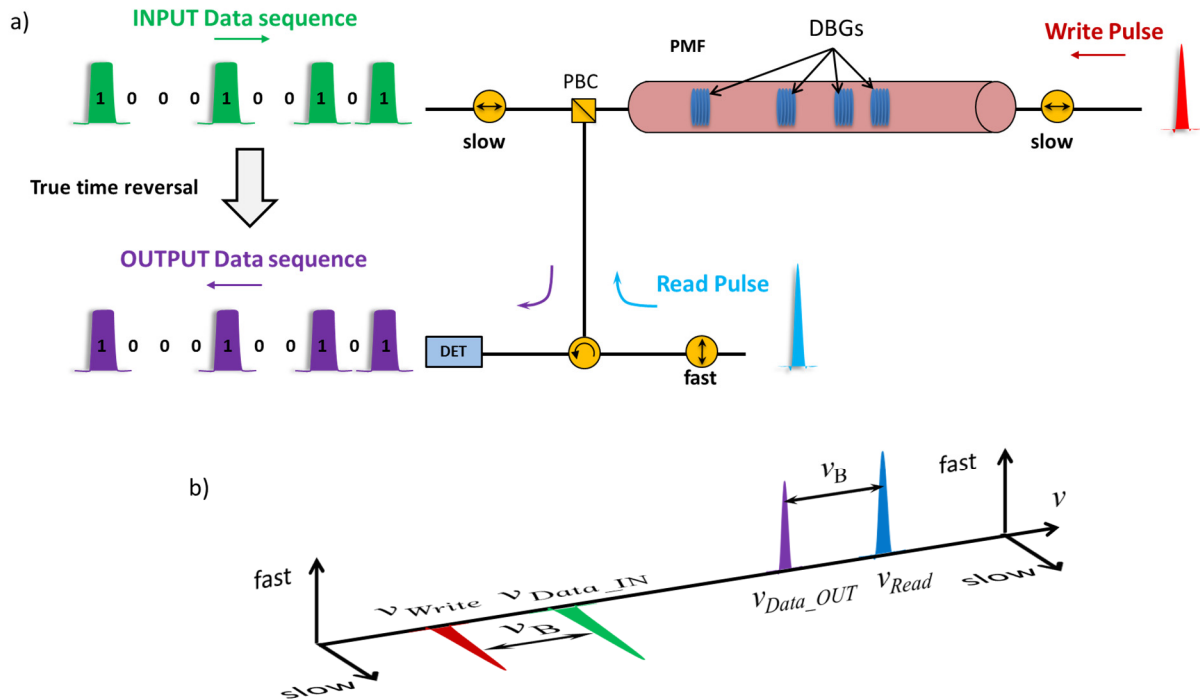

Figure 61. a) Schematic diagram to realize true time reversal using DBG principle. b) State of polarization and relative optical frequencies of the interacting waves.

The read pulse interacts with the stored dynamic Brillouin gratings, generating the reflected signal at frequency $v_{Data\_OUT} = v_r - v_B$. Reflected signal in time domain represents the data sequence but inverted in time, since the last bit of the input data sequence is the first to be retrieved.

To realize true time reversal of the optical data packet a 20 m PM fiber was used as a storing medium. Figure 62 (a) shows 101001 input bit sequence where each square-like pulse has duration of about 2 ns. Write and read pulse had square shape with width of 2 ns. Read pulse was lunched ~ 2 ns after the last bit of the input data packet in order to achieve maximum retrieval efficiency. Experimentally obtained time reversed data packet is shown in Figure 62 (b), together with the ideally reversed input sequence. Short distorted impulse at around 2 ns is the residual of the write pulse along the fast axis as a result of finite extinction ratio of the polarization maintaining components. Note that the bit sequence in the output data packet is 100101, which is time reversed input sequence. It is clear that pulses in the output data packet are distorted in comparison with ideally reversed. This can be explained by the filtering effect during the writing and reading processes. Ideal time reversed waveform could be theoretically obtained only when write and read pulses are infinitely short pulses. Amplitudes of the output data packet are also different mainly due to the exponential decay of the dynamic Brillouin gratings ($\exp(-t/2\tau_p)$). By looking at the time reversal procedure it is clear that the first bit to be stored is the last to be retrieved and vice versa. Thus, first bit in the input sequence experiences the largest amplitude distortion due to the attenuation of the DBG, since this bit is stored longer in the form of acoustic excitation. Figure 62 (b) also shows the time reversed data sequence with numerical post-correction for the exponential decay where phonon lifetime of 6 ns was used. Post-corrected output data sequence resembles that of ideal reversed input, while there are still some discrepancies in amplitude. This mismatch might originate from inhomogeneity of the PM fiber. Due to the birefringence fluctuation along the fiber, DBG efficiency might depend on the position.
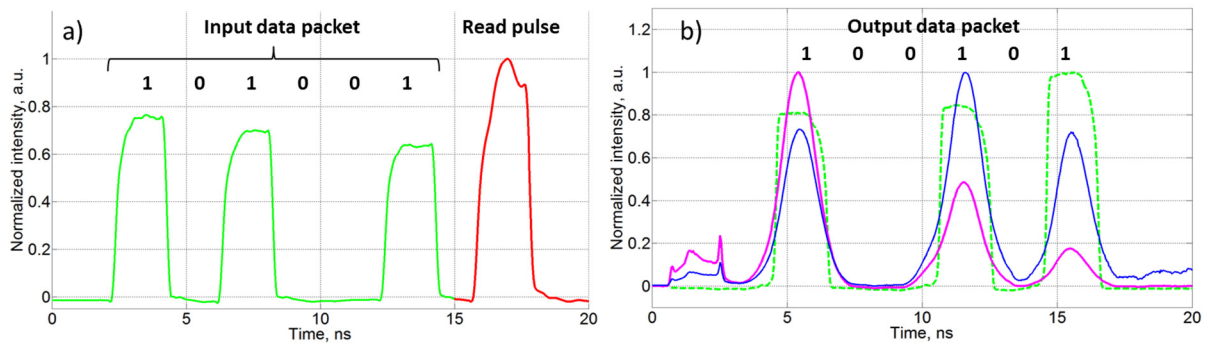

Figure 62. a) Input data packet (green line) consisting of 6 bits, 101001 together with read pulse (red line). b) Experimentally obtained time inverted output data packet consisting 6 bit with 100101 sequence without any post-correction (magenta curve) and with the exponential post-correction (blue curve). Ideal reversed input data packet (green dashed line).

To demonstrate that broadening of retrieved data pulses strongly depends on the write and read processes and that amplitude distortion is mainly determined by the DBG decay NRZ 2.5 Gbit/s data packet with bit sequence of 11101 was used to perform true time reversal. 350 ps write pulse was used to store the data in fiber, and 300 ps Gaussian-like read

pulse was used to recover time reversed data packet. Figure 63 (a),(b) and (d) depict initial data packet, write and read pulses used in experiment, respectively. Experimentally obtained time reversed data sequence of 10111 is shown in Figure 63 (c). Clearly the amplitude of the retrieved data is uniform showing only minor decay at the end of the data packet. Moreover it should be noted that phonon lifetime of a fiber is a deterministic parameter, and thus even data packets showing large amplitude distortion due to the acoustic decay can be post-processed. In addition retrieved data shows negligible broadening improving the reversal fidelity.
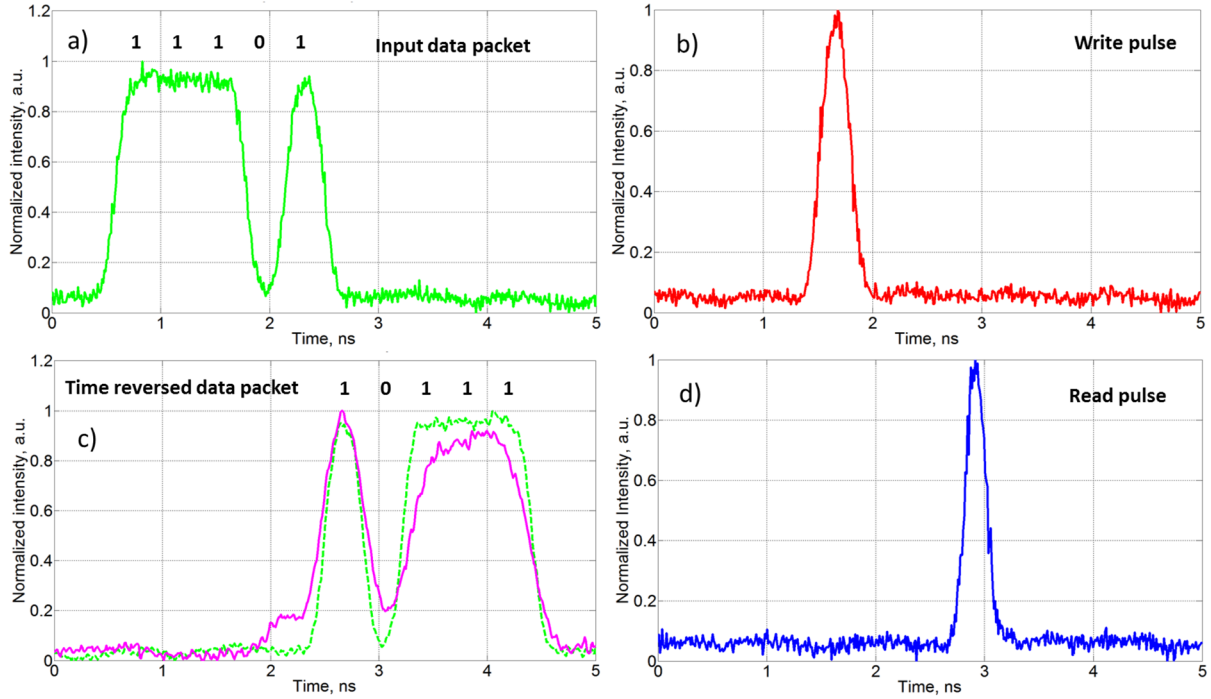

Figure 63. a) input 2.5 Gbit/s data packet with bit sequence of 11101; b) 350 ps write pulse; c) experimentally obtained (magenta line) and ideal (green dashed line) time reversed data sequence of 10111 bits; d) 300 ps read pulse.

In conclusion dynamic Brillouin grating is a unique phenomenon which can be used for various optical signal processing operations. We experimentally demonstrate that localized dynamic Brillouin grating can be used for all-optical differentiation, integration and time reversal. In addition many other signal functionalities can be realized using DBG. For instance phase modulation of the pump waves can generate DBG which represents an autocorrelation of the function which drives the phase modulator. Moreover localized DBG can be potentially used to realize logic gates: AND, NOT and others.

Bibliography

1.   A. E. Willner, Z. Bo, Z. Lin, Y. Lianshan, and I. Fazal, "Optical Signal Processing Using Tunable Delay Elements Based on Slow Light," Selected Topics in Quantum Electronics, IEEE Journal of **14**, 691-705 (2008).

2.   S. A. Hamilton, B. S. Robinson, T. E. Murphy, S. J. Savage, and E. P. Ippen, "100 Gb/s Optical Time-Division Multiplexed Networks," J. Lightwave Technol. **20**, 2086 (2002).

3.   D. K. Hunter, M. C. Chia, and I. Andonovic, "Buffering in optical packet switches," Lightwave Technology, Journal of **16**, 2081-2094 (1998).

4.   I. Fazal, O. Yilmaz, S. Nuccio, B. Zhang, A. E. Willner, C. Langrock, and M. M. Fejer, "Optical data packet synchronization and multiplexing using a tunable optical delay based on wavelength conversion and inter-channelchromatic dispersion," Opt. Express **15**, 10492-10497 (2007).

5.   J. Capmany, and D. Novak, "Microwave photonics combines two worlds," Nat Photon **1**, 319-330 (2007).

6.   S. Chin, L. Thévenaz, J. Sancho, S. Sales, J. Capmany, P. Berger, J. Bourderionnet, and D. Dolfi, "Broadband true time delay for microwave signal processing, using slow light based on stimulated Brillouin scattering in optical fibers," Opt. Express **18**, 22599-22613 (2010).

7.   J. Sancho, S. Chin, M. Sagues, A. Loayssa, J. Lloret, I. Gasulla, S. Sales, L. Thevenaz, and J. Capmany, "Dynamic Microwave Photonic Filter using Separate Carrier Tuning based on Stimulated Brillouin Scattering in Fibers," Photonics Technology Letters, IEEE **PP**, 1-1.

8.   J. Sancho, N. Primerov, S. Chin, Y. Antman, A. Zadok, S. Sales, and L. Thévenaz, "Tunable and reconfigurable multi-tap microwave photonic filter based on dynamic Brillouin gratings in fibers," Opt. Express **20**, 6157-6162 (2012).

9.   B. L. Anderson, S. A. Collins, E. A. Beecher, C. A. Klein, and S. B. Brown, "Optically produced true-time delays for phased antenna arrays," Appl. Opt. **36**, 8493-8503 (1997).

10.   J. L. Corral, J. Marti, J. M. Fuster, and R. I. Laming, "True time-delay scheme for feeding optically controlled phased-array antennas using chirped-fiber gratings," Photonics Technology Letters, IEEE **9**, 1529-1531 (1997).

11.   W. Xue, S. Sales, J. Capmany, and J. Mørk, "Wideband 360° microwave photonic phase shifter based on slow light in semiconductor optical amplifiers," Opt. Express **18**, 6156-6163 (2010).

12.   P. Daqing, and Z. Quing, "Power-efficient grating-based scanning optical delay line for Optical Coherence Tomography," in *Biomedical Topical Meeting*(Optical Society of America, 2004), p. FH23.

13.   L. J. Wang, A. Kuzmich, and A. Dogariu, "Gain-assisted superluminal light propagation," Nature **406**, 277-279 (2000).

14.   L. V. Hau, S. E. Harris, Z. Dutton, and C. H. Behroozi, "Light speed reduction to 17 metres per second in an ultracold atomic gas," Nature **397**, 594-598 (1999).

15.   M. D. Stenner, D. J. Gauthier, and M. A. Neifeld, "The speed of information in a ´fast-light/' optical medium," Nature **425**, 695-698 (2003).

16.   J. Mørk, R. Kjær, M. van der Poel, and K. Yvind, "Slow light in a semiconductor waveguide at gigahertz frequencies," Opt. Express **13**, 8136-8145 (2005).

17.   Y. A. Vlasov, M. O'Boyle, H. F. Hamann, and S. J. McNab, "Active control of slow light on a chip with photonic crystal waveguides," Nature **438**, 65-69 (2005).

18.   F. Xia, L. Sekaric, and Y. Vlasov, "Ultracompact optical buffers on a silicon chip," Nat Photon **1**, 65-71 (2007).

19.   M. Gonzalez-Herraez, K. Y. Song, and L. Thevenaz, "Optically controlled slow and fast light in optical fibers using stimulated Brillouin scattering," Applied Physics Letters **87**, - (2005).

20.   L. Thevenaz, "Slow and fast light in optical fibres," Nature Photonics **2**, 474-481 (2008).

21.   J. Sharping, Y. Okawachi, and A. Gaeta, "Wide bandwidth slow light using a Raman fiber amplifier," Opt. Express **13**, 6092-6098 (2005).

22.   E. Shumakher, A. Willinger, R. Blit, D. Dahan, and G. Eisenstein, "Large tunable delay with low distortion of 10 Gbit/s data in a slow light system based onnarrow band fiber parametric amplification," Opt. Express **14**, 8540-8545 (2006).

23.   K. Y. Song, K. Lee, and S. B. Lee, "Tunable optical delays based on Brillouin dynamic grating in optical fibers," Opt. Express **17**, 10344-10349 (2009).

24.   R. W. Boyd, *Nonlinear optics* (Academic Press, Amsterdam ; Boston, 2008).

25.   J. S. Dura, "Photonic-assisted RF Signal Processing based on Slow and Fast Light Technological Platforms," in *Department of Communications*(Polytechnical University of Valencia, Valencia, 2012).

26.   J. A. L. Soler, "Slow Light Eects in Photonic Integrated Circuits with Application to Microwave Photonics," in *Department of Communications*(Polytechnical University of Valencia, Valencia, 2012).

27.   K. Y. Song, and H. J. Yoon, "Observation of narrowband intrinsic spectra of Brillouin dynamic gratings," Opt. Lett. **35**, 2958-2960.

28.   A. Melloni, M. Frasca, A. Garavaglia, A. Tonini, and M. Martinelli, "Direct measurement of electrostriction in optical fibers," Opt. Lett. **23**, 691-693 (1998).

29.   Y. Antman, N. Primerov, J. Sancho, L. Thevenaz, and A. Zadok, "Localized and stationary dynamic gratings via stimulated Brillouin scattering with phase modulated pumps," Opt. Express **20**, 7807-7821 (2012).

30.   Y. Antman, N. Primerov, J. Sancho, L. Thevenaz, and A. Zadok, "Long Variable Delay and Distributed Sensing Using Stationary and Localized Brillouin Dynamic Gratings," (Optical Society of America, 2012), p. JW2A.24.

31.   Y. Antman, N. Primerov, J. Sancho, L. Thevenaz, and A. Zadok, "Variable delay using stationary and localized Brillouin dynamic gratings," S. M. Shahriar, and F. A. Narducci, eds. (SPIE, San Francisco, California, USA, 2012), pp. 82730C-82738.

32.   K. Hotate, and Z. He, "Synthesis of Optical-Coherence Function and Its Applications in Distributed and Multiplexed Optical Sensing," J. Lightwave Technol. **24**, 2541 (2006).

33.   M. Santagiustina, and L. Ursini, "Dynamic Brillouin gratings permanently sustained by chaotic lasers," Opt. Lett. **37**, 893-895 (2012).

34.   J. Capmany, B. Ortega, and D. Pastor, "A tutorial on microwave photonic filters," Lightwave Technology, Journal of **24**, 201-229 (2006).

35.   D. Cotter, R. J. Manning, K. J. Blow, A. D. Ellis, A. E. Kelly, D. Nesset, I. D. Phillips, A. J. Poustie, and D. C. Rogers, "Nonlinear Optics for High-Speed Digital Information Processing," science **286**, 1523-1528 (1999).

36.   J. Azaa, "Ultrafast Analog All-Optical Signal Processors Based on Fiber-Grating Devices," Photonics Journal, IEEE **2**, 359-386 (2010).

37.   M. Kulishov, and J. Azaña, "Long-period fiber gratings as ultrafast optical differentiators," Opt. Lett. **30**, 2700-2702 (2005).

38.   Y. Park, J. Azaña, and R. Slavík, "Ultrafast all-optical first- and higher-order differentiators based on interferometers," Opt. Lett. **32**, 710-712 (2007).

39.   M. A. Preciado, V. Garcia-Muñoz, and M. A. Muriel, "Ultrafast all-optical Nth-order differentiatorbased on chirped fiber Bragg gratings," Opt. Express **15**, 7196-7201 (2007).

40.   M. A. Preciado, and M. A. Muriel, "Ultrafast all-optical Nth-order differentiator and simultaneous repetition-rate multiplier of periodic pulse train," Opt. Express **15**, 12102-12107 (2007).

41.   R. Slavík, Y. Park, M. Kulishov, R. Morandotti, and J. Azaña, "Ultrafast all-optical differentiators," Opt. Express **14**, 10699-10707 (2006).

42.   N. Q. Ngo, S. F. Yu, S. C. Tjin, and C. H. Kam, "A new theoretical basis of higher-derivative optical differentiators," Optics Communications **230**, 115-129 (2004).

43.   M. Li, D. Janner, J. Yao, and V. Pruneri, "Arbitrary-order all-fiber temporal differentiator based on a fiber Bragg grating: design and experimental demonstration," Opt. Express **17**, 19798-19807 (2009).

44.   N. K. Berger, B. Levit, B. Fischer, M. Kulishov, D. V. Plant, and J. Azaña, "Temporal differentiation of optical signals using a phase-shifted fiber Bragg grating," Opt. Express **15**, 371-381 (2007).

45.   N. Q. Ngo, "Optical integrator for optical dark-soliton detection and pulse shaping," Appl. Opt. **45**, 6785-6791 (2006).

46.   N. Quoc Ngo, "Design of an optical temporal integrator based on a phase-shifted fiber Bragg grating in transmission," Opt. Lett. **32**, 3020-3022 (2007).

47.   R. Slavík, Y. Park, N. Ayotte, S. Doucet, T.-J. Ahn, S. LaRochelle, and J. Azaña, "Photonic temporal integrator for all-optical computing," Opt. Express **16**, 18202-18214 (2008).

48.   J. Azaña, "Proposal of a uniform fiber Bragg grating as an ultrafast all-optical integrator," Opt. Lett. **33**, 4-6 (2008).

49.   L. R. Chen, S. D. Benjamin, P. W. E. Smith, J. E. Sipe, and S. Juma, "Ultrashort pulse propagation in multiple-grating fiber structures," Opt. Lett. **22**, 402-404 (1997).

50.   I. Y. Dodin, and N. J. Fisch, "Dynamic volume holography and optical information processing by Raman scattering," Optics Communications **214**, 11 (2002).

51.   Z. Zhu, D. J. Gauthier, and R. W. Boyd, "Stored Light in an Optical Fiber via Stimulated Brillouin Scattering," science **318**, 1748-1750 (2007).

52.   M. Fink, and et al., "Time-reversed acoustics," Reports on Progress in Physics **63**, 1933 (2000).

53.   H. T. Nguyen, J. B. Andersen, and G. F. Pedersen, "The potential use of time reversal techniques in multiple element antenna systems," Communications Letters, IEEE **9**, 40-42 (2005).

54.   D. Marom, D. Panasenko, R. Rokitski, P.-C. Sun, and Y. Fainman, "Time reversal of ultrafast waveforms by wave mixing of spectrally decomposed waves," Opt. Lett. **25**, 132-134 (2000).

55.   D. A. B. Miller, "Time reversal of optical pulses by four-wave mixing," Opt. Lett. **5**, 300-302 (1980).

56.   N. W. Carlson, L. J. Rothberg, A. G. Yodh, W. R. Babbitt, and T. W. Mossberg, "Storage and time reversal of light pulses using photon echoes," Opt. Lett. **8**, 483-485 (1983).

57.   F. Coppinger, A. S. Bhushan, and B. Jalali, "Time reversal of broadband microwave signals," Electronics Letters **35**, 1230-1232 (1999).

58.   A. Rebane, J. Aaviksoo, and J. Kuhl, "Storage and time reversal of femtosecond light signals via persistent spectral hole burning holography," Applied Physics Letters **54**, 93-95 (1989).

Chapter 5.

Distributed temperature and stress sensing using DBG

Distributed fiber sensing is an area of research which has a history of more than 30 years. The reasons why fiber-optic sensors showed up as a competitive technology are numerous. For example sensors can be very lightweight, small, compact, easily muliplexable, immune to electro-magnetic interference, require no electrical power at the sensing point, and can be potentially produced at low cost [1]. Moreover probably one of the main advantages of fiber optic sensing techniques over the conventional sensor technologies is the capability to perform distributed measurement of the parameter of interest. Such sensors can determine single or multiple measurands as a function of location along the entire length of the sensing fiber. Applications of distributed fiber sensors include measurement of strain [2-5], temperature [6-8], pressure [9], electric and magnetic fields [10], UV radiation and vibrations [11]. Another field of application can be stress monitoring in large civil structures, leakage and crack detection in pipelines, power cables, pressure vessels and others [12, 13].

First distributed measurements of the scattered light were proposed at the end of 1970s. Rayleigh backscattered light from the pulsed wave was recorded on the oscilloscope to determine the fiber attenuation coefficient [14]. This technique later became known as an optical time domain reflectometry (OTDR). Information about the fiber attenuation, connector positions, and fault locations can be retrieved from the time trace of the variations in backscattering light intensity. With wide implementation of optical fibers in communication networks this technique became one of the standards to estimate fiber's length, overall attenuation, splice losses in the fiber link. Operation of such a distributed sensor can be understood easily. An intense pulse is sent into the fiber and Rayleigh backscattered light is recorded as a function of time. Knowing the speed of light in silica time domain waveform can be represented in spatial domain, allowing finding fault locations inside the fiber where scattered light has abnormally high intensities. In 1982 OTDR technique was first time used to measure distributed temperature along the fiber [15]. Later on another scattering mechanism was used for distributed measurements. In 1983 Raman scattering was used to determine the wavelength dependent loss of the fiber using OTDR [16]. Polarization optical time-domain reflectometry was proposed to measure the distribution along the length of the fiber different external influences, such as magnetic field, electric field, temperature, and mechanical stress [17]. This technique is based on monitoring of the polarization state of the back-reflected light, which is affected by the above mentioned influences. Just two years later Raman scattering was successfully exploited to realize distributed measurement of the temperature along the 1-km-long fiber [18]. Sensor was implemented using the time-resolved measurement of the ratio between the temperature-independent Stokes and temperature-dependent anti-Stokes Raman backscattered signal along the fiber. Nowadays Raman distributed temperature sensor is commercially available technology, which offers sensing

distances of 2-10 km with meter spatial resolution and 0.1 ^{0}C temperature resolution. The main challenge for Raman based DTS is low backscattered intensity of the anti-Stockes light. This in turn requires high peak powers of the pump pulses and highly sensitive detection schemes. That is why it is difficult to increase the sensing range for more than 10 km for Raman distributed sensors. Actually since useful signal is quite weak, multimode fibers are preferable to collect more scattered light. The downside of using the multimode fiber is intermodal dispersion, which makes spreading of the pump pulse and thus spatial resolution of 1 m is difficult to keep after 10 km.

Frequency modulated continuous wave method is realized using modulation the optical frequency of the source with a saw tooth waveform. This way the spectrum of the scattered light carries the spatial distribution of the measured variable. Interference of the reference beams and reflected light is detected and analyzed [19]. In optical coherence domain reflectometry an optical coherence function is synthesized in a sensing fiber, which returns the measured variable information at a certain distance. Another way to extract spatial information is to use interferometric system, such as Sagnac loop together with Michelson or another Sagnac interferometer.

By exploring another inelastic scattering component of the scattered light Brillouin distributed sensor was proposed as alternative technique to the classical OTDR [20]. The principle of operation can be understood by looking at the Figure 7.1. Optical pump pulse is launched inside the fiber under test and a continuous wave probe signal is propagating through the fiber in the opposite direction.
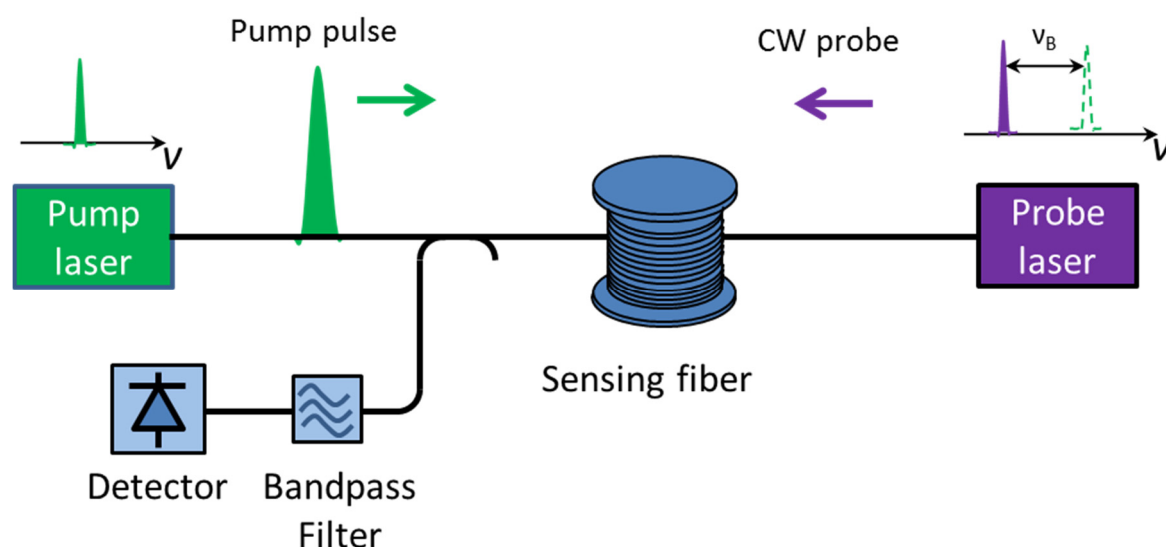

Figure 64. Experimental realization of the BOTDA technique. Frequency of the probe laser is down-shifted from the Pump laser by the Brillouin shift of the fiber.

The probe intensity is amplified through the stimulated Brillouin scattering process if the frequency difference between the optical waves is tuned to the Brillouin frequency shift of the fiber. By measuring the time decay of the probe wave it is possible to determine the length-dependent fiber attenuation. This technique was named as Brillouin optical time domain analysis (BOTDA). It was soon figured out that Brillouin scattering has other potentialities such as to measure distribution of the temperature and stress along the fiber [21-

23]. This was possible because Brillouin frequency shift of the fiber is linearly proportional to strain and temperature. Importantly optical signal power in BOTDA can be several times higher than that measured in conventional OTDA. Brillouin based techniques yields long-distance sensors with good spatial resolution. Experiments demonstrating sensing range of more than 100 km have been demonstrated using Brillouin distributed sensor systems [24, 25]. Optical coherence domain reflectometry (OCDR) and optical coherence domain analysis (OCDA) are two techniques which employ frequency modulation of continuous optical waves to generate complex coherence function inside the sensing fiber, which returns the measured-variable information from a certain distance. OCD techniques offer cm-scale spatial resolution, but the measurement range is rather limited to a maximum of few kilometers. Good reviews of different distributed fiber sensors techniques can be found in [1, 12, 13, 26-28]

In this chapter we describe the Brillouin optical time domain technique. Mechanisms of BOTDA sensor which allow distributed sensing of temperature and stress will be outlined. Limitations of this technique will be also explained. Novel BOTDA techniques based on Brillouin dynamic grating will be presented. First technique is based on the generation of BDG inside the PM fibers. Record spatial resolution of ~1 cm of all existing BOTDA system is demonstrated using this technique. Another DBG based sensor is demonstrated using PRBS phase modulation. Experimental realization and performance will be demonstrated showing truly random access sensor.

5.1. Brillouin distributed time domain sensors.

After demonstrating by Horiguchi et etc. the first realization of BOTDA sensors to measure the attenuation of the fiber it was anticipated that sensor based on stimulated Brillouin scattering can be also used to measure temperature and stress. The reason for this was that stimulated Brillouin scattering is a process where strict phase matching condition has to be satisfied for process to occur. The later condition comes from the fact that optical phonons involved in the process of Stimulated Brillouin scattering have relatively long lifetime in optical fibers, resulting in the Brillouin resonance of only ~27 MHz in standard single mode fibers. As it was demonstrated in previous chapters Brillouin shift in optical fibers is determined by the acoustic velocity, refractive index and wavelength of the pump through the relation:

$$v_B = \frac{2nV}{\lambda_p} \qquad (4.1.1)$$

Moreover in chapter 4 it was demonstrate that acoustic velocity in the silica fibers is related to the bulk modulus through relation (4.1.55):

$$V^2 = \frac{1}{C_s \rho} = \frac{K}{\rho} \qquad (4.1.2)$$

where C_s is adiabatic compressibility, K is the bulk modulus, and ρ is density of the silica. It is clear that since material density of the fiber is temperature dependent than the acoustic velocity is changing with temperature resulting in a shift of Brillouin frequency. As it is clear from equation 7.1.1 Brillouin frequency shift can be changed due to the change in acoustic velocity and also due to the change in refractive index of the fiber. In the case of applied tensile stress v_B changes mainly due to the change in acoustic velocity rather than due to the refractive index. Various measurements showed that by applying the longitudinal stress to the fiber under test Brillouin shift moves linearly to the higher frequencies with a slope of ~551 MHz/% ε [12, 29]. It should be pointed out that strain coefficient is different for fibers with different geometries and different composition. On the other hand variation of Brillouin shift due to the temperature in the range from 20 C to 1620 C is mainly given by the change in refractive index, and change in acoustic velocity is only 7%. Many research groups were investigating the dependence of Brillouin shift with temperature and stress. The latest measurements shows that in the range from 200 up to 600 K Brillouin shift of the fiber moves linearly with temperature with the slope of ~1.2 MHz/C. Temperature dependence coefficient of the Brillouin shift is also slightly changed depending on the chemical composition of the core and cladding of the fiber, ranging from 1.17 to 1.36 MHz/ C. In addition dopant concentration of the core changes the value of the Brillouin shift itself as well as the width of Brillouin resonance [30, 31]. This way using temperature and stress dependence of the Brillouin shift of the fiber it was possible to build quite simple technique to measure the distributed temperature and stress, simply by measuring the peak of the Brillouin interaction between the probe and pump wave. To retrieve the peak of Brillouin interaction at any location along the fiber sweeping of the CW probe frequency is performed. By determining the peak of the Brillouin shift as a function of distance distributed profile of the temperature or strain can be easily retrieved.

BOTDA technique possesses several advantages over other distributed techniques such as low attenuation in standard single mode fibers can provide several tens of kilometers of measurement range, information about measurand is retrieved from frequency measurement as opposed to intensity-based techniques, and stimulated process of Brillouin scattering offer high signal-to-noise ratio. As for disadvantages of the system we can mention following sides: BOTDA system requires access to two ends of the sensing fiber, which can be a problem in some applications, in addition Brillouin interaction depends on the interference efficiency of the pump and probe waves, which means that polarization of interacting optical waves should be the same for maximum interference. As polarization of the light in single mode fiber changes randomly along its length Brillouin interaction will vary with position. This requires application of polarization diversity scheme or polarization scrambling, which increases the measurement time. And probably the main limitation of the BOTDA system is the spatial resolution is restricted to 1 m due to the acoustic lifetime. This limitation comes from the fact that if pump pulse spectrum spreads over the bandwidth larger than the natural Brillouin gain spectrum, reflected signal show a spectrum which will be given by the convolution between pump pulse and natural Brillouin spectra [32]. Moreover Brillouin gain is reduced when pump pulse width is decreased. To precisely determine the

peak of the broad gain spectrum is quite difficult, which as consequence reduces the measurement accuracy.

Several modern techniques were demonstrated in order to overcome limitation of the spatial resolution. For example in 2000 Hotate *et al.* proposed Brillouin optical correlation analysis. In this method by using correlation point between the two frequency modulated continuous optical waves it is possible to localize the Brillouin interaction between the two waves in a controlled position inside the fiber. Moreover width of the correlation point where stimulated Brillouin scattering occurs can be controlled by changing the frequency modulation parameters. Spatial resolution down to 1 cm was demonstrated using this technique. The only severe drawback of proposed scheme is that high spatial resolution comes at the expense of measurement range. This fact limits the measurement range to several tens of meters if spatial resolution is wished to be kept in the order of cm.

Later, several new schemes were proposed to offer cm scale spatial resolution using time-domain techniques. Such techniques use pre-excitation of the acoustic wave with long pre pulse or a CW residual component of the short pump pulse, where pump pulse can be bright, dark or phase pulse [33-36]. Short pump pulses with time duration much shorter than phonon lifetime (τ_p) are used in such techniques. By using slow and inertial behavior of the acoustic wave fast changes in pump wave can be reflected by the acoustic wave which was generated by the pre excitation part of the pump wave. Short reflected part of the pump wave induces a brief stamp on the counter-propagating probe wave. Using fast detector such brief stamp in the receiving probe gives information about temperature or stress inside the fiber at very short precise position determined by the short feature of the pump wave. Since acoustic wave is activated by the CW (or quasi CW) optical wave Brillouin gain spectrum has its natural width. Thus methods using pre-activation of acoustic wave offer high sensitivity to temperature and strain together with high-spatial resolution. While dark or bright pump pulse based techniques show similar performances in term of sensing range and spatial resolution, π phase pump pulse technique called Brillouin Echo Distributed Sensing (BEDS) offers twice better response in identical power conditions due to the higher contrast of the imprinted stamp on the probe wave. BEDS system demonstrated 5 cm spatial resolution over the 5 km long fiber.

5.2. Distributed sensing using dynamic Brillouin grating.

Dynamic Brillouin grating principle can also be used for distributed temperature and strain sensing. There are two possibilities to realize distributed sensor using DBG. One way is to generate the acoustic wave all along the sensing fiber and obtain the amplitude of the acoustic wave with a read signal at each point along the fiber. In this technique spatial resolution is given by the reading process or in another way how close in space we can sample the amplitude of the acoustic wave along the fiber. Another way is to localize the generation of the dynamic Brillouin grating at a specific position inside the fiber and then retrieve the parameters of the DBG at this specific position. By sweeping the DBG localization point

distribution of the acoustic wave parameters and consequently temperature and/or stress distribution can be retrieved along the whole sensing fiber. In this case spatial resolution is given by the ability of the system to localize the SBS interaction. In the following sections we consider both sensing techniques using DBG principle.

5.2.1. Principle of DBG based OTDA

Consider a situation when dynamic Brillouin grating is generated in the polarization maintaining fiber through SBS process as shown in Figure. 7.2. Two counter-propagating pump pulses at the optical frequencies v_{p1} and v_{p2}, where $v_{p1} - v_{p2} = v_B$, are launched along the one primary polarization axis of the PMF under test. In this case acoustic wave is generated all along the fiber due to SBS interaction between the two pump waves. In this case both waves are chosen in such way that generated acoustic wave has maximum amplitude along the entire sensing fiber. For this reason pump 1 wave is pulsed. First of all this drastically raise its peak power. Moreover this procedure limits the interacting length between the two pump waves avoiding massive power transfer from pump 1 to pump 2. In CW operation power transfer can deplete the pump 1 wave resulting in generation of the acoustic grating only within few meters of the fiber. On the other hand pulse width of pump 1 must not be too short to avoid Brillouin gain broadening. As it was mentioned before when pump pulse spectrum becomes broader (typically < 10 ns) than that of the natural Brillouin gain spectrum width acquired gain spectrum broadens according to the convolution of the natural BGS with the normalized pump power spectrum. This fact degrades the accuracy of the measurements. This is the main limitation of the all classic BOTDA techniques.

After the narrowband DBG was generated by the *x*-polarized pump waves *y*-polarized probe pulse is launched to read the amplitude of the grating. The overall probe reflection will be given by the spectral overlap between the DBG spectrum and probe pulse spectrum. Moreover the amplitude also depends on the strength of the DBG which is proportional to the frequency separation between two pump waves. This way by changing the frequency difference between the pump waves it is possible to generate DBG with different frequency and amplitude and retrieve the Brillouin gain spectrum at each position inside the fiber. It should be pointed out that spatial resolution is determined by the duration of the probe pulse, while the bandwidth of the Brillouin gain is related to the duration of pump 1. Thus high spatial resolution BOTDA can be realized while keeping narrow effective BGS. In this situation probe reflection from DBG can be compared with the reflection of probe pulse from FBG. The overall reflected waveform is a coherent sum of the reflected components generated as the input pulse propagates through the dynamic grating. Thus there is no bandwidth limitation from the DBG when using short probe pulse. Actually short probe pulse experiences a reflection proportional to the local grating amplitude and its backscattered time distribution provides a map of the DBG local amplitude.
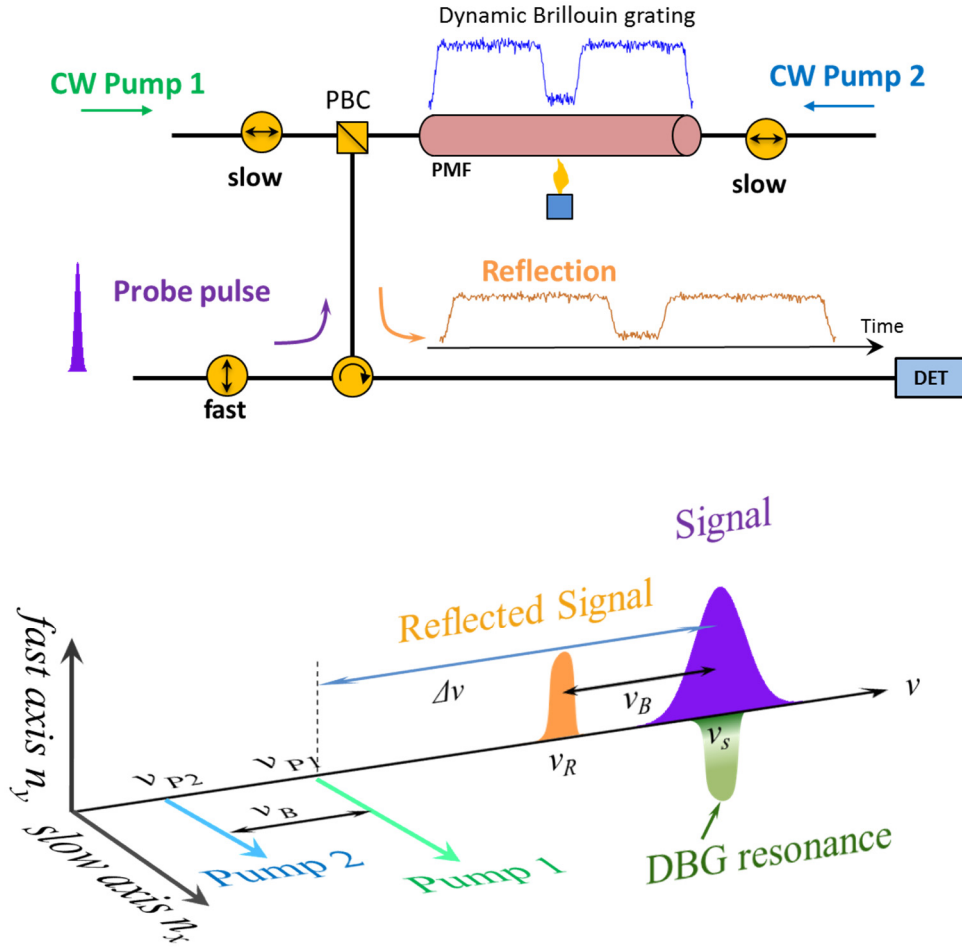
Figure 65. Schematic representation of a DBG-based distributed sensor. Two continuous wave pumps are polarized along the *x*-axis (slow) and probe pulse is polarized along the *y*-axis (fast).

5.2.1.1.   Experimental implementation.

Experimental setup to realize DBG based distributed sensor is depicted in Figure 7.3. Two distributed feedback laser diodes (DFB LD) were used to generate pump and probe waves. 20 m PM fiber was used as a sensing medium with Brillouin frequency of ~10.82 GHz at the 1551 nm. Temperatures of the two 1.5 cm sections of the fiber under test were controlled by thermo-electric cooler (TEC) as shown in Figure 7.3. Emission from DFB-LD 1 was divided by the 50/50 fiber coupler. Light in the lower arm of the coupler was used to generate 30 ns square pump 1 pulse with repetition rate of 1 MHz using an electro-optic modulator (EOM 1) and a pulse generator. After generation pump 1 pulse was amplified to 26 dBm using Er-doped amplifier (EDFA), polarized along the slow axis using in-line polarizer and launched into the fiber. Light from the upper arm of the coupler was amplitude modulated at frequency in the vicinity of v_B using EOM2 and radio frequency generator. Afterwards pump2 was amplified using another EDFA up to 14 dBm and launched inside the fiber along the slow axis counter-propagating to the pump 1 pulse.

To generate probe pulse another laser diode was used (DFB-LD 2). Using gain-switching technique 116 ps bell-shaped pulse was obtained. After amplification by another EDFA probe pulse was polarized along the fast axis and redirected to the FUT using polarization maintaining circulator in the same direction as pump 1 pulse. Launching of probe pulse was synchronized to pump 1 pulse so that probe pulse enters the fiber under test directly after the pump 1 pulse. This secures that dynamic Brillouin grating is generated efficiently with the long pump 1 pulse before being interrogated by the probe pulse.
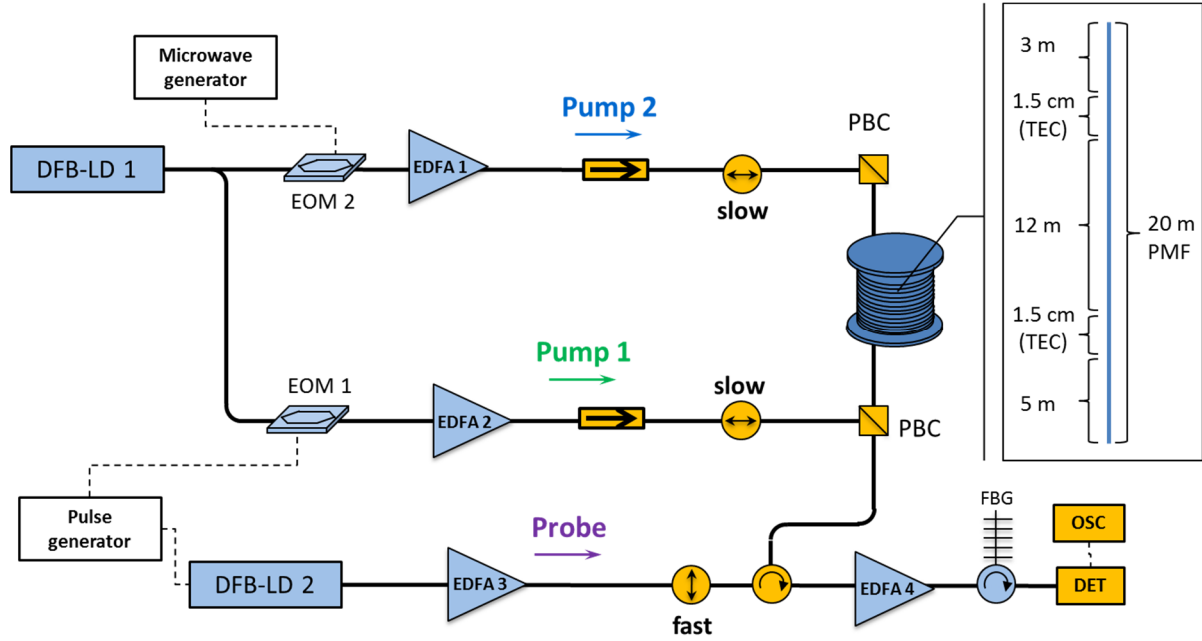
Figure 66. Experimental setup to realize high spatial resolution DBG based BOTDA using polarization maintaining fiber. EOM: electro-optical modulator; FBG: fiber Bragg grating; EDFA – Er-doped fiber amplifier; PBC: polarization beam combiner; DET: photodetector; OSC: oscilloscope.

The reflection of the probe pulse while propagation through the DBG was redirected to the detecting part using circulator. Prior detection by 12 GHz photodetector reflection is amplified by another EDFA and spectrally cleaned up by tunable bandpass filter. Amplification and filtering is necessary due to the leakage of the pump waves, which in turn is a result of finite extinction ratio of polarization maintaining components. The reflection of the probe wave by dynamic Brillouin grating was observed when probe frequency was set 44 GHz higher than that of the pump 1 frequency.

Fiber under test was kept at 24 ^{0}C during the experiment. Temperature differences of -5, +25 and +50 ^{0}C were applied to two 1.5 cm segments of the fiber under test using TEC. For each temperature change we obtained reflection of the probe pulse while sweeping the frequency difference from 10.77 GHz to 10.92 GHz between pump 1 and pump 2 waves. Reflected waveform was obtained using 32 times averaging for each frequency spacing between the pump waves. Frequency scan was accomplished with 1 MHz step. Figures 7.4 (a-c) show distributions of the Brillouin gain spectrum along the fiber for different applied temperature changes. Determining the peak of the Brillouin gain curve at each position distribution of the Brillouin frequency shift along the fiber was measured.
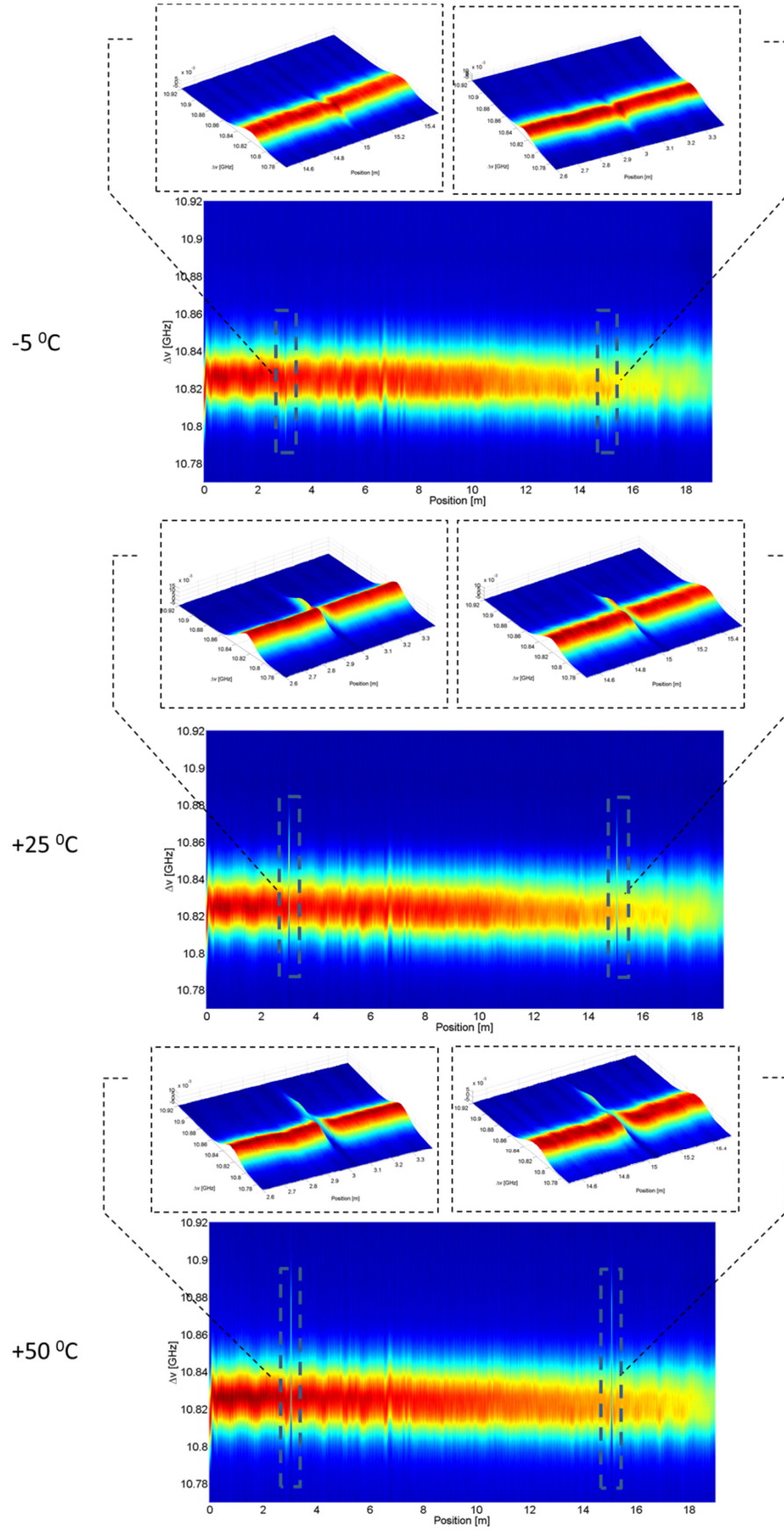
Figure 67. 3-d plots of distributed Brillouin gain spectra for three temperature differences applied – ΔT= -5, +25, and +50 ⁰C, respectively. Zoomed views at the positions of the hot spots are provided in the dashed boxes.

Results are presented in the Figure 7.5. Clear shifts of the Brillouin frequency are observed at the heated sections confirming high spatial resolution of the measurements. The zoomed views of the temperature-controlled section are also shown in Figure 7.5. The gradual transition of the Brillouin shift over several cm between the heated segment and the rest of the fiber is due to the heat conduction along the fiber. Thermal diffusion length is estimated around 3 cm in a 125 um silica fiber. Slight discrepancies between the measurement results of two heated sections comes from the imperfect contact between the fiber and the TEC. Temperature change applied to the fiber results in a decrease of the amplitude of the reflected signal due to the shift of the dynamic Brillouin grating spectrum. Thermal dependence of the fiber birefringence shifts the central reflection frequency of the DBG with the amount of 50 MHz/K [37]. In our experiment 7 GHz probe pulse spectrum secures a sufficient signal-to-noise ratio over a fairly large temperature range.
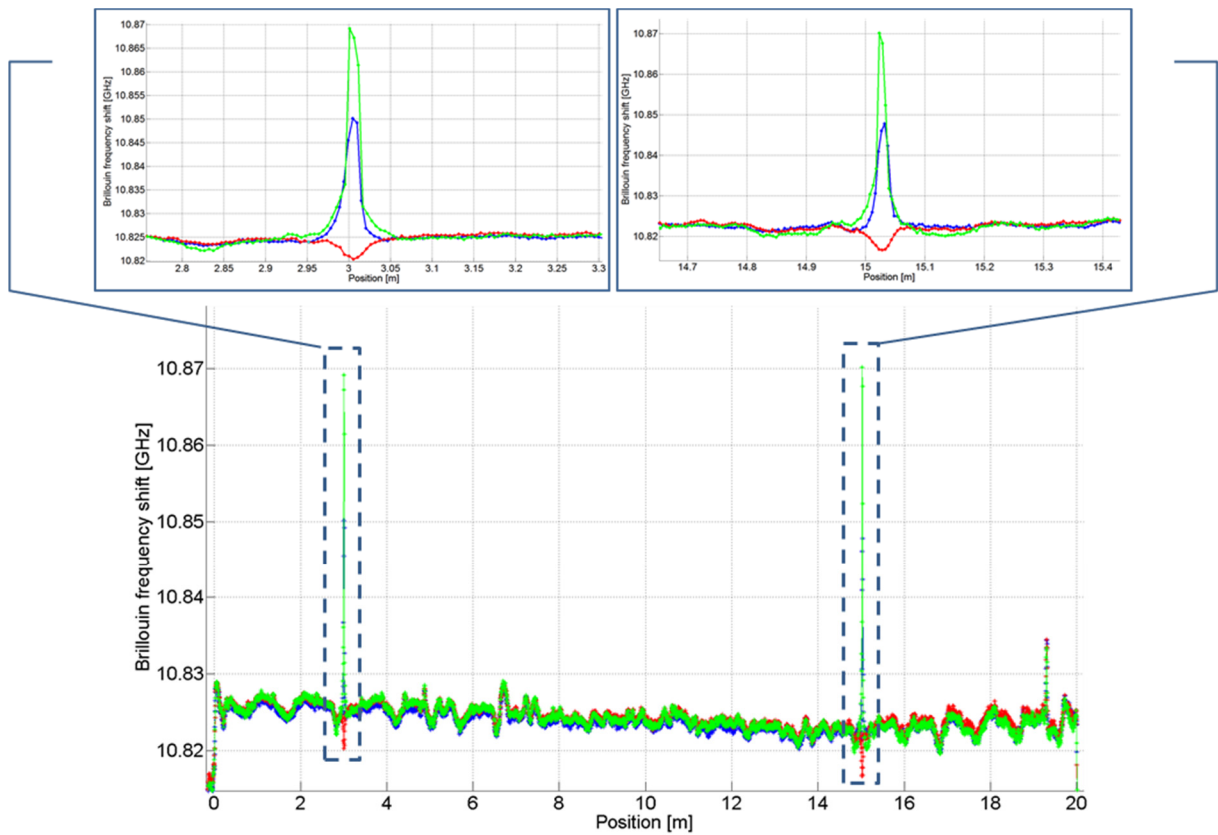
Figure 68. Distribution of the Brillouin frequency along the fiber under test, where temperature change of -5 (red curve), +25 (blue curve), and +50 ^{0}C (green curve) was applied to two 1.5 cm sections.

It is clear that cm and sub-cm resolution BOTDA system can be realized using DBG principle in a polarization-maintaining fiber. As it was demonstrated spatial resolution is no longer limited by the spectrum of the probe pulse, since in the proposed technique probe pulse is negligibly involved in the acoustic grating generation. The sensing range can be certainly extended to several hundreds of meters. On the other hand km range will be difficult to reach since polarization of the waves is unlikely to be maintained over this distance. In addition critical power for amplified spontaneous scattering will be reached for CW pump 2 wave.

5.2.2. Correlation based BOTDA.

Another possibility to implement DBG based distributed temperature and strain sensor is to localize the Brillouin interaction inside the specific position of the fiber under test and read the properties of the acoustic wave at this position with a probe wave. In standard BOTDA systems localization of the Brillouin interaction between two optical waves is achieved using amplitude modulation of one of the waves, normally pump wave. Than spatial information about Brillouin interaction at a given position can be extracted knowing time of flight of the pump pulse. In this technique the shorter pump pulses of course provide finer spatial resolution. On the other hand pulses shorter than acoustic damping time of around 12 ns result in a weaker SBS interaction and broader reflection spectrum, which in turn worsen the measurement accuracy. This fact limits the resolution of classical BOTDA systems to 1 m. Several methods were employed to overcome this limitation offering an order-of-magnitude higher spatial resolution, but with higher complexity of the experimental setup.

One of the alternate approaches is called Brillouin optical correlation domain analysis [38, 39]. This technique relies on synchronous frequency modulation of both pump and probe wave. Normally single laser source is used to generate pump an probe waves. Using sine modulation of the output laser frequency in the form $f = f_0 + \Delta f \sin\left(2\pi f_m t\right)$ produces periodic correlation peaks inside the sensing fiber where two lightwaves meet with a frequency difference for SBS to occur. In all other locations between the correlation peaks frequency difference between the pump and probe wave is constantly changed with time prohibiting the SBS to occur. In this case spatial resolution is determined by the width of the correlation peak and is given by $\Delta z = V_g \Delta v_B / (2\pi f_m \Delta f)$, where V_g is the group velocity of the optical wave, Δv_B is Brillouin bandwidth, f_m is the modulation frequency of light source, and Δf is the modulation amplitude of light source. On the other hand distance between the correlation peaks determines the measurement range of the sensor and is given by the expression $L_m = V_g / (2 f_m)$. The system parameters are chosen, so that only one peak is placed inside the sensing fiber. As it can be seen spatial resolution and measurement range are both inversely related to the modulation frequency, which establish a trade-off relation in BOCDA performance. Apparently, higher resolution in BOCDA sensor comes with expense in measurement range. Thus BOCDA sensors offer centimetric spatial resolution but over a limited distance of several meters. Number of resolved points can be defined as $N = L_m / \Delta z = 2\pi \Delta f / \left(\Delta v_B\right)$ and in classical BOCDA is lower than 600 due to the limitation that Δf can't exceed $v_B / 2$. Recent developments showed that double-modulation can be implemented to enlarge the measurement range while maintain the spatial resolution [40], demonstrating improvement in N up to 5690. New BOTDA systems can achieve several thousand resolved points [36], but still cm-scale spatial resolution with large number of resolution points remains scientific challenge to overcome.

Here we propose end experimentally demonstrate novel type of distributed Brillouin temperature and/or stress fiber sensor based on PRBS [41]. Performance of the new sensor was tested in polarization maintaining fiber and standard single mode fiber. Spatial resolution

of 1 cm was achieved demonstrating resolution similar to BOCDA technique while eliminating the spatial resolution-measurement range trade-off.

5.2.2.1. **Principle of operation**

As it was demonstrated in previous chapter SBS interaction of two optical waves can be localized using phase modulation of both waves by common PRBS sequence. Obviously such local interaction inside the fiber can be used to realize distributed sensor. Consider a situation when pump and probe waves are conterpropagate in optical fiber with their frequency difference equal to the Brillouin shift of the fiber. Moreover both waves are phase-modulated by a common pseudo random bit sequence, whose symbol duration T is much shorter than phonon lifetime. As a result of phase modulation SBS-induced grating can be efficiently generated to the steady state value only at the specific position in fiber where optical waves are correlated, or in other words at the positions where phase difference between the pump and the probe wave is constant over time. Since gain of the probe wave is restricted only along the correlation peak by measuring the spectral profile of the DBG temperature or stress applied to fiber can be revealed at this position.

Localization of the DBG at the correlation peak can be represented by the schematic illustration shown in Figure 7.6. The width of the correlation peak determines the spatial resolution of the distributed sensor, and it is given by $\Delta z = V_g T / 2$, where , where V_g is the group velocity of light and T is symbol duration of PRBS sequence. In all other locations except correlation peak acoustic amplitude averages out to zero with time, thus inhibiting the SBS interaction between pump and probe wave. Separation between the adjacent correlation peaks determines the measurement range and is given by the $L = M V_g T / 2$, where M is PRBS code length. It is clear that measurement range can be easily controlled by changing the PRBS length while retaining high resolution. Thus proposed sensor is free from the trade-off measurement range-spatial resolution which is inherent to BOCDA systems. PRBS generators are capable to provide sequences with length up to $2^{31} - 1$ which results in several hundred kilometers range with 1 cm spatial resolution. Moreover it should be pointed that while phase modulated optical waves have broad power spectral density, which reduces depletion effects due to spontaneous Brillouin scattering, acoustic wave at the correlation point has spectral profile that is close to the natural Brillouin gain spectrum (~30 MHz). Gain spectrum of the probe at the correlation point is given by the convolution of the natural Brillouin gain linewidth and spectrum of the pump-probe beat at the given position inside the fiber. At the correlation point beat spectrum of optical waves resembles delta function. By varying the pump probe frequency difference the beat spectrum can be shifted along the frequency. Gain experienced by the probe wave at the correlation point varies according the Brillouin gain spectrum at this position. Thus, the BGS at the correlation peak is reflected on the variation in the probe power at the fiber output end.
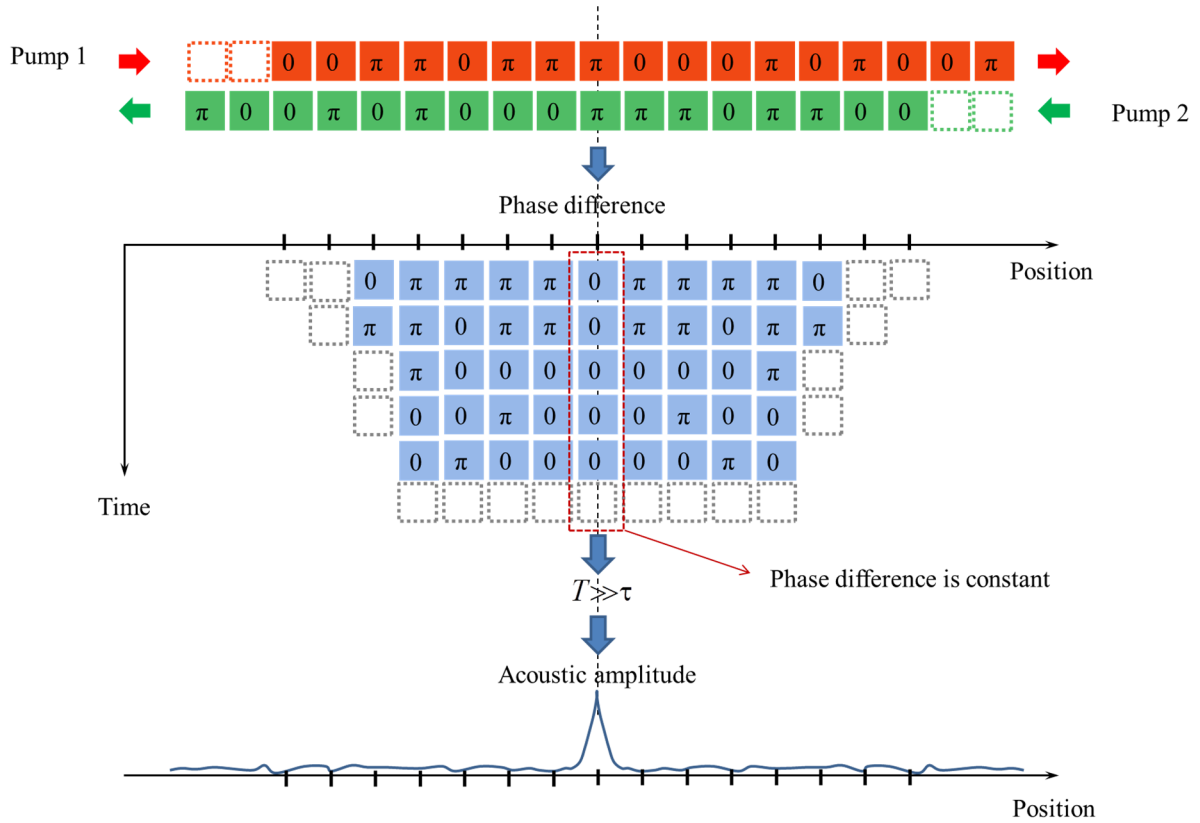
Figure 69. Principle to realize PRBS DBG based distributed temperature/stress sensor.

5.2.2.2.   Experimental setup and results

A detailed sketch of experimental setup realizing proposed sensor is shown in Figure 70. Light from a distributed feed-back laser (DFB-LD) operating at 1550 nm is launched into phase electro-optic modulator which is driven by the PRBS generator. Microwave generator is used to drive the clock rate of the PRBS generator. RF signal from microwave generator determines the symbol duration of the PRBS sequence. RF frequency was changed in the range 8-12 GHz, corresponding to the spatial resolution of 0.9 and 1.3 cm. PRBS code length of $M = 2^{15} - 1$ was set on the PRBS generator securing that only one correlation peak is present in the fiber under test. Output voltage of the PRBS generator was adjusted to reach V_π of the EOM. Phase modulated laser emission is splited into probe and pump arms using fiber coupler. Light in the probe arm was amplitude modulated at frequency v in the vicinity of fiber v_B using distinct electro-optic modulator (EOM 2) and the microwave generator (MG 2). Bias voltage of the EOM 2 was adjusted to suppress the carrier wave. This way probe wave consisted of the two sidebands at frequencies $v_{DFB-LD} \pm v$. After probe signal was launched into delay fiber of 4 km in order to place a higher order correlation peak inside the sensing fiber. Path imbalance between the probe and pump arms allows control of correlation peak position inside the sensing fiber. Probe wave was amplified by the EDFA and launched inside the one end of the fiber under test through fiber isolator. Light in the pump branch was

amplitude modulated at low frequency to be used for lock-in detection. High gain EDFA was used to amplify the pump power to 500 mW. After scrambling the polarization pump wave was redirected to the other end of the fiber under test through circulator. Polarization scrambling was used to avoid polarization dependence of the SBS interaction.

Since joint phase modulation is used for both optical waves periodic correlation peaks are generated with separation of $L = MV_gT/2$. By changing the symbol length T position of the all correlation peaks can be changed except for the central one. If a delay fiber is much longer than a total length of components in the experimental setup order of correlation peak inside the sensing fiber can be estimated as $N = round\left(D/(2L)\right) = round(D/(MV_gT))$, where D is the length of the delay fiber. It can be shown that the higher the number of the correlation peak placed inside the sensing fiber the lower the increment in the symbol duration needed to shift peak along the fiber. In our experiment 1 MHz variation in clock rate corresponded to the change in correlation peak position by 34 cm. Change of the clock rate by 1 MHz changes the spatial resolution by the amount of 6.9×10^{-7} m. To scan the sensing fiber of 40 m 117 MHz change in the clock rate is needed. This means that spatial resolution from the begging to the end of the fiber changes by the negligible amount of $\sim8\times10^{-5}$ m.
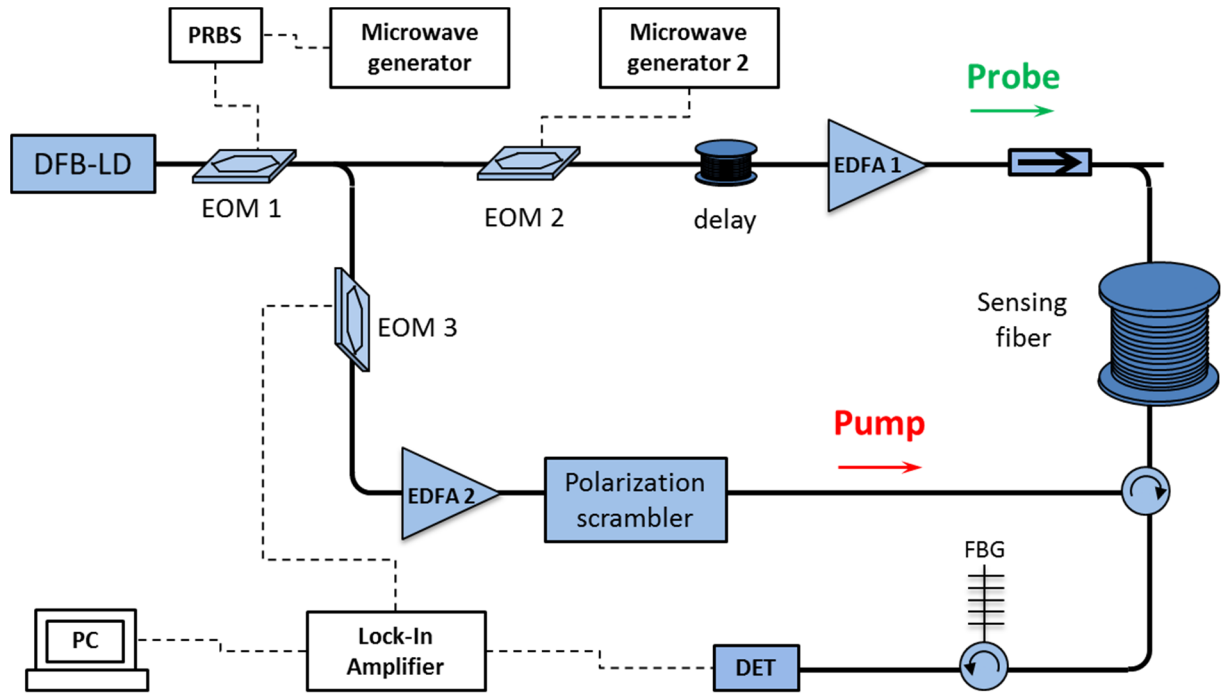
Figure 70. Experimental setup demonstrating random access SBS based distributed sensor.

Probe exiting the sensing fiber is redirected to the detection part using circulator. Lower sideband of the probe at frequency $v_{DFB-LD} - v$ was filtered using fiber Bragg grating and detected by a photo-diode. The detected current was analyzed by the lock-in amplifier. Brillouin gain spectrum at each fiber position was reconstructed by measuring the amplification of the power as a function of modulation frequency v.

Measured distribution of the Brillouin gain spectrum of the 40 m fiber is plotted in the Figure 7.8 (a). Spatial resolution of the measurement was set to 1 cm. 7 cm section of the

sensing fiber was heated using TEC. Time constant of the locking amplifier was set to 300 µsec. Brillouin gain was measured as a function of the pump-probe frequency offset with 1 MHz step and the location of the correlation peak. Zoomed part of the Brillouin gain distribution around the 7 cm heated section is shown in Figure 7.8 (b), where clear shift of the Brillouin frequency is observed demonstrating the high spatial resolution of the measurements. Experiment was repeated while length of the heated section of the fiber was changed to 1 cm. Figure 7.9 (a) shows measurements of an entire 40 m fiber, and Figure 7.9 (b) demonstrates Brillouin gain distribution around 1 cm heated section. It clear that 1 cm temperature event is clearly distinguished. In order to determine the Brillouin shift measured Brillouin gain spectrum at each position was fitted to a Lorenzian shape, and the peak of the curve was considered as a Brillouin shift. Figure 7.10 shows distribution of the Brillouin frequency shift as a function of position. 1 cm hot spot is clearly visible. The standard deviation on the estimated Brillouin frequency shift along the uniform fiber section is 0.5 MHz, corresponding to a temperature accuracy of ± 0.5 ^{0}C. Measurement range of 40 m and spatial resolution of 1 cm give 4000 resolved points. Note that measurement range can be easily increased. The maximum measurement range will be ultimately limited by the signal-to-noise ratio. The signal amplification over a cm-long correlation peak is weak, while fluctuations due to the residual off-peak scattering scale with the length of the sensing fiber. Nose fluctuations can be averaged out, but this requires longer measurement time. Moreover measurements over some hundreds of meters with fine spatial resolution require a substantial amount of time. Predicted maximum measurement range can be in the order of 1 km for 1 cm resolution, which results in impressive value of 100'000 resolution points.
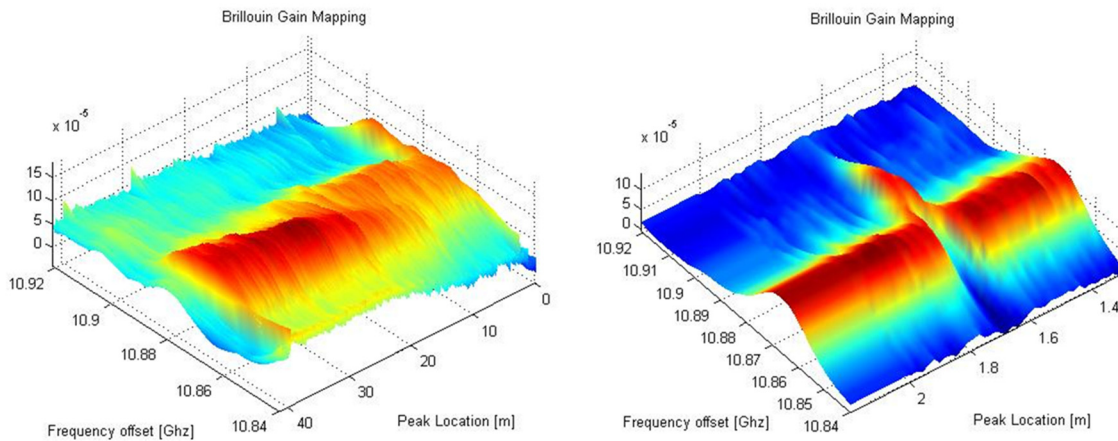
Figure 71. a) Brillouin gain spectra distribution of a 40-m-long fiber with 7 cm heated section. b) zoomed part of the Brillouin gain distribution around heated section.
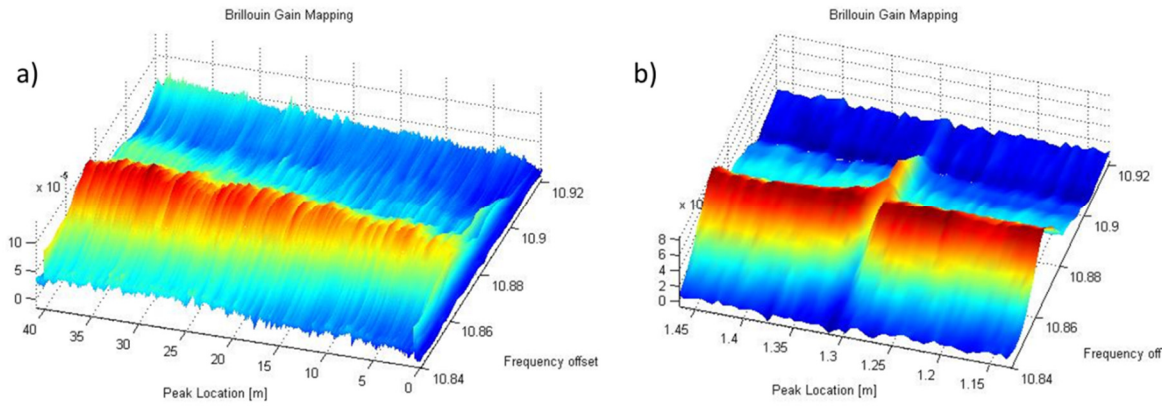
Figure 72. a) 3-d map of the Brillouin gain spectra along the 40 m fiber, where 1 cm heated section is located at the position around 1.3 m. b) Zoomed view of the heated section.
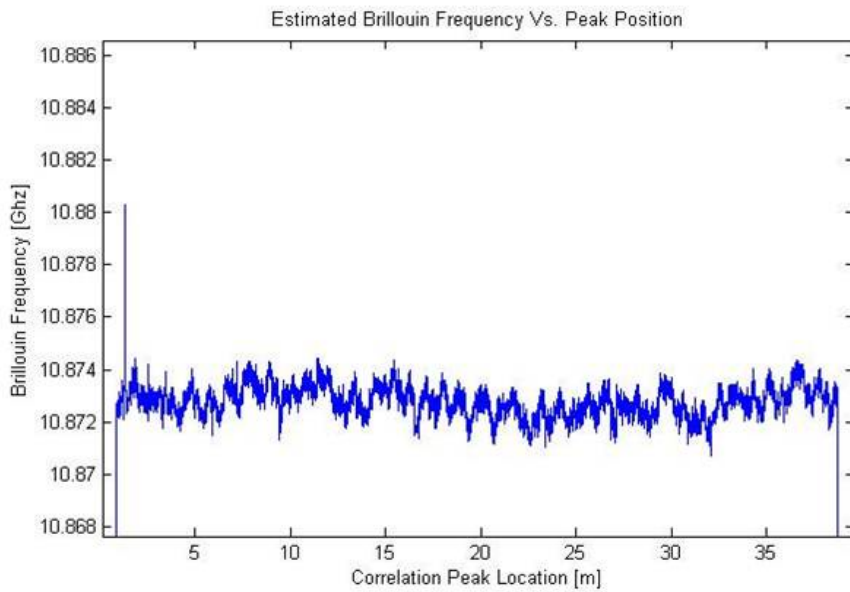
Figure 73. Distribution of the Brillouin frequency along the 40-m-long standard single mode fiber where 1 cm short section is heated.

In summary, experimental realization of the distributed temperature/stress sensor based on PRBS phase modulation was successfully demonstrated. 1 cm and 7 cm temperature change events were detected in 40 m standard single mode sensing fiber, demonstrating high spatial resolution. The 40 m measurement range offers 4000 resolved points, which remains challenging using alternative techniques. Measurement range can be certainly increased up to several hundred meters, while kilometer ranges seems difficult to reach. Probe amplification over cm-long correlation peak will be ultimately buried in noise due to the residual off-peak scattering for long measurement ranges. Thus main limitation for measurement range comes from the signal-to-noise ratio. Moreover to measure kilometer long distances with cm spatial resolution will take substantial amount of time, which is practically inconvenient. More importantly it should be stressed that spatial resolution is completely decorrelated from the measurement range in contrast to BOCDA based techniques.

Bibliography

1.   A. D. Kersey, "A Review of Recent Developments in Fiber Optic Sensor Technology," Optical Fiber Technology **2**, 291-317 (1996).
2.   L. Thevenaz, M. Nikles, A. Fellay, M. Facchini, and P. Robert, "Truly distributed strain and temperature sensing using embedded optical fibers," Smart Structures and Materials 1998: Sensory Phenomena and Measurement Instrumentation for Smart Structures and Materials **3330**, 301-314, 450 (1998).
3.   D. Uttamchandani, B. Culshaw, M. S. Overington, M. Parsey, M. Facchini, and L. Thevenaz, "Distributed sensing of strain in synthetic fibre rope and cable constructions using optical fibre sensors," Fiber Optic Sensor Technology and Applications **3860**, 273-275, 556 (1999).
4.   S. Liehr, P. Lenke, M. Wendt, K. Krebber, M. Seeger, E. Thiele, H. Metschies, B. Gebreselassie, and J. C. Munich, "Polymer Optical Fiber Sensors for Distributed Strain Measurement and Application in Structural Health Monitoring," Sensors Journal, IEEE **9**, 1330-1338 (2009).
5.   H. N. N. Yasue, J. Masuda, H. Kino, T. Nakamura, T. Yamaura, "Concrete Pipe Strain Measurement Using Optical Fiber Sensor," Ieice Transactions on Electronics **E83-C**, 486-474 (2000).
6.   K. Y. Song, S. Chin, N. Primerov, and L. Thévenaz, "Time-Domain Distributed Fiber Sensor With 1 cm Spatial Resolution Based on Brillouin Dynamic Grating," J. Lightwave Technol. **28**, 2062-2067.
7.   L. Thevenaz, M. Facchini, A. Fellay, M. Nikles, and P. Robert, "Field tests of distributed temperature and strain measurement for smart structures," Cleo(R)/Pacific Rim 2001, Vol I, Technical Digest, 490-491, 651 (2001).
8.   L. Thevenaz, M. Nikles, A. Fellay, M. Facchini, and P. Robert, "Applications of distributed Brillouin fibre sensing," International Conference on Applied Optical Metrology **3407**, 374-381, 554 (1998).
9.   W. J. Bock, M. S. Nawrocka, and W. Urbanczyk, "Highly sensitive fiber-optic sensor for dynamic pressure measurements," Instrumentation and Measurement, IEEE Transactions on **50**, 1085-1088 (2001).
10.   L. Palmieri, and A. Galtarossa, "Reflectometric fiber optic sensor for distributed measurement of intense magneto-static fields," in *Sensors, 2011 IEEE*(2011), pp. 117-120.
11.   Z. Zhang, and X. Bao, "Distributed optical fiber vibration sensor based on spectrum analysis of Polarization-OTDR system," Opt. Express **16**, 10240-10247 (2008).
12.   S. F. Mafang, "Brillouin Echoes for Advanced Distributed Sensing in Optical Fibres," in *School of Engineering*(EPFL, Lausanne, 2011).
13.   D. Alasia, "Advanced Trends in Nonlinear Optics Applied to Distributed Optical-Fiber Sensors," in *School of Engineering*(EPFL, Lausanne, 2006).
14.   M. K. Barnoski, and S. M. Jensen, "Fiber waveguides: a novel technique for investigating attenuation characteristics," Appl. Opt. **15**, 2112-2115 (1976).
15.   A. Y. a. P. Hartog, D.N. , "Remote measurement of temperature distribution using an optical fibre," in *8th European Conference on Optical Communication*(Cannes, 1982).
16.   M. Nakazawa, and M. Tokuda, "Measurement of the fiber loss spectrum using fiber Raman optical-time-domain reflectometry," Appl. Opt. **22**, 1910-1914 (1983).
17.   A. J. Rogers, "Polarization-optical time domain reflectometry: a technique for the measurement of field distributions," Appl. Opt. **20**, 1060-1074 (1981).
18.   J. P. Dakin, D. J. Pratt, G. W. Bibby, and J. N. Ross, "Distributed optical fibre Raman temperature sensor using a semiconductor light source and detector," Electronics Letters **21**, 569-570 (1985).

19. I. P. Giles, D. Uttam, B. Cylshaw, and D. E. N. Davies, "Coherent optical-fibre sensors with modulated laser sources," Electronics Letters **19**, 14-15 (1983).

20. T. Horiguchi, and M. Tateda, "Optical-fiber-attenuation investigation using stimulated Brillouin scattering between a pulse and a continuous wave," Opt. Lett. **14**, 408-410 (1989).

21. T. Horiguchi, T. Kurashima, and M. Tateda, "A technique to measure distributed strain in optical fibers," Photonics Technology Letters, IEEE **2**, 352-354 (1990).

22. T. Kurashima, T. Horiguchi, and M. Tateda, "Distributed-temperature sensing using stimulated Brillouin scattering in optical silica fibers," Opt. Lett. **15**, 1038-1040 (1990).

23. D. Culverhouse, F. Farahi, C. N. Pannell, and D. A. Jackson, "Potential of stimulated Brillouin scattering as sensing mechanism for distributed temperature sensors," Electronics Letters **25**, 913-915 (1989).

24. X. Angulo-Vinuesa, S. Martin-Lopez, P. Corredera, and M. Gonzalez-Herraez, "Raman-assisted Brillouin optical time-domain analysis with sub-meter resolution over 100 km," Opt. Express **20**, 12147-12154 (2012).

25. Y. Dong, L. Chen, and X. Bao, "Time-division multiplexing-based BOTDA over 100km sensing length," Opt. Lett. **36**, 277-279 (2011).

26. I. Alasaarela, P. Karioja, and H. Kopola, "Comparison of distributed fiber optic sensing methods for location and quantity information measurements," Optical Engineering **41**, 181-189 (2002).

27. T. Luc, "Review and Progress on Distributed Fibre Sensing," in *Optical Fiber Sensors*(Optical Society of America, 2006), p. ThC1.

28. L. Thévenaz, "Brillouin distributed time-domain sensing in optical fibers: state of the art and perspectives," Frontiers of Optoelectronics in China **3**, 13-21 (2010).

29. T. Horiguchi, T. Kurashima, and M. Tateda, "Tensile strain dependence of Brillouin frequency shift in silica optical fibers," Photonics Technology Letters, IEEE **1**, 107-108 (1989).

30. N. Shibata, R. G. Waarts, and R. P. Braun, "Brillouin-gain spectra for single-mode fibers having pure-silica, GeO2-doped, and P2O5-doped cores," Opt. Lett. **12**, 269-271 (1987).

31. M. Nikles, L. Thevenaz, and P. A. Robert, "Brillouin gain spectrum characterization in single-mode optical fibers," Journal of Lightwave Technology **15**, 1842-1851 (1997).

32. E. Lichtman, R. G. Waarts, and A. A. Friesem, "Stimulated Brillouin scattering excited by a modulated pump wave in single-mode fibers," Lightwave Technology, Journal of **7**, 171-174 (1989).

33. X. Bao, A. Brown, M. DeMerchant, and J. Smith, "Characterization of the Brillouin-loss spectrum of single-mode fibers by use of very short (<10-ns) pulses," Opt. Lett. **24**, 510-512 (1999).

34. V. Lecoeuche, D. J. Webb, C. N. Pannell, and D. A. Jackson, "Transient response in high-resolution Brillouin-based distributed sensing using probe pulses shorter than the acoustic relaxation time," Opt. Lett. **25**, 156-158 (2000).

35. A. W. Brown, B. G. Colpitts, and K. Brown, "Distributed sensor based on dark-pulse Brillouin scattering," Photonics Technology Letters, IEEE **17**, 1501-1503 (2005).

36. S. M. Foaleng, M. Tur, J. C. Beugnot, and L. Thevenaz, "High Spatial and Spectral Resolution Long-Range Sensing Using Brillouin Echoes," Lightwave Technology, Journal of **28**, 2993-3003 (2010).

37. K.-Y. Song, W. Zou, Z. He, and K. Hotate, "Correlation-based distributed measurement of a dynamic grating spectrum generated in stimulated Brillouin scattering in a polarization-maintaining optical fiber," Opt. Lett. **34**, 1126-1128 (2009).

38.   K. Hotate, and S. S. L. Ong, "Distributed dynamic strain measurement using a correlation-based Brillouin sensing system," Photonics Technology Letters, IEEE **15**, 272-274 (2003).
39.   K. Hotate, and M. Tanaka, "Distributed fiber Brillouin strain sensing with 1-cm spatial resolution by correlation-based continuous-wave technique," Photonics Technology Letters, IEEE **14**, 179-181 (2002).
40.   Y. Mizuno, Z. He, and K. Hotate, "Measurement range enlargement in Brillouin optical correlation-domain reflectometry based on double-modulation scheme," Opt. Express **18**, 5926-5933 (2010).
41.   A. Zadok, Y. Antman, N. Primerov, A. Denisov, J. Sancho, and L. Thevenaz, "Random-access distributed fiber sensing," Laser & Photonics Reviews **6**, L1-L5 (2012).

Conclusions and perspectives

The Dynamic Brillouin grating is a unique phenomenon which can be produced in optical fibers using Stimulated Brillouin Scattering. This thesis has been focused on the generation and investigation of dynamic Brillouin grating in optical fibers, as well as the proposal of potential applications of DBG in various fields of photonics. Certainly, DBG can be considered as a unique flexible tool for a wide range of applications ranging from optical storage and analog processing of optical signals to distributed sensing. One of the initial motivations to investigate DBG in optical fibers was the realization of an optical buffer or memory. Even though isolated pulses or short data packets can be delayed by an impressive time of more than a microsecond it should be pointed out that the acoustic wave decay time restricts the length of the processed packets. Moreover the exponential decay of the acoustic phonons imprints an amplitude distortion on the delayed signal, which needs to be corrected. In optical fibers the time decay constant is around 10-12 ns and it is difficult to find another suitable material with substantially longer phonon lifetimes. The acoustic lifetime is also a limiting factor for the maximum delay of continuous data streams, since it requires periodic regeneration of the grating within the time it completely decays. Thus, the maximum delay for data streams is in the order of 10 ns when intensity pump pulses are used to generate the DBG. On the other hand buffer times of several ns can be used to process microwave photonic signals, where delays of one period are sufficient for most applications. Moreover, short delays are also required to synchronize digital data streams in time or wavelength division multiplexed systems. Having a longer acoustic lifetime would allow us to delay longer packets or regenerate DBG with longer pump pulses repetition rate. Moreover, a longer lifetime also means that the DBG amplitude will be larger since it scales with the phonon lifetime. Longer phonon lifetime would only change the time for the DBG to reach the saturation level. Probably, the ideal case would be to have fibers with materials in which the interference pattern of the pump pulses can be permanently inscribed and erased by another optical wave similar to holographic techniques.

Another limitation of DBG for signal processing is the low reflectivity, which in turn requires relatively high pump powers for the DBG generation. Probably one way to enhance the DBG reflectivity is to use a medium with higher Brillouin gain coefficient (g). For example, chalcogenide fibers have g in the order of 60×10^{-11} m/W which is around 25 times larger than in silica fibers. Another candidate can be telluride microstructured fibers where the Brillouin gain coefficient is one order of magnitude higher than in silica fibers. The main disadvantage of chalcogenides fibers comes with their relatively high loss and low damage threshold compared to silica fibers.

Another problem comes from the fact that today's applications in telecommunication require speeds in the order of several tens or hundreds of Gbits/s. This issue requires very short length of DBG in order to provide a bandwidth that covers most of the signal bandwidth,

but this in turn will reduce the DBG reflectivity. It seems like the challenge to realize optical memory with large dynamic buffer range together with high reconfiguration time is still open. Probably the closest technique that allows a practical implementation is wavelength conversion and fiber dispersion system, where delays up to several microseconds are also possible, but the reconfiguration time is far from perfect. On the other hand, the PRBS technique to generate a localized DBG is a very flexible method. The only limitation here comes from the noise associated with residual gratings outside the correlation peak. A possible solution to this problem can be the use of a double modulation approach. For example, on top of phase modulation pump waves can be amplitude or frequency modulated, such as BOCDA. Such complex modulation schemes can potentially reduce the off peak noise and potentially allow for the realization of an optical delay line for continuous data signals with long storage time and an ideal reconfiguration time. Another solution to noise reduction might be found in utilizing different sequences, In addition the PRBS technique is also a very attractive tool to realize tunable microwave photonic filters. By adjusting the number of correlation peaks inside the fiber, the number of filter taps can be easily controlled demonstrating easy scalability.

Even though for the moment dynamic Brillouin grating cannot provide a tool to realize an optical buffer for high speed data signals it has good potential to be applied in optical signal processing. As it was demonstrated in this thesis, a first order optical differentiator and an integrator were realized using the DBG principle for the first time. We should point out that for a DBG based integrator the integration window can be easily adjusted by simply changing the length of the dynamic grating. In addition since the induced refractive index modulation is very small, long gratings and accordingly long integration windows can be generated without substantial change in the reflected energy along the entire grating. On the other hand, birefringence fluctuations along the fiber will result in amplitude fluctuation of induced dynamic grating, leading to distortions of the integrated waveform. For the DBG based differentiator it is also important to have fiber with uniform birefringence. It should be pointed out that the birefringence uniformity of PM fibers should be technologically addressed, because, at the moment, there is no control of the birefringence parameter during the manufacturing process. Moreover bandwidth of write and read pulses directly defines the operational bandwidth of the differentiator. Thus read and write pulses should have a bandwidth larger than the bandwidth of the differentiating waveform. For the time reversal operation the main limitation is again the acoustic time constant. Moreover the exponential decay of the reversed data needs to be compensated. It is interesting that the DBG principle can also be used to develop setups performing logic gates, such as OR, AND, and others. It should be pointed out that here the acoustic decay time constant is a limiting factor for the operation speed of the logic gate, since the generated grating has to completely decay before the logic gate is ready to estimate the next bit combination. Thus the 10 ns decay time limits the operation speed of the DBG logic gates to around 100 MHz.

Probably the most promising field for DBG application is fiber optic distributed sensing. As it was demonstrated distributed temperature and stress DBG sensors with cm scale spatial resolution can be easily constructed for measurement ranges over several

hundred meters. DBG sensor based on Brillouin optical-time domain analysis with 1 cm spatial resolution was demonstrated in this thesis. It should be pointed out that using a dynamic Brillouin grating approach it was possible to break the trade-off of high spatial resolution and the Brillouin gain broadening inherent to classical BOTDA configurations. Moreover 1 cm spatial resolution is certainly not the limit of the proposed scheme. Probably the limitation will come from nonlinear effects when the probe pulse is reduced to few ps. In addition, the group velocity dispersion after a certain distance can severely broaden the probe pulse impairing the spatial resolution. Pulse-based DBG sensors can be implemented in different configurations as in the case of the standard Brillouin technique. Both, time domain analysis, where two-end approach to the sensing fiber is needed, and reflectometric principle, with one end access to the sensing fiber, can be easily implemented using a DBG sensor.

PRBS DBG technique has also very unique advantages over other different schemes. First of all this is the only truly random access sensor with spatial resolution completely decorrelated from the maximum measurement range. At the moment the main limitation of the PRBS technique is the noise coming from the residual gratings outside the correlation peak. This noise ultimately will limit the measurement range of the PRBS DBG based sensor due to reduced signal-to-noise ratio. In order to overcome this limitation, probably a double modulation scheme will be required. The combination of frequency modulation (BOCDA, ramp) and phase modulation (PRBS) might result in a drastic reduction of the off peak noise. Moreover fast electrical instruments for the clock rate of the PRBS and Brillouin shift sweep are needed to reduce the measurement time of the PRBS DBG sensor when long measurement range and high spatial resolution are needed. As it was demonstrated using PRBS phase modulation of the pump waves, the amplitude of the acoustic wave is given by the autocorrelation function of the PRBS. This means that using other forms of pump phase modulation it is possible to realize an optical autocorrelator. In addition it should be stressed that dynamic Brillouin grating is one of the few tools available nowadays to measure the distributed birefringence of polarization maintaining fibers with high spatial resolution.

In conclusion dynamic Brillouin grating is a unique phenomenon which will find new applications in many fields of optical signal processing and distributed fiber optic sensors. Additional research is necessary to study unique property of the DBG such as optical phase conjugation. In addition, an interesting field of research can be the investigation of DBG phenomenon in integrated optics.

Appendix A.

Solution for the acoustic wave amplitude where equal pump pulses are used.

First, we write the pump pulses in time domain with different widths:

$$A_1 = u\left(t - \frac{z}{V_g}\right) - u\left(t - T_1 - \frac{z}{V_g}\right) \tag{1.1}$$

$$A_2 = u\left(t - t_0 + \frac{z}{V_g}\right) - u\left(t - t_0 - T_2 + \frac{z}{V_g}\right) \tag{1.2}$$

Calculation of the acoustic wave amplitude for the pump pulses with different widths. We consider two different situations: $T_1 > T_2$ and $T_2 > T_1$.

Let us consider first situation when $T_1 > T_2$. In this case expression for the product of two pump pulses will be:

$$A_{p1} A_{p2}^* = P_1^0 P_2^0 \alpha \beta^* \begin{cases} u(t - z/V_g) \times u(t - z_0/V_g + z/V_g) = \begin{cases} u(t - \frac{z_0 - z}{V_g}) & z < \frac{z_0}{2} \\ u(t - z/V_g) & z \geq \frac{z_0}{2} \end{cases} \\ -u(t - T_1 - z/V_g) \times -u(t - T_2 - \frac{z_0 - z}{V_g}) = \begin{cases} = u(t - T_2 - \frac{z_0 - z}{V_g}) & z \leq \frac{z_0}{2} + \frac{(T_2 - T_1)V_g}{2} \\ = u(t - T_1 - \frac{z}{V_g}) & z > \frac{z_0}{2} + \frac{(T_2 - T_1)V_g}{2} \end{cases} \\ u(t - \frac{z}{V_g}) \times -u(t - T_2 - \frac{z_0 - z}{V_g}) = \begin{cases} -u(t - T_2 - \frac{z_0 - z}{V_g}) & z < \frac{z_0}{2} + \frac{T_2 V_g}{2} \\ -u(t - \frac{z}{V_g}) & z \geq \frac{z_0}{2} + \frac{T_2 V_g}{2} \end{cases} \\ -u(t - T_1 - \frac{z}{V_g}) \times u(t - \frac{z_0 - z}{V_g}) = \begin{cases} -u(t - T_1 - \frac{z}{V_g}) & z > \frac{z_0}{2} - \frac{T_1 V_g}{2} \\ -u(t - \frac{z_0 - z}{V_g}) & z \leq \frac{z_0}{2} - \frac{T_1 V_g}{2} \end{cases} \end{cases} \tag{1.3}$$

Thus, we have five segments of the fiber where product takes the following form:

$$A_{p1}A_{p2}^* = P_1^0 P_2^0 \alpha\beta^* \begin{cases} 0 & 0 < z \le \dfrac{z_0}{2} - \dfrac{T_1 V_g}{2} \\[2ex] u(t - \dfrac{z_0 - z}{V_g}) - u(t - T_1 - z/V_g) & \dfrac{z_0}{2} - \dfrac{T_1 V_g}{2} < z \le \dfrac{z_0}{2} + \dfrac{(T_2 - T_1)V_g}{2} \\[2ex] u(t - \dfrac{z_0 - z}{V_g}) - u(t - T_2 - \dfrac{z_0 - z}{V_g}) & \dfrac{z_0}{2} + \dfrac{(T_2 - T_1)V_g}{2} < z \le \dfrac{z_0}{2} \\[2ex] u(t - \dfrac{z}{V_g}) - u(t - T_2 - \dfrac{z_0 - z}{V_g}) & \dfrac{z_0}{2} < z \le \dfrac{z_0}{2} + \dfrac{T_2 V_g}{2} \\[2ex] 0 & \dfrac{z_0}{2} + \dfrac{T_2 V_g}{2} < z \end{cases} \tag{1.4}$$

Taking the Laplace transform of the expression (1.4) results in:

$$\widetilde{A_{p1}A_{p2}^*} = P_1^0 P_2^0 \alpha\beta^* \begin{cases} 0 & 0 < z \le \dfrac{z_0}{2} - \dfrac{T_1 V_g}{2} \\[2ex] \dfrac{e^{-\frac{z_0 - z}{V_g}s}}{s} - \dfrac{e^{-(T_1 + z/V_g)s}}{s} & \dfrac{z_0}{2} - \dfrac{T_1 V_g}{2} < z \le \dfrac{z_0}{2} + \dfrac{(T_2 - T_1)V_g}{2} \\[2ex] \dfrac{e^{-\frac{z_0 - z}{V_g}s}}{s} - \dfrac{e^{-\left(T_2 + \frac{z_0 - z}{V_g}\right)s}}{s} & \dfrac{z_0}{2} + \dfrac{(T_2 - T_1)V_g}{2} < z \le \dfrac{z_0}{2} \\[2ex] \dfrac{e^{-\frac{z}{V_g}s}}{s} - \dfrac{e^{-\left(T_2 + \frac{z_0 - z}{V_g}\right)s}}{s} & \dfrac{z_0}{2} < z \le \dfrac{z_0}{2} + \dfrac{T_2 V_g}{2} \\[2ex] 0 & \dfrac{z_0}{2} + \dfrac{T_2 V_g}{2} < z \end{cases} \tag{1.5}$$

Inserting the expression (1.5) in the equation for the acoustic wave (3.19) we obtain:

$$\tilde{\rho}(z,s) = ig_1 P_1^0 P_2^0 \alpha\beta^* \begin{cases} 0 & 0 < z \le \dfrac{z_0}{2} - \dfrac{T_1 V_g}{2} \\[2mm] \dfrac{e^{-\frac{z_0-z}{V_g}s}}{s(s+\Gamma_A)} - \dfrac{e^{-(T_1+z/V_g)s}}{s(s+\Gamma_A)} & \dfrac{z_0}{2} - \dfrac{T_1 V_g}{2} < z \le \dfrac{z_0}{2} + \dfrac{(T_2-T_1)V_g}{2} \\[3mm] \dfrac{e^{-\frac{z_0-z}{V_g}s}}{s(s+\Gamma_A)} - \dfrac{e^{-\left(T_2+\frac{z_0-z}{V_g}\right)s}}{s(s+\Gamma_A)} & \dfrac{z_0}{2} + \dfrac{(T_2-T_1)V_g}{2} < z \le \dfrac{z_0}{2} \\[3mm] \dfrac{e^{-\frac{z}{V_g}s}}{s(s+\Gamma_A)} - \dfrac{e^{-\left(T_2+\frac{z_0-z}{V_g}\right)s}}{s(s+\Gamma_A)} & \dfrac{z_0}{2} < z \le \dfrac{z_0}{2} + \dfrac{T_2 V_g}{2} \\[3mm] 0 & \dfrac{z_0}{2} + \dfrac{T_2 V_g}{2} < z \end{cases} \quad (1.6)$$

Using cover-up method we can write each fraction in the expression (1.6) as a sum of fractions with simpler denominator:

$$\tilde{\rho}(z,s) = ig_1 P_1^0 P_2^0 \alpha\beta^* \begin{cases} 0 & 0 < z \le \dfrac{z_0}{2} - \dfrac{T_1 V_g}{2} \\[2mm] \dfrac{e^{-\frac{z_0-z}{V_g}s}}{s\Gamma_A} - \dfrac{e^{-\frac{z_0-z}{V_g}s}}{\Gamma_A(s+\Gamma_A)} - \dfrac{e^{-(T_1+z/V_g)s}}{s\Gamma_A} + \dfrac{e^{-(T_1+z/V_g)s}}{\Gamma_A(s+\Gamma_A)} & \dfrac{z_0}{2} - \dfrac{T_1 V_g}{2} < z \le \dfrac{z_0}{2} + \dfrac{(T_2-T_1)V_g}{2} \\[3mm] \dfrac{e^{-\frac{z_0-z}{V_g}s}}{s\Gamma_A} - \dfrac{e^{-\frac{z_0-z}{V_g}s}}{\Gamma_A(s+\Gamma_A)} - \dfrac{e^{-\left(T_2+\frac{z_0-z}{V_g}\right)s}}{s\Gamma_A} + \dfrac{e^{-\left(T_2+\frac{z_0-z}{V_g}\right)s}}{\Gamma_A(s+\Gamma_A)} & \dfrac{z_0}{2} + \dfrac{(T_2-T_1)V_g}{2} < z \le \dfrac{z_0}{2} \\[3mm] \dfrac{e^{-\frac{z}{V_g}s}}{s\Gamma_A} - \dfrac{e^{-\frac{z}{V_g}s}}{\Gamma_A(s+\Gamma_A)} - \dfrac{e^{-\left(T_2+\frac{z_0-z}{V_g}\right)s}}{s\Gamma_A} + \dfrac{e^{-\left(T_2+\frac{z_0-z}{V_g}\right)s}}{\Gamma_A(s+\Gamma_A)} & \dfrac{z_0}{2} < z \le \dfrac{z_0}{2} + \dfrac{T_2 V_g}{2} \\[3mm] 0 & \dfrac{z_0}{2} + \dfrac{T_2 V_g}{2} < z \end{cases} \quad (1.7)$$

Taking the inverse Laplace transform we obtain the expression for the acoustic wave in time and distance domain when width of pump 1 pulse is longer than that of the pump 2 pulse, $T_1 > T_2$:

$$\rho(z,t) = \frac{ig_1 P_1^0 P_2^0 \alpha\beta^*}{\Gamma_A} \begin{cases} 0 & 0 < z \le \frac{z_0}{2} - \frac{T_1 V_g}{2} \\[2mm] u(t - \frac{z_0 - z}{V_g})\left(1 - e^{-\Gamma_A(t - \frac{z_0 - z}{V_g})}\right) - u(t - T_1 - z/V_g)\left(1 - e^{-\Gamma_A(t - T_1 - z/V_g)}\right) & \frac{z_0}{2} - \frac{T_1 V_g}{2} < z \le \frac{z_0}{2} + \frac{(T_2 - T_1)V_g}{2} \\[2mm] u(t - \frac{z_0 - z}{V_g})\left(1 - e^{-\Gamma_A(t - \frac{z_0 - z}{V_g})}\right) - u(t - T_2 - \frac{z_0 - z}{V_g})\left(1 - e^{-\Gamma_A\left(t - T_2 - \frac{z_0 - z}{V_g}\right)}\right) & \frac{z_0}{2} + \frac{(T_2 - T_1)V_g}{2} < z \le \frac{z_0}{2} \\[2mm] u(t - \frac{z}{V_g})\left(1 - e^{-\Gamma_A(t - \frac{z}{V_g})}\right) - u(t - T_2 - \frac{z_0 - z}{V_g})\left(1 - e^{-\Gamma_A\left(t - T_2 - \frac{z_0 - z}{V_g}\right)}\right) & \frac{z_0}{2} < z \le \frac{z_0}{2} + \frac{T_2 V_g}{2} \\[2mm] 0 & \frac{z_0}{2} + \frac{T_2 V_g}{2} < z \end{cases}$$

(1.8)

Second situation when width of the pump 2 pulse is longer than that of the pump 1, $T_2 > T_1$. Then we can write the product of amplitudes of two pump pulses as:

$$A_{p1}A_{p2}^* = P_1^0 P_2^0 \alpha\beta^* \begin{cases} u(t - z/V_g) \times u(t - z_0/V_g + z/V_g) = \begin{cases} u(t - \frac{z_0 - z}{V_g}) & z < \frac{z_0}{2} \\[2mm] u(t - z/V_g) & z \ge \frac{z_0}{2} \end{cases} \\[6mm] -u(t - T_1 - z/V_g) \times -u(t - T_2 - \frac{z_0 - z}{V_g}) = \begin{cases} = u(t - T_2 - \frac{z_0 - z}{V_g}) & z \le \frac{z_0}{2} + \frac{(T_2 - T_1)V_g}{2} \\[2mm] = u(t - T_1 - \frac{z}{V_g}) & z > \frac{z_0}{2} + \frac{(T_2 - T_1)V_g}{2} \end{cases} \\[6mm] u(t - \frac{z}{V_g}) \times -u(t - T_2 - \frac{z_0 - z}{V_g}) = \begin{cases} -u(t - T_2 - \frac{z_0 - z}{V_g}) & z < \frac{z_0}{2} + \frac{T_2 V_g}{2} \\[2mm] -u(t - \frac{z}{V_g}) & z \ge \frac{z_0}{2} + \frac{T_2 V_g}{2} \end{cases} \\[6mm] -u(t - T_1 - \frac{z}{V_g}) \times u(t - \frac{z_0 - z}{V_g}) = \begin{cases} -u(t - \frac{z_0 - z}{V_g}) & z \le \frac{z_0}{2} - \frac{T_1 V_g}{2} \\[2mm] -u(t - T_1 - \frac{z}{V_g}) & z > \frac{z_0}{2} - \frac{T_1 V_g}{2} \end{cases} \end{cases}$$

(1.9)

This will define 5 sections of the fiber where product will take following form:

$$A_{p1}A_{p2}^* = P_1^0 P_2^0 \alpha\beta^* \begin{cases} 0 & 0 < z \le \dfrac{z_0}{2} - \dfrac{T_1 V_g}{2} \\[2ex] u(t - \dfrac{z_0 - z}{V_g}) - u(t - T_1 - z/V_g) & \dfrac{z_0}{2} - \dfrac{T_1 V_g}{2} < z \le \dfrac{z_0}{2} \\[2ex] u(t - \dfrac{z}{V_g}) - u(t - T_1 - \dfrac{z}{V_g}) & \dfrac{z_0}{2} < z \le \dfrac{z_0}{2} + \dfrac{(T_2 - T_1)V_g}{2} \\[2ex] u(t - \dfrac{z}{V_g}) - u(t - T_2 - \dfrac{z_0 - z}{V_g}) & \dfrac{z_0}{2} + \dfrac{(T_2 - T_1)V_g}{2} < z \le \dfrac{z_0}{2} + \dfrac{T_2 V_g}{2} \\[2ex] 0 & \dfrac{z_0}{2} + \dfrac{T_2 V_g}{2} < z \end{cases} \quad (1.10)$$

We take the Laplace transform of (1.10):

$$\widetilde{A_{p1}A_{p2}^*} = P_1^0 P_2^0 \alpha\beta^* \begin{cases} 0 & 0 < z \le \dfrac{z_0}{2} - \dfrac{T_1 V_g}{2} \\[2ex] \dfrac{e^{-\frac{z_0 - z}{V_g}s}}{s} - \dfrac{e^{-(T_1 + z/V_g)s}}{s} & \dfrac{z_0}{2} - \dfrac{T_1 V_g}{2} < z \le \dfrac{z_0}{2} \\[3ex] \dfrac{e^{-\frac{z}{V_g}s}}{s} - \dfrac{e^{-\left(T_1 + \frac{z}{V_g}\right)s}}{s} & \dfrac{z_0}{2} < z \le \dfrac{z_0}{2} + \dfrac{(T_2 - T_1)V_g}{2} \\[3ex] \dfrac{e^{-\frac{z}{V_g}s}}{s} - \dfrac{e^{-\left(T_2 + \frac{z_0 - z}{V_g}\right)s}}{s} & \dfrac{z_0}{2} + \dfrac{(T_2 - T_1)V_g}{2} < z \le \dfrac{z_0}{2} + \dfrac{T_2 V_g}{2} \\[3ex] 0 & \dfrac{z_0}{2} + \dfrac{T_2 V_g}{2} < z \end{cases} \quad (1.11)$$

Using the equation (3.19) we write the expression for the acoustic wave as:

$$\tilde{\rho}(z,s) = ig_1 P_1^0 P_2^0 \alpha\beta^* \begin{cases} 0 & 0 < z \le \dfrac{z_0}{2} - \dfrac{T_1 V_g}{2} \\[2em] \dfrac{e^{-\frac{z_0-z}{V_g}s}}{s\Gamma_A} - \dfrac{e^{-\frac{z_0-z}{V_g}s}}{\Gamma_A(s+\Gamma_A)} - \dfrac{e^{-(T_1+z/V_g)s}}{s\Gamma_A} + \dfrac{e^{-(T_1+z/V_g)s}}{\Gamma_A(s+\Gamma_A)} & \dfrac{z_0}{2} - \dfrac{T_1 V_g}{2} < z \le \dfrac{z_0}{2} \\[2em] \dfrac{e^{-\frac{z}{V_g}s}}{s\Gamma_A} - \dfrac{e^{-\frac{z}{V_g}s}}{\Gamma_A(s+\Gamma_A)} - \dfrac{e^{-\left(T_1+\frac{z}{V_g}\right)s}}{s\Gamma_A} + \dfrac{e^{-\left(T_1+\frac{z}{V_g}\right)s}}{\Gamma_A(s+\Gamma_A)} & \dfrac{z_0}{2} < z \le \dfrac{z_0}{2} + \dfrac{(T_2-T_1)V_g}{2} \\[2em] \dfrac{e^{-\frac{z}{V_g}s}}{s\Gamma_A} - \dfrac{e^{-\frac{z}{V_g}s}}{\Gamma_A(s+\Gamma_A)} - \dfrac{e^{-\left(T_2+\frac{z_0-z}{V_g}\right)s}}{s\Gamma_A} + \dfrac{e^{-\left(T_2+\frac{z_0-z}{V_g}\right)s}}{\Gamma_A(s+\Gamma_A)} & \dfrac{z_0}{2} + \dfrac{(T_2-T_1)V_g}{2} < z \le \dfrac{z_0}{2} + \dfrac{T_2 V_g}{2} \\[2em] 0 & \dfrac{z_0}{2} + \dfrac{T_2 V_g}{2} < z \end{cases}$$

(1.12)

And finally taking the Laplace transform we can obtain the expression for the acoustic wave when width of the pump 2 pulse is longer than that of the pump 1, $T_2 > T_1$:

$$\rho(z,t) = \frac{ig_1 P_1^0 P_2^0 \alpha\beta^*}{\Gamma_A} \begin{cases} 0 & 0 < z \le \dfrac{z_0}{2} - \dfrac{T_1 V_g}{2} \\[2em] u(t - \dfrac{z_0-z}{V_g})\left(1 - e^{-\Gamma_A(t-\frac{z_0-z}{V_g})}\right) - u(t - T_1 - z/V_g)\left(1 - e^{-\Gamma_A(T_1+z/V_g)}\right) & \dfrac{z_0}{2} - \dfrac{T_1 V_g}{2} < z \le \dfrac{z_0}{2} \\[2em] u(t - \dfrac{z}{V_g})\left(1 - e^{-\Gamma_A(t-\frac{z}{V_g})}\right) - u(t - T_1 - \dfrac{z}{V_g})\left(1 - e^{-\Gamma_A\left(T_1+\frac{z}{V_g}\right)}\right) & \dfrac{z_0}{2} < z \le \dfrac{z_0}{2} + \dfrac{(T_2-T_1)V_g}{2} \\[2em] u(t - \dfrac{z}{V_g})\left(1 - e^{-\Gamma_A(t-\frac{z}{V_g})}\right) - u(t - T_2 - \dfrac{z_0-z}{V_g})\left(1 - e^{-\Gamma_A\left(T_2+\frac{z_0-z}{V_g}\right)}\right) & \dfrac{z_0}{2} + \dfrac{(T_2-T_1)V_g}{2} < z \le \dfrac{z_0}{2} + \dfrac{T_2 V_g}{2} \\[2em] 0 & \dfrac{z_0}{2} + \dfrac{T_2 V_g}{2} < z \end{cases}$$

(1.13)

Appendix B.

Solutions of the integrals (3.49) and (3.50)

First we solve integral $\widetilde{R}'(s, z=0)$.

$$\widetilde{R}'(s,z=0)=\int_{\frac{z_0}{2}-\frac{TV_g}{2}}^{\frac{z_0}{2}} e^{-\frac{s}{V_g}z}\left(-u\left(T-\frac{z_0}{2V_g}+\frac{z}{V_g}\right)e^{-\Gamma_A\left(T-\frac{z_0}{V_g}+\frac{z}{V_g}\right)}+u\left(\frac{z_0}{2V_g}-\frac{z}{V_g}\right)e^{-\Gamma_A\left(\frac{z_0}{2V_g}-\frac{z}{V_g}\right)}\right)\frac{e^{-\tau s}e^{-\frac{z}{V_g}s}}{s}\left(1-e^{-T_s s}\right)dz$$

(1.14)

We can see that within the integration limits step function always equal to 1, thus we can write (3.49) as:

$$\widetilde{R}'(s,z=0)=\int_{\frac{z_0}{2}-\frac{TV_g}{2}}^{\frac{z_0}{2}} e^{-\frac{s}{V_g}z}\left(e^{-\Gamma_A\left(\frac{z_0}{2V_g}-\frac{z}{V_g}\right)}-e^{-\Gamma_A\left(T-\frac{z_0}{V_g}+\frac{z}{V_g}\right)}\right)\frac{e^{-\tau s}e^{-\frac{z}{V_g}s}}{s}\left(1-e^{-T_s s}\right)dz \qquad (1.15)$$

Multiplying terms inside the integral (1.14) we obtain:

$$\widetilde{R}'(s,z=0)=\frac{e^{-\tau s}}{s}\left(1-e^{-T_s s}\right)\left(e^{-\frac{\Gamma_A z_0}{2V_g}}\int_{\frac{z_0}{2}-\frac{TV_g}{2}}^{\frac{z_0}{2}}e^{-\left(\frac{2s}{V_g}-\frac{\Gamma_A}{V_g}\right)z}dz-e^{-\Gamma_A T+\frac{\Gamma_A z_0}{2V_g}}\int_{\frac{z_0}{2}-\frac{TV_g}{2}}^{\frac{z_0}{2}}e^{-\left(\frac{2s}{V_g}+\frac{\Gamma_A}{V_g}\right)z}dz\right)(1.16)$$

$$\widetilde{R}'(s,z=0)=\frac{e^{-\tau s}}{s}\left(1-e^{-T_s s}\right)\left(\frac{e^{-\frac{\Gamma_A z_0}{2V_g}}V_g}{2s-\Gamma_A}\left(e^{-\left(\frac{2s}{V_g}-\frac{\Gamma_A}{V_g}\right)\left(\frac{z_0}{2}-\frac{TV_g}{2}\right)}-e^{-\left(\frac{2s}{V_g}-\frac{\Gamma_A}{V_g}\right)\frac{z_0}{2}}\right)-\frac{e^{-\Gamma_A T+\frac{\Gamma_A z_0}{2V_g}}}{2s-\Gamma_A}\left(e^{-\left(\frac{2s}{V_g}+\frac{\Gamma_A}{V_g}\right)\left(\frac{z_0}{2}-\frac{TV_g}{2}\right)}-e^{-\left(\frac{2s}{V_g}+\frac{\Gamma_A}{V_g}\right)\frac{z_0}{2}}\right)\right)$$

(1.17)

(1.17) can be further simplified:

$$\widetilde{R}'(s,z=0)=\frac{e^{-\tau s}}{s}\left(1-e^{-T_s s}\right)\frac{V_g}{2}\left(\frac{1}{s-\frac{\Gamma_A}{2}}\left(e^{-\left(\frac{z_0}{V_g}-T\right)s}e^{-\frac{\Gamma_A T}{2}}-e^{-\frac{z_0}{V_g}s}\right)-\frac{e^{-\Gamma_A T}}{s-\frac{\Gamma_A}{2}}\left(e^{-\left(\frac{z_0}{V_g}-T\right)s}e^{+\frac{\Gamma_A T}{2}}-e^{-\frac{z_0}{V_g}s}\right)\right)$$

(1.18)

$$\widetilde{R}'(s,z=0)=e^{-\tau s}\left(1-e^{-T_s s}\right)\frac{V_g}{\Gamma_A}\left(\frac{e^{-\frac{\Gamma_A T}{2}}e^{-\left(\frac{z_0}{V_g}-T\right)s}}{s-\frac{\Gamma_A}{2}}-\frac{e^{-\frac{\Gamma_A T}{2}}e^{-\left(\frac{z_0}{V_g}-T\right)s}}{s}-\frac{e^{-\frac{z_0}{V_g}s}}{s-\frac{\Gamma_A}{2}}+\frac{e^{-\frac{z_0}{V_g}s}}{s}-e^{-\Gamma_A T}\left(\frac{e^{-\left(\frac{z_0}{V_g}-T\right)s}e^{+\frac{\Gamma_A T}{2}}}{s}-\frac{e^{-\left(\frac{z_0}{V_g}-T\right)s}e^{+\frac{\Gamma_A T}{2}}}{s+\frac{\Gamma_A}{2}}-\frac{e^{-\frac{z_0}{V_g}s}}{s}+\frac{e^{-\frac{z_0}{V_g}s}}{s+\frac{\Gamma_A}{2}}\right)\right)$$

$$(1.19)$$

We define a new function $\widetilde{f}(s,z=0)$ as:

$$\widetilde{f}(s,z=0)=\left(\frac{e^{-\frac{\Gamma_A T}{2}}e^{-\left(\frac{z_0}{V_g}-T\right)s}}{s-\frac{\Gamma_A}{2}}-\frac{e^{-\frac{\Gamma_A T}{2}}e^{-\left(\frac{z_0}{V_g}-T\right)s}}{s}-\frac{e^{-\frac{z_0}{V_g}s}}{s-\frac{\Gamma_A}{2}}+\frac{e^{-\frac{z_0}{V_g}s}}{s}-e^{-\Gamma_A T}\left(\frac{e^{-\left(\frac{z_0}{V_g}-T\right)s}e^{+\frac{\Gamma_A T}{2}}}{s}-\frac{e^{-\left(\frac{z_0}{V_g}-T\right)s}e^{+\frac{\Gamma_A T}{2}}}{s+\frac{\Gamma_A}{2}}-\frac{e^{-\frac{z_0}{V_g}s}}{s}+\frac{e^{-\frac{z_0}{V_g}s}}{s+\frac{\Gamma_A}{2}}\right)\right)$$

$$(1.20)$$

Then it is clear from expression (1.19), that:

$$\widetilde{R}'(s,z=0)=e^{-\tau s}\left(1-e^{-T_s s}\right)\widetilde{f}(s,z=0)$$

$$(1.21)$$

By using properties of the Laplace transform we can see that:

$$R'(t,z=0)=f(t-\tau,z=0)-f(t-\tau-T_s,z=0)$$

$$(1.22)$$

So, by taking the inverse Laplace transform of the $\widetilde{f}(s)$, we can easily write the expression in time domain for the $R'(t,z=0)$. Thus:

$$f(t,z=0)=\frac{V_g}{\Gamma_A}\left(u\left(t-\frac{z_0}{V_g}+T\right)\cdot\left\{e^{\frac{\Gamma_A}{2}\left(t-\frac{z_0}{V_g}\right)}-2e^{\left(\frac{\Gamma_A T}{2}\right)}+e^{-\frac{\Gamma_A}{2}\left(t-\frac{z_0}{V_g}+2T\right)}\right\}+u\left(t-\frac{z_0}{V_g}\right)\left\{1-e^{\frac{\Gamma_A}{2}\left(t-\frac{z_0}{V_g}\right)}+e^{-\Gamma_A T}-e^{-\frac{\Gamma_A}{2}\left(t-\frac{z_0}{V_g}+2T\right)}\right\}\right)$$

$$(1.23)$$

Using (1.22) function $R'(t)$ will have form:

$$R'(t,z=0)=\frac{V_g}{\Gamma_A}\left(u\left(t-\frac{z_0}{V_g}+T-\tau\right)\cdot\left\{e^{\frac{\Gamma_A}{2}\left(t-\frac{z_0}{V_g}-\tau\right)}-2e^{\left(\frac{\Gamma_A T}{2}\right)}+e^{-\frac{\Gamma_A}{2}\left(t-\frac{z_0}{V_g}+2T-\tau\right)}\right\}+u\left(t-\frac{z_0}{V_g}-\tau\right)\left\{1-e^{\frac{\Gamma_A}{2}\left(t-\frac{z_0}{V_g}-\tau\right)}+e^{-\Gamma_A T}-e^{-\frac{\Gamma_A}{2}\left(t-\frac{z_0}{V_g}+2T-\tau\right)}\right\}\right)-$$

$$\frac{V_g}{\Gamma_A}\left(u\left(t-\frac{z_0}{V_g}+T-\tau-T_s\right)\cdot\left\{e^{\frac{\Gamma_A}{2}\left(t-\frac{z_0}{V_g}-\tau-T_s\right)}-2e^{\left(\frac{\Gamma_A T}{2}\right)}+e^{-\frac{\Gamma_A}{2}\left(t-\frac{z_0}{V_g}+2T-\tau-T_s\right)}\right\}+u\left(t-\frac{z_0}{V_g}-\tau-T_s\right)\left\{1-e^{\frac{\Gamma_A}{2}\left(t-\frac{z_0}{V_g}-\tau-T_s\right)}+e^{-\Gamma_A T}-e^{-\frac{\Gamma_A}{2}\left(t-\frac{z_0}{V_g}+2T-\tau-T_s\right)}\right\}\right)$$

$$(1.24)$$

Now we solve the integral for the second part of the reflected wave, $\widetilde{R}''(s,z=0)$:

$$\widetilde{R}''(s,z=0)=\int_{\frac{z_0}{2}}^{\frac{z_0}{2}+\frac{TV_g}{2}}e^{-\frac{s}{V_g}z}\left(-u\left(T+\frac{z_0}{2V_g}-\frac{z}{V_g}\right)e^{-\Gamma_A\left(T+\frac{z_0}{2V_g}-\frac{z}{V_g}\right)}+u\left(-\frac{z_0}{2V_g}+\frac{z}{V_g}\right)e^{-\Gamma_A\left(-\frac{z_0}{2V_g}+\frac{z}{V_g}\right)}\right)\frac{e^{-\tau s}e^{-\frac{z}{V_g}s}}{s}\left(1-e^{-T_s s}\right)dz$$

$$(1.25)$$

We can see that within the integration limits step function always equal to 1, thus we can write (1.25) as:

$$\widetilde{R}^{"}(s,z=0) = \int_{\frac{z_0}{2}}^{\frac{z_0}{2}+\frac{TV_g}{2}} e^{-\frac{s}{V_g}z}\left(-e^{-\Gamma_A\left(T+\frac{z_0}{2V_g}-\frac{z}{V_g}\right)}+e^{-\Gamma_A\left(-\frac{z_0}{2V_g}+\frac{z}{V_g}\right)}\right)\frac{e^{-\tau s}e^{-\frac{z}{V_g}s}}{s}\left(1-e^{-T_s s}\right)dz \quad (1.26)$$

Following the same procedure, we obtain:

$$\widetilde{R}^{"}(s,z=0) = \frac{e^{-\tau s}}{s}\left(1-e^{-T_s s}\right)\left(e^{\frac{\Gamma_A z_0}{2V_g}}\int_{\frac{z_0}{2}}^{\frac{z_0}{2}+\frac{TV_g}{2}}e^{-\frac{(2s+\Gamma_A)}{V_g}z}dz - e^{-\Gamma_A\left(\frac{z_0}{2V_g}+T\right)}\int_{\frac{z_0}{2}}^{\frac{z_0}{2}+\frac{TV_g}{2}}e^{-\frac{(2s-\Gamma_A)}{V_g}z}dz\right)(1.27)$$

Solving the integrals inside the brackets we get:

$$\widetilde{R}^{"}(s,z=0) = \frac{e^{-\tau s}}{s}\left(1-e^{-T_s s}\right)\left(\frac{e^{\frac{\Gamma_A z_0}{2V_g}}V_g}{2s+\Gamma_A}\left(e^{-\frac{(2s+\Gamma_A)z_0}{V_g}\frac{z_0}{2}}-e^{-\frac{(2s+\Gamma_A)(z_0+TV_g)}{V_g}\frac{}{2}}\right)-\frac{e^{-\Gamma_A\left(\frac{z_0}{2V_g}+T\right)}V_g}{2s-\Gamma_A}\left(e^{-\frac{(2s-\Gamma_A)z_0}{V_g}\frac{z_0}{2}}-e^{-\frac{(2s\Gamma_A)(z_0+TV_g)}{V_g}\frac{}{2}}\right)\right)$$

$$(1.28)$$

Rearranging the terms we arrive to the following equation:

$$\widetilde{R}^{"}(s,z=0) = \frac{e^{-\tau s}}{s}\left(1-e^{-T_s s}\right)\left(\frac{V_g}{2s+\Gamma_A}\left(e^{\frac{z_0}{V_g}s}-e^{-\left(\frac{z_0}{V_g}+T\right)s}-e^{-\frac{\Gamma_A T}{2}}\right)-\frac{e^{-\Gamma_A T}V_g}{2s-\Gamma_A}\left(e^{-\frac{z_0}{V_g}s}-e^{-\left(\frac{z_0}{V_g}+T\right)s}-e^{\frac{\Gamma_A T}{2}}\right)\right)$$

$$(1.29)$$

Separating the fractions to simpler fractions we arrive at:

$$\widetilde{R}^{"}(s,z=0) = e^{-\tau s}\left(1-e^{-T_s s}\right)\frac{V_g}{\Gamma_A}\left(\frac{e^{-\frac{z_0}{V_g}s}}{s}-\frac{e^{-\frac{z_0}{V_g}s}}{s+\frac{\Gamma_A}{2}}-\frac{e^{\frac{\Gamma_A T}{2}}e^{-\left(\frac{z_0}{V_g}+T\right)s}}{s}+\frac{e^{\frac{\Gamma_A T}{2}}e^{-\left(\frac{z_0}{V_g}+T\right)s}}{s+\frac{\Gamma_A}{2}}-\frac{e^{-\Gamma_A T}e^{-\frac{z_0}{V_g}s}}{s-\frac{\Gamma_A}{2}}+\frac{e^{-\Gamma_A T}e^{-\frac{z_0}{V_g}s}}{s}+\frac{e^{\frac{\Gamma_A T}{2}}e^{-\left(\frac{z_0}{V_g}+T\right)s}}{s-\frac{\Gamma_A}{2}}-\frac{e^{\frac{\Gamma_A T}{2}}e^{-\left(\frac{z_0}{V_g}+T\right)s}}{s}\right)$$

$$(1.30)$$

Now we designate the function in brackets as $g(s,z=0)$:

$$g(s,z=0) = \left(\frac{e^{-\frac{z_0}{V_g}s}}{s}-\frac{e^{-\frac{z_0}{V_g}s}}{s+\frac{\Gamma_A}{2}}-\frac{e^{\frac{\Gamma_A T}{2}}e^{-\left(\frac{z_0}{V_g}+T\right)s}}{s}+\frac{e^{\frac{\Gamma_A T}{2}}e^{-\left(\frac{z_0}{V_g}+T\right)s}}{s+\frac{\Gamma_A}{2}}-\frac{e^{-\Gamma_A T}e^{-\frac{z_0}{V_g}s}}{s-\frac{\Gamma_A}{2}}+\frac{e^{-\Gamma_A T}e^{-\frac{z_0}{V_g}s}}{s}+\frac{e^{\frac{\Gamma_A T}{2}}e^{-\left(\frac{z_0}{V_g}+T\right)s}}{s-\frac{\Gamma_A}{2}}-\frac{e^{\frac{\Gamma_A T}{2}}e^{-\left(\frac{z_0}{V_g}+T\right)s}}{s}\right)$$

$$(1.31)$$

Using the properties of Laplace transform we can write that:

$$R^{"}(t,z=0) = \frac{V_g}{\Gamma_A}\left[g(t-\tau,z=0) - g(t-\tau-T_s,z=0)\right]$$

(1.32)

Inverse Laplace transform of equation (1.31) results in:

$$g(t,z=0) = u(t-\frac{z_0}{V_g}) - e^{-\frac{\Gamma_A}{2}\left(t-\frac{z_0}{V_g}\right)}u\left(t-\frac{z_0}{V_g}\right) - e^{-\frac{\Gamma_A T}{2}}u\left(t-\frac{z_0}{V_g}-T\right) + e^{-\frac{\Gamma_A T}{2}}e^{\frac{\Gamma_A}{2}\left(t-\frac{z_0}{V_g}-T\right)}u\left(t-\frac{z_0}{V_g}-T\right) -$$

$$e^{-\Gamma_A T}e^{\frac{\Gamma_A}{2}\left(t-\frac{z_0}{V_g}\right)}u\left(t-\frac{z_0}{V_g}\right) + e^{-\Gamma_A T}u\left(t-\frac{z_0}{V_g}\right) + e^{-\frac{\Gamma_A T}{2}}e^{\frac{\Gamma_A}{2}\left(t-\frac{z_0}{V_g}-T\right)}u\left(t-\frac{z_0}{V_g}-T\right) - e^{-\frac{\Gamma_A T}{2}}u\left(t-\frac{z_0}{V_g}-T\right)$$

(1.33)

Equation (1.33) can be written in simpler form:

$$g(t,z=0) = u(t-\frac{z_0}{V_g})\left[1 - e^{-\frac{\Gamma_A}{2}\left(t-\frac{z_0}{V_g}\right)} - e^{\frac{\Gamma_A}{2}\left(t-\frac{z_0}{V_g}-2T\right)} + e^{-\Gamma_A T}\right] + u\left(t-\frac{z_0}{V_g}-T\right)\left[e^{-\frac{\Gamma_A}{2}\left(t-\frac{z_0}{V_g}\right)} - 2e^{-\frac{\Gamma_A T}{2}} + e^{\frac{\Gamma_A}{2}\left(t-\frac{z_0}{V_g}-2T\right)}\right]$$

(1.34)

Using the equation (1.32) we can write the final form of the $R^{"}(t,z=0)$:

$$R^{"}(t,z=0) = \frac{V_g}{\Gamma_A}\left\{u(t-\frac{z_0}{V_g}-\tau)\left[1 - e^{-\frac{\Gamma_A}{2}\left(t-\frac{z_0}{V_g}-\tau\right)} - e^{\frac{\Gamma_A}{2}\left(t-\frac{z_0}{V_g}-2T-\tau\right)} + e^{-\Gamma_A T}\right] + u\left(t-\frac{z_0}{V_g}-T-\tau\right)\left[e^{-\frac{\Gamma_A}{2}\left(t-\frac{z_0}{V_g}-\tau\right)} - 2e^{-\frac{\Gamma_A T}{2}} + e^{\frac{\Gamma_A}{2}\left(t-\frac{z_0}{V_g}-2T-\tau\right)}\right] -$$

$$u(t-\frac{z_0}{V_g}-\tau-T_s)\left[1 - e^{-\frac{\Gamma_A}{2}\left(t-\frac{z_0}{V_g}-\tau-T_s\right)} - e^{\frac{\Gamma_A}{2}\left(t-\frac{z_0}{V_g}-2T-\tau-T_s\right)} + e^{-\Gamma_A T}\right] + u\left(t-\frac{z_0}{V_g}-T-\tau-T_s\right)\left[e^{-\frac{\Gamma_A}{2}\left(t-\frac{z_0}{V_g}-\tau-T_s\right)} - 2e^{-\frac{\Gamma_A T}{2}} + e^{\frac{\Gamma_A}{2}\left(t-\frac{z_0}{V_g}-2T-\tau-T_s\right)}\right]\right\}$$

(1.35)

Finally we can write the reflected wave at the position z=0 as:

$$R(z=0,t) = R^{'}(t,z=0) + R^{"}(t,z=0)$$

(1.36)

Appendix C.

Solution of the integrals (3.56), (3.57), and (3.58).

We repeat the integral (3.56) herein:

$$\widetilde{R}'(s,z=0)=\int_{\frac{z_0}{2}-\frac{T_1 V_g}{2}}^{\frac{z_0}{2}+\frac{(T_2-T_1)V_g}{2}} e^{-\frac{s}{V_g}z}\left(-u\left(\frac{z_0}{2V_g}+\frac{T_1}{2}+\frac{T_2}{2}-\frac{z_0}{2V_g}+\frac{z}{V_g}\right)e^{-\Gamma_A\left(\frac{z_0}{2V_g}+\frac{T_1}{2}+\frac{T_2}{2}-\frac{z_0}{2V_g}+\frac{z}{V_g}\right)}+u\left(\frac{z_0}{2V_g}+\frac{T_1}{2}+\frac{T_2}{2}-T_1-\frac{z}{V_g}\right)e^{-\Gamma_A\left(\frac{z_0}{2V_g}+\frac{T_1}{2}+\frac{T_2}{2}-T_1-\frac{z}{V_g}\right)}\right)e^{-\tau s}\frac{e^{-\frac{z}{V_g}s}}{s}\left(1-e^{-T_s s}\right)dz$$

(1.37)

First we see that step function are all the time positive in the range of integration, thus we can rewrite the integral (1.37) as:

$$\widetilde{R}'(s,z=0)=\int_{\frac{z_0}{2}-\frac{T_1 V_g}{2}}^{\frac{z_0}{2}+\frac{(T_2-T_1)V_g}{2}} e^{-\frac{s}{V_g}z}\left(-e^{-\Gamma_A\left(\frac{z_0}{2V_g}+\frac{T_1}{2}+\frac{T_2}{2}-\frac{z_0}{2V_g}+\frac{z}{V_g}\right)}+e^{-\Gamma_A\left(\frac{z_0}{2V_g}+\frac{T_1}{2}+\frac{T_2}{2}-T_1-\frac{z}{V_g}\right)}\right)\frac{e^{-\tau s}e^{-\frac{z}{V_g}s}}{s}\left(1-e^{-T_s s}\right)dz$$

(1.38)

By taking the constants out of the integral we arrive to:

$$\widetilde{R}'(s,z=0)=\frac{e^{-\tau s}}{s}\left(1-e^{-T_s s}\right)\left[-e^{-\Gamma_A\left(\frac{T_1}{2}+\frac{T_2}{2}-\frac{z_0}{2V_g}\right)}\int_{\frac{z_0}{2}-\frac{T_1 V_g}{2}}^{\frac{z_0}{2}+\frac{(T_2-T_1)V_g}{2}} e^{-\frac{s}{V_g}z-\Gamma_A\frac{z}{V_g}}dz+e^{-\Gamma_A\left(\frac{z_0}{2V_g}-\frac{T_1}{2}+\frac{T_2}{2}\right)}\int_{\frac{z_0}{2}-\frac{T_1 V_g}{2}}^{\frac{z_0}{2}+\frac{(T_2-T_1)V_g}{2}} e^{-\frac{s}{V_g}z+\Gamma_A\frac{z}{V_g}}dz\right]$$

(1.39)

Now we can solve two integrals in the expression (1.39):

$$\widetilde{R}'(s,z=0)=\frac{e^{-\tau s}}{s}\left(1-e^{-T_s s}\right)\left[-\frac{e^{-\Gamma_A\left(\frac{T_1}{2}+\frac{T_2}{2}-\frac{z_0}{2V_g}\right)}V_g}{2s+\Gamma_A}\left\{e^{-\frac{z_0}{V_g}s+T_1 s}e^{-\frac{\Gamma_A z_0}{2V_g}+\frac{\Gamma_A T_1}{2}}-e^{-\frac{z_0}{V_g}s-(T_2-T_1)s}e^{-\frac{\Gamma_A z_0}{2V_g}-\frac{\Gamma_A(T_2-T_1)}{2}}\right\}+\frac{e^{-\Gamma_A\left(\frac{z_0}{2V_g}-\frac{T_1}{2}+\frac{T_2}{2}\right)}V_g}{2s-\Gamma_A}\left\{e^{-\frac{z_0}{V_g}s+T_1 s}e^{\frac{\Gamma_A z_0}{2V_g}-\frac{\Gamma_A T_1}{2}}-e^{-\frac{z_0}{V_g}s-(T_2-T_1)s}e^{\frac{\Gamma_A z_0}{2V_g}+\frac{\Gamma_A(T_2-T_1)}{2}}\right\}\right]$$

(1.40)

Equation (1.40) can be further simplified:

$$\widetilde{R}'(s,z=0)=\frac{e^{-\tau s}}{s}\left(1-e^{-T_s s}\right)V_g\left[-\frac{e^{-\Gamma_A\left(\frac{T_1}{2}+\frac{T_2}{2}-\frac{z_0}{2V_g}\right)}V_g}{2s+\Gamma_A}\left\{e^{-\frac{z_0}{V_g}s+T_1 s}e^{-\frac{\Gamma_A z_0}{2V_g}+\frac{\Gamma_A T_1}{2}}-e^{-\frac{z_0}{V_g}s-(T_2-T_1)s}e^{-\frac{\Gamma_A z_0}{2V_g}-\frac{\Gamma_A(T_2-T_1)}{2}}\right\}+\frac{e^{-\Gamma_A\left(\frac{z_0}{2V_g}-\frac{T_1}{2}+\frac{T_2}{2}\right)}V_g}{2s-\Gamma_A}\left\{e^{-\frac{z_0}{V_g}s+T_1 s}e^{+\frac{\Gamma_A z_0}{2V_g}-\frac{\Gamma_A T_1}{2}}-e^{-\frac{z_0}{V_g}s-(T_2-T_1)s}e^{+\frac{\Gamma_A z_0}{2V_g}+\frac{\Gamma_A(T_2-T_1)}{2}}\right\}\right]$$

(1.41)

After multiplying the exponential terms inside the square brackets we obtain:

$$\widetilde{R}'(s,z=0)=\frac{e^{-\tau s}}{2}\left(1-e^{-T_s s}\right)V_g\left[-\frac{e^{-\left(\frac{z_0}{V_g}-T_1\right)s}}{s\left(s+\frac{\Gamma_A}{2}\right)}e^{\frac{\Gamma_A T_2}{2}}+\frac{e^{-\left(\frac{z_0}{V_g}+(T_2-T_1)\right)s}}{s\left(s+\frac{\Gamma_A}{2}\right)}e^{-\Gamma_A T_2}+\frac{e^{-\left(\frac{z_0}{V_g}-T_1\right)s}}{s\left(s-\frac{\Gamma_A}{2}\right)}e^{\frac{\Gamma_A T_2}{2}}-\frac{e^{-\left(\frac{z_0}{V_g}+(T_2-T_1)\right)s}}{s\left(s-\frac{\Gamma_A}{2}\right)}\right]$$

(1.42)

Using the cover-up method we write the expression (1.42) as:

$$\widetilde{R}\,'(s,z=0)=\frac{e^{-\tau s}}{\Gamma_A}\left(1-e^{-T_s s}\right)V_g\left[-\frac{e^{-\frac{\Gamma_A T_2}{2}}e^{-\left(\frac{z_0}{V_g}-T_1\right)s}}{s}+\frac{e^{-\frac{\Gamma_A T_2}{2}}e^{-\left(\frac{z_0}{V_g}-T_1\right)s}}{\left(s+\frac{\Gamma_A}{2}\right)}+\frac{e^{-\Gamma_A T_2}e^{-\left(\frac{z_0}{V_g}+(T_2-T_1)\right)s}}{s}-\frac{e^{-\Gamma_A T_2}e^{-\left(\frac{z_0}{V_g}+(T_2-T_1)\right)s}}{s\left(s+\frac{\Gamma_A}{2}\right)}+\frac{e^{-\frac{\Gamma_A T_2}{2}}e^{-\left(\frac{z_0}{V_g}-T_1\right)s}}{\left(s-\frac{\Gamma_A}{2}\right)}-\frac{e^{-\frac{\Gamma_A T_2}{2}}e^{-\left(\frac{z_0}{V_g}-T_1\right)s}}{s}-\frac{e^{-\left(\frac{z_0}{V_g}+(T_2-T_1)\right)s}}{\left(s-\frac{\Gamma_A}{2}\right)}+\frac{e^{-\left(\frac{z_0}{V_g}+(T_2-T_1)\right)s}}{s}\right]$$

(1.43)

Now if we define a new function $\widetilde{f}\,'(s)$ as

$$\widetilde{f}\,'(s)=\left[-\frac{e^{-\frac{\Gamma_A T_2}{2}}e^{-\left(\frac{z_0}{V_g}-T_1\right)s}}{s}+\frac{e^{-\frac{\Gamma_A T_2}{2}}e^{-\left(\frac{z_0}{V_g}-T_1\right)s}}{\left(s+\frac{\Gamma_A}{2}\right)}+\frac{e^{-\Gamma_A T_2}e^{-\left(\frac{z_0}{V_g}+(T_2-T_1)\right)s}}{s}-\frac{e^{-\Gamma_A T_2}e^{-\left(\frac{z_0}{V_g}+(T_2-T_1)\right)s}}{s\left(s+\frac{\Gamma_A}{2}\right)}+\frac{e^{-\frac{\Gamma_A T_2}{2}}e^{-\left(\frac{z_0}{V_g}-T_1\right)s}}{\left(s-\frac{\Gamma_A}{2}\right)}-\frac{e^{-\frac{\Gamma_A T_2}{2}}e^{-\left(\frac{z_0}{V_g}-T_1\right)s}}{s}-\frac{e^{-\left(\frac{z_0}{V_g}+(T_2-T_1)\right)s}}{\left(s-\frac{\Gamma_A}{2}\right)}+\frac{e^{-\left(\frac{z_0}{V_g}+(T_2-T_1)\right)s}}{s}\right]$$

(1.44)

we can see that according to the properties of Laplace transform:

$$R\,'(t,z=0)=\frac{V_g}{\Gamma_A}\left[f(t-\tau)-f(t-\tau-T_s)\right]$$

(1.45)

Taking the inverse Laplace transform of the expression (1.44) we get:

$$f\,'(t,z=0)=-u\left(t-\left(\frac{z_0}{V_g}-T_2\right)\right)\left[2e^{-\frac{\Gamma_A T_2}{2}}-e^{-\frac{\Gamma_A}{2}\left(t-\frac{z_0}{V_g}+T_1+T_2\right)}-e^{-\frac{\Gamma_A}{2}\left(t-\frac{z_0}{V_g}+T_1-T_2\right)}\right]-u\left(t-\left(\frac{z_0}{V_g}+(T_2-T_1)\right)\right)\left[e^{-\frac{\Gamma_A}{2}\left(t-\frac{z_0}{V_g}-(T_2-T_1)+2T_2\right)}-e^{-\Gamma_A T_2}-1+e^{-\frac{\Gamma_A}{2}\left(t-\frac{z_0}{V_g}-(T_2-T_1)\right)}\right]$$

(1.46)

Thus, using equation (1.45) we can write the expression for $R\,'(t,z=0)$:

$$R\,'(t,z=0)=\frac{V_g}{\Gamma_A}\left(u\left(t-\frac{z_0}{V_g}+T_1-\tau\right)\cdot\left\{+e^{\frac{\Gamma_A}{2}\left(t-\frac{z_0}{V_g}+T_1-T_2-\tau\right)}-2e^{\left(-\frac{\Gamma_A T_2}{2}\right)}+e^{-\frac{\Gamma_A}{2}\left(t-\frac{z_0}{V_g}+T_1+T_2-\tau\right)}\right\}+u\left(t-\frac{z_0}{V_g}-T_2+T_1-\tau\right)\left\{1-e^{-\frac{\Gamma_A}{2}\left(t-\frac{z_0}{V_g}-T_2+T_1-\tau\right)}+e^{-\Gamma_A T}-e^{-\frac{\Gamma_A}{2}\left(t-\frac{z_0}{V_g}+T_2+T_1-\tau\right)}\right\}\right)-$$

$$\frac{V_g}{\Gamma_A}\left(u\left(t-\frac{z_0}{V_g}+T_1-\tau-T_s\right)\cdot\left\{+e^{\frac{\Gamma_A}{2}\left(t-\frac{z_0}{V_g}+T_1-T_2-\tau-T_s\right)}-2e^{\left(-\frac{\Gamma_A T_2}{2}\right)}+e^{-\frac{\Gamma_A}{2}\left(t-\frac{z_0}{V_g}+T_1+T_2-\tau-T_s\right)}\right\}+u\left(t-\frac{z_0}{V_g}-T_2+T_1-\tau-T_s\right)\left\{1-e^{-\frac{\Gamma_A}{2}\left(t-\frac{z_0}{V_g}-T_2+T_1-\tau-T_s\right)}+e^{-\Gamma_A T}-e^{-\frac{\Gamma_A}{2}\left(t-\frac{z_0}{V_g}+T_2+T_1-\tau-T_s\right)}\right\}\right)$$

(1.47)

Now we find the solution for the second part of the reflection $\widetilde{R}\,''(s,z=0)$:

$$\widetilde{R}\,''(s,z=0)=\int_{\frac{z_0}{2}+\frac{(T_2-T_1)V_g}{2}}^{\frac{z_0}{2}}e^{-\frac{s}{V_g}z}\left(-u\left(\frac{z_0}{2V_g}+\frac{T_1}{2}+\frac{T_2}{2}-\frac{z_0}{V_g}+\frac{z}{V_g}\right)e^{-\Gamma_A\left(\frac{z_0}{2V_g}+\frac{T_1}{2}+\frac{T_2}{2}-\frac{z_0}{V_g}+\frac{z}{V_g}\right)}+u\left(\frac{z_0}{2V_g}+\frac{T_1}{2}+\frac{T_2}{2}-T_2-\frac{z_0}{V_g}+\frac{z}{V_g}\right)e^{-\Gamma_A\left(\frac{z_0}{2V_g}+\frac{T_1}{2}+\frac{T_2}{2}-T_2-\frac{z_0}{V_g}+\frac{z}{V_g}\right)}\right)\frac{e^{-\tau s}e^{-\frac{z}{V_g}s}}{s}\left(1-e^{-T_s s}\right)dz$$

(1.48)

As before we can eliminate step function since in the region of integration they equal to unity. Thus, we rewrite (1.48) as:

$$\widetilde{R}^{"}(s,z=0)=\frac{e^{-\tau s}}{s}\left(1-e^{-T_s s}\right)\left[e^{-\Gamma_A\left(-\frac{z_0}{2V_g}+\frac{T_1}{2}+\frac{T_2}{2}\right)}\int_{\frac{z_0}{2}+\frac{(T_2-T_1)V_g}{2}}^{\frac{z_0}{2}}e^{-\left(\frac{2s}{V_g}+\frac{\Gamma_A}{V_g}\right)z}dz-e^{-\Gamma_A\left(-\frac{z_0}{2V_g}+\frac{T_1}{2}+\frac{T_2}{2}\right)}\int_{\frac{z_0}{2}+\frac{(T_2-T_1)V_g}{2}}^{\frac{z_0}{2}}e^{-\left(\frac{2s}{V_g}+\frac{\Gamma_A}{V_g}\right)z}dz\right]$$

$$(1.49)$$

Integral in the expression (1.49) can be factored out:

$$\widetilde{R}^{"}(s,z=0)=\frac{e^{-\tau s}}{s}\left(1-e^{-T_s s}\right)\int_{\frac{z_0}{2}+\frac{(T_2-T_1)V_g}{2}}^{\frac{z_0}{2}}e^{-\left(\frac{2s}{V_g}+\frac{\Gamma_A}{V_g}\right)z}dz\left[e^{-\Gamma_A\left(-\frac{z_0}{2V_g}+\frac{T_1}{2}+\frac{T_2}{2}\right)}-e^{-\Gamma_A\left(-\frac{z_0}{2V_g}+\frac{T_1}{2}+\frac{T_2}{2}\right)}\right]\quad(1.50)$$

Solving the integral we obtain:

$$\widetilde{R}^{"}(s,z=0)=\frac{e^{-\tau s}}{s}\left(1-e^{-T_s s}\right)\frac{V_g}{2s+\Gamma_A}\left(e^{-\left(\frac{2s+\Gamma_A}{V_g}\right)\frac{(z_0+(T_2-T_1)V_g)}{2}}-e^{-\left(\frac{2s+\Gamma_A}{V_g}\right)\frac{z_0}{2}}\right)\left[e^{-\Gamma_A\left(-\frac{z_0}{2V_g}+\frac{T_1}{2}+\frac{T_2}{2}\right)}-e^{-\Gamma_A\left(-\frac{z_0}{2V_g}+\frac{T_1}{2}+\frac{T_2}{2}\right)}\right]$$

$$(1.51)$$

Rearranging the terms we get:

$$\widetilde{R}^{"}(s,z=0)=\frac{e^{-\tau s}}{s}\left(1-e^{-T_s s}\right)\frac{V_g}{2}\left(\frac{e^{-\left(\frac{z_0}{V_g}+(T_2-T_1)\right)s}e^{-\Gamma_A\left(\frac{z_0}{2V_g}+\frac{(T_2-T_1)}{2}\right)}}{s\left(s+\frac{\Gamma_A}{2}\right)}-\frac{e^{-\frac{z_0}{V_g}s}e^{-\frac{\Gamma_A z_0}{2V_g}}}{s\left(s+\frac{\Gamma_A}{2}\right)}\right)\left[e^{-\Gamma_A\left(-\frac{z_0}{2V_g}+\frac{T_1}{2}+\frac{T_2}{2}\right)}-e^{-\Gamma_A\left(-\frac{z_0}{2V_g}+\frac{T_1}{2}+\frac{T_2}{2}\right)}\right]$$

$$(1.52)$$

Using cover-up method we write simpler fractions inside the brackets of (1.52):

$$\widetilde{R}^{"}(s,z=0)=e^{-\tau s}\left(1-e^{-T_s s}\right)\frac{V_g}{\Gamma_A}e^{-\frac{\Gamma_A T_2}{2}}\left(e^{+\frac{\Gamma_A T_1}{2}}-e^{-\frac{\Gamma_A T_2}{2}}\right)\left(e^{-\frac{\Gamma_A(T_2-T_1)}{2}}\left[\frac{e^{-\left(\frac{z_0}{V_g}+(T_2-T_1)\right)s}}{s}-\frac{e^{-\left(\frac{z_0}{V_g}+(T_2-T_1)\right)s}}{s+\frac{\Gamma_A}{2}}\right]-\frac{e^{-\frac{z_0}{V_g}s}}{s}+\frac{e^{-\frac{z_0}{V_g}s}}{s+\frac{\Gamma_A}{2}}\right)\quad(1.53)$$

We define new function $\widetilde{f}^{"}(s)$ as:

$$\widetilde{f}^{"}(s)=e^{\frac{\Gamma_A(T_2-T_1)}{2}}\left[\frac{e^{-\left(\frac{z_0}{V_g}+(T_2-T_1)\right)s}}{s}-\frac{e^{-\left(\frac{z_0}{V_g}+(T_2-T_1)\right)s}}{s+\frac{\Gamma_A}{2}}\right]-\frac{e^{-\frac{z_0}{V_g}s}}{s}+\frac{e^{-\frac{z_0}{V_g}s}}{s+\frac{\Gamma_A}{2}}\quad(1.54)$$

Thus, we can see that $R^{"}(t,z=0)$ will be given as:

$$R''(t, z=0) = \frac{V_g}{\Gamma_A} e^{-\frac{\Gamma_A T_2}{2}} \left(e^{+\frac{\Gamma_A T_1}{2}} - e^{-\frac{\Gamma_A T_2}{2}} \right) \left[f''(t-\tau) - f''(t-\tau-T_s) \right] \tag{1.55}$$

We find the Laplace transform of (1.54):

$$f''(t) = u\left(t - \frac{z_0}{V_g} - (T_2 - T_1) \right) \left[e^{-\Gamma_A \frac{(T_2-T_1)}{2}} - e^{-\frac{\Gamma_A}{2}\left(t - \frac{z_0}{V_g} \right)} \right] + u\left(t - \frac{z_0}{V_g} \right) \left[e^{-\frac{\Gamma_A}{2}\left(t - \frac{z_0}{V_g} \right)} - 1 \right] \tag{1.56}$$

So now we can write the expression for the $R''(t, z=0)$:

$$R''(t, z=0) = \frac{V_g}{\Gamma_A} \left(e^{-\frac{\Gamma_A}{2}(T_1-T_2)} - e^{-\frac{\Gamma_A}{2}(T_1+T_2)} \right) \left[u\left(t - \frac{z_0}{V_g} - T_2 + T_1 - \tau \right) \cdot \left\{ e^{-\frac{\Gamma_A(T_2-T_1)}{2}} - e^{-\frac{\Gamma_A}{2}\left(t - \frac{z_0}{V_g} - \tau \right)} \right\} + u\left(t - \frac{z_0}{V_g} - \tau \right) \left\{ e^{} \right. \right.$$

$$\left(u\left(t - \frac{z_0}{V_g} - T_2 + T_1 - \tau - T_s \right) \cdot \left\{ e^{-\frac{\Gamma_A(T_2-T_1)}{2}} - e^{-\frac{\Gamma_A}{2}\left(t - \frac{z_0}{V_g} - \tau - T_s \right)} \right\} + u\left(t - \frac{z_0}{V_g} - \tau - T_s \right) \left\{ e^{-\frac{\Gamma_A}{2}\left(t - \frac{z_0}{V_g} - \tau - T_s \right)} - 1 \right\} \right) \right]$$

$$\tag{1.57}$$

Now we find the solution for the last part of the reflected wave $R'''(t, z=0)$. We start with the expression:

$$\widetilde{R'''}(s, z=0) = \int_{\frac{z_0}{2}}^{\frac{z_0}{2}+\frac{T_2 V_g}{2}} e^{-\frac{s}{V_g}z} \left(-u\left(\frac{z_0}{2V_g} + \frac{T_1}{2} + \frac{T_2}{2} - \frac{z}{V_g} \right) e^{-\Gamma_A\left(\frac{z_0}{2V_g} + \frac{T_1}{2} + \frac{T_2}{2} - \frac{z}{V_g} \right)} + u\left(\frac{z_0}{2V_g} + \frac{T_1}{2} + \frac{T_2}{2} - T_2 - \frac{z_0}{V_g} + \frac{z}{V_g} \right) e^{-\Gamma_A\left(\frac{z_0}{2V_g} + \frac{T_1}{2} + \frac{T_2}{2} - T_2 - \frac{z_0}{V_g} + \frac{z}{V_g} \right)} \right) \frac{e^{-\tau s} e^{-\frac{z}{V_g}s}}{s} \left(1 - e^{-T_s s} \right) dz$$

$$\tag{1.58}$$

As in previous solutions we see that step functions take equal to 1 for the region of integration. Thus, we rewrite (1.58) as:

$$\widetilde{R'''}(s, z=0) = \frac{e^{-\tau s}}{s} \left(1 - e^{-T_s s} \right) \left[e^{-\Gamma_A\left(-\frac{z_0}{2V_g} + \frac{T_1}{2} - \frac{T_2}{2} \right)} \int_{\frac{z_0}{2}}^{\frac{z_0}{2}+\frac{T_2 V_g}{2}} e^{-\frac{(2s+\Gamma_A)}{V_g}z} dz - e^{-\Gamma_A\left(\frac{z_0}{2V_g} + \frac{T_1}{2} + \frac{T_2}{2} \right)} \int_{\frac{z_0}{2}}^{\frac{z_0}{2}+\frac{T_2 V_g}{2}} e^{-\frac{(2s-\Gamma_A)}{V_g}z} dz \right]$$

$$\tag{1.59}$$

Solving the integrals results in:

$$\widetilde{R'''}(s, z=0) = \frac{e^{-\tau s}}{s} \left(1 - e^{-T_s s} \right) \left[e^{-\Gamma_A\left(-\frac{z_0}{2V_g} + \frac{T_1}{2} - \frac{T_2}{2} \right)} \frac{V_g}{2s+\Gamma_A} \left\{ e^{-\frac{(2s+\Gamma_A)}{V_g}\frac{z_0}{2}} - e^{-\frac{(2s+\Gamma_A)(z_0+T_2 V_g)}{V_g}\frac{}{2}} \right\} - e^{-\Gamma_A\left(\frac{z_0}{2V_g} + \frac{T_1}{2} + \frac{T_2}{2} \right)} \frac{V_g}{2s-\Gamma_A} \left\{ e^{-\frac{(2s-\Gamma_A)z_0}{V_g}\frac{}{2}} - e^{-\frac{(2s-\Gamma_A)(z_0+T_2 V_g)}{V_g}\frac{}{2}} \right\} \right]$$

$$\tag{1.60}$$

Rearranging (1.60) we get:

$$\widetilde{R}''(s,z=0)=\frac{e^{-\tau s}}{s}\left(1-e^{-T_s s}\right)\left[e^{-\Gamma_A\left(-\frac{z_0}{2V_g}+\frac{T_1}{2}-\frac{T_2}{2}\right)}\frac{V_g}{2s+\Gamma_A}\left\{e^{-\frac{z_0}{V_g}s}e^{\frac{\Gamma_A z_0}{V_g 2}}-e^{-\left(\frac{z_0}{V_g}+T_2\right)s}e^{-\frac{\Gamma_A z_0}{V_g 2}-\frac{\Gamma_A T_2}{2}}\right\}-e^{-\Gamma_A\left(\frac{z_0}{2V_g}+\frac{T_1}{2}+\frac{T_2}{2}\right)}\frac{V_g}{2s-\Gamma_A}\left\{e^{-\frac{z_0}{V_g}s}e^{\frac{\Gamma_A z_0}{V_g 2}}-e^{-\left(\frac{z_0}{V_g}+T_2\right)s}e^{\frac{\Gamma_A z_0}{V_g 2}+\frac{\Gamma_A T_2}{2}}\right\}\right]$$

$$(1.61)$$

We can simplify further (1.61) as:

$$\widetilde{R}''(s,z=0)=\frac{e^{-\tau s}}{s}\left(1-e^{-T_s s}\right)\frac{V_g}{2}\left[e^{-\Gamma_A\left(\frac{T_1}{2}-\frac{T_2}{2}\right)}\left\{\frac{e^{-\frac{z_0}{V_g}s}}{s+\frac{\Gamma_A}{2}}-\frac{e^{-\left(\frac{z_0}{V_g}+T_2\right)s}e^{-\frac{\Gamma_A T_2}{2}}}{s+\frac{\Gamma_A}{2}}\right\}-e^{-\Gamma_A\left(\frac{T_1}{2}+\frac{T_2}{2}\right)}\left\{\frac{e^{-\frac{z_0}{V_g}s}}{s-\frac{\Gamma_A}{2}}-\frac{e^{-\left(\frac{z_0}{V_g}+T_2\right)s}e^{\frac{\Gamma_A T_2}{2}}}{s-\frac{\Gamma_A}{2}}\right\}\right]$$

$$(1.62)$$

Using cover up method we arrive at:

$$\widetilde{R}''(s,z=0)=e^{-\tau s}\left(1-e^{-T_s s}\right)\frac{V_g}{\Gamma_A}\left[e^{-\Gamma_A\left(\frac{T_1}{2}-\frac{T_2}{2}\right)}\left\{\frac{e^{-\frac{z_0}{V_g}s}}{s}-\frac{e^{-\frac{z_0}{V_g}s}}{s+\frac{\Gamma_A}{2}}-\frac{e^{-\left(\frac{z_0}{V_g}+T_2\right)s}e^{-\frac{\Gamma_A T_2}{2}}}{s}+\frac{e^{-\left(\frac{z_0}{V_g}+T_2\right)s}e^{-\frac{\Gamma_A T_2}{2}}}{s+\frac{\Gamma_A}{2}}\right\}-e^{-\Gamma_A\left(\frac{T_1}{2}+\frac{T_2}{2}\right)}\left\{\frac{e^{-\frac{z_0}{V_g}s}}{s-\frac{\Gamma_A}{2}}-\frac{e^{-\frac{z_0}{V_g}s}}{s}-\frac{e^{-\left(\frac{z_0}{V_g}+T_2\right)s}e^{\frac{\Gamma_A T_2}{2}}}{s-\frac{\Gamma_A}{2}}+\frac{e^{-\left(\frac{z_0}{V_g}+T_2\right)s}e^{\frac{\Gamma_A T_2}{2}}}{s}\right\}\right]$$

$$(1.63)$$

We define new function $\widetilde{f}'''(s)$ as:

$$\widetilde{f}'''(s)=e^{-\Gamma_A\left(\frac{T_1}{2}-\frac{T_2}{2}\right)}\left\{\frac{e^{-\frac{z_0}{V_g}s}}{s}-\frac{e^{-\frac{z_0}{V_g}s}}{s+\frac{\Gamma_A}{2}}-\frac{e^{-\left(\frac{z_0}{V_g}+T_2\right)s}e^{-\frac{\Gamma_A T_2}{2}}}{s}+\frac{e^{-\left(\frac{z_0}{V_g}+T_2\right)s}e^{-\frac{\Gamma_A T_2}{2}}}{s+\frac{\Gamma_A}{2}}\right\}-e^{-\Gamma_A\left(\frac{T_1}{2}+\frac{T_2}{2}\right)}\left\{\frac{e^{-\frac{z_0}{V_g}s}}{s-\frac{\Gamma_A}{2}}-\frac{e^{-\frac{z_0}{V_g}s}}{s}-\frac{e^{-\left(\frac{z_0}{V_g}+T_2\right)s}e^{\frac{\Gamma_A T_2}{2}}}{s-\frac{\Gamma_A}{2}}+\frac{e^{-\left(\frac{z_0}{V_g}+T_2\right)s}e^{\frac{\Gamma_A T_2}{2}}}{s}\right\}$$

$$(1.64)$$

Using the properties of Laplace transform we can see that:

$$\widetilde{R}''(s,z=0)=\frac{V_g}{\Gamma_A}\left[f'''(t-\tau)-f'''(t-\tau-T_s)\right]$$

$$(1.65)$$

We find the inverse Laplace transform of the equation (1.64):

$$f'''(t)=u\left(t-\frac{z_0}{V_g}\right)\left\{e^{-\frac{\Gamma_A(T_1-T_2)}{2}}-e^{-\frac{\Gamma_A}{2}\left(t-\frac{z_0}{V_g}+T_1-T_2\right)}-e^{-\frac{\Gamma_A}{2}\left(t-\frac{z_0}{V_g}-T_1-T_2\right)}+e^{-\frac{\Gamma_A(T_1+T_2)}{2}}\right\}+u\left(t-\frac{z_0}{V_g}-T_2\right)\left\{e^{-\frac{\Gamma_A}{2}\left(t-\frac{z_0}{V_g}+T_1-T_2\right)}-2e^{-\frac{\Gamma_A T_1}{2}}+e^{\frac{\Gamma_A}{2}\left(t-\frac{z_0}{V_g}-T_1-T_2\right)}\right\}$$

$$(1.66)$$

Thus, using (1.65) we arrive to the expression of $R'''(t,z=0)$ in the following form:

$$R''(t,z=0)=\frac{V_g}{\Gamma_A}\left[u\left(t-\frac{z_0}{V_g}-\tau\right)\cdot\left\{\mathrm{e}^{-\Gamma_A\left(\frac{T_1}{2}-\frac{T_2}{2}\right)}-e^{-\frac{\Gamma_A}{2}\left(t-\frac{z_0}{V_g}+T_1-T_2-\tau\right)}-e^{+\frac{\Gamma_A}{2}\left(t-\frac{z_0}{V_g}-T_1-T_2-\tau\right)}+\mathrm{e}^{-\Gamma_A\left(\frac{T_1}{2}+\frac{T_2}{2}\right)}\right\}+u\left(t-\frac{z_0}{V_g}-T_2-\tau\right)\left\{e^{-\frac{\Gamma_A}{2}\left(t-\frac{z_0}{V_g}-T_2+T_1-\tau\right)}-2e^{-\frac{\Gamma_A T}{2}}+e^{\frac{\Gamma_A}{2}\left(t-\frac{z_0}{V_g}-T_2-T_1-\tau\right)}\right\}-\right.$$

$$\left(u\left(t-\frac{z_0}{V_g}-\tau-T_s\right)\cdot\left\{\mathrm{e}^{-\Gamma_A\left(\frac{T_1}{2}-\frac{T_2}{2}\right)}-e^{-\frac{\Gamma_A}{2}\left(t-\frac{z_0}{V_g}+T_1-T_2-\tau-T_s\right)}-e^{+\frac{\Gamma_A}{2}\left(t-\frac{z_0}{V_g}-T_1-T_2-\tau-T_s\right)}+\mathrm{e}^{-\Gamma_A\left(\frac{T_1}{2}+\frac{T_2}{2}\right)}\right\}+u\left(t-\frac{z_0}{V_g}-T_2-\tau-T_s\right)\left\{e^{-\frac{\Gamma_A}{2}\left(t-\frac{z_0}{V_g}-T_2+T_1-\tau-T_s\right)}-2e^{-\frac{\Gamma_A T}{2}}+e^{\frac{\Gamma_A}{2}\left(t-\frac{z_0}{V_g}-T_2-T_1-\tau-T_s\right)}\right\}\right)\right]$$

$$(1.67)$$

Nikolay Primerov

Ch. du Bochet 29   29 years
1025 St. Sulpice, Switzerland   Single
Mobile: +41 79 26 63 673   Russian
nikolayprimerov@gmail.com
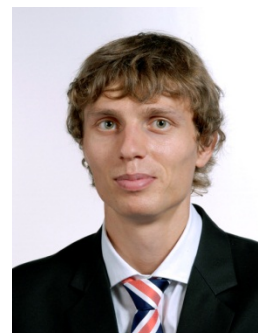
Professional Experience

| 2008 – present | **EPFL, Group for Fiber Optics**, **Ph.D.** |

2008 – present   **EPFL, Group for Fiber Optics**, **Ph.D.**
During my Ph.D. in the field of Nonlinear Fiber Optics I developed and experimentally demonstrated:

- **High resolution temperature and stress distributed fiber sensors**;
  - ✓ New sensor has record **spatial resolution of 1 cm;**
  - ✓ Best paper at 20th Conference on Optical Fiber Sensors (OFS20), Edinburg, Scotland (2009);
- **All-optical signal delay lines** (optical memory) using dynamic grating reflectors **for telecommunication and radio frequency signals**;
  - ✓ Distortionless delay line with expanded buffer time;
- Dynamic grating based **optical processor**, which allows **true time reversal** of data packets, **optical integration and differentiation**;
  - ✓ Processor can perform new operations at high data rates;
  - ✓ Best student paper award (2nd place) from Optical Society of America at the Photonics congress in Toronto, Canada (2011).

Collaborations with researchers from Spain, Korea and Israel resulted in considerable number of articles for top ranked scientific journals and world known conferences.

Acquired competences: organization, creativity, team work

2005 - 2008   **Company "Silver fiber optics", Russia. Process developer**
As one of the 3 process engineers I conceptualized and constructed a **new plant for growing crystals** of solid solution of silver halides.
New plant offers:
  - ✓ **×10 faster growing speed** without deterioration of optical properties;
  - ✓ **improved homogeneity** of the doped crystals;
From new crystals we extruded high plasticity, nontoxic and non-hygroscopic fibers transparent in extended spectral range (2-20 um). Doped fibers are **the first fiber scintillators** for detection of ionizing radiation.
- **3 patents obtained**.

Acquired competences: communication, team work

2003 – 2005 (summer vacations)   **Company of industrial services "PAUK", Ekaterinburg, Russia**
Industrial rope access alpinist.
As a **leader of the 4-10 alpinist team** it was my responsibility to oversee and deliver the performed construction or/and cleaning services to the customer. Customers were: Trade Center with facilities of ~4000 m^2, office skyscrapers, government buildings, etc.

Acquired competence: responsibility, fatigue management

Education

2008-01.2013	**Ph.D. degree in Photonics, Swiss Federal Institute of Technology (EPFL), Group for fiber optics, directed by Prof. Luc Thévenaz**
	Certificates for **Project management** and **Breakthrough Thinking** courses
2005-2010	**Ph. D. degree in Materials for Electronics, General Physics Institute of Russian Academy of Sciences, Moscow, Russia**
	New silver halide based crystals and optical fibers for mid-infrared spectrum
2003-2005	**Master Degree in Materials for Electronics, Ural Federal University, Ekaterinburg, Russia**
	Constructed and tested new plant for crystal growth based on Bridgmen technique with axial vibration of the melt.
	Growth of semiconductor thin films for development of visible, infrared detectors, and chemical sensors. Development of printed circuit boards for electronic devices

Technical and Computer skills

- ✓ Fiber optic technology with profound knowledge of optical delay lines, distributed temperature/strain sensors, signal processing, and microwave photonics. Short pulse generation. Chromatic dispersion measurement.
- ✓ Infrared crystal growth techniques, with emphasis on Czochralski and Bridgmen-Stockbarger methods
- ✓ Labview, Matlab, Origin, Latex, MS Office, basics in Phyton and AutoCAD

Languages

Russian: Mother tongue
English: Fluent in writing, reading and speaking, C2 European Language Portfolio
French: Intermediate, A2 European Language Portfolio
German: Basics

Activities and Interests

I spend my free time rock or ice climbing in mountains, where I find my "perfect" environment. In 2007 I won the **Ice Climbing World Championship** which was held in Saas-Fee, Switzerland. If I'm not in mountains you can find me playing football/beach volleyball with my friends.

Publications

Journal papers

1. A. Zadok, Y. Antman, N. Primerov, A. Denisov and J. Sancho et al. Random-access distributed fiber sensing, in Laser & Photonics Reviews, p. doi: 10.1002/lpor.201200013, 2012.
2. Y. Antman, N. Primerov, J. Sancho Dura, L. Thévenaz and A. Zadok. Localized and stationary dynamic gratings via stimulated Brillouin scattering with phase modulated pumps, in Optics Express, vol. 20, num. 7, p. 7807, 2012.
3. J. Sancho, N. Primerov, S. Chin, Y. Antman and A. Zadok et al. Tunable and reconfigurable multi-tap microwave photonic filter based on dynamic Brillouin gratings in fibers, in Optics Express, vol. 20, num. 6, p. 6157-6162, 2012.
4. S. Chin, N. Primerov and L. Thevenaz. Sub-centimeter Spatial Resolution in Distributed Fibre Sensing, based on Dynamic Brillouin Grating in Optical Fibers, in IEEE Sensors Journal, vol. 12, num. 1, p. 189-194, 2012.
5. Z. Shmilovitch, N. Primerov, A. Zadok, A. Eyal and S. Chin et al. Dual-pump push-pull polarization control using stimulated Brillouin scattering, in Optics Express, vol. 19, num. 27, p. 25873-25880, 2011.
6. K. Y. Song, S. Chin, N. Primerov and L. Thevenaz. Time-Domain Distributed Fiber Sensor With 1 cm Spatial Resolution Based on Brillouin Dynamic Grating, in Journal of Lightwave Technology, vol. 28, num. 14, p. 2062-2067, 2010.

Conference proceedings

1. N. Primerov, Y. Antman, J. Sancho, A. Zadok and L. Thevenaz. Brillouin distributed sensing using localized and stationary dynamic gratings. Conference on Optical Sensing and Detection II, Brussels, BELGIUM, Proceedings of SPIE, 2012.
2. N. Primerov, Y. Antman, J. Sancho Dura, A. Zadok and L. Thévenaz. Brillouin distributed sensing using localized and stationary dynamic gratings. Photonics Europe - Optical Sensing and Detection II, Brussels, Belgium, Proceedings of SPIE, 2012.
3. Y. Antman, N. Primerov, J. Sancho Dura, L. Thévenaz and A. Zadok. Long Variable Delay and Distributed Sensing Using Stationary and Localized Brillouin Dynamic Gratings. Optical Fiber Communication Conference (OFC), Los Angeles, California, 2012.
4. Y. Antman, N. Primerov, J. Sancho Dura, L. Thévenaz and A. Zadok. Variable delay using stationary and localized Brillouin dynamic gratings. Photonics West - Advances in Slow and Fast Light V, San Francisco, California, USA, 2012.
5. L. Thévenaz, S. Foaleng Mafang, S. H. Chin, N. Primerov and K.-Y. Song. High Spatial and Spectral Resolution Long-Range Sensing Using Brillouin Echoes. Frontiers in Optics, San Jose, California, 2011.
6. L. Thevenaz, N. Primerov, S. Chin and M. Santagiustina. Dynamic Brillouin gratings: A new tool in fibers for all-optical signal processing. 2011 IEEE Photonics Conference (IPC), Arlington, VA, USA, 2011.
7. S. Chin, N. Primerov, S. Sales and L. Thevenaz. Tunable multiplication of the repetition rate of an optical pulse train using dynamic Brillouin gratings in optical fibers. 12th European Quantum Electronics Conference CLEO EUROPE/EQEC, Munich, Germany, 2011.
8. S. H. Chin, N. Primerov and L. Thévenaz. Movable dynamic grating-based optical delay line in polarization maintaining fibers. Slow and Fast Light (SL), Toronto, Canada, 2011.

9. N. Primerov, S. H. Chin, L. Thévenaz, L. Ursini and M. Santagiustina. All-optical calculus based on dynamic Brillouin grating reflectors in optical fibers. Slow and Fast Light (SL), Toronto, Canada, 2011.

10. Z. Shmilovich, A. Eyal, M. Tur, A. Zadok and N. Primerov et al. Polarization pulling based on stimulated Brillouin scattering in a dual-pump configuration . 21st International Conference on Optical Fiber Sensors, Ottawa, Canada, 2011.

11. L. Thévenaz, S. Foaleng Mafang, K.-Y. Song, S. H. Chin and J.-C. Beugnot et al. Recent progress towards centimetric spatial resolution in distributed fibre sensing. Fourth European Workshop on Optical Fibre Sensors, Porto, Portugal, Proceedings of SPIE-The International Society for Optical Engineering, 2010.

12. L. Thevenaz, S. M. Foaleng, K.-Y. Song, S. Chin and N. Primerov et al. Advanced Brillouin-based distributed optical fibre sensors with sub-meter scale spatial resolution. 36th European Conference and Exhibition on Optical Communication - (ECOC 2010), Torino, Italy, 2010.

13. S. Chin, N. Primerov and L. Thevenaz. Photonic delay line for broadband optical signals, based on dynamic grating reflectors in fibers. 2010 36th European Conference and Exhibition on Optical Communication - (ECOC 2010), Torino, Italy, 2010.

14. S. H. Chin, N. Primerov, K.-Y. Song, L. Thévenaz and M. Santagiustina et al. True Time Reversal via Dynamic Brillouin Gratings in Polarization Maintaining Fibers. Nonlinear Photonics (NP), Karlsruhe, Germany, 2010.

15. N. Primerov, S. H. Chin, K.-Y. Song and L. Thévenaz. Ultra Wide Range Tunable Delay Line Using Dynamic Grating Reflectors in Optical Fibers. Optical Fiber Communication Conference (OFC), San Diego, California, USA, 2010.

16. K.-Y. Song, S. Chin, N. Primerov and L. Thevenaz. Time-domain distributed sensor with 1 cm spatial resolution based on Brillouin dynamic gratings. 20th International Conference on Optical Fibre Sensors, Edinburgh, United Kingdom, 2009.